Shock-physics based enhancement of Reynolds stress turbulence models for high-speed flows

Submitted in partial fulfillment of the requirements
for the degree of

Doctor of Philosophy

by

Jagadish Babu Vemula
(Roll No. 134010005)

Supervisor:
Prof. Krishnendu Sinha

Department of Aerospace Engineering
Indian Institute of Technology Bombay

2021

Acceptance Certificate

Department of Aerospace Engineering
Indian Institute of Technology Bombay

The thesis entitled "Shock-physics based enhancement of Reynolds stress turbulence models for high-speed flows" submitted by Jagadish Babu Vemula (Roll No. 134010005) may be accepted for being evaluated.

Date: 8 March 2021

Prof. Krishnendu Sinha

Approval Sheet

This thesis entitled "Shock-physics based enhancement of Reynolds stress turbulence models for high-speed flows" by Jagadish Babu Vemula is approved for the degree of Doctor of Philosophy.

Examiners

Supervisor (s)

Chairman

Date: 10 March 2021

Place: Mumbai

Declaration

I declare that this written submission represents my ideas in my own words and where others' ideas or words have been included, I have adequately cited and referenced the original sources. I declare that I have properly and accurately acknowledged all sources used in the production of this dissertation. I also declare that I have adhered to all principles of academic honesty and integrity and have not misrepresented or fabricated or falsified any idea/data/fact/source in my submission. I understand that any violation of the above will be a cause for disciplinary action by the Institute and can also evoke penal action from the sources which have thus not been properly cited or from whom proper permission has not been taken when needed.

Jagadish Babu Vemula

Date: 4^{th} March, 2021 (Roll No. 134010005)

Abstract

The interaction of shock waves with turbulence has a significant effect on high-speed flows. These include shockwave/turbulent boundary-layer interaction and shock-induced mixing flowfields encountered in hypersonic air-breathing vehicles. The shock wave amplifies the turbulent fluctuations and drastically alters the Reynolds stresses in a turbulent flow. It also imparts significant anisotropy to the post-shock turbulence field. Two-equation turbulence models based on the eddy viscosity assumption, like $k - \epsilon$ and $k - \omega$, cannot predict the shock-induced anisotropy in Reynolds stresses. The objective of the present work is to capture the anisotropy across a shock wave using Reynolds stress based turbulence models.

We study the canonical interaction of homogeneous isotropic turbulence passing through a normal shock. Existing Reynolds stress model predictions are grossly inaccurate in behind the shock, especially at high Mach numbers. We propose a physics-based improvement to the Reynolds stress transport equation in the form of shock unsteadiness effect [Sinha *et al.*, Physics of Fluids, 15, 2003]. The resulting model is found to match DNS data for a range of Mach numbers, and is a significant improvement over existing Reynolds stress models. Numerical errors encountered at shock waves are also analyzed and the model equations are cast in conservative form to obtain physically-consistent results with successive grid refinement.

Next, the physical concepts of shock-unsteadiness and pressure-strain redistribution among the principal Reynolds stresses are incorporated in an algebraic form. An explicit algebraic Reynolds stress model (EARSM) is considered, and it is modified using shock-physics based on linear interaction analysis and DNS data. It allows us to predict the shock-induced anisotropy in Reynolds stresses at a much lower computational cost than full Reynolds stress transport models. The shock-unsteadiness modified EARSM is applied to oblique shockwave/boundary-layer interaction at Mach 5. The computed surface properties are compared to experimental measurements, and the results are found to be better than those reported previously using two-equation models.

Keywords: turbulence models; explicit algebraic Reynolds stress models; shock-turbulence interaction; shock-unsteadiness; Reynolds stress; anisotropy; shockwave/boundary-layer interaction.

Table of Contents

List of Figures

List of Tables

List of Symbols

Roman Symbols

$\mathbf{k}$	complex wavenumber vector, also denoted as $\vec{k}$
$\mathcal{V}$	volume
$\vec{V}$	velocity vector
a	speed of sound: $\sqrt{\frac{\gamma p}{\rho}}$ (or) $\sqrt{\gamma R T}$
c_p	specific heat capacity at constant pressure
c_v	specific heat capacity at constant volume
E	total energy: $c_v T + \frac{u_i^2}{2}$
H	Total enthalpy
k	turbulent kinetic energy: $\frac{\widetilde{u_i'' u_i''}}{2}$ (or) $\frac{\overline{u_i' u_i'}}{2}$
M	Mach number: $\frac{\widetilde{u}}{\overline{a}}$ (or) $\frac{\overline{u}}{\overline{a}}$
M_t	turbulent Mach number: $\frac{\widetilde{u_i'' u_i''}}{\overline{a}}$ (or) $\frac{\overline{u_i' u_i'}}{\overline{a}}$
p	pressure
Pr	Prandtl number: $\frac{\mu c_p}{\kappa}$
q_i	heat conduction term in the i^{th} direction: $-\kappa \frac{\partial T}{\partial x_i}$
R	Specific gas constant
R_{ij}	Reynolds stress tensor: $\widetilde{u_i'' u_j''}$ (or) $\overline{u_i' u_j'}$
R_{kk}	twice of turbulent kinetic energy
Re	Mean flow Reynolds number: $\frac{\overline{\rho}\,\overline{u}_1 L}{\overline{\mu}}$

Re_λ	Reynolds number based on Taylor lengthscale: $\frac{\bar{\rho}\, u'_{1,rms}\, \lambda}{\bar{\mu}}$
s	entropy
T	temperature
t	Time
T_{ref}	reference temperature for the gas
u, v, w	velocity components in the x, y, z directions.
u_i	velocity in the i^{th} direction
x, y, z	streamwise (shock-normal), transverse and spanwise directions.
x_i	spatial coordinate in the i^{th} direction
κ_0	highest wavenumber

Greek Symbols

δ_{ij}	Kronecker delta
δ_s	physical shock thickness
Δt	time step in the numerical simulations
Δx	grid spacing in the streamwise direction
Δy	grid spacing in the transverse direction
ϵ	dissipation rate of turbulent kinetic energy
ϵ_{ij}	dissipation rate tensor
η	Kolmogorov length scale: $\frac{\nu^{3/4}}{\epsilon^{-1/4}}$
γ	Ratio of specific heats
κ	thermal conductivity coefficient: $\frac{\mu\, c_p}{Pr}$
λ	Taylor lengthscale: $\frac{\overline{u'_\alpha u'_\alpha}}{\left(\frac{\partial u'_\alpha}{\partial x_\alpha}\right)^2}$ (no summation)
μ	dynamic viscosity: $\mu_{ref}\, \frac{T}{T_{ref}}$
μ_{ref}	reference dynamic viscosity for the gas

ν	kinematic viscosity: $\frac{\mu}{\rho}$
∂	partial difference operator
ρ	density
τ	turbulent time scale
ε_{ijk}	Levi-Civita symbol
ξ	displacement of shock front in the instantaneous frame of reference
ξ_t	shock unsteadiness (or corrugation) velocity in the instantaneous frame of reference
$\xi_{y/z}$	slope of the shock front in the instantaneous frame of reference for the $(x, y)/(x, z)$ plane.
e_{ij}	Anisotropy of dissipation rate tensor

Superscripts

$\overline{f}$	Reynolds average of the variable f, averaged over time and homogeneous directions
$\widetilde{f}$	Favre average of the variable f, mass-weighted average over time and homogeneous directions
f'	Reynolds fluctuation of the variable f
f''	Favre fluctuation of the variable f
f^*	indicates dimensional value of the variable f

Subscripts

∂_i	derivative with respect to index i. Implicitly denoted as derivative with respect to the spatial coordinate in the i^{th} direction
∂_t	derivative with respect to time
f_0	value of f at the initial time

f_α	to denote that the index α of the variable f should not be summed up when repeated
f_d	downstream value of f, also indicated as f_2 in one-dimensional case
f_{in}	value of f at the inlet of the domain
f_u	upstream value of f, also indicated as f_1 in one-dimensional case

Abbreviations

1D, 2D, 3D	one-, two-, three-dimensional
ARSM	**A**legrabic **R**eynolds **S**tress **M**odel
CFD	**C**omputational **F**luid **D**ynamics
CFL	**C**ourant, **F**riedrich, **L**ewy number
DNS	**D**irect **N**umerical **S**imulation
EARSM	**E**xplicit **A**legrabic **R**eynolds **S**tress **M**odel
LES	**L**arge **Eddy** **S**imulation
LHS	**L**eft **H**and **S**ide
LIA	**L**inear **I**nteraction **A**nalysis
NS	**N**avier-**S**tokes
RANS	**R**eynolds **A**veraged **N**avier-**S**tokes
RDT	**R**apid **D**istortion **T**heory
RH	**R**ankine-**H**ugoniot
RHS	**R**ight **H**and **S**ide
RK4	4^{th}-order **R**unge-**K**utta method
RSM	**R**eynolds **S**tress **M**odel
SBLI	**S**hockwave/**B**oundary-**L**ayer **I**nteraction
STI	**S**hock **T**urbulence **I**nteraction

SU	**S**hock **U**nsteadiness
TKE	**T**urbulent **K**inetic **E**nergy

Chapter 1

Introduction

1.1 Motivation

Shockwave/boundary-layer interaction (SBLI) plays an essential performance factor in high-speed flows. SBLIs occur on external or internal surfaces with a very complex flow structure when the boundary layer subjected to an adverse pressure gradient due to the shock interaction. The geometric complexity in a realistic aerospace vehicle makes it difficult to understand and analyze the SBLIs. The complex configuration can be broken down into simpler geometries, which can isolate different kinds of SBLIs. These simplified geometries are called canonical configurations such as compression corner, oblique shockwave impingement, cylinder-flare, cone-flare, and three-dimensional configurations such as single-fin, axial corner, and double-fin, as shown in Fig. (1.1).

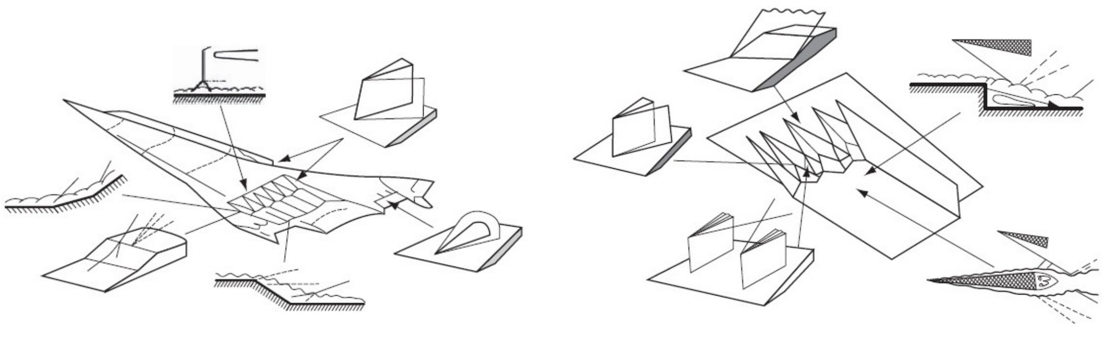

(a) (b)

Figure 1.1: Shockwave/boundary-layer interactions over a high-speed vehicle [1]

.

SBLIs are typical in aircraft propulsion systems, such as scramjet engines at any Mach number ranging from transonic to hypersonic. The shockwave presence introduces additional drag, increased aerodynamic heating, and unsteady loads [2, 3]. Unstart and severe structural damage and a reduction in vehicle performance, are some of the drastic effects of uncontrolled SBLI.

Figure (1.2) shows the canonical configuration schematic, where an oblique shock is impinging on a turbulent boundary layer. A strong shock impinging on the boundary layer leads to a highly adverse pressure gradient, causing a separation close to the impingement point. Points S and R show the extent of the separation bubble. The presence of a separation region, separation shock, and reflected shock add the complexity to the flow topology. The region where the reflected shock is close to the wall experiences peak heat and pressure loads. However, SBLIs benefit in some cases, such as the increase in the turbulence level enhances fuel-air mixing in scramjet combustion chambers, thus improving its efficiency.

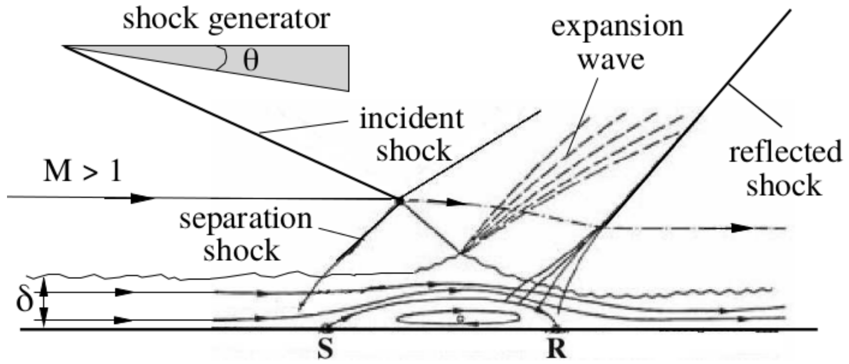

Figure 1.2: Schematic of oblique shock wave impingement on a turbulent boundary layer[1].

The injection of a sonic jet into a supersonic crossflow (JICF) is seen in air/fuel injection techniques used in scramjet combustors and thrust vectoring of supersonic aircraft and rockets. The resulting flow field consists of complex flow features of shock-wave/turbulent boundary-layer interaction including lambda shock, separation bubble, barrel shock, Mach disk, and secondary recirculation regions (see Fig 1.3). It becomes essential to numerically predict such features with reasonably good accuracy to determine their sensitivity to the geometric design and the extent of the jet mixing and penetration into a supersonic crossflow. The problem has simple geometric requirements but with a complicated flow structure, making it an excellent choice to test different turbulence models behaviour at high flow speeds.

The injected jet, being under-expanded, expands into the crossflow and simultaneously deflected downstream by it. On the other hand, the crossflow sees this jet as an obstruction - this leads to the formation of a bow shock just upstream of the injection slot.

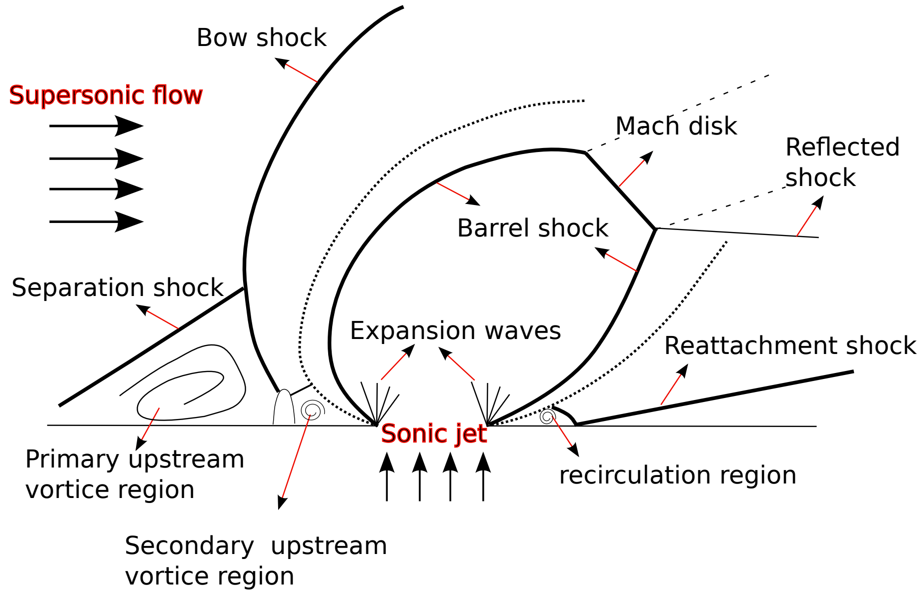

Figure 1.3: Schematic of sonic jet in supersonic cross flow with barrel shock formation within the jet boundary.

Due to this strong jet induced bow shock, the incoming boundary layer is subjected to a high adverse pressure gradient causing it to separate and form a recirculation bubble. Two-three vortices are typically seen within this bubble, termed as primary, secondary, and tertiary vortices based on their relative sizes. There is also a separation shock present before the bow shock as a result of this recirculation zone.

The bow shock and the separation shock form a lambda shock pattern, visualized in Fig 1.3. Post bow shock, we have the free shear layer of the jet curving into the flow. The expansion fans arising within the under-expanded jet hit the jet boundary (shear layer) and reflect as compression waves. These compression waves merge and create a barrel-shock inside the jet boundary and a Mach disk terminates this barrel shock. The Mach disk is a normal shockwave like structure that will be seen as a plane in two-dimensional flow and a circular disk in three-dimensional flow. Downstream of the jet, there is again a recirculation zone and the supersonic flow over the downstream recirculation zone turns itself by formation a reattachment shock. The vortices (located upstream and downstream) have a more complex structure in the three-dimensional flow.

Computational fluid dynamic (CFD) simulation of turbulent high-speed flows employ Reynolds averaged Navier-Stokes (RANS) equations, where mathematical modeling of various unclosed terms in the transport equations is a common practice. Initially, Boussinesq [4] proposed the first eddy viscosity based turbulence model. Other pioneering works in developing the turbulence models are the first two-equation model by Kolmogorov [5], the first Reynolds stress transport model (RSM) by Rotta [6] and the first algebraic Reynolds stress model (ARSM) by Rodi [7].

In one and two-equation turbulence models framework, mostly the Reynolds stress closure is dependent on the Boussinesq hypothesis. Turbulence models, such as standard $k-\epsilon$ and standard $k-\omega$ based on the Boussinesq hypothesis, neglect the Reynolds stresses flow history and cannot predict the anisotropy in Reynolds stresses as they model the total effect of the amplification in the form of turbulent kinetic energy. Whereas in RSMs, individual transport equations are solved for Reynolds stresses, which accounts for flow history and transport effects of turbulent fluctuations. These models are ideally suited to capture the anisotropy in turbulence.

Engineering turbulence flows like SBLI are very complex, with various turbulence effects within the single flowfield. RANS methods are usually employed to simulate such flows, where turbulence models account for turbulent fluctuations in the mean flowfield. The most critical aspect of engineering turbulence models is the common platform for all kinds of flows. Thus, explicit algebraic Reynolds stress models based on the two-equation framework showed some modest improvements to predict the Reynolds stresses and its anisotropy within affordable computational cost [8].

Shock-turbulence interaction (STI) is the origin and necessary study to understand the SBLI cases; therefore, several studies focus on it. The interaction of turbulent fluctuations with the shockwave lies at the heart of these phenomena. An essential feature of STI is the anisotropic nature of Reynolds stresses generated downstream of the shock wave. It eliminates other effects like boundary-layer gradients, flow separation, shear layer attachment, and streamline curvature present in SBLI flows. Despite the geometrical simplicity, the model problem exhibits a range of physical effects. These include turbulence anisotropy, baroclinic torques, generation of acoustic waves, and unsteady shock oscillations.

Across the shockwave, a theoretical analysis tool, such as linear interaction analysis (LIA) and direct numerical simulation (DNS) data, show different amplification in the Reynolds stresses along streamwise and transverse directions [9, 10]. Capturing the anisotropy in turbulence and the complex flow-features, such as shock-induced flow separation and high localized heating, is challenging for RANS simulations, and a significant amount of research exists in the literature [11–13].

1.2 Scope

This thesis provides the numerical performance of the Reynolds stress-based turbulence models in canonical STI. We examine the correlation between the principal Reynolds stresses in canonical STI using LIA and the available DNS data. We study the physical mechanisms responsible for the post-shock evolution of the Reynolds stresses and the anisotropy in the turbulence with varying upstream incoming Mach numbers, and proposed improvements to the existing turbulence models.

For RSM, the transport equations of the Reynolds stresses are modified to capture the essential physics and the anisotropy in the turbulence across the shockwave. Within two-equation turbulence model framework, explicit algebraic Reynolds stress models (EARSM) are more affordable than RSMs in the engineering CFD prediction tools. The algebraic equations for the Reynolds stresses were developed for the shockwave using LIA, and incorporated in existing EARSM. The results obtained using the modified EARSM for SBLI flows are found to improve the flow prediction significantly than the conventional turbulence models.

This dissertation is organized as follows,

- Chapter 2 provides the governing equations for the compressible turbulent flow and a brief introduction to the turbulence models, such as RSM, ARSM, and linear eddy viscosity-based turbulence models.

- Chapter 3 presents the literature survey on the turbulence closures proposed for the turbulence models, and their application in STI and SBLI flows; followed by the objectives of the current work.

- Chapter 4 gives the procedure for simplifying transport equations adopted from the three existing Reynolds stress models and applying them to the canonical STI. The Reynolds stresses obtained from the models were validated against the available DNS data presented by Larsson *et al.* [9, 10]. Based on the physics of the unsteady shock oscillations induced by the incoming turbulence, improvements were proposed to the existing model transport equations for Reynolds stresses and dissipation rate of turbulent kinetic energy. A detailed study of the shock-unsteadiness (SU) mechanism and incorporating the SU correction are provided in this chapter.

- Chapter 5 provides insight into the numerical error at the shockwaves and its theoretical analysis. A robust conservative formulation for the Reynolds stress model transport equations is proposed, and it is found to be a good match with the DNS data over a range of Mach numbers. Next, the effect of grid refinement with different numerical schemes on the enhancement of turbulence across the shockwave is presented.

- Chapter 6 provides the evaluation of the Wallin and Johansson [8] EARSM model for the canonical STI against the RSM and DNS data. Using LIA, the principal Reynolds stresses were written in the algebraic form to capture the anisotropy in turbulence and limit the turbulence enhancement across the shockwave. The new algebraic Reynolds stress model shows significant improvement in comparison with the DNS data. The post-shock evolution of the turbulence obtained using the modified EARSM is discussed thoroughly in this chapter.

- Chapter 7 gives detail simulation methodology and application of the modified EARSM to SBLI flows. Details of Schulein *et al.* [14] experiments for oblique shock impingement on the turbulent boundary layer configuration with different shock strengths are provided. A comparison of the solution obtained using the modified EARSM turbulence model with the experimental data are presented and discussed. The modified model shows a good improvement in capturing the realistic flowfield, such as shock structure, separation bubble size, and surface properties.

Chapter 2

Background

This chapter presents a brief description of the RANS equations and the turbulent transport equations with the turbulence closures for RSMs, two-equation eddy viscosity-based turbulence models, and EARSMs used to solve the turbulent compressible flow.

2.1 Reynolds averaging

The general equations describing the time and space evolution of continuum compressible viscous fluids are the Navier-Stokes equations and are given as,

$$\frac{\partial \rho}{\partial t} + \frac{\partial(\rho u_i)}{\partial x_i} = 0, \tag{2.1}$$

$$\frac{\partial(\rho u_i)}{\partial t} + \frac{\partial(\rho u_i u_j)}{\partial x_j} = -\frac{\partial p}{\partial x_i} + \frac{\partial \tau_{ij}}{\partial x_j}, \tag{2.2}$$

$$\frac{\partial(\rho E)}{\partial t} + \frac{\partial(\rho H u_j)}{\partial x_j} = \frac{\partial(\tau_{ij} u_i)}{\partial x_j} - \frac{\partial(q_j)}{\partial x_j}. \tag{2.3}$$

Here, the Einstein convention on repeated indices is applied. The system of Eqs. (2.1) - (2.3) is not closed, and some assumptions are made to provide suitable closure relations. In the present work, the fluid of interest (air) is a Newtonian fluid so that the viscous stresses can be considered proportional to the traceless strain rate tensor. Consequently, the viscous stress tensor τ_{ij}, which characterizes the specific property of the fluid when subject to stresses, can be written as

$$\tau_{ij} = 2\mu\left(\frac{1}{2}\left(\frac{\partial u_i}{\partial x_j} + \frac{\partial u_j}{\partial x_i}\right) - \frac{1}{3}\frac{\partial u_k}{\partial x_k}\delta_{ij}\right). \tag{2.4}$$

Sutherland's formula describes the variation of the dynamics viscosity μ for a wide range of temperatures as

$$\frac{\mu(T)}{\mu_0} = \frac{T_0 + T_s}{T + T_s}\left(\frac{T}{T_0}\right)^{3/2}, \tag{2.5}$$

where the Sutherland constant is equal to $T_s = 110.6\ K$ for air. The value of reference temperature (T_0) and reference viscosity (μ_0) are 273.15 K and 1.716E-5 $kg/(m.s)$, respectively. Fourier's law for heat conduction, which states a proportionality between the heat flux (q_i) and the temperature gradient is assumed as

$$q_i = -\lambda \frac{\partial T}{\partial x_i}, \text{ and } \lambda = \frac{c_p \mu}{Pr}, \tag{2.6}$$

where λ is the thermal conductivity of the fluid, c_p is the specific heat at constant pressure, and Pr is the Prandtl number equal to 0.72. The static pressure p is obtained by the equation of state for an ideal gas as

$$p = \rho R T, \tag{2.7}$$

where R is the universal gas constant with the value of 287.058 $J.kg^{-1}K^{-1}$. The total energy E is the sum of the internal energy and the kinetic energy, and are defined as

$$E = c_v T + \frac{1}{2} u_k u_k. \tag{2.8}$$

The total enthalpy H, that appears in the total energy equation is defined as

$$H = E + \frac{p}{\rho}. \tag{2.9}$$

For compressible flows, contributions due to gravity-related terms are generally not included in total enthalpy, as the stagnation temperature is a measure of the fluid's total energy. The relations between the specific heat at constant pressure c_p and the specific heat at constant volume c_v are given as

$$R = c_p - c_v, \text{ and } \gamma = \frac{c_p}{c_v}. \tag{2.10}$$

Turbulent solution of Navier-Stokes equations is entirely chaotic, spatial, and temporally complex. To obtain flow characteristics at an affordable computational cost, we adopted a statistical approach. For a stationary turbulent flow, the instantaneous velocity u_i is expressed as the sum of a mean $\overline{u}_i$ and a fluctuating part u_i'.

$$u_i(x,t) = \overline{u}_i(x) + u_i'(x,t), \tag{2.11}$$

where the overbar represents the Reynolds averaging and is defined as

$$\overline{u}_i(x) = \lim_{\tau \to \infty} \frac{1}{\tau} \int_{t_0}^{t_0+\tau} u_i(x,t) dt. \tag{2.12}$$

Here, time τ is very long relative to the maximum period of the velocity fluctuations. The equations averaged at this point are known as Reynolds averaged Navier-Stokes simulation (RANS). When the flow is compressible, we must account for density and temperature fluctuations, besides pressure and velocity fluctuations. Therefore we use density-weighted averaging. The Favre-averaging or mass-averaging for velocity is defined as

$$\widetilde{u_i}(x) = \frac{1}{\overline{\rho}} \lim_{\tau\to\infty} \frac{1}{\tau} \int_{t_0}^{t_0+\tau} \rho(x,t) u_i(x,t) dt, \tag{2.13}$$

where $\overline{\rho}$ is the conventional Reynolds-averaged density. The Favre averaging can also be written in terms of the Reynolds-averaging as

$$\overline{\rho}\widetilde{u_i} \equiv \overline{\rho u_i} = \overline{\rho}\ \overline{u_i} + \overline{\rho' u_i'}. \tag{2.14}$$

When we use Favre averaging, the instantaneous velocity is decomposed into the mass-averaged part, $\widetilde{u_i}$, and a fluctuating part, u_i''

$$u_i = \widetilde{u_i} + u_i''. \tag{2.15}$$

Therefore, RANS equations are given as

$$\begin{aligned}
\frac{\partial\overline{\rho}}{\partial t} + \frac{\partial(\overline{\rho}\widetilde{u_k})}{\partial x_k} &= 0, && (2.16)\\
\frac{\partial(\overline{\rho}\widetilde{u_i})}{\partial t} + \frac{\partial(\overline{\rho}\widetilde{u_i}\widetilde{u_k})}{\partial x_k} + \frac{\partial(\overline{\rho}R_{ik})}{\partial x_k} &= \frac{\partial\overline{p}}{\partial x_i} + \frac{\partial\overline{\tau}_{ik}}{\partial x_k}, && (2.17)\\
\frac{\partial(\overline{\rho}E)}{\partial t} + \frac{\partial(\overline{\rho}H\widetilde{u_k})}{\partial x_k} + \frac{\partial(\overline{\rho}R_{ik}\widetilde{u_i})}{\partial x_k} &= \frac{\partial(\overline{\tau}_{ik}\widetilde{u_i})}{\partial x_k} - \frac{\partial(\overline{q}_k)}{\partial x_k} + D_k - \frac{\partial q_k}{\partial x_k}. && (2.18)
\end{aligned}$$

Additional terms appear in momentum and energy equations after the averaging process. The term

$$\overline{\rho}R_{ij} = \overline{\rho u_i'' u_j''} \tag{2.19}$$

is the Reynolds stress tensor and represents the correlation between two different fluctuating velocity components. The term

$$D_k = \frac{\partial}{\partial x_k}\left(\frac{1}{2}\overline{\rho u_i'' u_i'' u_k''} - \overline{u_i'' \tau_{ik}}\right) \tag{2.20}$$

is related to the turbulent transport and the diffusion term. The term

$$q_k = \overline{\rho h'' u_k''} \tag{2.21}$$

represents the turbulent heat flux.

The RANS approach introduces new unknown quantities into the equations, and we solve additional equations related to the mean variables so that the number of unknowns and equations are equal. Reynolds stress model (RSM) equations are the most accurate level of modeling used along with RANS equations [15, 16]. RSM is also referred to as the second-order closure model as the turbulent transport equations are written for the second-order correlations of the fluctuating velocity components. These models solve each component of the symmetric Reynolds stress tensor, plus an additional equation for the length scale. The transport equations for the Reynolds stress tensor can be mathematically derived from the momentum equations.

2.2 Reynolds stress transport equations

Turbulence model based on the transport equations for the individual Reynolds stresses have the natural potential to deal with the dynamics of inter-component energy transfer. In a simpler form, the Reynolds stress tensor transport equation is written as

$$\frac{\partial \overline{\rho} R_{ij}}{\partial t} + \frac{\partial \overline{\rho}\widetilde{u_k} R_{ij}}{\partial x_k} = P_{ij} + \phi_{ij} + d_{ij} - \overline{\rho}\epsilon_{ij} + K_{ij} + \frac{2}{3}\phi_p \delta_{ij}, \tag{2.22}$$

where ρ is the density, $R_{ij} = \widetilde{u_i'' u_j''}$ is the Reynolds stress tensor, δ_{ij} is the Kronecker delta, and $\widetilde{u_i}$ is the mean velocity. Tilde and overbar indicate Favre and Reynolds averaging, respectively, whereas double prime represents Favre fluctuation. Here Favre decomposition is used for all terms except density and pressure. The second term on the left-hand side of Eq. (2.22) represents the convection term. The terms on the right side of Eq. (2.22) are in order, production, pressure-strain correlation, diffusion, dissipation, direct compressibility effect, and pressure dilatation terms.

$P_{ij} = -\overline{\rho} R_{jl}\widetilde{u_{i,l}} - \overline{\rho} R_{il}\widetilde{u_{j,l}}$ is the production of Reynolds stress due to mean velocity gradients, where $\widetilde{u_{i,l}}$ represents $\partial\widetilde{u_i}/\partial x_l$ and x_l denotes Cartesian space coordinates with l = 1,2,3. Here, the production term is in terms of Reynolds stresses and does not require modeling. However, the most important quantity to be modeled in the Reynolds stress model is the pressure-strain correlation.

In the compressible flow, the velocity gradient tensor is not traceless, so the pressure-strain correlation can be written in terms of isotropic (dilatation) and deviatoric parts. The deviatoric part of the pressure-strain correlation term is given by $\phi_{ij} = \overline{p'(u''_{i,j} + u''_{j,i} - 2/3 u''_{l,l}\delta_{ij})}$. In the turbulent flow, the energy is redistributed among the Reynolds stresses along with the turbulence production or dissipation. Depending on the behavior, the pressure-strain correlation is decomposed into two parts depending on the type of contribution, namely, the slow and rapid pressure-strain terms. The slow pressure-strain term is also referred to as the return-to-isotropy term and represents turbulence–turbulence interaction. It is modeled as $\phi^s_{ij} = C_1 \overline{\rho}\epsilon a_{ij}$ [6], where C_1 is a model coefficient and a_{ij} is the anisotropy. This model is motivated from the homogeneous anisotropic turbulence decaying without any mean velocity gradients in the flow.

The rapid pressure-strain term (ϕ^r_{ij}) responds directly to the change in mean velocity gradients and is of the same form as of production term in Eq. (2.22). It tends to redistribute the energy from the Reynolds stress component, where the production is significantly large compared to other components, consequently reducing the anisotropy in Reynolds stresses. The following are three turbulent closures for the rapid part of the pressure-strain correlation, which have been applied to compressible flows with shock-waves.

The model proposed in Gerolymos *et al.* [17–19] is based on the isotropization of production in turbulence [20], and is given as

$$\phi^r_{ij} = -C_2(P_{ij} - \frac{2}{3}\delta_{ij}P_k). \tag{2.23}$$

Here $P_k = P_{kk}/2$, and the model coefficient C_2 is $0.75\sqrt{A}$ as per Gerolymos *et al.* [18] model, where the flatness parameter, $A = 1$ - $\frac{9}{8}(A_2 - A_3)$, with the anisotropy tensor invariants $A_2 = a_{ik}a_{ki}$ and $A_3 = a_{ik}a_{kj}a_{ji}$. For isotropic turbulence, the value of A is one as A_2 and A_3 tend to zero. The rapid part of the pressure-strain term in the Zha and Knight [21] model is developed for isotropic turbulent flows subjected to sudden distortion (high mean strain). As per the model,

$$\phi^r_{ij} = C_{c2}\overline{\rho}kS^*_{ij}, \tag{2.24}$$

with C_{c2}=0.17, and $S^*_{ij} = \widetilde{u_{i,j}} + \widetilde{u_{j,i}}$. The model closure is a direct extension of the incompressible form, so the trace of ϕ^r_{ij} does not vanish for compressible flows. Lee *et al.* [22] proposed a new formulation of the pressure-strain term, using the Poisson equation for pressure fluctuations in varying density flows. As per the model,

$$\begin{aligned}\phi^r_{ij} = &- C_{p2}(P_{ij} - \frac{2}{3}\delta_{ij}P_k) - C_3(D_{ij} - \frac{2}{3}\delta_{ij}P_k)\\ &- C_4k\overline{\rho}\left(S^*_{ij} - \frac{2}{3}S^*_{kk}\delta_{ij}\right) - C_5\overline{\rho}ka_{ij}\frac{\partial\widetilde{u_l}}{\partial x_l} + C_6\overline{\rho}R_{mm}\frac{\partial\widetilde{u_l}}{\partial x_l}\delta_{ij}\\ &+ \frac{1}{3}C_7P_k\delta_{ij},\end{aligned} \tag{2.25}$$

where $D_{ij} = -\overline{\rho}R_{ik}\widetilde{u}_{k,j} - \overline{\rho}R_{jk}\widetilde{u}_{k,i}$, $C_{p2} = 0.76$, $C_3 = 0.10$, $C_4 = 0.18$, $C_5 = 0.14$, and $C_6 = 0.35$. The first three terms are identical to Quasi-Isotropic (LRR-QI) model of Launder *et al.* [23], and the following two terms are additional terms that arise due to mean dilatation. The last term is the production term generated by compressibility effect and is neglected [22].

All the above Reynolds stress closures use Rotta's [6] model for the slow pressure-strain term, where the model coefficient varies between different models. For Gerolymos *et al.* [18] model, the coefficient C_1 is given as $1 + 2.58AA_2^{\frac{1}{4}}\left[1 - exp\left[-\left(\frac{Re_T}{150}^2\right)\right]\right]$ and the value is 1 for isotropic turbulence. Here, Re_T is the turbulent Reynolds number. The coefficient of slow pressure term for Zha and Knight [21] model is given as $C_{c1} = 4.325$ and the Lee *et al.* [22] model uses $C_{p1} = 1.5$.

Diffusion term $d_{ij} = (-\overline{\rho}\widetilde{u_i''u_j''u_l''} - \overline{p'u_j''}\delta_{il} - \overline{p'u_i''}\delta_{jl} + \mu R_{ij,l})_{,l}$ includes turbulent diffusive flux, pressure diffusion, and viscous diffusion. The turbulent and pressure diffusion terms are modeled by Daly and Harlow [24] using the generalised gradient diffusion hypothesis. Launder *et al.* [20] proposed an improved model for the triple correlation tensor, which is given as $\widetilde{u_i''u_j''u_k''} = -C_s(k/\epsilon)(R_{il}R_{jk,l} + R_{jl}R_{ki,l} + R_{kl}R_{ij,l})$, where C_s is 0.11. The viscous diffusion term is in the form of Reynolds stresses and does not require modeling. The dissipation of Reynolds stresses at the smallest scales of turbulence due to viscous effects is represented as $\overline{\rho}\epsilon_{ij} = \overline{\sigma_{jl}u_{i,l}''} + \overline{\sigma_{il}u_{j,l}''}$, where σ_{jl} is the viscous stress. According to Kolmogorov's hypothesis, the smallest scales of motion are assumed to be isotropic and the dissipation tensor is modeled as $\epsilon_{ij} = \frac{2}{3}\epsilon\delta_{ij}$.

Favre-averaging introduces new terms in the transport equation involving mass-averaged velocity fluctuations and pressure-dilatation due to the deviatoric part of pressure-strain correlation. These terms have no counterpart in incompressible transport equations. Direct compressibility effects through variation in density are represented by $K_{ij} = -\overline{u_i''}\,\overline{p}_{,j} - \overline{u_j''}\,\overline{p}_{,i} + \overline{u_i''}\,\overline{\sigma_{jl,l}} + \overline{u_j''}\,\overline{\sigma_{il,l}}$. Here, $\overline{u_i''}$ is related to the turbulent mass flux as $-\overline{\rho' u_i'}/\overline{\rho}$. It plays an important role in problems involving turbulent mixing [25, 26] and high-Mach number flows with significant thermodynamic fluctuations upstream of the shockwave [27]. The last term, $\phi_p = \overline{p'u_{l,l}''}$ is the pressure dilatation term, and is modeled in terms of turbulent Mach number (M_t) by Pantano and Sarkar [28].

The distinction between turbulent shear stresses and principal Reynolds stresses is dependent on the choice of the coordinate system. An essential distinction can be made between isotropic and anisotropic stresses. The isotropic part of the Reynolds stress is $\frac{2}{3}k\delta_{ij}$, where $k = \dfrac{1}{2}\overline{u_i''u_i''}$ is the TKE and the deviatoric (anisotropic) part is

$$a_{ij} = R_{ij} - \frac{2}{3}k\delta_{ij}. \tag{2.26}$$

The normalized anisotropy tensor used extensively is given as

$$b_{ij} = \frac{a_{ij}}{2k} = \frac{R_{ij}}{R_{ii}} - \frac{1}{3}\delta_{ij}. \tag{2.27}$$

In terms of these anisotropy tensors, the Reynolds stress tensor is written as

$$R_{ij} = \frac{2}{3}k\delta_{ij} + a_{ij} \tag{2.28}$$

$$= \quad 2k\left(\frac{1}{3}\delta_{ij} + b_{ij}\right). \tag{2.29}$$

TKE is associated with the eddies in a turbulent flow and mathematically, it can be quantified by measuring the root mean square (RMS) velocity fluctuations. By taking the trace of the Reynolds stress transport equation, we will arrive at the TKE equation. The TKE equation is given by

$$\frac{\partial \overline{\rho} k}{\partial t} + \frac{\partial \overline{\rho}\widetilde{u}_j k}{\partial x_j} = -\overline{\rho} R_{ij}\frac{\partial \widetilde{u}_i}{\partial x_j} - \overline{\rho}\epsilon + \frac{\partial}{\partial x_j}[\overline{\tau_{ji}u_i''} - \frac{\overline{\rho u_i'' u_i'' u_j''}}{2} - \overline{p' u_j''}]. \tag{2.30}$$

Here, $\epsilon = \nu \overline{\frac{\partial u_i''}{\partial x_k}\frac{\partial u_i''}{\partial x_k}}$ is the dissipation rate of the TKE per unit mass.

The first term in the left-hand side is the time rate of change of the turbulent kinetic energy k, whereas the second term in the left-hand side represents the change of net turbulent kinetic energy flux. The first term in the right-hand side, $\overline{\rho} R_{ij}\frac{\partial \widetilde{u}_i}{\partial x_j}$ denotes work done by the velocity gradient or the mean strain rate against the turbulent stress, i.e., kinetic energy is transformed from the mean flow to the turbulent flow which is the primary source of the turbulence. That is why this term is often called a turbulence production term. The second term in the right-hand side signifies the work done by the fluctuating velocity gradient against the viscous stress. It transfers the turbulent kinetic energy into internal energy and often known as the dissipation of turbulence. The term in the right-hand side denoting by $\overline{\tau_{ji}u_i''}$ represents the diffusion or transfer of turbulent kinetic energy from one fluid lump to another by the molecular transport and known as molecular diffusion. The term with the triple velocity fluctuation correlation signifies the transport rate of the turbulent kinetic energy by the fluctuating velocity or the transport of Reynolds stresses by the turbulent fluctuating velocities. The last term in the right-hand side represents the pressure diffusion by the turbulent fluctuating velocity.

The transport equation for the turbulent dissipation rate is modeled as

$$\frac{\partial \overline{\rho}\epsilon}{\partial t} + \frac{\partial \overline{\rho}\widetilde{u}_k\epsilon}{\partial x_k} = -C_{\epsilon 1}\overline{\rho}R_{il}\frac{\epsilon}{k}\frac{\partial \widetilde{u}_i}{\partial x_l} - C_{\epsilon 2}\overline{\rho}\frac{\epsilon^2}{k} + C_\epsilon \overline{\rho}\frac{\partial}{\partial x_l}\left(\frac{k}{\epsilon}R_{il}\frac{\partial \epsilon}{\partial x_l}\right), \tag{2.31}$$

and this form is used by all the turbulence models. The terms on the right-hand side of this equation are, in order, production, dissipation, and diffusion terms. Here, $C_{\epsilon 1} = 1.44$, $C_{\epsilon 2} = 1.92$, and $C_\epsilon = 0.15$ are the empirical constants taken from Launder *et al.* [23]. The equation is analogous to Eq. (2.30) except for mass averaged velocity fluctuation and pressure-strain correlation terms.

2.3 Boussinesq hypothesis

All the turbulent models use a gradient diffusion analogy to close the turbulent correlation terms. The gradient diffusion analogy states that turbulent transport of any scalar quantity, ϕ in turbulent flow, can be represented as the mean gradient of that scalar quantity, ϕ. The physical idea behind this analogy is that the stress created by the molecular transport is directly proportional to the mean velocity gradient, so the turbulent transport of scalar quantity can be mathematically written as

$$\overline{u'_j\phi'} \propto \frac{\partial\overline{\phi}}{\partial x_j},$$

Boussinesq [4] used this analogy and hypothesized that the Reynolds stress tensor is proportional to the mean strain-rate tensor. He also states that the momentum transfer occurs in turbulent flow by the fluid lumps, so-called turbulent eddies can be modeled with an eddy viscosity μ_T. The same thing is happening when the fluid particles in motion transfer their momentum by the molecular viscosity. Mathematically it is given by the following expression

$$\overline{\rho}R_{ij} = 2\mu_T S^*_{ij} - \frac{2}{3}\overline{\rho}k\delta_{ij}, \tag{2.32}$$

where,

$$S^*_{ij} = \frac{1}{2}\left(\frac{\partial\widetilde{u_i}}{\partial x_j} + \frac{\partial\widetilde{u_j}}{\partial x_i}\right) - \frac{1}{3}\frac{\partial\widetilde{u_k}}{\partial x_k}\delta_{ij}.$$

Any stress similar terms which are governed from the momentum flux transport can be expressed in this form. The turbulent transport of turbulent kinetic energy terms in the energy and turbulent kinetic equation, and the viscous diffusion term in the energy equation modeled as

$$\overline{\rho u''_j \frac{u''_i u''_i}{2}} = \frac{\mu_T}{\sigma_k}\frac{\partial k}{\partial x_j},$$

where σ_k is the closure constant coefficient.

The turbulent terms are modeled in terms of turbulent and mean variables, which can be easily solved, thus closing the governing equations. The 'n-equation' turbulent model means that n new turbulent transport equation(s) is(are) solved apart from mean conservation equations. In this section, we discuss the two-equation turbulent models because of their popularity in aerospace applications. Two extra transport equations are solved in the two-equation turbulent model approach for the turbulent flow field quantities. Compared to one-equation turbulence models, these models provide an equation not only for computation of TKE but also for the turbulence length scale or equivalent. The choice of the type of turbulence length scale variable is arbitrary. Two of the most popular dependent variables for the second variable are the dissipation rate, ϵ, and specific dissipation rate, ω. Other variables most commonly used are k times the length scale (kl), vorticity fluctuations squared (ω'), eddy viscosity (ν_T) and time scale (τ).

The $k-\epsilon$ model is the best known two-equation turbulence model because of its understanding and usage. Jones and Launder [29] developed the $k-\epsilon$ turbulence model and given as

$$\frac{\partial(\overline{\rho}k)}{\partial t} + \frac{\partial(\overline{\rho}k\widetilde{u}_j)}{\partial x_j} = -\overline{\rho}R_{ij}\frac{\partial\widetilde{u}_i}{\partial x_j} - \overline{\rho}\epsilon_{ij} + \frac{\partial}{\partial x_j}\left[\left(\mu + \frac{\mu_T}{\sigma_k}\right)\frac{\partial k}{\partial x_j}\right], \tag{2.33}$$

$$\frac{\partial(\overline{\rho}\epsilon)}{\partial t} + \frac{\partial(\overline{\rho}\epsilon\overline{u}_j)}{\partial x_j} = -C_{1\epsilon}\frac{\epsilon}{k}\left(\overline{\rho}R_{ij}\frac{\partial\overline{u}_i}{\partial x_j}\right) - C_{2\epsilon}\frac{\overline{\rho}\epsilon^2}{k} + \frac{\partial}{\partial x_j}\left[\left(\mu + \frac{\mu_T}{\sigma_\epsilon}\right)\frac{\partial\epsilon}{\partial x_j}\right]. \tag{2.34}$$

The eddy viscosity with the Boussinesq approximation [4] is calculated as

$$\mu_T = c_\mu\frac{\overline{\rho}k^2}{\epsilon}, \tag{2.35}$$

considering a turbulence time scale (length scale) and velocity scale, where c_μ is a model coefficient with the value of 0.09. The $k-\epsilon$ model is used widely in practical engineering calculations. The standard $k-\epsilon$ model is mostly used for attached flows with thin shear layers. The model fails to reproduce the correct flow behavior in many important flow simulations, such as adverse pressure gradients, bluff-body flows, separation, streamline curvature, swirl, buoyancy, turbulence driven secondary motion, compressibility, and unsteady flows [15].

Wilcox [15] used a specific turbulence dissipation rate, ω, and proposed the $k-\omega$ turbulence model (referred to as the standard $k-\omega$ turbulence model). Here ω is defined implicitly using the turbulence kinetic energy, k, and the turbulence dissipation, ϵ and given as $\epsilon/(k\beta^*)$. The transport equations for k and ω are given as

$$\frac{\partial(\overline{\rho}k)}{\partial t} + \frac{\partial(\overline{\rho}\overline{u}_j k)}{\partial x_j} = -\overline{\rho}R_{ij}\frac{\partial\overline{u}_i}{\partial x_j} - \beta^*\overline{\rho}\omega k + \frac{\partial}{\partial x_j}\left[\left(\mu + \frac{\mu_t}{\sigma_k}\right)\frac{\partial k}{\partial x_j}\right],$$

$$\frac{\partial(\overline{\rho}\omega)}{\partial t} + \frac{\partial(\overline{\rho}\overline{u}_j\omega)}{\partial x_j} = -\alpha\frac{\omega}{k}\left(\overline{\rho}R_{ij}\frac{\partial\overline{u}_i}{\partial x_j}\right) - \beta\overline{\rho}\omega^2 + \frac{\partial}{\partial x_j}\left[\left(\mu + \frac{\mu_t}{\sigma_\omega}\right)\frac{\partial\omega}{\partial x_j}\right],$$

with the coefficients, $\beta^* = 0.09,\ \ \alpha = 5/9,\ \ \beta = 3/4,\ \ \sigma_k = 0.5,\ \ \sigma_\omega = 0.5$. The eddy viscosity is calculated as

$$\mu_T = \frac{\overline{\rho}k}{\omega}. \tag{2.36}$$

The $k-\omega$ model has been used in many engineering flows, especially in aerodynamics applications. It can reproduce the flowfield with an adverse pressure gradient and predicts separation better than the other eddy viscosity-based turbulence models.

2.4 Weak equilibrium approximation

Algebraic Reynolds stress models (ARSMs) and nonlinear turbulent viscosity models are the simpler and more straightforward closures derived from the Reynolds stress closures. The RSM can be reduced to a set of algebraic equations by introducing an approximation for the transport terms, which determines the local Reynolds stresses implicitly as a function of k, ϵ or ω, and the mean velocity gradients. Due to these approximations, the ARSMs are less general and less accurate than the RSMs. However, RSMs provide some physical insights into these ARSMs.

Depending on the consistency of the approximations, Rodi [7] introduced a more general weak-equilibrium assumption. Here, the spatial and temporal variation of the R_{ij} is expressed in terms of variation of a_{ij} and k. In the weak-equilibrium assumption, the variations in R_{ij}/k are neglected and the variations in R_{ij} due to those in k are retained. For the mean convection term this leads to the approximation

$$\frac{DR_{ij}}{Dt} = \frac{R_{ij}}{k}\frac{Dk}{Dt} + k\frac{D}{Dt}\left(\frac{R_{ij}}{k}\right), \tag{2.37}$$

The same approximation applied to the entire transport equation yields,

$$\frac{DR_{ij}}{Dt} \approx \frac{R_{ij}}{k}\frac{Dk}{Dt} = \left(\frac{R_{ij}}{k}\right)(P_k - \epsilon). \tag{2.38}$$

2.4.1 Implicit algebraic Reynolds stress model (IARSM)

When the Reynolds stress transport equation is subject to the "weak-equilibrium" assumption, a set of simultaneous non-linear algebraic equations is obtained. Rodi [7] proposed that this set of non-linear equations for Reynolds stresses to be solved numerically. However, the iterative numerical solution of the set of algebraic equations can be computationally expensive, nullifying the advantage of a two-equation model over second-order closures.

Pope [16] obtained the semi-explicit solutions for the Reynolds stresses by presuming that the only contribution of the anisotropy stress tensor. In order to completely close the expression for the Reynolds stresses, Pope's methodology requires the numerical solution of a single non-linear equation for the production to dissipation ratio,

$$\frac{R_{ij}}{k}\left[\frac{P_k}{\epsilon} - 1\right] = \frac{P_{ij}}{\epsilon} + \frac{\Phi_{ij}}{\epsilon} - \frac{\epsilon_{ij}}{\epsilon}. \tag{2.39}$$

Here,

$$\begin{aligned} P_{ij} &= -R_{jl}\widetilde{u_{i,l}} - R_{il}\widetilde{u_{j,l}}, \\ \epsilon_{ij} &= \frac{2}{3}\epsilon\delta_{ij}, \end{aligned}$$

$$\begin{aligned}
\Phi_{ij} &= \Phi^s_{ij} + \Phi^r_{ij}, \\
\Phi^r_{ij} &= -\frac{C_2+8}{11}\left(P_{ij} - \frac{2}{3}P_k\delta_{ij}\right) + \frac{30C_2-2}{55}k\left(\widetilde{u_{i,j}} + \widetilde{u_{j,i}}\right) \\
&- \frac{8C_2-2}{11}\left(D_{ij} - \frac{2}{3}P_k\delta_{ij}\right), \\
\Phi^s_{ij} &= C_1\epsilon a_{ij}.
\end{aligned}$$

Here the mean velocity gradient tensor is split into a mean strain and a mean vorticity tensor as the terms on left and right hand side of above equation involves in terms of velocity gradients. Symbols S_{ij} and Ω_{ij} are used to represent these tensors and are normalized with the turbulent time-scale assumed

$$S_{ij} = \tau S^*_{ij},$$

and

$$\Omega_{ij} = \frac{\tau}{2}\left[\frac{\partial\widetilde{u_i}}{\partial x_j} - \frac{\partial\widetilde{u_j}}{\partial x_i}\right],$$

where the turbulent time-scale is defined as

$$\tau = \frac{k}{\epsilon}.$$

Rapid pressure strain term is represented by isotropization of the production (LRR-IP) closure of Launder *et al.* [23], and Rotta's closure [6] for slow pressure strain term. Now, it is possible to rewrite the production, pressure-strain closure and dissipation rate in terms of S_{ij}, Ω_{ij} and a_{ij} by normalizing with the dissipation rate ϵ as,

$$\begin{aligned}
\frac{P_{ij}}{\epsilon} &= -\frac{4}{3}S_{ij} - \left(a_{ik}S_{kj} + a_{kj}S_{ik}\right) + a_{ik}\Omega_{kj} - a_{kj}\Omega_{ik}, \\
\frac{\epsilon_{ij}}{\epsilon} &= \frac{2}{3}\delta_{ij}, \\
\frac{\Phi^r_{ij}}{\epsilon} &= \frac{4}{5}S_{ij} + \frac{9C_2+6}{11}\left(a_{ik}S_{kj} + a_{kj}S_{ik} - \frac{2}{3}a_{km}S_{mk}\delta_{ij}\right) \\
&+ \frac{7C_2-10}{11}\left(a_{ik}\Omega_{kj} - a_{kj}\Omega_{ik}\right), \\
\frac{\Phi^s_{ij}}{\epsilon} &= C_1 a_{ij}.
\end{aligned}$$

When the above equations for the production term, the dissipation rate term, the slow redistribution term and the rapid redistribution terms are inserted to the Eq. (2.39), the implicit algebraic equation for the Reynolds stress anisotropy tensor is then obtained as

$$\begin{aligned}
\left(C_1 - 1 + \frac{P_k}{\epsilon}\right)a_{ij} &= -\frac{8}{15}S_{ij} + \frac{7C_2+1}{11}\left(a_{ik}\Omega_{kj} - a_{kj}\Omega_{ik}\right) \\
&- \frac{5-9C_2}{11}\left(a_{ik}S_{kj} + a_{kj}S_{ik} - \frac{2}{3}a_{km}S_{mk}\delta_{ij}\right) \qquad (2.40)
\end{aligned}$$

Eq. (2.40) represents a non-linear relation, since the production to dissipation rate ratio is defined as

$$\frac{P_k}{\epsilon} \equiv a_{ik} S_{ki} \tag{2.41}$$

The value of C_2 is 0.5 Launder *et al.* [20] and $C_1 = 1.8$ [6].

2.4.2 Explicit algebraic Reynolds stress model (EARSM)

The implicit ARSM relation for the Reynolds stress anisotropy tensor is numerically and computationally cumbersome since there is no diffusion or damping term in the equation. The turbulence closure where the Reynolds stresses are explicitly related to the mean flowfield is called explicit algebraic Reynolds stress model. The procedure used to obtain an explicit form is to avoid the non-linearity, by considering the production to dissipation ratio P/ϵ as an extra unknown. The most general form for a_{ij} in terms of S_{ij} and Ω_{ij} consists of ten tensorially independent groups to which all higher-order tensor combinations can be reduced with the aid of the Cayley-Hamilton theorem.

$$\begin{aligned}
a_{ij} &= \beta_1 S_{ij} + \beta_2 \left(S_{ik}S_{kj} - II_S\delta_{ij}/3\right) + \beta_3\left(\Omega_{ik}\Omega_{kj} - II_\Omega\delta_{ij}/3\right) + \beta_4\left(S_{ik}\Omega_{kj} - \Omega_{ik}S_{kj}\right)\\
&+ \beta_5\left(S_{ik}S_{kl}\Omega_{lj} - \Omega_{ik}S_{kl}S_{lj}\right) + \beta_6\left(S_{ik}\Omega_{kl}\Omega_{lj} + \Omega_{ik}\Omega_{kl}S_{lj} - IV\delta_{ij}/3\right)\\
&+ \beta_7\left(S_{ik}S_{kl}\Omega_{lp}\Omega_{pj} + \Omega_{ik}\Omega_{kl}S_{lp}S_{pj} - 2V\delta_{ij}/3\right)\\
&+ \beta_8\left(S_{ik}\Omega_{kl}S_{lp}S_{pj} - S_{ik}S_{kl}\Omega_{lp}S_{pj}\right) + \beta_9\left(\Omega_{ik}S_{kl}\Omega_{lp}\Omega_{pj} - \Omega_{ik}\Omega_{kl}S_{lp}\Omega_{pj}\right)\\
&+ \beta_{10}\left(\Omega_{ik}S_{kl}S_{lp}\Omega_{pq}\Omega_{qj} - \Omega_{ik}\Omega_{kl}S_{lp}S_{pq}\Omega_{qj}\right).
\end{aligned}$$

The number of independent scalar invariants is limited to five in the case of three-dimensional mean flow

$$\begin{aligned}
II_S &= S_{kl}S_{lk},\\
II_\Omega &= \Omega_{kl}\Omega_{lk},\\
III_S &= S_{kl}S_{lm}S_{mk},\\
IV &= S_{kl}\Omega_{lm}\Omega_{mk},\\
V &= S_{kl}S_{lm}\Omega_{mn}\Omega nk.
\end{aligned}$$

In the ARSM Eq. (2.40), the last term contribution to the turbulence anisotropy is quite small (precisely zero). The equation is further simplified as (still in terms of P_k/ϵ)

$$\left(C_1 - 1 + \frac{P_k}{\epsilon}\right)a_{ij} = -\frac{8}{15}S_{ij} + \frac{7C_2+1}{11}(a_{ik}\Omega_{kj} - \Omega_{ik}a_{kj}). \tag{2.42}$$

The value of C_2 in the rapid redistribution model was originally suggested to be 0.4 by Launder *et al.* [20], but more recent studies suggested a higher value close to 5/9. The simplified implicit algebraic Reynolds stress Eq. (2.42) is then multiplied by 9/4 to get a similar formulation as

$$Na_{ij} = -\frac{6}{5}S_{ij} + (a_{ik}\Omega_{kj} + \Omega_{ik}a_{kj}) \tag{2.43}$$

where N is related to the production to dissipation rate ratio as

$$N = c_1' + \frac{9}{4}\frac{P_k}{\epsilon} \tag{2.44}$$

where

$$c_1' = \frac{9}{4}(C_1 - 1) \tag{2.45}$$

Here c_1' is the Rotta coefficient and is set to 1.8. The simplifications made the equation system quasi-linear, as the tensor equation for a_{ij} is linear, and the corresponding scalar equation for N is non-linear. The solution for the simplified ARSM equation is presented by using different approaches, which are available in literature [8, 30–33]. The approach discussed above are for incompressible flows. For compressible flows, incompressible models can be directly extended by using Favre-averaged turbulent quantities.

2.5 Summary

RANS equations govern the mean flow with additional turbulent transport equations for the Reynolds stresses, turbulent kinetic energy, and turbulent length scale. All the flow variables are Favre-averaged except for pressure and density. Eddy viscosity-based two-equation turbulence models give the necessary flow behavior, but they have ample assumptions. In the RSM transport equations, the pressure strain correlation plays a significant role in redistributing the turbulent fluctuations, and several turbulence closures are proposed. ARSMs can reduce computational cost and numerical stiffness in comparison with RSMs. EARSM is much more numerically robust and computational cost-effective.

Chapter 3

Review of literature

Interaction of shock waves with turbulent boundary layer can result in complex flow pattern in high-speed flows. These include boundary layer separation and flow reattachment, free shear layers, multiple shock, expansion waves, and their interaction,. As a result, SBLI often result in high surface pressure and heat transfer rates.

One of the primary purposes of the present study is to gain insight into RANS modeling of principal Reynolds stresses in shock-dominated flows, which affects the turbulence anisotropy, separation bubble size, and surface properties. In section (3.1), we briefly explain the modification and development of the turbulence closure under eddy viscosity based models, RSMs and ARSMs. Subsequently, in section (3.2), we describe SBLI canonical configuration and highlight the inability of existing turbulence models to predict the surface properties.

A canonical shock-turbulence interaction configuration is assumed to be a simple yet insightful configuration subjected to theoretical and numerical study. A detailed understanding of the STI model problem is presented in section (3.3). Some of the useful outcomes of studying STI on developing physics-based models for SBLI are also discussed in this section, followed by the present work objectives.

3.1 Turbulence closures

3.1.1 Eddy viscosity based two-equations models

The standard turbulence models, such as $k - \epsilon$ and $k - \omega$ turbulence models, cannot predict the location of the separation shock, size of the separation region, and mean velocity profiles downstream of the interaction. Several modifications have been proposed to improve predictions, e.g., realizability constraint [34], compressibility correction [35, 36], length-scale modification [36], and rapid compression correction [36]. Limiting the ratio of production to the dissipation rate of turbulent kinetic energy to some value or limiting the production itself is often used by some turbulence models such as shear stress transport (SST) model [37], and Wray-Agrawal model [38]. However, the turbulence models based on eddy viscosity assumption show poor performance in strong SBLIs.

Morgan *et al.* [39] investigated the cause of modeling errors in two-equation turbulence models and RSMs in prediction of the size of the separation bubble and turbulence quantities. Hamlington and Dahm [40] modified the standard two-equation formulation to account for the flow history of the Reynolds stress tensor. Sinha *et al.* [42] modified the turbulent kinetic energy equation with shock-unsteadiness correction and showed improvement over standard one- and two-equation turbulence models. The shock unsteadiness model of Sinha *et al.* [41] is described further in section 3.3.

3.1.2 Reynolds stress models

Compared to the two-equation models, RSMs have an additional pressure-strain correlation term, which models the redistribution of turbulent fluctuations in all directions. Earlier studies in second-moment closure models provide various approximations for the pressure-strain correlation terms [6, 23, 43, 44]. Rotta [6] modeled the pressure-strain closure for decaying homogeneous turbulence without any mean strain in the flow. Extending Rotta's concept, Launder, Reece, and Rodi [23] proposed a general closure for the pressure-strain correlation, which is linear in Reynolds stresses, and the model was referred to as the quasi-isotropic model (LRR-QI). Later, they proposed a different model by retaining the dominant term in the pressure-strain correlation; the simplified version is known as isotropization of the production Reynolds stress model (LRR-IP). The rapid pressure-strain term tends to isotropize the turbulence production in this model.

Lumley [44] developed a nonlinear model for the pressure-strain correlation, which reduces to the LRR-QI model when the nonlinear anisotropy tensor terms are neglected. Speziale, Sarkar, and Gatski (SSG) [43] postulated a quadratically nonlinear anisotropy tensor model using a different approach compared to Lumley [44]. Adopting the LRR-IP model, Gibson and Launder [45] modified the pressure-containing correlations by adding wall correction for the fluctuating pressure field. Later, Launder and Shima [46] proposed a new model extending the Gibson and Launder [45] model to incorporate near-wall viscous sublayer effects by optimizing the model coefficients.

The closure models discussed above are for incompressible flows. For compressible flows, incompressible models are directly extended by replacing the Reynolds-averaged Reynolds stresses with Favre-averaged Reynolds stresses. Gerolymos *et al.* [17–19, 47] followed this approach for Launder and Shima RSM [46] by using modified dissipation equation from Launder and Sharma [20]. They developed three different models that are independent of geometry/wall topology. In Ref.[18], the coefficient of the rapid pressure-strain correlation term is retained. In Ref.[17], the coefficient is modified to provide a numerically robust model. Further improvements are made in Ref. [17], and the model in Ref.[19] includes specific modeling for pressure-diffusion, non-linear inhomogeneous terms in the slow pressure-strain term model and a separate model for the dissipation rate tensor anisotropy. The models are applied to various flows, some of which are separated flows on supersonic compression ramps and three-dimensional SBLIs [17–19, 47–50].

Taking into account the compressibility effects, Lee *et al.* [22] modified the pressure-strain correlation of the LRR-QI model and additionally considered dilatation-dissipation and the mass-averaged fluctuations. They applied the model to zero-pressure gradient supersonic turbulent boundary layers and curved compression surfaces. A good match is observed for measured quantities like skin friction, mean velocity, and turbulent energy profiles with experimental results. In a similar approach, Ladiende [51] used LRR-IP model with pressure-dilatation and dilatation-dissipation correction. The model was applied to supersonic turbulent boundary layers with an adverse pressure gradient and found to give a good match with experimental results.

Gnedin and Knight [52] developed a model by extending Rotta's model, with an additional compressibility correction term in the dissipation rate, proposed by Pantano and Sarkar [28], and Zeman [53]. Zha and Knight [21] adopted the Gnedin and Knight model and simulated three-dimensional crossing shock-wave/turbulent boundary-layer interactions. When compared to experimental results, heat transfer and pressure profiles are found to be in better agreement than the two-equation model. Some other improvements in modeling of the unclosed terms in RSM for SBLI are reported in Vieira *et al.* [54] and Liu *et al.* [55]. Wilcox [15] proposed a stress-transport model based on Launder, Reece and Rodi's pressure-strain closure and specific dissipation rate, ω. The model was applied to SBLI over the compression corner and reflecting shocks, and the predictions are found to be better than standard two-equation models.

3.1.3 Algebraic Reynolds stress models

Rodi [7] proposed the weak equilibrium assumption and gave physical insights to improve the model. Following a similar approach, Pope [16] was the first to propose using the ten tensor groups to form a consistent explicit relation. He suggested an effective-viscosity approach and introduced a finite tensor polynomial to formulate the effective-viscosity according to the Cayley-Hamilton theorem. He also derived a relation for two-dimensional mean flows leaving the production to dissipation rate ratio (P_k/ϵ) implicit.

This approach was later extended and solved for three-dimensional mean flows by Taulbee [31] for the particular case of $C_2 = 5/9$ and by Gatski and Speziale [33] for a general linear pressure-strain model. To develop a fully explicit ARSM, Gatski and Speziale [33] proposed an EARSM by linearising the production to dissipation rate term to be its equilibrium value. Later, Jongen and Gatski [56] extended the EARSM of Gatski and Speziale [33] by considering the production to dissipation rate equilibrium.

Girimaji [30] pointed out that ARSMs are not entirely explicit and not always self-consistent. He derived an exact solution to the non-linear weak-equilibrium equation for incompressible two-dimensional mean flows. Wallin and Johansson [8] have independently shown that this equation has a closed and fully explicit solution that can be expressed in a compact form. They simplified the algebraic equation for the Reynolds stress anisotropy tensor by setting the model coefficients to specific values. Recently, Gomez and Girimaji [57] proposed a compressible EARSM reflecting three-stage behavior using gradient Mach number, which mainly focuses on the compressible mixing layer.

Coratekin *et al.* [58] studied the SBLI flows using the EARSM model [8] developed by Wallin and Johansson. They applied the model to three different configurations, such as two-dimensional supersonic inlet at Mach 3.0, two-dimensional triple-ramp flow at Mach 7.3, and three-dimensional double fin at Mach 3.95. For all the geometries, the EARSM computed surface pressure distribution showed a better match with the experimental data compared with SA and $k - \omega$ turbulence models. On the other hand, all the turbulence models show a very poor prediction of heat transfer.

3.2 Oblique shock impingement

In a practical inlet configuration of the high speed air-breathing vehicles, presence of shock waves with the geometric variations add to the overall complexity of the flowfield. These shock waves impinge on the vehicle body and have multiple reflection to form a train of shocks and expansion waves between the vehicle body and the cowl plate. Further, they interact with the boundary layer on the walls and can result in flow separation due to strong adverse pressure gradient. The shockwave/boundary-layer interaction often results in a complex flow pattern, comprising of additional shock waves, expansion waves, shear layer and separation bubble. The separation bubbles are highly viscous, and hence increase the stagnation pressure loss. Peak values of pressure, skin friction and heat transfer rates are found at reattachment point. The separation bubble acts as a blockage to the flow inside the inlet duct and can result in inlet unstart. It is therefore important to predict the shock/boundary-layer interaction flowfield in a scramjet inlet.

The two-dimensional oblique shock impingement case with a flat plate and an external shock wave generator with a deflection angle of θ finds application in the analysis of internal flows such as air intakes of high-speed air-breathing engines. An inviscid supersonic flow over the shock generator produces an incident oblique shock. This incident shock impinges on a flat plate and gets reflected. The shock strength at the impingement point is given by the total inviscid pressure rise across the incident shock and the reflected shock. The incident oblique shock interacts with the turbulent boundary layer on the plate and results in a complex flow pattern (see Fig. (3.1)).

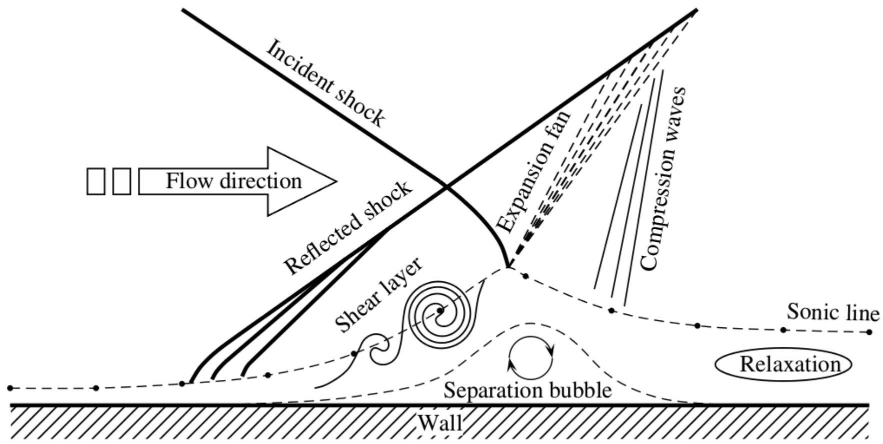

Figure 3.1: Illustration of a typical oblique shockwave/boundary-layer interaction.

The adverse pressure gradient across the incident oblique shock causes the boundary layer to separate on the flat plate and forms a separation bubble. An oblique separation shock is generated due to the blockage caused by the separation bubble. The interaction of incident shock and separation shock generates additional shocks. The boundary layer turns to form a shear layer over the separation bubble. The shear layer attaches back on the plate and forms compression waves, which coalesce to form a reattachment shock. The correct prediction of the separation bubble size determines the correct flow topology in terms of shock angles, the strength of shock waves, and expansion fan formation.

For the configuration mentioned above, Schulien *et al.* [14] carried experimental investigation for different deflection angles of 6°, 10°, and 14° with Mach number of 5, unit Reynolds number, Re_∞ of $37 \times 10^7\ m^{-1}$. Flowfield schlieren images, wall pressure, skin friction, and heat transfer measurements have been carried out. These configurations have been computed by different researchers [12] using different turbulence models for predicting surface pressure and skin friction. In general, it was observed that the computed wall pressure and skin friction values match closely for lower deflection angles and show large variation at larger angles when compared to experimental data.

Gerolymos *et al.* [17–19, 47] applied different Reynolds stress models to the strongest oblique shock impingement case of Schulein *et al.* [14] experiment. The modified RSM improved the prediction of upstream influence and underestimated the height of the recirculation zone. All the turbulence models failed to predict the correct shape of wall friction distribution at and downstream of the reattachment flow region, as shown in Fig. (3.2).

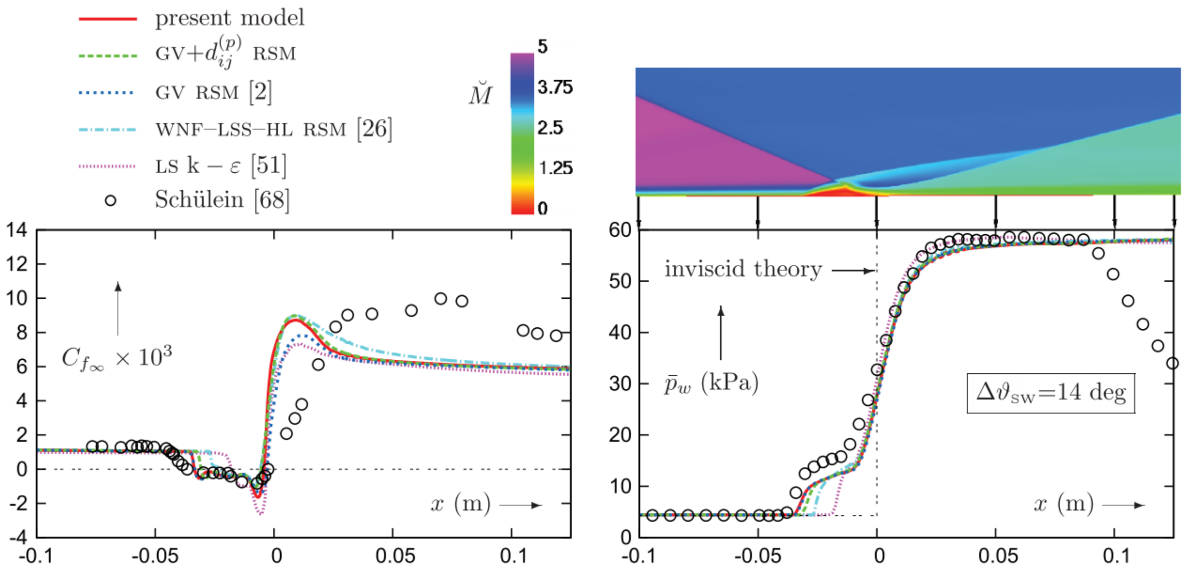

Figure 3.2: Comparison of streamwise distributions of wall-pressure and skin-friction obtained using different turbulence models for the incident oblique shock wave/turbulent boundary-layer interaction flow [47].

Fedorova *et al.* [59, 60] used the Wilcox 1988 $k-\omega$ model [15] to study the Schulein impinging shock experiment for shock generator angles of 6°, 10°, and 14°. No grid study was discussed, and the sensitivities of the results to freestream turbulence levels and wall spacing were not addressed. They found good agreement for the surface pressure at all shock generator angles. The skin friction was accurately predicted for the smaller generator angles, but the recovery skin-friction levels were underpredicted for the 14° case.

Nance and Hassan [61] used the $k-\zeta$ turbulence model to examine the Schulein *et al.* [14] experiments. In the paper, a grid sensitivity study is mentioned, but no results are presented. Also, sensitivities to wall y^+ values and freestream turbulence levels are not discussed. The cases with 10° and 14° shock generators were studied. Both wall pressure and skin friction obtained using EARSM and $k-\zeta$ turbulence model show the

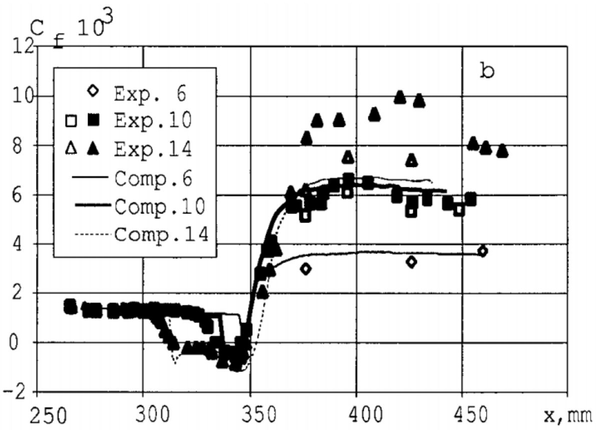

Figure 3.3: Comparison of experimental data and computed skin friction for 14° case from Fedorova *et al.* [59].

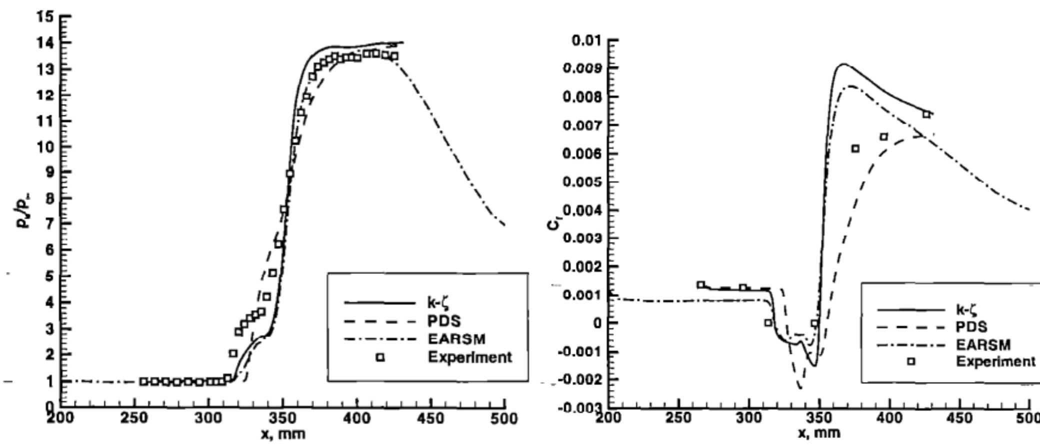

(a) (b)

Figure 3.4: Comparison of (a) wall pressure and (b) skin friction for 14° case from Nance and Hassan [61].

discrepancies in capturing the separation bubble size and gives a high value of the skin friction coefficient at the reattachment point, shown in Fig. (3.4).

Xiao *et al.* [62] used the $k - \zeta$ turbulence model and a new model for calculating the turbulent Prandtl number, to examine the Schulein *et al.* [14] experiments. Numerical simulations were carried for 10° and 14° shock boundary layer interaction flows with no grid sensitivity study. The variable Prandtl number turbulence model showed improvement in capturing the separation bubble size compared with the fixed Prandtl number model. The heat flux is overpredicted in the interaction and recovery regions, and the peak heating at the reattachment point is exceedingly high, shown in Fig. (3.5).

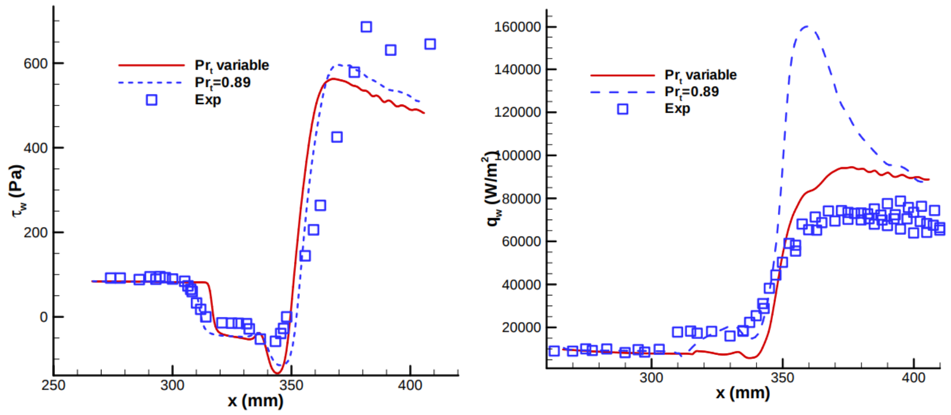

(a) (b)

Figure 3.5: Computed and measured (a) skin friction and (b) heat transfer for 14° case from Xiao *et al.* [62].

Brown [63] has used SST, $k-\omega$, and Spalart-Allmaras (SA) turbulence models with compressibility corrections to examine the Schulein *et al.* [14] experiments. SST turbulence model showed better improvement in capturing the separation bubble and wall heat transfer than $k-\omega$ and SA turbulence models. Still, it underpredicts the separation bubble by 25-40 percent (See Fig. (3.6)).

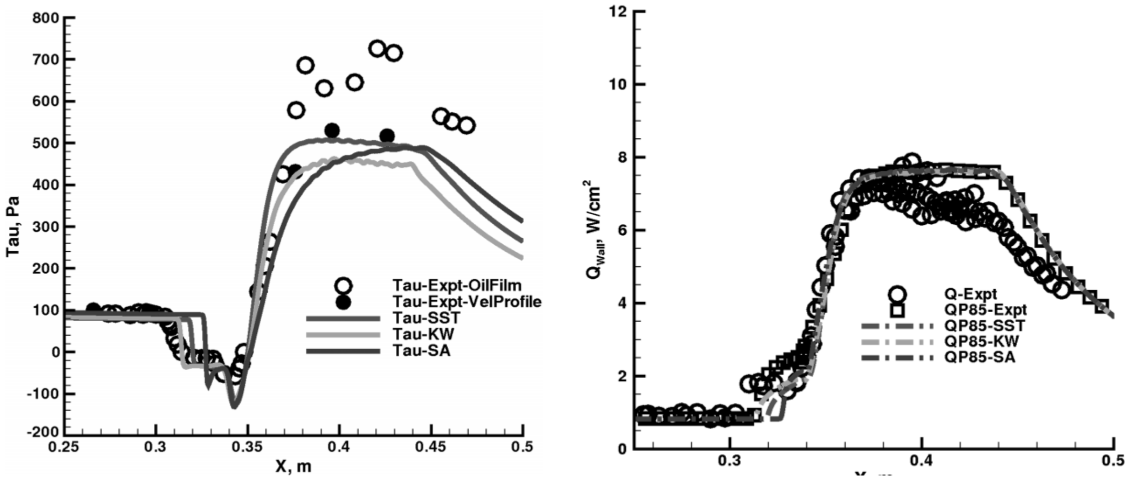

(a) (b)

Figure 3.6: Schulein Mach 5, 14^0 separation case, (a) skin friction and (b) heat transfer.

The oblique shock impingement with θ = 14° and 10° at Mach 5 was computed by Lindblad [64] using two different EARSM based on $k-\omega$ turbulence models. Fig. (3.7) shows the skin friction generated from two different codes with the same Wallin and Johansson EARSM turbulence model [8]. The results show different trends of skin friction distribution for the 10° case. As per the author's explanation, the difference may be due to the implementation of wall boundary conditions or inflow velocity profile used in the computation, which do not match the experimental profile perfectly.

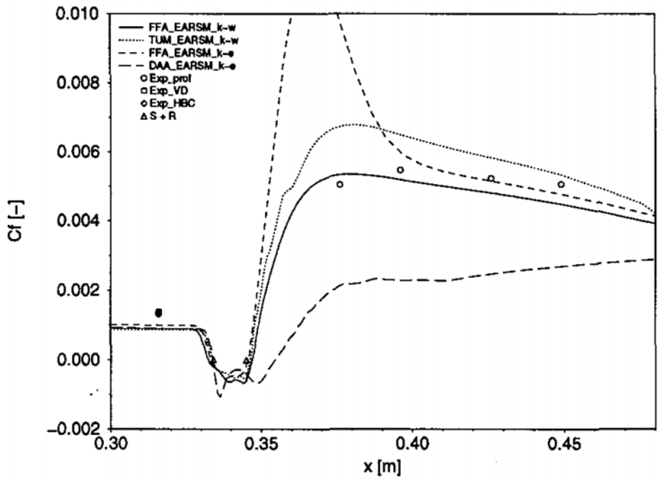

Figure 3.7: Comparison of experimental data and computed skin friction for 14° case from Lindblad *et al.* [64].

Impinging shockwave/turbulent layer interaction flowfield is also studied using DNS [65–70] and LES [71–73] for the supersonic Mach numbers less the 3. However, each study mainly focused on adopting shock-capturing schemes and prescribe inflow turbulence differently. Li & Coleman [65] performed DNS study for an oblique shockwave impinging upon a turbulent boundary layer at Mach 2.0 with inflow displacement-thickness Reynolds number of 3775. They have used a synthetic technique to generate inflow condition. They did not provide the details of low-frequency unsteadiness and quantitative data on turbulence fluctuations or correlations for the interaction.

Priebe *et al.*[66] and Wu *et al.* [67] carried out DNS for a reflected shockwave/turbulent boundary-layer interaction with the inflow conditions of Mach number=2.9 and incoming boundary layer with Re_θ =2400. The study provided the evolution of the mean and fluctuating quantities throughout the interaction. They identified that the peak turbulence intensity was in the detached shear layer, implying a mixing-layer mechanism leads to the turbulence amplification. Pirozzoli & Grasso [68] conducted the DNS of impingement shockwave turbulent layer interaction configuration at Mach 2.25 and Re_θ = 3725 with the deflection angle through the incident shock of 8.1 degree. They used a seventh-order-accurate weighted-essentially nonoscillatory (WENO) scheme for the spatial discretization of the inviscid fluxes. They proposed an acoustic-feedback mechanism in the separation bubble for instability of the shock motion. Similar to Wu *et al.* [67], they found that the turbulence was amplified in the mixing layer with its largest values away from the wall. Both the turbulence kinetic energy and its production term were found to reach their maxima inside the mixing layer. Therefore, they concluded that the mixing layer formation was primarily responsible for the amplification of turbulence. Later, Pirozzoli & Bernardini [69] performed DNS study on SBLI and confirmed again that the maximum production of turbulence kinetic energy in SWTBLI is due to the lift-up vortical structures in the mixing layer.

Recently, Fang *et al.*[70] carried out the DNS study on the turbulence amplification in shock-wave/turbulent boundary layer interaction. Three-dimensional numerical simulations were performed for the incoming freestream Mach number of 2.25 and the Reynolds number based on the nominal boundary layer thickness at the inlet plane of 11277. They analysed the turbulence amplification in the interaction region and proposed a new turbulence amplification mechanism based on the DNS data analysis. Similar to Wu *et al.* [66, 67] study, the amplification of high turbulence level of turbulent kinetic energy in the near-wall region is seen and explained with the proposed mechanism.

Garnier & Sagaut[71] presented large-eddy simulation results for an oblique SWTBLI problem for Mach 2.3, and Reynolds number depended on displacement thickness of 19132 with flow deflection through the incident shock generated by corner angle of 8 degree. Oblique shock wave strength is high enough to produce a separation of the boundary layer. The Reynolds number of the flowfield did not match the experimental data, and their study does not analyze low-frequency shock unsteadiness motion. Moreover, they saw a discrepancy in the prediction of Reynolds shear stress terms.

Touber and Sandham [72] performed LES for the interaction between an impinging oblique shock-wave generated by an 8-degree wedge interacting and a turbulent boundary layer at a freestream Mach number of 2.3. They carried out a detailed investigation of low-frequency shock unsteadiness in a turbulent shock-induced separation bubble and showed good agreement with the IUSTI group's experiments. They proposed an inflow generation method based on the digital filter (DF) technique, which does not introduce any energetically significant low frequencies into the domain.

Morgan *et al.*[73] carried out LES for parametric studies of impinging shock for various wedge angles, Reynolds numbers, streamwise and spanwise domain sizes. They found that the Reynolds number did not have any significant effect on the separation bubble size. Increasing the wedge angle led to an increased size of the interaction region. Many aspects of STBLI, such as shock unsteadiness, turbulence amplification, and mean flow modification induced by shock distortion, separation, and reattachment criteria, have been studied using RANS, LES and DNS. Understanding the fundamental physics, accurate predictions, scaling laws, effective means to control the interaction regions, and governing the dynamics of shockwave/turbulent boundary layer interactions are the primary focus of these numerical studies.

3.3 Shock-turbulence interaction

Canonical STI is the most fundamental problem where a one-dimensional mean flow carrying three-dimensional homogeneous isotropic turbulence interacts with a nominally normal shock (see Fig. (4.1)). The shock wave amplifies the turbulence and makes it anisotropic. It also generates acoustic energy and causes a sudden change in the length scales of turbulence. The turbulent fluctuations passing through the shockwave make it unsteady about its mean position, as shown in the figure. Thus, canonical STI exhibits many of the essential features of high-speed flows with shock waves. This is the simplest model problem to isolate the shock physics on the turbulence field. Rankine-Hugoniot

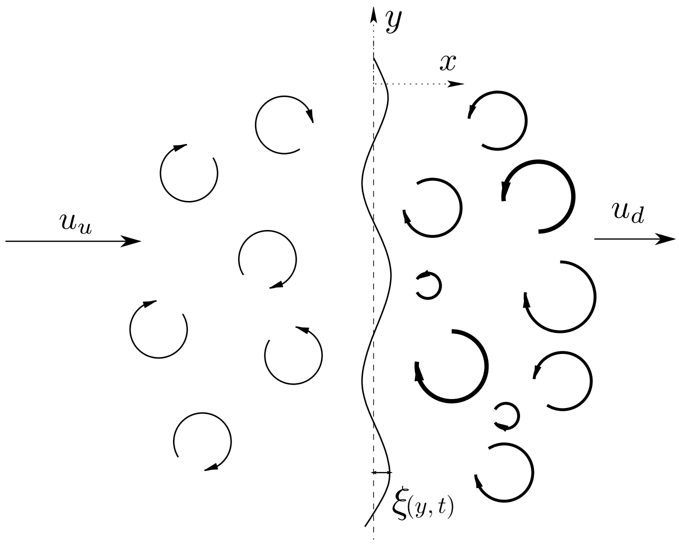

Figure 3.8: Schematic of canonical shock-turbulence interaction.

relations govern the mean flow quantities across the shockwave and are given as,

$$\rho_u u_u = \rho_u u_d \tag{3.1}$$

$$\rho_u u_u^2 + p_u = \rho_d u_d^2 + p_d \tag{3.2}$$

$$c_p T_u + \frac{1}{2} u_u^2 = c_p T_d + \frac{1}{2} u_d^2 \tag{3.3}$$

Here u, ρ, p, and T are instantaneous quantities of velocity, density, pressure, and temperature. The upstream and downstream flow is denoted by subscript u and d, respectively.

Turbulence passing through the shock gets amplified and enhances various turbulence quantities, such as TKE and its dissipation rate. The main advantage of studying the STI problem is the isolation of the net effect of the strong gradients of mean quantities imposed on the turbulence by the shock.

Figure (3.9a) reproduced from Sinha *et al.* [74] shows the comparison of streamwise evolution of turbulent kinetic energy computed by different turbulence models with DNS data. A normal shock wave with a Mach number of 1.5 is located at $x = 3$. At the inlet station, the values of Taylor micro-scale based Reynolds number and the turbulent Mach number are 6.7 and 0.17. The TKE is normalized by its values immediately upstream of the shock wave. Turbulence dissipates from its inlet value upstream of the shock due to the zero mean velocity gradient and gets amplified across the shock. The TKE decays faster in the downstream compared to upstream of the shock due to an increase in the dissipation rate of turbulence.

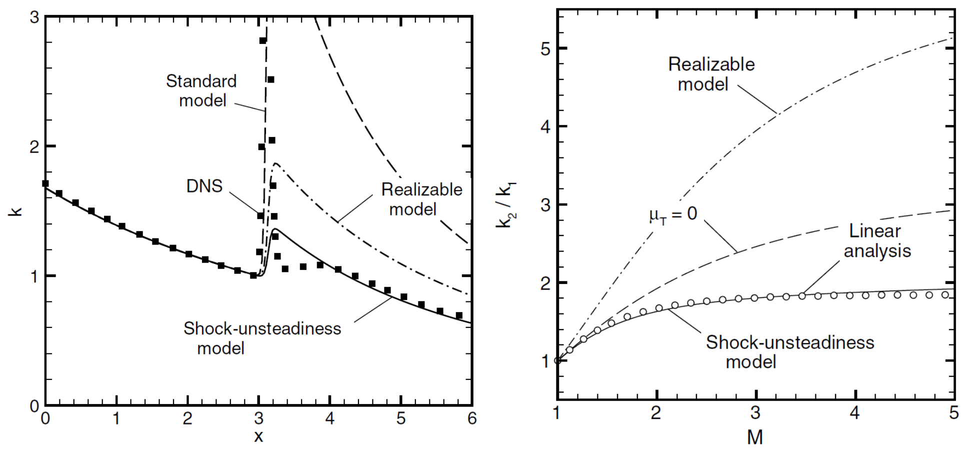

(a) (b)

Figure 3.9: Amplification of turbulent kinetic energy in canonical STI: (a) streamwise evolution in a Mach 1.5 interaction and (b) jump across shock waves for varying Mach numbers, reproduced with permission from Sinha *et al.* [74].

At the shock, the DNS data shows a very high value of TKE due to the unsteady motion of the shock and does not represent turbulence fluctuations. There is a non-monotonic variation in the TKE immediately after the shock, and the behavior is due to the acoustic decay described by Mahesh *et al.* [75]. In Fig. (3.9), the standard $k-\epsilon$ model and realizable $k-\epsilon$ model overpredicts the DNS data, whereas the TKE predicted by the shock-unsteadiness model shows a good match with DNS. The amplification of TKE also matches well with the linear theory for a range of Mach numbers shown in Fig. (3.9b).

The physical insights from the study of canonical shock turbulence interaction have been used towards the development of turbulence models for the shock dominant flows.

3.3.1 Theoretical analysis

Theoretical analysis of canonical STI has been carried by many researchers using linear interaction analysis (LIA). In this approach, the inviscid shock wave is treated as a discontinuity, and the upstream turbulence field is decomposed into Fourier modes. The heart of this theory is the elementary interaction of a two-dimensional plane wave with the distorted and unsteady normal shock wave as shown in Fig. (3.10). For a given upstream Mach number and plane wave incidence angle, the theory predicts the disturbance waves generated downstream of the shock. The superposition of the single wave results for a specified upstream energy spectrum yields the downstream statistics for three-dimensional turbulence [75].

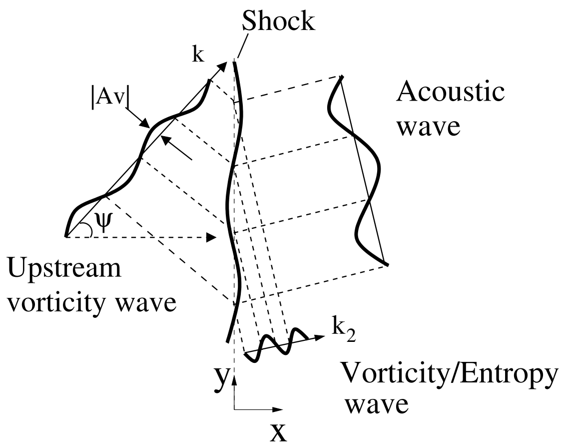

Figure 3.10: A single vortical wave interacts with a shock to yield three waves downstream of the shock.

For the first time, Kovasznay [76] decomposed turbulence of compressible flow into three fundamental modes: vorticity, entropy, and acoustic modes. Three independent equations govern these modes. He also demonstrated that the modes propagate independently when the turbulence intensity is small, and interact with each other at larger intensities. Ribner [77] formulated LIA to study the interaction between a single vortical planar wave and a normal shock and to see the acoustic and entropy waves generation downstream of the shock. Ribner [78] extended his earlier work on the single-wave and three-dimensional analysis to study the acoustic energy flux behind the shock upon interacting with a turbulence field containing only small vortical fluctuations. In this work, he showed that the acoustic flux generated varied linearly with the shock density ratio.

High-speed flows can have non-negligible thermodynamic fluctuations, and their effect on shock-turbulence interaction has been studied earlier [27, 75]. In a linear framework, Quadros *et al.* [79] studied the turbulent heat flux generation across the shock when the isotropic homogeneous turbulence interacts with the shock. Sethuraman *et al.* [80] studied the thermodynamic fluctuations across the shock, and using the LIA theory, they developed models for the thermodynamic variances. LIA is also extensively used to study the shock-induced mixing [25, 26], astrophysical problems, such as supernova explosion [81] and RMI [26]. These studies have shown that linear theory is indeed a powerful tool in analyzing some of the essential physics of the shock-turbulence interaction over almost five decades.

In the three dimensional space, the upstream turbulent field of the shock is considered to be isotropic, and it is represented as a superposition of planar 2D waves. Figure (3.11) shows the schematic of the 3D turbulence obtained by the superposition of 2D waves. Here x-axis corresponds to the shock-normal direction, and y and z correspond to the shock-parallel direction. $x - x_r$ is a plane making an angle ϕ to the $x - y$ plane and axisymmetric about the x-axis. Now consider a vortical wave having wavenumber, k in the $x - x_r$ plane, making an angle ψ to the x-axis and the amplitude of the vortical wave is represented by $|A_v|$. In the linear framework, each of the waves interacts with the shock independently. The interaction of this single vorticity wave with the shock can be

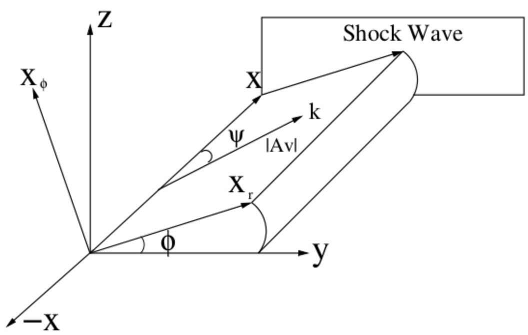

Figure 3.11: Plane wave in the $x - x_r$ plane normal to the shock.

treated as a two-dimensional interaction in the $x - x_r$ plane. The Reynolds stress tensor R_{ij} upstream of the shock along x and x_r direction is represented in Fourier space.

The Reynolds stress contribution from an individual wave of wavenumber k for this upstream turbulence takes the expression,

$$E_{ij} = \frac{E(\mathrm{k})}{4\pi \mathrm{k}^2}\left(\delta_{ij} - \frac{\mathrm{k}_i \mathrm{k}_j}{\mathrm{k}^2}\right), \tag{3.4}$$

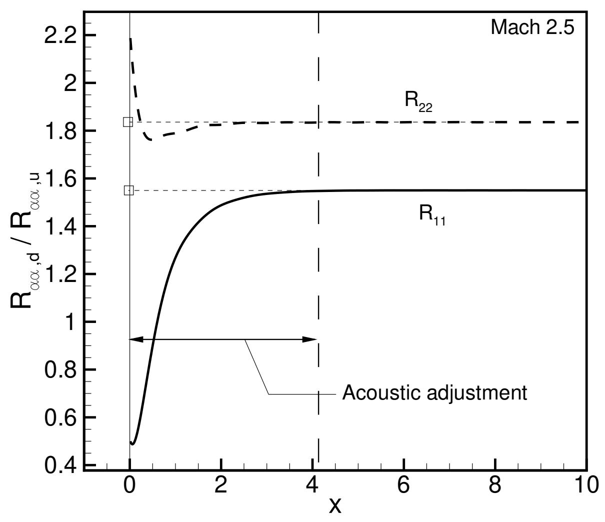

Figure 3.12: Streamwise evolution of the Reynolds stresses in a Mach 2.5 canonical STI predicted by the linear interaction analysis (LIA) for a purely vortical upstream turbulence.

where $E(\mathrm{k})$ is the upstream energy spectrum and the Reynolds stress contribution upstream of the shock can be written as

$$E_{11} + E_{22} + E_{33} = 2\frac{E(\mathrm{k})}{4\pi \mathrm{k}^2}, \tag{3.5}$$

where E_{22} and E_{33} are the Reynolds stresses along y and z directions, respectively. We obtain the three-dimensional streamwise Reynolds stress downstream of the shock, i.e.,

$$\frac{R_{11,d}}{R_{11,u}} = 4\pi \int_{\mathrm{k}=0}^{\infty} \int_{\psi=0}^{\pi/2} E_{11} \mathrm{k}^2 \sin\psi d\psi d\mathrm{k}. \tag{3.6}$$

The above integral is symmetric about ψ, and the solution is independent of ϕ. In a similar manner, the transverse Reynolds stresses can be obtained by integrating,

$$\frac{R_{22,d}}{R_{22,u}} = \frac{R_{33,d}}{R_{33,u}} = \frac{4\pi}{2} \int_{\mathrm{k}=0}^{\infty} \int_{\psi=0}^{\pi/2} \left(E_{rr} + \frac{E(\mathrm{k})}{4\pi \mathrm{k}^2} \right) \mathrm{k}^2 \sin\psi d\psi d\mathrm{k}. \tag{3.7}$$

E_{11} and E_{rr} behind the shock wave are determined once the $E(\mathrm{k})$ are specified. The turbulent statistics behind the shock for the upstream spectrum are obtained by integrating over all the upstream wavenumbers for varying values of ψ and ϕ considering the integral volume and integrating the energy spectra E_{11} and E_{rr} over the volume. The post-shock Reynolds stresses predicted by the LIA are plotted in Fig. (3.12). Detail formulations of LIA for the case of vorticity waves interacting with a normal shock wave are given in Refs. [75, 79, 80].

3.3.2 Numerical simulations

Numerical analysis of canonical STI has been carried by using DNS, LES, and RANS. One of the early studies of shock-turbulence interaction using the DNS was carried out by Lee *et al.* [82]. They studied the amplification of TKE, distortion of the shock front, and thermodynamic fluctuations using DNS and LIA. Mahesh *et al.* [75, 83] used DNS to study the turbulent statistics across the shock with two different upstream turbulent fields, such as turbulent acoustic field [83] and vorticity-entropy turbulent field [75]. Apart from the effect of turbulent fluctuations and entropy fluctuations, they also explored Morkovin's hypothesis across the shock. They showed that a negative correlation between velocity and temperature fluctuation in the upstream of the shock resulted in a higher amplification of turbulence fluctuations. Comparison of LIA and numerical simulations were found to be satisfactory.

Influence of the upstream turbulence, such as solenoidal, vorticity-entropy and vorticity-acoustic turbulent field on the post-shock turbulence statistics was studied by Jamme *et al.* [84]. Larsson and Lele [9] considered a wide range of upstream Mach numbers (1.27 - 6.0) and turbulent Mach numbers (0.16 - 0.38) and studied their effect on the downstream turbulent statistics and change in length scales across the shock. Their study showed the need for a finer grid size in the post-shock region, highlighting the under-resolved nature of the previous DNS studies of canonical STI. Shock distortion for various combinations of mean and turbulent Mach numbers was also studied in detail.

Larsson *et al.* [10] also presented DNS cases with varying Reynolds number and investigated the effect of upstream Mach-, turbulent Mach- and Reynolds number on various turbulent statistics such as TKE amplification and post-shock anisotropy. They also show for the first time that the influence of upstream Reynolds- and turbulent Mach number is minimal on the turbulence kinetic energy amplification. Sethuraman *et al.* [80] presented additional DNS cases to Larsson *et al.* [10] study for different turbulent intensity at Reynolds number based on the Taylor scale of 33. They showed the effect of the mean flow Mach number, the turbulent Mach number, and the Taylor lengthscale Reynolds number on the evolution of thermodynamic fluctuations.

Figure (3.13) reproduced from Larsson *et al.* [10] shows the comparison of amplification of the Reynolds stresses and TKE obtained from DNS data with LIA. An initially homogeneous isotropic disturbance field is converted into an axisymmetric turbulence field by the normal shock. DNS data of Larsson *et al.* [9, 10] show the anisotropy in Reynolds stresses for a range of shock strengths. The Reynolds stresses in streamwise, and transverse directions are amplified differently across the shock wave. The Reynolds stresses and its anisotropy behind the shock, however, do not match between DNS and

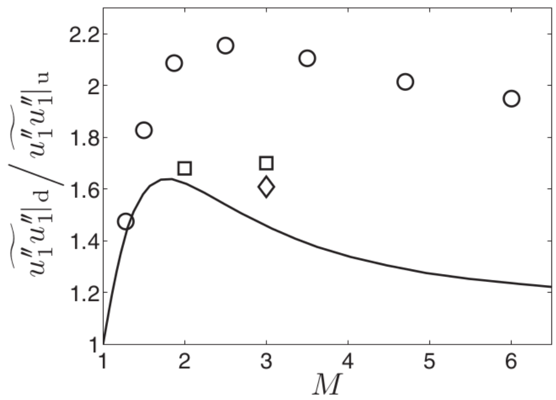

(a) Streamwise Reynolds stress

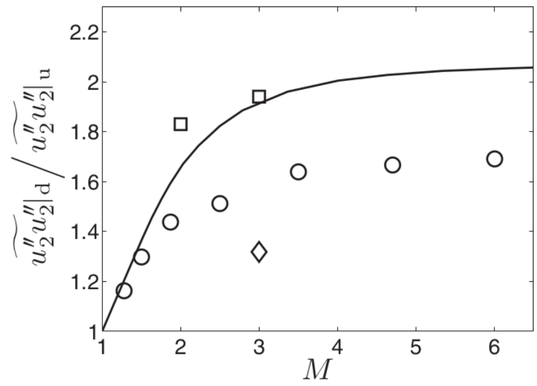

(b) Transverse Reynolds stress

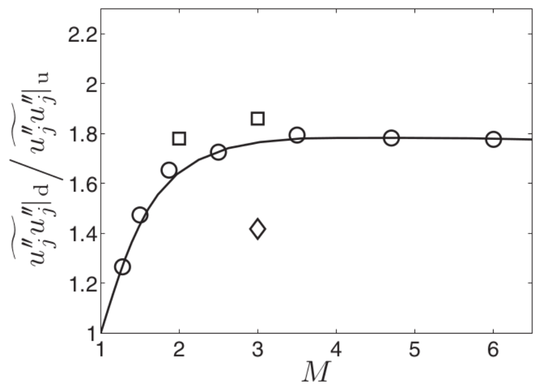

(c) TKE

Figure 3.13: Amplification of the Reynolds stresses and TKE from the DNS at M_t = 0.22 (circles), computations by Lee *et al.* [82] (squares), experiment by Barre *et al.* [85] (diamond), and LIA taken from Lee *et al.* [82] (lines). The results have been extrapolated from the far field to the mean shock location [10].

LIA, except for weak shock interactions (M<1.3). On the other hand, LIA and DNS data for TKE amplification match very well for the entire range of Mach number (see Fig. (3.13c)). This could be because of the post-shock non-linear effects. They also compared numerical simulation results with that of Barre *et al.* [85] experiments and find good agreement for Reynolds stress amplification across the shock.

Ryu and Livescu [86] carried out a high-resolution DNS study to resolve the shock structure in canonical STI. They studied the effect of the turbulent Mach number on the post-shock streamwise and transverse Reynolds stresses, and on the transverse vorticity variance. The turbulent statistics were analyzed for the upstream turbulent Mach number varying between 0.02 - 0.27, for a given upstream Mach- and Reynolds number. Livescu and Ryu [87] carried out shock-resolved DNS cases at Taylor Reynolds number of 180, much higher than the previously considered values, and upstream Mach number up to 10. The effect of the upstream Mach number on the downstream vortical structures was studied in detail. Tian *et al.* [88] studied the interaction of a Mach 2 shock wave with isotropic turbulence with (multi-fluid) and without (single-fluid) variable compositions. They compared the conditional expectation of density, pressure and temperature fluctuations amongst each other, and investigated whether they followed an isentropic scaling behind the shock.

LES computations of the shock/turbulence interactions has been performed by some researchers. Most of their work deals with two problems, first is subgrid models closures and second is numerical dissipation of the shock capturing schemes [94]. Garnier *et al.* [89] performed LES of the canonical STI for two different Mach number 1.2 and 2.0, and compared the evolution of the normal Reynolds stresses with the available DNS data of Lee *et al.* [82]. To capture the effect of the shock corrguation on the turbulence, they used four different sub-grid models along with mesh refinement. They concluded that the numerical dissipation of the shock capturing schemes cover the effect of the subgrid-scale model.

Ducros *et al.* [90] studied the turbulence scales affected by the numerical dissipation used to capture the shock. They investigated the shock/turbulence interaction using large-eddy simulations for high Reynolds number. They developed the shock sensor based on the local property of the compressibility to capture the shock by triggering artificial dissipation. Braun *et al.* [91, 92] performed LES of the canonical STI using a hybrid stretched-vortex model as the subgrid-scale model (SGS) for the regions away from the shock. At the shock, the weighted essential non-oscillatory (WENO) numerical scheme was applied. To ensure the correct SGS kinetic energy, they used a modified adaptive mesh refinement (AMR) procedure at the shock. They investigated the anisotropy in Reynolds stresses primarily, which was later used along with the LIA theory to develop a model, which would account for the shock-unsteadiness effects in RANS simulations of canonical STI.

Comparisons of explicit [89, 93] and implicit [95] LES approaches have further explored the relative effectiveness of different SGS models downstream of a shock. Also shock/turbulence interaction in internal flows has been studied using LES [96–98] of pseudo shock train in a constant area supersonic isolator with rectangular cross-section. Various shock-capturing methods like hyperviscosity and WENO schemes were used and compared. There analysis presents the evolution of mean flow quantities and Reynolds stresses, pressure-dilatation correlations, turbulent kinetic energy (TKE) budget for the unsteadiness of the shock train.

3.3.3 RANS modeling

Schwarzkopf *et al.* [99] proposed a second-moment closure model for variable density flows and applied the model to homogeneous STI. Braun *et al.* [91] extended the model of Schwarzkopf *et al.* [99] to investigate the Reynolds stresses and its anisotropy for STI problem. Braun *et al.* [91] model match reasonably with LIA predictions. However, the individual Reynolds stress amplifications predicted by these models have shown limited agreement with DNS data. Griffond *et al.* [26, 100] modified the Gregoire *et al.* [101] RSM to match results for STI. Following the same approach, Griffond and Soulard [100] evaluated three augmented RSMs that have an additional transport equation for the density related correlation against LIA data.

Within the RANS framework using two-equation eddy viscosity turbulence models, Sinha *et al.* [41] studied the amplification of TKE in a canonical STI. RANS models based on eddy viscosity assumption were shown to overpredict the TKE amplification across the shock. They modeled the damping effect of shock oscillation on the TKE amplification using LIA results. Implementing the shock-unsteadiness (SU) effect improved the TKE amplification to match the DNS trend.

Veera and Sinha [27] considered the presence of incoming temperature fluctuation to model the TKE amplification in canonical shock-turbulence interaction. The TKE equation budget was studied using LIA, and the dominant mechanism through which the upstream velocity-temperature correlation affects the TKE amplification was studied. These mechanisms were modeled using the linear theory results, and the final model correctly predicted the amplification of TKE in comparison with the DNS data.

Sinha [74] derived a transport equation for enstrophy in the canonical STI framework. Enstrophy, defined as the mean-square vorticity fluctuation, is directly related to the dissipation rate ϵ. The dominant terms responsible for enstrophy amplification were identified and modeled using the linear theory, and the critical physics was incorporated in the ϵ framework. The new model predicted the correct amplification in the dissipation rate across the shock for varying upstream Mach number. In [27, 41, 74], they studied shock unsteadiness effect on the TKE and dissipation rate in the STI. Figure (3.14) reproduced from Sinha [74] shows the comparison of amplification of the TKE and its dissipation rate obtained from SU model with DNS data.

Sinha and Balasridhar [102] studied the numerical error arising in the modeled transport equation for TKE and ϵ applied to canonical STI. The error was associated with the nonconservative nature of the source terms in the TKE and ϵ equations. This error was studied as a function of shock strength, grid resolution, and upstream turbulence level. The model equations were then cast into equivalent conservative forms; significant im-

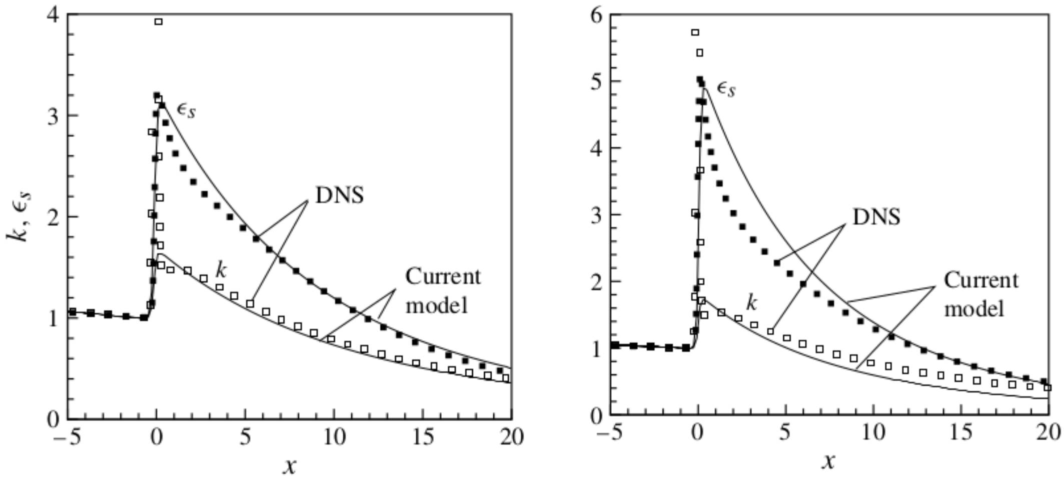

(a) Mach 2.5 (b) Mach 3.5

Figure 3.14: Shock-unsteadiness model [74] predictions (lines) for turbulent kinetic energy and solenoidal dissipation rate in the STI compared DNS data (symbols) [9, 10].

provement in the model predictions was observed, matching the DNS data and the linear theory.

Considering purely vortical turbulence in the upstream of the shock, Quadros *et al.* [79] studied the canonical STI using LIA and from the DNS data of Larsson *et al.* [9] for understanding the turbulent heat flux correlation. The physical insights from the study have been used towards the development of a simple model for the turbulent energy flux [103]. Recently, Sethuraman & Sinha [80], developed the models for the temperature, density, entropy, and pressure variances using LIA and the earlier works of Sinha *et al.* [41] and Quadros & Sinha [103]. The developed models predict the modification of turbulence due to the passage of the shock accurately.

3.3.4 Application of shock-unsteadiness (SU) model to SBLI

The modeling insights obtained in the canonical STI configuration have proven useful in modeling the SBLI flows. Sinha *et al.* [41] argued that these limitations in RANS computations are partly due to the shock-unsteadiness effect. In canonical flows, such as STI, when the turbulent flow interacts with a steady mean shock wave, it distorts the shock and makes unsteady in its mean position. This shock unsteadiness effect is not captured implicitly in the RANS simulations as they are based on time-averaged quantities. Moreover, the conventional turbulence models have no mechanism to include the shock-unsteadiness effect on the mean flow.

Pasha and Sinha [104] modified the $k - \omega$ and Spalart-Allmaras turbulence models based on the shock-unsteadiness factor and applied the shock-unsteadiness model to the case of an oblique shock interacting with a turbulent boundary layer. The new model showed appreciable improvement in the separation region size and the wall pressure prediction over the conventional RANS model, as shown in Fig. (3.15). Pasha and Sinha [105] also studied the hypersonic cone-flare configuration using the shock-unsteadiness model. Significant improvement in the separation size and wall pressure predictions was observed, and a modest improvement in the wall heat flux was also seen as compared with the conventional $k - \omega$ model.

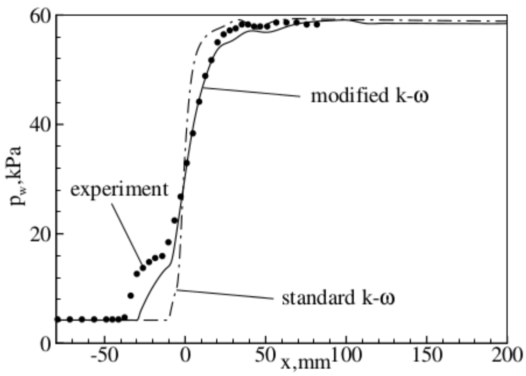

(a)

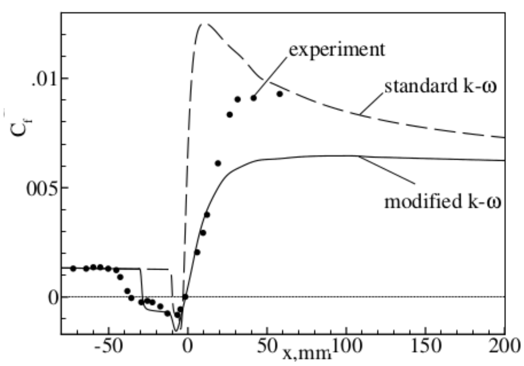

(b)

Figure 3.15: Comparison of (a) wall pressure and (b) skin friction coefficient for $\theta = 14^0$ computed using standard $k{-}\omega$ and shock-unsteadiness modified $k{-}\omega$ models over a larger domain up to 500 mm downstream of interaction region, compared with experimental data of Schulein *et al.* [14]

The highlight of their work [42, 104] was the implementation of the shock-unsteadiness correction [41] in the presence of multiple shocks- and expansion waves. To incorporate the shock-unsteadiness effect in the turbulence models, one needs to identify the shock waves and high compression regions in the flow. Pasha and Sinha [104] used the shock function, f_s to identify the shock and calculated the local shock strength using shock normal Mach number. Here, shock-unsteadiness correction is a function of upstream normal Mach number, M_n to shockwaves and shock identifying function, f_s. Computing the upstream shock Mach number is not trivial for flows involving multiple shock interactions, where the shock topology is not known a priori (see Ref. [104]). This kind of CFD implementation of the shock-unsteadiness correction makes the model non-local.

Pasha and Sinha [104] carried out the preliminary simulations to get an estimation of the shock location, shape, and strength. The approach increases the computational time and human effort to obtain the final results using the shock-unsteadiness model. To overcome the limitation, Roy *et al.* [106] modified the shock-unsteadiness correction in terms of the local density ratio, which is used to represent the shock strength. This eliminates the non-local nature of the shock-unsteadiness model, and the flow-physics of the original shock-unsteadiness model remain unchanged (see Ref. [106]).

3.4 Objective

The current work aims to study the amplification of Reynolds stresses across weak and strong shocks, and provide physical insights using LIA, DNS, and RANS simulations. One of STI's essential features is the shock-unsteadiness effect [41], which is not incorporated in standard turbulence models such as $k-\epsilon$ and $k-\omega$ when used in shock-dominated problems. This results in a high prediction of TKE, which is significantly more than those observed in DNS/LIA data. The inclusion of the shock-unsteadiness effect leads to an accurate prediction of the amplification of TKE across the shockwave by damping its excessive production.

The objective of the present study is to

1. evaluate the existing RSM and EARSM against available DNS data for canonical shock-turbulence interaction

2. study the implementation of the shock-physics based modification in existing turbulence models and develop modeling strategies to capture the Reynolds stresses and its anisotropy.

3. apply the modified Reynolds stress-based turbulence models to flows with SBLI and compare results with experimental data.

3.5 Summary

The chapter presents the development of eddy viscosity based two-equation turbulence models, RSMs, and EARSMs, including their application to the flows with SBLI. Correct prediction of the separation bubble size in SBLIs is essential to obtain the accurate flowfield topology and its wall data. Predicting the correct size of the separation bubble is also critical for many high-speed flow applications like supersonic inlets. The survey shows that existing turbulence models cannot correctly predict the size of the separation bubble and flow properties at and down the reattachment region for strong shocks. The reason may be because the turbulence models do not account for the shock-unsteadiness effects inherent in SBLI. This deficiency motivated us to study STI and get a brief understanding of shock physics, to develop the models to predict the realistic turbulence across the shock.

Chapter 4

Reynolds stress models applied to STI

In this chapter, first, we describe the canonical STI model problem, and the evolution of turbulence statistics using DNS data presented by Larsson *et al.* [9, 10] and a theoretical tool, known as LIA. Next, we present the evaluation of existing RSMs for the amplification of turbulence statistics against the DNS data. A brief understanding of the STI using the LIA and incorporating the improvement based on the linear theory in existing turbulence models are provided in subsequent sections. Last, the anisotropy generated across the shockwave is quantified for varying shockwave strengths using the anisotropy invariant mapping.

4.1 Canonical STI

Canonical STI is the most fundamental problem where a one-dimensional uniform mean flow carrying three-dimensional homogeneous isotropic turbulence ($\overline{u'^2}(R_{11}) = \overline{v'^2}(R_{22}) = \overline{w'^2}(R_{33})$) interacts with a nominally normal shockwave. Turbulence passing through the shockwave gets enhance and amplify the turbulence quantities. The homogeneous and isotropic initial turbulent field becomes axisymmetric ($R_{11} \neq R_{22} = R_{33}$) after the shockwave interaction. It is the simplest model problem to isolate the shockwave physics. The upstream disturbance field is assumed to be purely vortical, such that there are no pressure, density, and temperature fluctuations in the incoming flow. Interaction of the upstream turbulence with the shockwave, distorts and oscillates the shockwave structure about its mean position with a displacement of $x = \xi(y, t)$ in the flow direction, as shown in Fig. (4.1). In the absence of turbulence, the shockwave is a planar as predicted by the inviscid theory. In the flowfield, the turbulence is enhanced because of mean velocity gradients across the shockwave. Amplification in the shock-normal Reynolds stress is

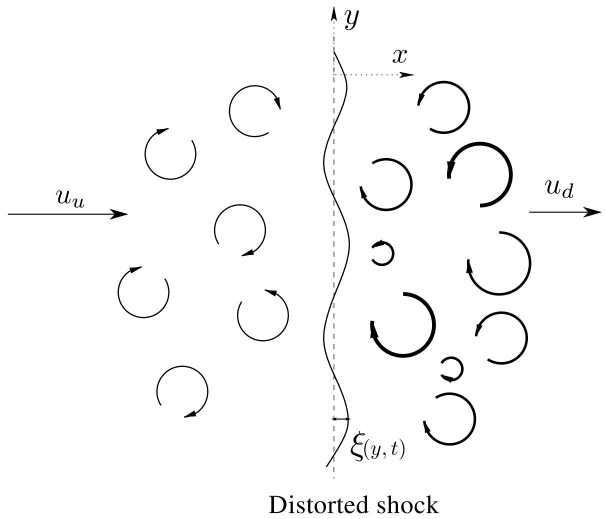

Figure 4.1: Schematic of homogeneous isotropic turbulence interacting with a normal shockwave distorted by the turbulent fluctuations passing through it.

usually more than the transverse components; thus the shockwave imparts a significant anisotropy to the turbulence.

Larsson *et al.* [9, 10] carried out a DNS study of the canonical STI problem for Mach numbers from 1.27 to 6 for varying turbulent Mach number, M_t, and Reynolds number based on Taylor microscale, Re_λ. Figure (4.2) shows streamwise evolution of the R_{11} and R_{22} obtained from the DNS data for Mach 2.5, where the respective shockwave-upstream values scale the Reynolds stresses. In the vicinity of unsteady shockwave region, the DNS data for R_{11} takes very high values, and outside, it rapidly increases from a low post-shock value to reach a local maximum at $\kappa_0 x^* = 4$. This corresponds to the acoustic adjustment region in LIA (see Fig. (4.2c)), where R_{11} increases due to the post-shock redistribution between the vortical and acoustic fluctuations as described by Mahesh *et al.* [75]. In the absence of viscous and non-linear effects in LIA, the Reynolds stresses reach asymptotic far-field values, whereas DNS data shows a monotonic decay far away from the shockwave ($\kappa_0 x^* > 4$). The transverse Reynolds stress R_{22} has a peak at the shockwave, followed by a rapid decrease in the acoustic adjustment region to reach the far-field value.

The extent of the acoustic adjustment region in the STI is about one wavelength of the most-energetic upstream wave number. This is equivalent to the integral scale of turbulence upstream of the shockwave, approximately equal to one boundary layer thickness in a SBLI. In a practical application such as in SBLI cases, this region is expected to be small, and the far-field values beyond this region become more prominent. We extrapolate the monotonic decay in R_{11} and R_{22} back to the shock center to obtain an equivalent far-

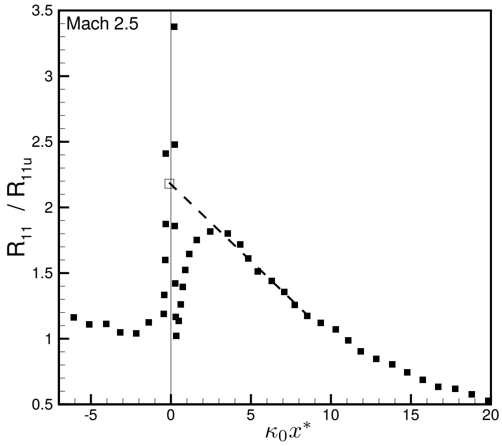

(a) R_{11}

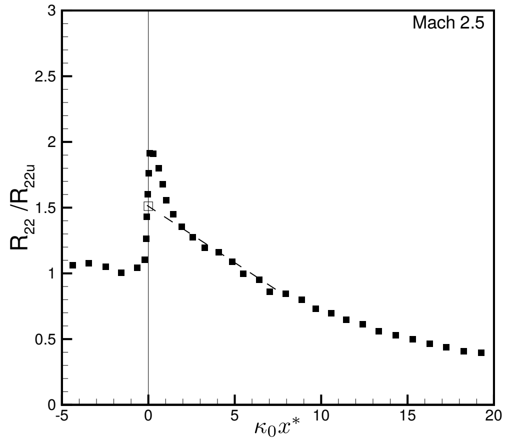

(b) R_{22}

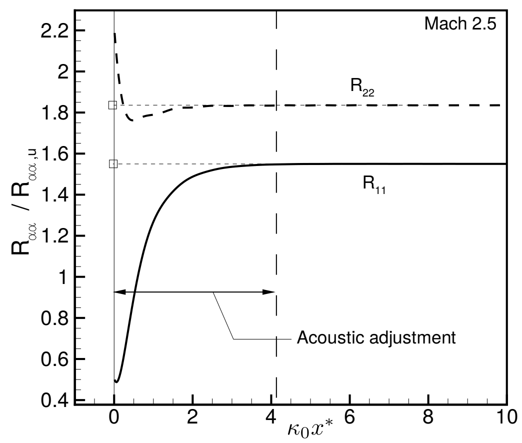

(c) R_{11} & R_{22} from LIA

Figure 4.2: Streamwise evolution of the Reynolds stresses in a Mach 2.5 canonical STI from the DNS data [9, 10]. The post-shock Reynolds stresses predicted by the LIA are plotted in (c).

field value from the DNS and more details are provided in Appendix B. An open square shows this value at $\kappa_0 x^* = 0$, and it serves as a benchmark for model evaluation, as discussed in the subsequent section. The extrapolated value includes the jump in Reynolds stresses at the shockwave as well as the net effect of the acoustic adjustment in the region immediately following the shockwave. Upstream of the shockwave, turbulence dissipates from its inlet value due to the zero mean velocity gradient. All the turbulent quantities such as Reynolds stresses and turbulent dissipation rate gets amplified across the shock. As a result of an increase in the dissipation rate of turbulence across the shockwave, the Reynolds stresses decay much faster downstream compared to upstream of the shockwave.

4.2 RSM simplified to canonical STI

For evaluating Reynolds stress transport equations in canonical STI, in the present work, we consider three existing RSMs adopted for compressible flows, and Favre decomposition is used for all terms except density and pressure. The transport equations for the Reynolds stresses are simplified to a steady one-dimensional form, applicable to the canonical STI problem. Note that the equation for R_{33} is identical to that of R_{22} for the current model problem.

For the Gerolymos *et al.* [18] model, equations for the shock-normal component R_{11} and the transverse component R_{22} are given by

$$\overline{\rho}\widetilde{u}\frac{\partial R_{11}}{\partial x} = -2\overline{\rho}R_{11}\frac{\partial \widetilde{u}}{\partial x} + \frac{4}{3}C_2\overline{\rho}R_{11}\frac{\partial \widetilde{u}}{\partial x} - C_1\overline{\rho}\epsilon a_{11} - \frac{2}{3}\overline{\rho}\epsilon, \tag{4.1}$$

$$\overline{\rho}\widetilde{u}\frac{\partial R_{22}}{\partial x} = -\frac{2}{3}C_2\overline{\rho}R_{11}\frac{\partial \widetilde{u}}{\partial x} - C_1\overline{\rho}\epsilon a_{22} - \frac{2}{3}\overline{\rho}\epsilon, \tag{4.2}$$

where $\widetilde{u}$ is the shock-normal mean velocity in the x-direction, and a_{11}, a_{22} are the anisotropy in the shock-normal and transverse Reynolds stresses, respectively. For isotropic turbulence, the coefficients reduce to $C_1 = 1$ and $C_2 = 0.75$. The first term on the right-hand side of Eq. (4.1) represents production, the second and the third term constitute rapid and slow parts of pressure-strain correlation, and the last term represents turbulent dissipation rate. For the transverse Reynolds stress given by Eq. (4.2), there is no production mechanism, that is, $P_{22} = P_{33} = 0$ (mean flow velocity gradient energizes the turbulence only in the axial component). The first two terms on the right-hand side of Eq. (4.2) therefore represent rapid and slow parts of pressure-strain, and the last term represents dissipation rate. The pressure-strain term redistributes energy from the streamwise Reynolds stress to the transverse Reynolds stresses, without affecting the TKE.

For Zha and Knight [21] model, equations for R_{11} and R_{22} simplify to

$$\overline{\rho}\widetilde{u}\frac{\partial R_{11}}{\partial x} = -2\overline{\rho}R_{11}\frac{\partial \widetilde{u}}{\partial x} + C_{c2}\overline{\rho}\left(R_{11} + 2R_{22}\right)\frac{\partial \widetilde{u}}{\partial x} - C_{c1}\overline{\rho}\epsilon a_{11} - \frac{2}{3}\overline{\rho}\epsilon, \tag{4.3}$$

$$\overline{\rho}\widetilde{u}\frac{\partial R_{22}}{\partial x} = -C_{c1}\overline{\rho}\epsilon a_{22} - \frac{2}{3}\overline{\rho}\epsilon. \tag{4.4}$$

The R_{11} equation has terms similar to those in Eq. (4.1), except for the contribution of both R_{11} and R_{22} in the rapid pressure-strain term. Comparing with Eq. (4.2), the R_{22} equation has no rapid pressure-strain term (since $\partial\widetilde{v}/\partial y = 0$). Therefore, the transverse Reynolds stresses R_{22} and R_{33} are not directly affected by the mean compression at the shockwave.

For Lee *et al.* model [22], the transport equations are given by

$$\bar{\rho}\widetilde{u}\frac{\partial R_{11}}{\partial x} = -2\bar{\rho}R_{11}\frac{\partial\widetilde{u}}{\partial x} + \bar{\rho}\left[\widehat{A}R_{11} + \widehat{B}R_{22}\right]\frac{\partial\widetilde{u}}{\partial x} - C_{p1}\bar{\rho}\epsilon a_{11} - \frac{2}{3}\bar{\rho}\epsilon, \tag{4.5}$$

$$\bar{\rho}\widetilde{u}\frac{\partial R_{22}}{\partial x} = \bar{\rho}\left[\widehat{C}R_{11} + \widehat{D}R_{22}\right]\frac{\partial\widetilde{u}}{\partial x} - C_{p1}\bar{\rho}\epsilon a_{22} - \frac{2}{3}\bar{\rho}\epsilon. \tag{4.6}$$

The coefficients of the rapid pressure-strain terms are grouped as, $\widehat{A} = \frac{4}{3}C_{p2} + \frac{4}{3}C_3 - \frac{2}{3}C_4 - \frac{2}{3}C_5 + C_6$, $\widehat{B} = \frac{2}{3}C_5 - \frac{4}{3}C_4$, $\widehat{C} = -\frac{2}{3}C_{p2} - \frac{2}{3}C_3 + \frac{1}{3}C_4 + \frac{1}{3}C_5 + C_6$, and $\widehat{D} = \frac{2}{3}C_4 - \frac{1}{3}C_5$. Across a normal shockwave, the contribution of the production and pressure-strain terms has the same form as in Eqs. (4.1) and (4.2), except for the contribution of both the Reynolds stress in rapid pressure-strain terms.

The conventional dissipation rate, ϵ, equation [29] is solved along with the Reynolds stress transport equations. Its simplified form for canonical STI is given as

$$\bar{\rho}\widetilde{u}\frac{\partial\epsilon}{\partial x} = -C_{\epsilon_1}\bar{\rho}R_{11}\frac{\partial\widetilde{u}}{\partial x} - C_{\epsilon_2}\bar{\rho}\frac{\epsilon^2}{k}, \tag{4.7}$$

with the coefficients, $C_{\epsilon_1} = 1.44$ and $C_{\epsilon_2} = 1.8$. We numerically integrate these equations using 4^{th} order accurate Runge–Kutta method for a specified mean flow profile across the shockwave. It can be shown that the results of the integration do not depend on (smooth) specified mean profile. The proof relies on switching from physical space to local compression space and is used in [26]. According to [109], the turbulent diffusion has a negligible effect across the shock, and it is neglected.

4.2.1 Input conditions

The normalized inlet values of Reynolds stresses, TKE, dissipation rate and specific dissipation rate are calculated from the DNS data, by considering the values (k_u, ϵ_u, and ω_u) immediately upstream of the shockwave. The non-dimensional values of k_u, ϵ_u and ω_u are calculated from

$$k_u = \frac{{M_t}^2}{2}, \quad \epsilon_u = \frac{5{M_t}^3}{\sqrt{3}\kappa_0\lambda^* Re_\lambda}, \quad \text{and} \quad \omega_u = \frac{5{M_t}^3}{\sqrt{3}\kappa_0\lambda^* Re_\lambda\beta^* k_u}, \tag{4.8}$$

with $\kappa_0\lambda^* = 0.84$ and $\epsilon = \beta^*\omega k$, where $\beta^* = 0.09$. The Taylor micro-scale is given by $\lambda^* = \sqrt{10\nu^* k^*/\epsilon^*}$ and the Reynolds number based on λ^* is defined as $Re_\lambda = \lambda^* u^*_{rms}/\nu^*$. The TKE, dissipation rate and specific dissipation rate are normalized as $k = k^*/a^{*2}_\infty$, $\epsilon = \epsilon^*/a^{*3}_\infty\kappa_0$ and $\omega = \omega^*/a^*_\infty\,\kappa_0$, respectively. Here, a^*_∞ is the freestream speed of sound.

Note that M_t and Re_λ in the DNS are reported at the location immediately upstream of the shockwave. The shock-upstream values k_u, ϵ_u and ω_u, thus obtained from Eq. (4.8) are extrapolated to the inlet section of the computational domain (subscript 0) using the homogeneous isotropic turbulence decay relations (see Appendix A).

$$\omega_0 = \omega_u \left[1 - \frac{\beta \omega_u x_{sh}}{\widetilde{u}_u}\right]^{-1}, \tag{4.9}$$

$$k_0 = k_u \left[1 + \frac{\beta \omega_0 x_{sh}}{\widetilde{u}_u}\right]^{\beta^*/\beta} \quad \text{or} \quad k_0 = k_u \left[1 + \frac{x_{shk}\epsilon_0}{\widetilde{u}_u n k_0}\right]^{n}, \tag{4.10}$$

$$\epsilon_0 = \epsilon_u \left[1 + \frac{x_{shk}\epsilon_0}{\widetilde{u}_u n k_0}\right]^{n+1}, \tag{4.11}$$

where, $n = 1/(C_{\epsilon 2} - 1)$ is the decay exponent with $C_{\epsilon 2} = 1.2$, and $x_{shk} = 6.83$ is the distance of shockwave from the inlet station, normalized with characteristic wave number κ_0. Subscripts 0 and u represent the inlet location and the location just upstream of the shockwave in the computational domain, which spans from the inlet at $\kappa_0 x^* = -7.6$ to the exit at $\kappa_0 x^* = 29.6$. The Reynolds stresses at the inlet boundary are given as

$$R_{11,0} = R_{22,0} = \frac{2}{3}k_0.$$

for isotropic turbulence upstream of the shockwave, and the Reynolds stresses are normalized in a way similar to the TKE. Normalized quantities which are defined as, $x = x^*\kappa_0$, $\rho = \rho^*/\rho^*_\infty$, $u = u^*/a^*_\infty$, $R_{11} = R^*_{11}/a^{*2}_\infty$, $R_{22} = R^*_{22}/a^{*2}_\infty$, $R_{33} = R^*_{33}/a^{*2}_\infty$, where $(.)^*$ represents the dimensional values of flow variables and $(.)_\infty$ represents the shockwave-upstream values. The characteristic length scale is taken from the incoming turbulence field with peak wave number κ_0 of 4. The normalized values of the Reynolds stresses, the TKE, the dissipation rate and the specific dissipation rate for the different test cases are listed in Table 4.1.

M	M_t	$k_0 \times 10^2$	$\epsilon_0 \times 10^3$	$\omega_0 \times 10^2$	$R_{11,0} \times 10^2$	$R_{22,0} \times 10^2$
1.27	0.15	1.48	0.421	31.61	0.99	0.99
1.50	0.15	1.45	0.410	31.42	0.97	0.97
1.87	0.22	2.78	1.08	43.20	1.86	1.86
2.50	0.22	2.66	1.04	42.90	1.79	1.79
3.50	0.22	2.60	1.00	42.64	1.74	1.74
4.70	0.22	2.55	0.978	42.48	1.70	1.70
6.00	0.22	2.52	0.964	42.38	1.68	1.68

Table 4.1: Normalised values of the turbulent kinetic energy, the streamwise and transverse Reynolds stresses, the turbulent dissipation rate and the turbulent specific dissipation rate in canonical shock-turbulence interaction for varying shock strengths.

4.2.2 Reynolds stress amplification

Figure (4.3) compares the amplification of R_{11} and R_{22} obtained from the DNS and the RSM equations for a range of shockwave strengths. The DNS data corresponds to the extrapolated shockwave values, and include the jump as well as the net effect of the rapid acoustic adjustment immediately downstream of the shockwave (see Appendix B). The model predictions are obtained by considering only the production and rapid pressure strain terms in the transport equations for R_{11} and R_{22}. The effect of dissipation and slow pressure strain terms is expected to be small a thin shockwave [41].

For the Gerolymos *et al.* [18] model, these terms can be integrated to get a closed form solution for the Reynolds stress amplifications across a shockwave.

$$\frac{R_{11d}}{R_{11u}} = \left[\frac{\widetilde{u}_u}{\widetilde{u}_d}\right]^{2-\frac{4}{3}C_2}, \tag{4.12}$$

$$\frac{R_{22d}}{R_{22u}} = 1 + \frac{C_2}{3-2C_2}\left[\frac{R_{11d}}{R_{11u}} - 1\right], \tag{4.13}$$

with subscripts u and d denoting the locations upstream and downstream of the shockwave respectively.

Neglecting the dissipation and slow pressure-strain terms, the R_{11} equation of the Zha and Knight [21] model reduces to,

$$\widetilde{u}\frac{\partial R_{11}}{\partial x} = \left[(-2 + C_{c2})R_{11} + 2C_{c2}R_{22u}\right]\frac{\partial \widetilde{u}}{\partial x}, \tag{4.14}$$

where the upstream value of the transverse Reynolds stress R_{22u} is used in the above equation, as it remains constant across the shock as per Eq. (4.4) without dissipation and slow pressure strain terms.

In the Lee *et al.* [22] model, the Reynolds stress transport equations retaining the production and rapid pressure-strain terms, are given as,

$$\widetilde{u}\frac{\partial R_{11}}{\partial x} = \widehat{A}R_{11}\frac{\partial \widetilde{u}}{\partial x} + \widehat{B}R_{22}\frac{\partial \widetilde{u}}{\partial x}, \tag{4.15}$$

$$\widetilde{u}\frac{\partial R_{22}}{\partial x} = \widehat{C}R_{11}\frac{\partial \widetilde{u}}{\partial x} + \widehat{D}R_{22}\frac{\partial \widetilde{u}}{\partial x}, \tag{4.16}$$

with the constants $\widehat{A} = -0.70$, $\widehat{B} = 0.14$, $\widehat{C} = -0.12$, and $\widehat{D} = 0.07$. Across the shockwave, Eqs. (4.14), (4.15), and (4.16) do not give closed-form solution for the amplification of turbulence quantities. Thus, we numerically integrate these equations using 4^{th} order accurate Runge–Kutta method (RK4) for a specified mean flow profile across the shockwave.

Figure (4.3) plots the amplification of the Reynolds stresses, dissipation rate, and the anisotropy in Reynolds stresses obtained using different models. The DNS data shows

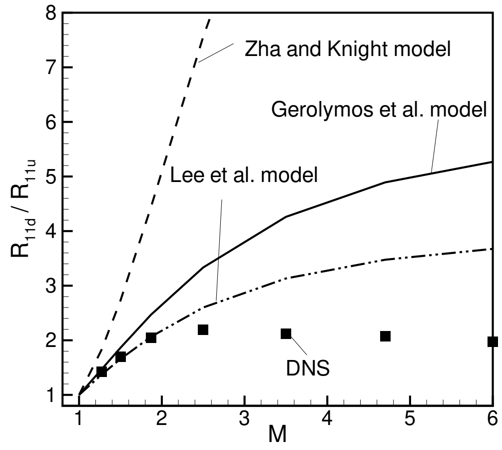

(a) R_{11} amplification

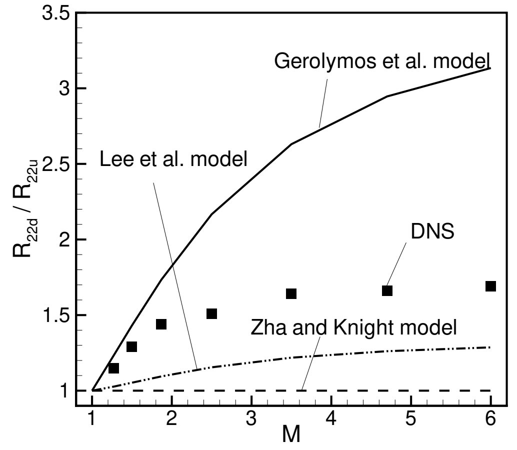

(b) R_{22} amplification

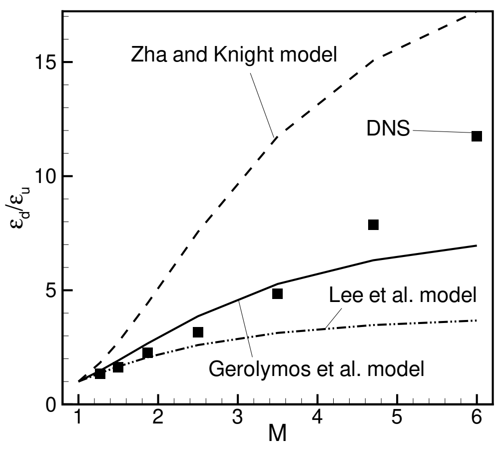

(c) ϵ amplification

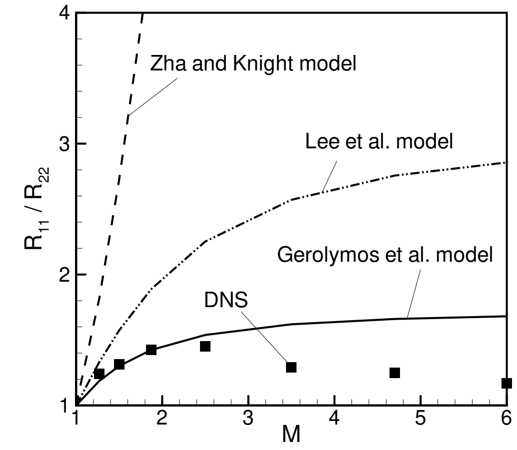

(d) R_{11}/R_{22} amplification

Figure 4.3: The amplification of R_{11}, R_{22}, ϵ and anisotropy(R_{11}/R_{22}) across the normal shock for varying Mach number, as obtained from DNS data [9, 10] and different Reynolds stress models.

that R_{11} amplifies across the shockwave upto Mach 2.5 and attains a peak amplification value of 2.15. For Mach numbers greater than 2.5, the amplification reduces from the peak value and saturates at a value of 2.0 across the shockwave. The amplification of the streamwise Reynolds stress, R_{11}, from the Zha and Knight [21] RSM predicts very high values for all Mach numbers. The R_{11} amplifications in the Gerolymos *et al.* [18] and Lee *et al.* [22] models, show increasing values before asymptotically reaching a constant value at high Mach numbers. Both the models have a good match with the DNS data at lower Mach numbers up to 1.5 and 1.87 respectively, beyond which they overpredict by upto a factor of 2.5. We note that the Gerolymos *et al.* [18] model results correspond to $C_2 = 0.75$, and the alternate forms of the model with $C_2 = 1$ proposed by [17, 19], would further overpredict R_{11} amplification.

Similar to R_{11}, the DNS data shows amplification in R_{22}, which gradually increases upto Mach 2.5 and saturates at a value of 1.7 for high Mach numbers. The amplification in R_{22} is monotonic across the shockwave for varying strengths, unlike R_{11}, which decreases slightly at high Mach numbers. Unlike the DNS data, the Zha and Knight [21] RSM predicts a constant value for all Mach numbers. The Gerolymos *et al.* [18] model overpredicts the DNS data by upto a factor of 2, whereas the Lee *et al.* [22] model underpredicts the R_{22} amplification; these two models indicate a gain in R_{22} from R_{11}, due to redistribution of energy. The Zha and Knight [21] model, on the other hand, yields no R_{22} amplification because of zero redistribution of energy from the shock-normal Reynolds stress.

In Fig. (4.3c), the amplification of the dissipation rate from the DNS data is shown; it increases steadily with increasing Mach number. In contrast, for all of the RSMs considered, the dissipation rate increases monotonically and saturates at high Mach numbers. The Gerolymos *et al.* [18] model predictions are comparable to the DNS amplification of ϵ up to Mach 3.5. On the other hand, the Lee *et al.* [22], and Zha and Knight [21] models underpredict and overpredict the ϵ jump by large factors for almost all the Mach numbers, respectively.

In the DNS data, the anisotropy of Reynolds stresses across the shockwave is seen to increase upto Mach number 1.87 and then decrease significantly at higher Mach numbers. For all RSMs, the anisotropy across the shockwave behaves similar to R_{11} amplification and does not reproduce the non-monotonic variation observed in the DNS data. The Zha and Knight [21] RSM and Lee *et al.* [22] RSM overpredict the anisotropy for all Mach numbers by factors larger than 2. The Gerolymos *et al.* [18] model shows a good match with the DNS data upto Mach number 2, but overpredicts for higher Mach numbers. Therefore, the Gerolymos *et al.* [18] model is considered for further development and it will be referred to as the baseline model in the subsequent sections.

4.3 Physics based model improvement

LIA is used by many researcher for studying the turbulence statistics of the canonical STI. In this approach, the inviscid shockwave is treated as a discontinuity and the upstream turbulence field is decomposed into Fourier modes. The elementary interaction of a two-dimensional plane wave with the deformed and unsteady normal shockwave forms the heart of this theory. For a given upstream Mach number and plane wave incidence angle, the theory predicts the disturbance waves generated downstream of the shockwave. Superposition of the single wave results for a specified upstream energy spectrum yields the downstream statistics for three-dimensional turbulence [75]. The theory also deals with shock-corrugation phenomena and its effect in post-shock turbulence.

4.3.1 Shock-unsteadiness correction

Sinha *et al.* [41] studied the amplification of turbulence in a canonical shock-turbulence interaction using LIA and to incorporate the effect of shock-unsteadiness, they derived the transport equation for the TKE by linearizing the governing equations about the unsteady distorted shockwave. The unsteady problem is converted to steady state by

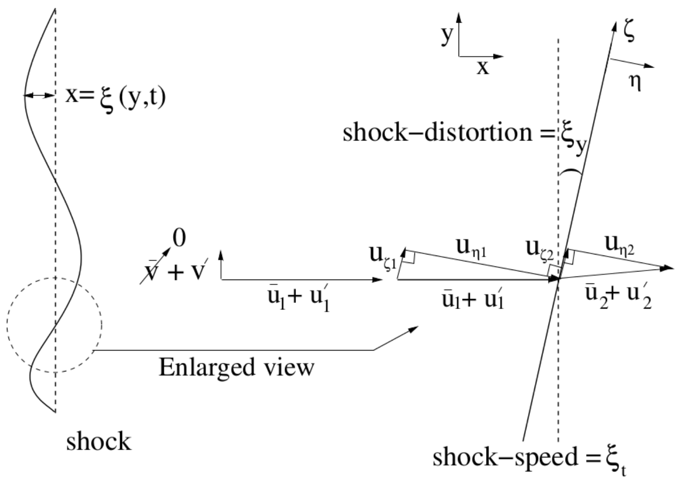

Figure 4.4: Homogeneous isotropic turbulence/shock interaction. Enlarged view depicting the velocity diagram with $\zeta - \eta$ coordinate system attached to the oblique shockwave. The normal and tangential components of velocity upstream and downstream of shock are shown.

fixing the coordinates to the shockwave, just as we are sitting on the shockwave, and in this frame of reference the shockwave is steady (see Fig. (4.4)). Here, the reference coordinate frame is attached to the instantaneous shockwave, and the turbulent fluctuations are assumed to be small compared to the changes in the mean flow quantities. The deviation of the shockwave from its mean location is represented by $x = \xi(y, t)$, and the temporal derivative, ξ_t, represents the instantaneous speed of the shockwave.

The linearized conservation equation of mass and momentum in the $\zeta - \eta$ coordinates are written. Here, the $\zeta-$ direction is tangential to shockwave and η is normal to it.

The viscous terms are neglected across shockwave and it is assumed that gradients in the shock-parallel direction are negligible. In Fig. (4.4) the part of the instantaneous shockwave is enlarged and shown for small shock-distortion ξ_y, $cos\xi_y \approx 1$ and $sin\xi_y \approx \xi_y$. Dropping the higher order terms the velocity components in ζ and η direction are given by,

$$u_\eta = (ucos\xi_y - vsin\xi_y) - \xi_t = (u - v\xi_y) - \xi_t = (\overline{u} + u') - \xi_t \tag{4.17}$$

$$u_\zeta = (usin\xi_y + vcos\xi_y) = u\xi_y + v = (\overline{u} + u')\xi_y + v = \overline{u}\xi_y + v' \tag{4.18}$$

Here, ξ_t is the linear shockwave velocity in the streamwise direction, overbar represents the Reynolds averaged and prime represents the fluctuation quantities. The continuity and momentum equations in the steady state $\zeta - \eta$ coordinate system are given by,

$$\frac{\partial}{\partial \eta}(\rho u_\eta) = 0 \tag{4.19}$$

$$(\rho u_\eta)\frac{\partial u_\eta}{\partial \eta} = -\frac{\partial p}{\partial \eta} \tag{4.20}$$

$$(\rho u_\eta)\frac{\partial u_\zeta}{\partial \eta} = 0 \tag{4.21}$$

Applying the chain rule of differentiation and substituting in above equations, we obtain,

$$\frac{\partial}{\partial x}(\overline{\rho} + \rho')(\overline{u} + u' - \xi_t) = 0 \tag{4.22}$$

$$(\overline{\rho} + \rho')(\overline{u} + u' - \xi_t)\frac{\partial}{\partial x}(\overline{u} + u' - \xi_t) = -\frac{\partial(\overline{p} + p')}{\partial x} \tag{4.23}$$

$$(\overline{\rho} + \rho')(\overline{u} + u' - \xi_t)\frac{\partial}{\partial x}(\overline{u}\xi_y + v') = 0 \tag{4.24}$$

Multiplying the x-momentum equation with u', Reynolds averaging and neglecting the higher order terms, we obtain,

$$\overline{\rho u}\frac{\partial}{\partial x}\frac{\overline{u'^2}}{2} = -\overline{\rho}\overline{u'^2}\frac{\partial \overline{u}}{\partial x} + \overline{\rho}\overline{u'\xi_t}\frac{\partial \overline{u}}{\partial x} - \overline{u'\frac{\partial p}{\partial x}} - \overline{u'\frac{\partial p'}{\partial x}} \tag{4.25}$$

The $y-$momentum equation is multiplied with v' and Reynolds averaged. In three-dimensional flow similar equation for $z-$ momentum equation is obtained and multiplied it with w' and Reynolds averaging gives,

$$\overline{\rho u}\frac{\partial}{\partial x}\frac{\overline{v'^2}}{2} = -\overline{\rho u}\overline{v'\xi_y}\frac{\partial \overline{u}}{\partial x} \tag{4.26}$$

$$\overline{\rho u}\frac{\partial}{\partial x}\frac{\overline{w'^2}}{2} = -\overline{\rho u}\overline{w'\xi_z}\frac{\partial \overline{u}}{\partial x} \tag{4.27}$$

It is assumed that $w' = v'$, hence $\overline{w'\xi_z} = \overline{v'\xi_y}$.

The above equations are for homogeneous isotropic turbulence interacting with a normal shockwave. The terms on LHS of the equations are the convection of streamwise, transverse and spanwise Reynolds stresses. The terms on RHS are in order as, the production of streamwise Reynolds stress, the shock-unsteadiness term, the production due to mean pressure gradient, which represents the effect of entropy fluctuations on the flow, the velocity pressure correlation, and the last two terms are due to shock-distortion. From linear analysis, $\overline{u'\xi_t} > 0$ and across the shockwave the dilatation $\partial\overline{u}/\partial x$ is negative. Hence the shock-unsteadiness term in the streamwise Reynolds stress equation is less than zero, i.e.,

$$\overline{u'\xi_t}\frac{\partial\overline{u}}{\partial x} < 0$$

The correlation $\overline{u'\xi_t}$ represents the coupling between unsteady shockwave motion and turbulent velocity fluctuations in the streamwise direction. It follows that incoming turbulent fluctuations and shockwave motion are in-phase and coupled, like if $u' > 0$, then $\xi_t > 0$ and if $u' < 0$, then $\xi_t < 0$. The closure model for the unclosed term $\overline{u'\xi_t}$ was based on the assumption that shock-unsteadiness is caused by turbulent fluctuations [41]. Therefore the term $\overline{u'\xi_t}$ is modeled as,

$$\overline{u'\xi_t} = b_1\overline{u'^2}$$

Using linear analysis, the model coefficient, b_1, is obtained as a function of the upstream mean flow Mach number (M) with respect to the normal shockwave.

$$b_1 = 0.4 + 0.6e^{2(1-M)} \tag{4.28}$$

Here, the combined effect of shock-distortion, production due to the mean pressure gradient and velocity pressure correlation in the STI vanishes at M =1. In order to include the effect at low Mach numbers, the model coefficient b_1 is replaced by b_1', where b_1' is obtained by modifying b_1 with an exponential function between the limits of $M \to 1$ and $M \to \infty$.

$$b_1' = b_{1\infty}\left(1 - e^{1-M}\right), \tag{4.29}$$

It also ensures that the shock-unsteadiness modification is not applied when $M < 1$. Here $b_{1\infty} = 0.4$ is the high Mach number limiting value of b_1 as obtained from LIA. Rearranging the Eq. (4.25) and accounting for the turbulent dissipation rate, we obtain,

$$\overline{\rho}\widetilde{u}\frac{\partial\widetilde{u''^2}}{\partial x} = -2\overline{\rho}\widetilde{u''^2}\frac{\partial\widetilde{u}}{\partial x} + 2\overline{\rho}\widetilde{u''\xi_t}\frac{\partial\widetilde{u}}{\partial x} - 2\overline{u''}\frac{\partial\overline{p}}{\partial x} - 2\overline{u''\frac{\partial p'}{\partial x}} - \overline{\rho}\epsilon_{ij}. \tag{4.30}$$

The above equation represents the transport equation of streamwise Reynolds stress for homogeneous isotropic turbulence interacting with a normal shockwave. We consider

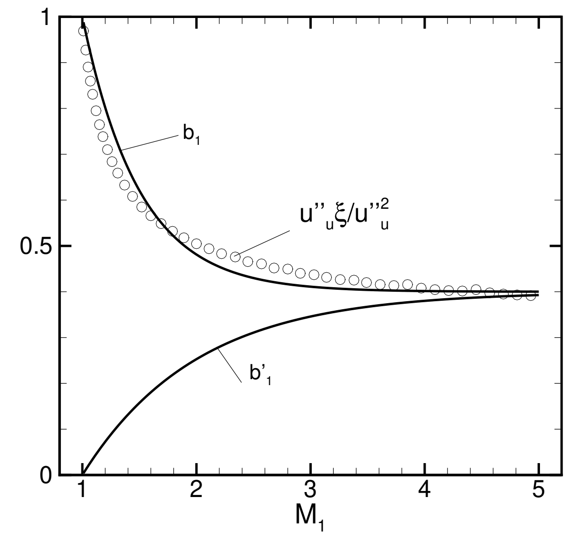

Figure 4.5: Variation of $\overline{u'\xi_t}/\overline{u'^2}$ as a function of upstream Mach number predicted by linear analysis [41], used to obtain model parameter b_1 and b_1'.

purely vortical turbulence upstream of the shock, and hence $\rho_1' = p_1' = T_1' = 0$. As a result, the production due to the mean pressure gradient is identically zero. For 1D mean flow, Eqs. (4.1) and (4.30) are identical, except the shock-unsteadiness correction term and the pressure-strain correlation closure.

In the present study, the shock-unsteadiness correction term is incorporated into the streamwise Reynolds stress equation of the baseline model [18]. The modified Reynolds stress transport equations are written as,

$$\widetilde{u}\frac{\partial R_{11}}{\partial x} = (-2 + 2b_1' + \frac{4}{3}C_2)R_{11}\frac{\partial \widetilde{u}}{\partial x} - C_1\epsilon a_{11} - \frac{2}{3}\epsilon, \qquad (4.31)$$

$$\widetilde{u}\frac{\partial R_{22}}{\partial x} = -\frac{2}{3}C_2 R_{11}\frac{\partial \widetilde{u}}{\partial x} - C_1\epsilon a_{22} - \frac{2}{3}\epsilon, \qquad (4.32)$$

which are identical to Eqs. (4.1) and (4.2), except for the shock-unsteadiness damping term with model coefficient b_1' given above.

4.3.2 Evaluation of the model

We evaluate the model in two steps. First, we compare the model predictions across the shock with the post-shock values of the DNS data extrapolated back to the mean shock wave location. For this, we consider the production and rapid pressure strain terms that are effective in the shock region and obtain a closed-form solution for the shock-jump in R_{11} and R_{22}. Comparison with the extrapolated DNS values assesses the efficacy of the model in capturing the jump across the shock and the net change in R_{11} and R_{22} due to the rapid post-shock acoustic adjustment. As noted earlier, the acoustic adjustment region is relatively small in size (for a realistic application) and its effect can be combined with the shock jump in Reynolds stresses. Also, the slow pressure strain term is neglected in this comparison, as it does not reproduce the physical effects observed in the acoustic adjustment region (see Appendix B).

As a second step, which follows in the next chapter, we solve the entire transport equations and compare the streamwise evolution of the Reynolds stresses with the DNS data. We also assess the effect of numerical error at the shock and devise ways to eliminate them. We note that the shock-jump predicted by the complete model equation matches the analytical results obtained by considering only the production and rapid pressure strain terms. By comparison, the decay of Reynolds stresses away from the shock (outside the acoustic adjustment region) is governed by the dissipation rate, and the slow pressure strain terms, which is modeled in terms of turbulence anisotropy. Modifications as per Sinha [74], are included in the model equation of ϵ to predict the correct decay rate of TKE, Reynolds stresses and their dissipation rate in STI cases. Therefore, the monotonic decay rate of Reynolds stresses downstream of the shock is determined by dissipation rate, ϵ.

The two stage evaluation of the Reynolds stress models, along with the extrapolation of the DNS data to the shock-center location, thus isolates the rapid effects at the shock wave from the slow decay and return to isotropy farther away from the shock. A similar procedure is adopted for the dissipation rate equation as well.

4.3.3 Principle Reynolds stresses

Neglecting the slow pressure-strain and dissipation rate terms in the R_{11} equation (cf. Eq. (4.31)), a closed-form solution for the amplification of R_{11} across the shock is obtained as

$$\frac{R_{11d}}{R_{11u}} = \left[\frac{\widetilde{u}_u}{\widetilde{u}_d}\right]^{2(1-b_1')-\frac{4}{3}C_2} . \tag{4.33}$$

In the new model, the value of the model coefficient, C_2, is reduced to 0.55 from the baseline model coefficient of $0.75\sqrt{A}$. This value compares well with $C_2 = 0.6$ in the Launder *et al.* [23] model for isotropic turbulence subjected to rapid distortion. Limiting the value of C_2 improves the R_{11} predictions and leads to a close comparison with the DNS data for R_{22} amplification across the shock wave.

Figure (4.6), show the map of different model coefficients proposed for the pressure-strain closure along with the new model coefficient. The resultant Reynolds stresses are not dependent on the individual values of C_1 and C_2, but on the parameter (1-C_2)/C_1. The line in Fig. (4.6), which corresponds to (1-C_2)/C_1 = 0.23 does provide a fitting value for various closures. In the present work, the proposed value of C_2 equal to 0.55 fit well with the C_1 of 1.8, as shown in figure.

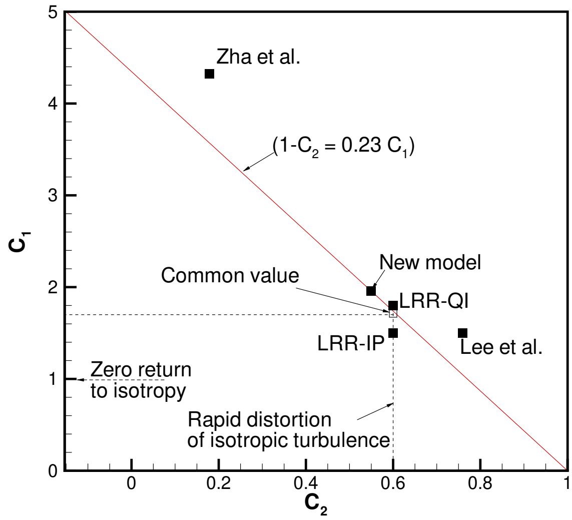

Figure 4.6: Map of proposals for coefficients (C_1 and C_2) in the pressure-strain model, ϕ_{ij}.

The amplification in the shock-normal Reynolds stress obtained using new model is plotted in Fig. (4.7a) as a function of the upstream Mach number and compared with the DNS data and the baseline model [18]. The amplification of R_{11} obtained with the new model has a trend similar to the DNS data and saturates to the value of 2.1 at high Mach numbers. The new model matches the DNS data upto Mach number 2.5 and slightly overpredicts the post-shock R_{11} for higher Mach numbers. The shock-unsteadiness damping term thus shows a significant improvement, compared to the baseline model, in the prediction of post-shock streamwise Reynolds stress.

The transverse Reynolds stress equation in the new model retains the same form as Eq. (4.2). The closed-form solution for the amplification of R_{22} across the shock is thus given by

$$\frac{R_{22d}}{R_{22u}} = 1 + \frac{C_2}{3(1-b_1') - 2C_2}\left[\frac{R_{11d}}{R_{11u}} - 1\right]. \tag{4.34}$$

Compared to the closed-form solution in Eq. (4.13), the R_{22} amplification obtained from the above equation includes the effect of shock-unsteadiness (through a model parameter b_1'). In comparison with the baseline model, the R_{22} amplification of the new model shows significant improvement, in Fig. (4.7b). The effect of shock-unsteadiness damping

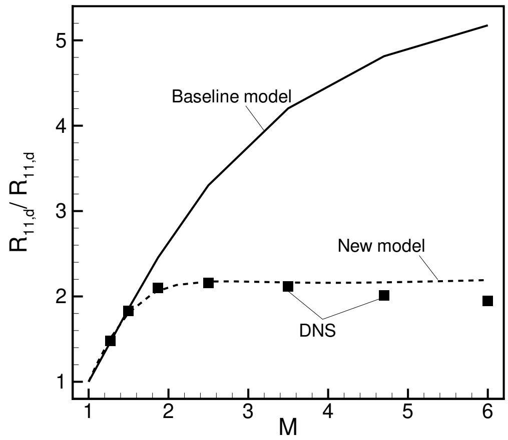

(a) R_{11} amplification

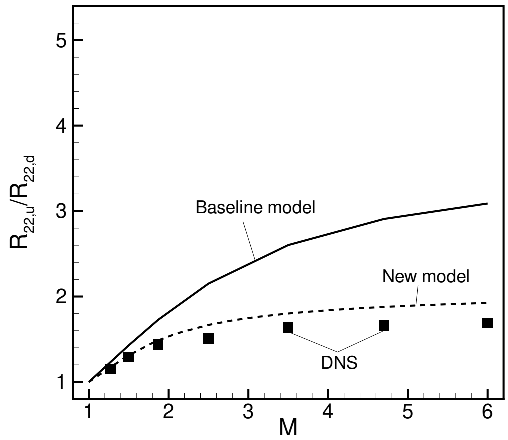

(b) R_{22} amplification

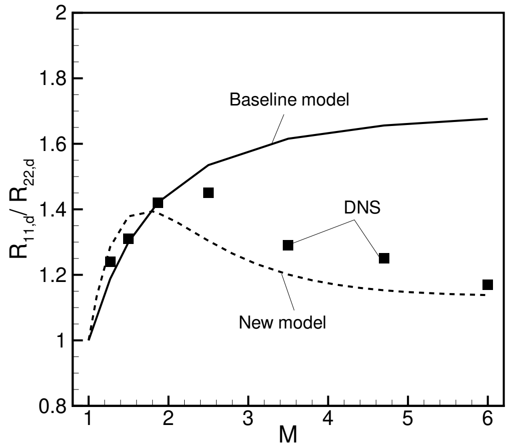

(c) R_{11}/R_{22}

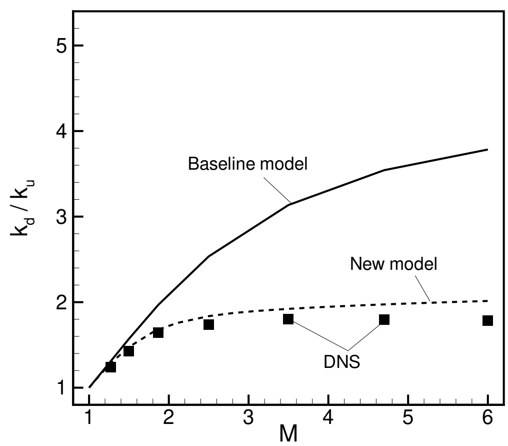

(d) TKE amplification

Figure 4.7: Comparison of the amplification in the R_{11}, R_{22}, anisotropy (R_{11}/R_{22}), and TKE of the baseline model (solid-line) and the present model (dash) with the DNS data (symbols) for varying shock strengths.

factor in R_{11} is also observed in the R_{22} amplification. The transverse Reynolds stress has a good match with the DNS data upto Mach 1.87, beyond which it overpredicts the amplification across the shock by about 10%. In Fig. (4.7c), the anisotropy of Reynolds stresses predicted by the new model shows the non-monotonic behaviour observed in the DNS data, and is a significant improvement from the baseline model. Comparison with the DNS data, shows that the new model overpredicts the anisotropy of Reynolds stresses for lower Mach numbers and underpredicts beyond Mach number 2. Figure (4.7d) shows that the amplification of TKE measured from the principal Reynolds stresses over the range of Mach numbers. It has a similar trend of the DNS data and slightly overpredicts the amplification for higher Mach numbers.

4.3.4 Turbulent dissipation rate

Dissipation rate for any turbulent flow determines the rate of decay of the turbulent quantities. In compressible flows, the dissipation rate is divided into two parts, a solenoidal part, ϵ_s and a dilatational part, ϵ_d. For incompressible homogeneous turbulence, the solenoidal dissipation rate ϵ_s can be written in terms of enstrophy and is given by $\epsilon_s = \overline{\nu}\overline{\omega_i''\omega_i''}$, where ν is the kinematic viscosity and ω_i is the vorticity component in the i direction (x, y and z directions).

Sinha [74] studied the evolution of enstrophy in shock/homogeneous turbulence interaction using LIA, and proposed a model for the dissipation rate of the turbulent kinetic energy. Following their work we use the enstrophy equation derived for the linearised Navier–Stokes equations. Similar to streamwise Reynolds stress, the equation for enstrophy is also written in a frame of reference attached to the unsteady shock wave, and is modeled as

$$\overline{u}\frac{\partial}{\partial x}(\overline{\omega_i''\omega_i''}) = -4\overline{\omega_z''^2}\frac{\partial\widetilde{u}}{\partial x} = -c_w\overline{\omega_i''\omega_i''}\frac{\partial\widetilde{u}}{\partial x}. \tag{4.35}$$

Here, the lower and upper limits of the model constant c_w is set by $\frac{\overline{\omega_i''\omega_i''}}{3} \leq \overline{\omega_z''^2} \leq \frac{\overline{\omega_i''\omega_i''}}{2}$, and a value of $c_w = 1.55$ shows a close match with linear analysis results.

The model equation for the solenoidal dissipation rate is thus written as,

$$\widetilde{u}\frac{\partial\epsilon_s}{\partial x} = \widetilde{u}\frac{\partial}{\partial x}(\overline{\omega_i''\omega_i''}\overline{\nu}) = \widetilde{u}\overline{\omega_i''\omega_i''}\frac{\partial\overline{\nu}}{\partial x} + \widetilde{u}\,\overline{\nu}\frac{\partial(\overline{\omega_i''\omega_i''})}{\partial x}, \tag{4.36}$$

where the dynamic viscosity, μ is a function of mean temperature $\widetilde{T}$, and is given by $\mu \propto \widetilde{T}^{\alpha}$ with α= 0.76. Across the shockwave, the change in kinematic viscosity is given as,

$$\frac{\partial\overline{\nu}}{\partial x} = -\frac{\overline{\mu}}{\overline{\rho}^2}\frac{\partial\overline{\rho}}{\partial x} + \frac{1}{\overline{\rho}}\frac{\partial\overline{\mu}}{\partial x} = \overline{\nu}\left[\frac{1}{\widetilde{u}}\frac{\partial\widetilde{u}}{\partial x} + \frac{\alpha}{\widetilde{T}}\frac{\partial\widetilde{T}}{\partial x}\right]. \tag{4.37}$$

Upon substitution of the change in kinematic viscosity in to the equation for solenoidal dissipation rate, we get

$$\widetilde{u}\frac{\partial\epsilon_s}{\partial x} = -c_w\epsilon_s\frac{\partial\widetilde{u}}{\partial x} + \epsilon_s\frac{\partial\widetilde{u}}{\partial x} + \alpha\epsilon_s\frac{\widetilde{u}}{\widetilde{T}}\frac{\partial\widetilde{T}}{\partial x}. \tag{4.38}$$

Using conservation of total enthalpy across the shockwave, the above equation is cast in a form similar to that in the conventional turbulence model as,

$$\overline{\rho}\,\widetilde{u}\frac{\partial\epsilon_s}{\partial x} = -\frac{2}{3}C_{\epsilon 1}\overline{\rho}\epsilon_s\frac{\partial\widetilde{u}}{\partial x} - C_{\epsilon 2}\overline{\rho}\frac{{\epsilon_s}^2}{k}, \tag{4.39}$$

where, $C_{\epsilon 1} = 1 + 0.21M$, and $C_{\epsilon 2} = 1.2$ taken from [74]. The closed-form solution for the amplification of ϵ across the shockwave is obtained by neglecting the last term [74].

$$\frac{\epsilon_d}{\epsilon_u} = \left[\frac{\widetilde{u_u}}{\widetilde{u_d}}\right]^{\frac{2}{3}C_{\epsilon 1}}. \tag{4.40}$$

The dissipation rate of the new model has excellent agreement with the DNS data (see

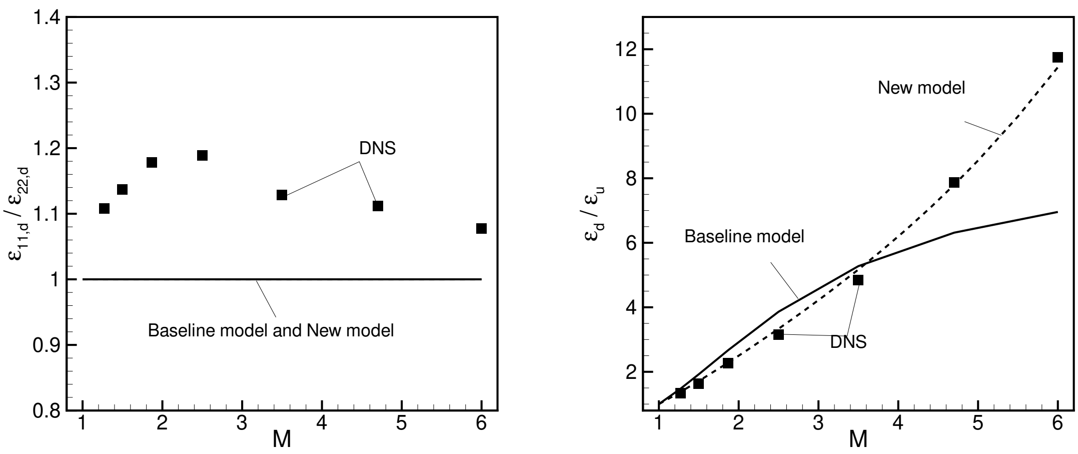

(a) $\epsilon_{11}/\epsilon_{22}$ amplification (b) ϵ amplification

Figure 4.8: Comparison of the anisotropy ($\epsilon_{11}/\epsilon_{22}$), and the amplification in the ϵ of the baseline model (solid-line) and the present model (dash) with the DNS data (symbols) for varying shock strengths.

Fig. (4.8b)), both qualitatively and quantitatively, for all ranges of Mach numbers. The baseline model predictions of the dissipation rate tensor grossly inaccurate, especially at high-Mach numbers. Both the models cannot capture the anisotropy in the dissipation rate tensor correctly as the models assume the dissipation rate tensor to be isotropic locally for high Reynolds number limit flows (see Fig. (4.8a)).

4.4 Anisotropy in the turbulence

Post-shock enhancement of the turbulence statistics is highly non-isotropic, and it is also found that the Reynolds stresses do not quickly return to isotropy [9, 10]. In an isotropic state, all the normal Reynolds stresses would be equal, $\widetilde{u_i'' u_j''} = R_{ij} = 2k\delta_{ij}/3$. Turbulence passing the nominally normal shockwave cause the Reynolds stresses to be unequal. A departure from the isotropic state provides a measure of the stress anisotropy state, which

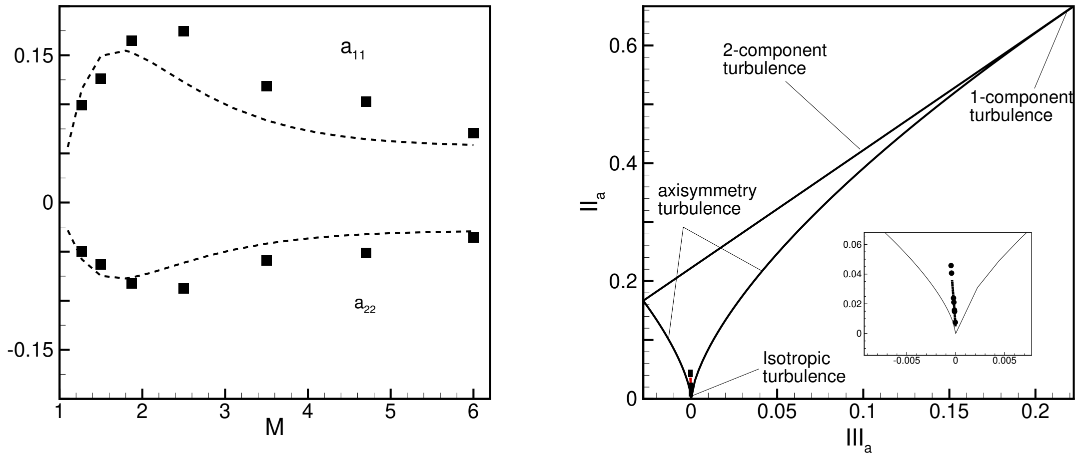

(a) (b)

Figure 4.9: Comparison of the anisotropy in the Reynolds stress tensor of the present model (dash) with the DNS data (symbols) for varying shockwave strengths (left), and invariant characteristics of the Reynolds stress tensor on the anisotropy invariant map (III, II) (right).

can be expressed in terms of deviatoric part of the stress tensor. It is given as,

$$R_{ij} = \underbrace{R_{ij} - \frac{2}{3}k\delta_{ij}}_{deviatoric} + \underbrace{\frac{2}{3}k\delta_{ij}}_{isotropic} . \tag{4.41}$$

Lumley [44] initially proposed the importance of the anisotropy in turbulence through the anisotropic tensor, which is dimensionless, has zero trace, and vanishes identically if the turbulence is isotropic. It is only the anisotropic part of stress tensor that transports momentum while the isotropic part is inactive, and in employing with the momentum equation, it can be included in the mean pressure term. Figure (4.9a) shows the comparison of the streamwise and transverse stress anisotropy against the DNS data. Reynolds stress anisotropies have a similar trend to the DNS data, and both reach the asymptotical values after Mach 5. The new model matches the DNS data upto Mach number 1.87 and underpredicts the post-shock a_{11} for higher Mach numbers. Similarly, a_{22} has a good match with the DNS data upto Mach 1.87, beyond which it slightly overpredicts for higher Mach numbers.

Using Reynolds stress anisotropies, the principal invariants (I_a, II_a, III_a) are obtained to quantify the level of anisotropy in the turbulence generated across the shockwave.

$$I_a = a_{ii}, \;\; II_a = a_{ij}a_{ji}, \;\; III_a = a_{ik}a_{kj}a_{ji} \tag{4.42}$$

where,

$$
\begin{aligned}
I_a &= a_{11} + a_{22} + a_{33} = 0, && (4.43)\\
II_a &= a_{11}^2 + a_{22}^2 + a_{33}^2 + 2(a_{12}^2 + a_{13}^2 + a_{23}^2), && (4.44)\\
III_a &= a_{11}^3 + a_{22}^3 + a_{33}^3 + 3a_{12}^2(a_{11} + a_{22}) + 3a_{13}^2(a_{11} + a_{33}) + 3a_{23}^2(a_{22} + a_{33}) + 6a_{12}a_{13}a_{23}. && (4.45)
\end{aligned}
$$

These invariants provide information about the behaviour of the Reynolds stress anisotropy in a compact way by considering them in principal coordinate axes. The first invariant (I_a) is the trace of the anisotropy tensor and is zero. The second invariant, II_a, is always positive and gives a direct measure of the stress anisotropy; the larger II_a, the more anisotropic is the stress field. The third invariant, III_a, comprises cubic products and thus can be positive or negative depending on anisotropy components. To visualize the physical insight of the anisotropy in turbulence, we plot these scalars in two-dimensional space known as anisotropy invariant mapping (AIM), shown in Fig. (4.9b). The plot shows the isotropic state of turbulence at the origin with two axisymmetry turbulence curves leaving from it (origin), and the line joining the limits of axisymmetric turbulence curves corresponds to two-component turbulence. The values of second and third invariants obtained using the new model lie within the boundaries of the triangular area and show the axisymmetric turbulence generated across the shockwave is within realizable constraint.

Kolmogorov [5] proposed the dissipation rate to be locally isotropic in the limit of large Reynolds number, where the dissipation is mostly dominated from the scales, which are much smaller than the large energetic ones. Hence, the dissipation process is solely determined by the dissipation rate ϵ, and the tensor ϵ_{ij} can be modeled as an isotropic function.

$$\epsilon_{ij} \simeq \frac{2}{3}\epsilon\delta_{ij}. \tag{4.46}$$

It is reasonable to note that the anisotropy in dissipation rate tensor would exist when a significant enough of anisotropy in the Reynolds stresses is generated across the shockwave. In the turbulent flows, the small scale anisotropy exists if the large scale statistics are highly anisotropic. Thus the anisotropy in the dissipation rate tensor is obtained by modeling the dissipation rate in terms of the known variables such as the Reynolds stress tensor R_{ij} and the mean velocity gradients $\partial\widetilde{u}_i/\partial x_j$. Initially, Rotta [6] proposed a model for the dissipation term, which is proportional to the normalized Reynolds stress tensor.

$$\epsilon_{ij} \simeq \frac{R_{ij}}{k}\epsilon. \tag{4.47}$$

The next level of approximation within the linear algebraic modeling context is that a portion of the turbulent dissipation tensor is isotropic, and the rest is proportional to the Reynolds stress tensor. This approach employs a linear interpolation, which combines the two discussed above models expressed by Eqs. (4.46) and (4.47),

$$\epsilon_{ij} \simeq A\frac{R_{ij}}{k}\epsilon + (1-A)\frac{2}{3}\epsilon\delta_{ij}. \tag{4.48}$$

Where the asymptotically behaviour of the blending function A is given as

$$A = 0, Re \to \infty \tag{4.49}$$

$$A = 1, Re \to 0 \tag{4.50}$$

Here, the proportional coefficient of A falls within intervals 0 and 1. It is assumed that the turbulent dissipation anisotropy tensor is linearly proportional to the anisotropy tensor of the Reynolds stress with the scalar coefficient A. Several authors [6, 44, 107] constructed the proportionality scalar A as a function of the turbulent Reynolds stress number i.e., $Re_t = k^2/\nu\epsilon$. In an alternate form, Hallback *et al.* [107] proposed a algebraic model equation to account the effects of an anisotropic dissipation rate in second-order moment closures of turbulent flows. Anisotropies of the dissipation rate tensor are expressed in terms of anisotropies of the Reynolds stress tensor as,

$$e_{ij} = \left(1+\alpha\left[\frac{1}{2}II_a - \frac{2}{3}\right]\right)a_{ij} - \alpha(a_{ik}a_{kj} - \frac{1}{3}II_a\delta_{ij}).$$

Here, the α value is set to a specific value of 3/4 [107]. The quantification of the level of anisotropy in the dissipation rate tensor through the principal invariants is shown in Fig. (4.11). Here, the invariants I_e, II_e and III_e are defined as

$$I_e = e_{11} + e_{22} + e_{33} = 0, \tag{4.51}$$

$$II_e = e_{11}^2 + a_{22}^2 + a_{33}^2 + 2(a_{12}^2 + a_{13}^2 + a_{23}^2), \tag{4.52}$$

$$III_e = e_{11}^3 + a_{22}^3 + a_{33}^3 + 3a_{12}^2(e_{11}+e_{22}) + 3a_{13}^2(e_{11}+e_{33}) + 3a_{23}^2(e_{22}+e_{33}) + 6e_{12}e_{13}e_{23}, \tag{4.53}$$

and the principal components of the dissipation rate tensor are calculated as

$$\epsilon_{ij} = \frac{e_{ij}}{\epsilon} + \frac{2}{3}\delta_{ij}. \tag{4.54}$$

Figure (4.10) shows the comparison of anisotropy in the dissipation rate tensor obtained by using Hallback *et al.* [107] algebraic model for the dissipation rate, against the DNS data. The model predictions match well with the DNS data.

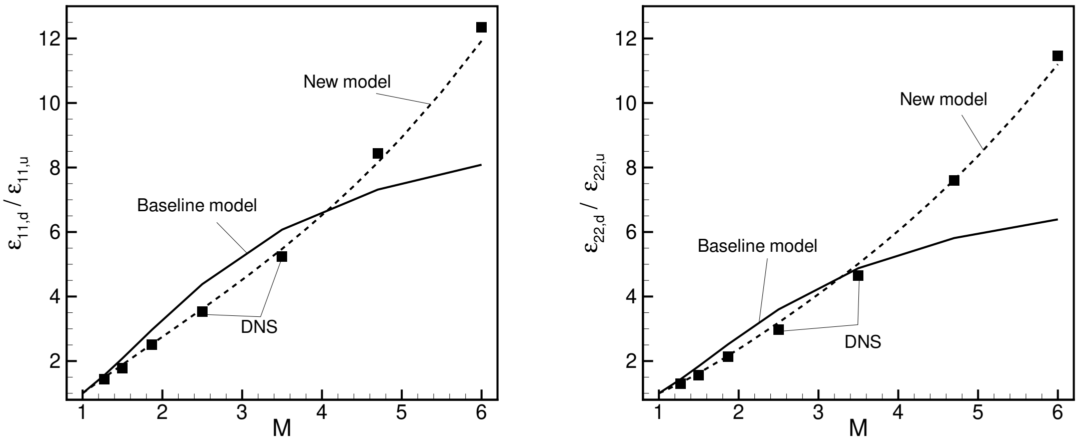

(a) ϵ_{11} amplification (b) ϵ_{22} amplification

Figure 4.10: Comparison of the amplification in the ϵ_{11} and ϵ_{22} across the shock obtained using Hallback *et al.,* [107] algebraic dissipation rate equation for the baseline model (solid-line) and the present model (dash) with the DNS data (symbols) for varying shock strengths.

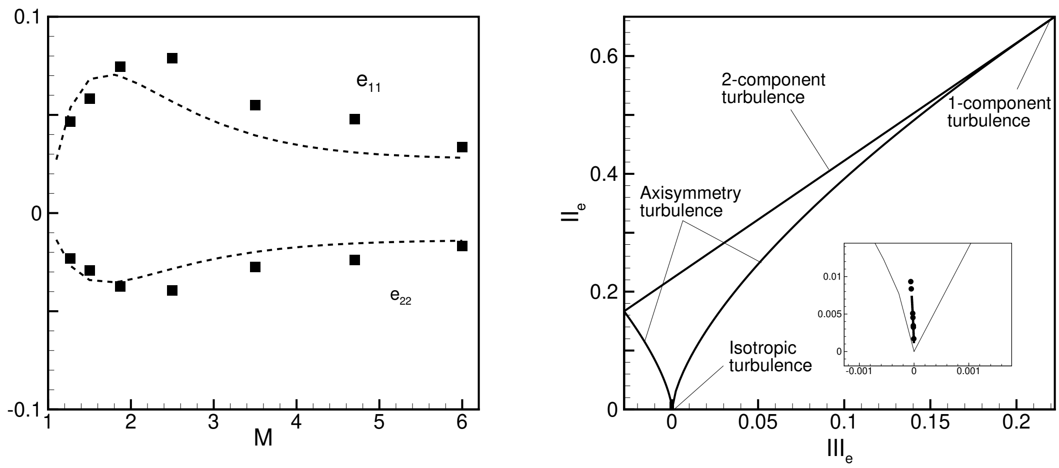

(a) (b)

Figure 4.11: Comparison of the anisotropy in the dissipation rate tensor of the present model (dash) with the DNS data (symbols) for varying shock strengths (left), and invariant characteristics of the dissipation rate tensor on the anisotropy invariant map (III, II) (right).

4.5 Summary

The canonical STI is the simplest model problem without any complexities, such as adverse pressure gradients or flow separation. It features the shock-corrugation effect and captures the anisotropy produced in the turbulence statistics across the shockwave. To understand the flow field and change in the turbulence statistics using RANS, we evaluated the three existing Reynolds stress models for canonical STI through the measurement of the turbulence enhancement and anisotropic nature of turbulence generated across the shockwave.

Existing model transport equations for Reynolds stresses are integrated across the shockwave to get the closed-form solution for the amplification in the Reynolds stresses and the dissipation rate across the shockwave. The closed-form solutions are compared with the DNS data and model predictions are found to be grossly inaccurate, especially at high-Mach numbers. Gerolymos *et al.* [18] model gives better results than the other RSMs and the model is considered for further improvement. We propose physics-based improvement to the streamwise Reynolds stress transport equation using the LIA. We incorporate the shock-unsteadiness correction into R_{11} transport equation and adopted the modified dissipation rate equation given by Sinha [74] for length scale. The resulting model captures the essential physics and the amplification in the Reynolds stresses and the dissipation rate match well with the DNS data for a range of Mach numbers.

In addition to turbulence enhancement across the shock, the new model also captures the anisotropy generated in the Reynolds stresses and the dissipation rate tensor. The nature of the turbulence is also quantified using the anisotropy invariant mapping, where the invariants lie with in the turbulence triangle and show the axisymmetric turbulence generated across the shockwave.

Chapter 5

Numerical error at the shock

The model predictions presented in the previous chapter are obtained by numerically integrating the transport equations using RK4 method for a specified mean flow with a simple hyperbolic tangent function. The integration step size is kept small so that the results are devoid of numerical error. On the other hand, in realistic CFD simulations, the mean flow variables at a shockwave are computed as part of the solution and are prone to numerical error at flow discontinuity. This chapter provides the numerical error analysis across the shockwave using the shock-capturing method and evaluating the effect on the turbulent statistics. Next, we present ways to eliminate the numerical error by recasting the transport equations in the conserved quantities. Further, the effect of grid refinement and different numerical schemes on the turbulence amplification are presented. Last, the model equations are generalized to multi-dimensional flows with oblique shockwaves.

5.1 Methodology

The modified transport equations for the principal Reynolds stresses and the turbulent dissipation rate based on linear theory are given as,

$$\overline{\rho}\widetilde{u}\frac{\partial R_{11}}{\partial x} = (-2 + 2b_1' + \frac{4}{3}C_2)\overline{\rho}R_{11}\frac{\partial \widetilde{u}}{\partial x} - C_1\overline{\rho}\epsilon a_{11} - \frac{2}{3}\overline{\rho}\epsilon, \tag{5.1}$$

$$\overline{\rho}\widetilde{u}\frac{\partial R_{22}}{\partial x} = -\frac{2}{3}C_2\overline{\rho}R_{11}\frac{\partial \widetilde{u}}{\partial x} - C_1\overline{\rho}\epsilon a_{22} - \frac{2}{3}\overline{\rho}\epsilon, \tag{5.2}$$

$$\overline{\rho}\,\widetilde{u}\frac{\partial \epsilon}{\partial x} = -\frac{2}{3}C_{\epsilon 1}\overline{\rho}\epsilon\frac{\partial \widetilde{u}}{\partial x} - C_{\epsilon 2}\overline{\rho}\frac{\epsilon^2}{k}, \tag{5.3}$$

where $b_1' = b_{1\infty}\left(1 - e^{1-M}\right)$ with M as upstream shock-normal Mach number, $b_{1\infty} = 0.4$, $C_2 = 0.55$, $C_1 = 1$, a_{11} and a_{22} are the anisotropy in the Reynolds stresses, $C_{\epsilon 1} = 1 + 0.21M$, and $C_{\epsilon 2} = 1.2$. We solve one-dimensional RANS equations along with the modified transport equations using a finite volume approach. The governing equations are written in a vector form as

$$\frac{\partial}{\partial t}\underbrace{\begin{bmatrix}\overline{\rho}\\ \overline{\rho}\widetilde{u}\\ \overline{\rho}\widetilde{E}\\ \overline{\rho}R_{11}\\ \overline{\rho}R_{22}\\ \overline{\rho}\epsilon\end{bmatrix}}_{U}+\frac{\partial}{\partial x}\underbrace{\begin{bmatrix}\overline{\rho}\widetilde{u}\\ \overline{\rho}\widetilde{u}^2+\overline{p}+\frac{2}{3}\overline{\rho}k\\ \overline{\rho}\widetilde{E}+\overline{p}\\ \overline{\rho}\widetilde{u}R_{11}\\ \overline{\rho}\widetilde{u}R_{22}\\ \overline{\rho}\widetilde{u}\epsilon\end{bmatrix}}_{F}=\underbrace{\begin{bmatrix}0\\ 0\\ 0\\ (-2+2b_1'+\frac{4}{3}C_2)\overline{\rho}R_{11}\frac{\partial\widetilde{u}}{\partial x}-C_1\overline{\rho}\epsilon a_{11}-\frac{2}{3}\overline{\rho}\epsilon\\ -\frac{2}{3}C_2\overline{\rho}R_{11}\frac{\partial\widetilde{u}}{\partial x}-C_1\overline{\rho}\epsilon a_{22}-\frac{2}{3}\overline{\rho}\epsilon\\ -\frac{2}{3}C_{\epsilon1}\overline{\rho}\epsilon\frac{\partial\widetilde{u}}{\partial x}-C_{\epsilon2}\overline{\rho}\frac{\epsilon^2}{k}\end{bmatrix}}_{S}. \tag{5.4}$$

Here, $[U]$ is the vector of the conserved variables, $[F]$ is the vector containing the inviscid fluxes and $[S]$ is the vector containing the source terms. Here, $\widetilde{E}$ is the total mean energy and is given by $\frac{\overline{p}}{\gamma-1}+\frac{1}{2}\overline{\rho}\widetilde{u}^2+\overline{\rho}k$ with $\gamma = 1.4$. The inviscid fluxes at cell faces are evaluated using the Lax-Friedrich (LF) scheme and the turbulent source terms are evaluated at the cell centers. The mean flow gradients in the production terms are discretized using a second-order accurate central difference scheme. Explicit time integration is achieved using the first order forward Euler method.

The equations consist of dimensionless and normalized quantities which are defined as, $x = x^*\kappa_0$, $t = t^*/(1/a^*_\infty\kappa_0)$, $\rho = \rho^*/\rho^*_\infty$, $u = u^*/a^*_\infty$, $T = T^*/T^*_\infty$, $p = p^*/(\rho^*_\infty a^{*2}_\infty)$, $R_{11} = R^*_{11}/a^{*2}_\infty$, $R_{22} = R^*_{22}/a^{*2}_\infty$, $R_{33} = R^*_{33}/a^{*2}_\infty$, $k = k^*/a^{*2}_\infty$, $\epsilon = \epsilon^*/a^{*3}_\infty\kappa_0$, where $(.)^*$ represents the dimensional values of flow variables and $(.)_\infty$ represents the shockwave upstream values. Here, t is time, T is temperature, and a^*_∞ is the mean speed of sound. The characteristic length scale is taken from the incoming turbulence field with peak wave number κ_0 of 4.

The whole domain is divided into grid cells and updated the solution over these grid cells at each time step. At each time step, flux is approximated at the interface of each cell. Then this flux is used to evolve the cell average values. LF scheme [112] being conservative and of the first order, is quite dissipative. A fixed CFL value of 0.2 is used for all the computations, which renders the LF scheme to be first-order accurate in space and time. The conservative form of the equation is given below, where the total flux can be seen as a combination of unstable flux and a term that gives the numerical diffusion as follows,

$$F^n_{i-\frac{1}{2}} = \frac{1}{2}\left[f(U^n_{i-1})+f(U^n_i)-\alpha(f(U^n_i)-f(U^n_{i-1}))\right] \tag{5.5}$$

where $\alpha = \Delta x/\Delta t$ is the numerical viscosity coefficient. Thus the U^{n+1}_i given by this method is

$$U^{n+1}_i = \frac{1}{2}\left(U^n_{i+1}-U^n_{i-1}\right)-\frac{\Delta x}{2\Delta t}\left[f(U^n_{i+1})-f(U^n_{i-1})\right] \tag{5.6}$$

The term that is similar to the diffusion term makes it a advection-diffusion equation, $U_t + f(U)_x = \beta U_{xx}$ with $\beta = (\Delta x)^2/(2\Delta t)$. But if $\Delta t/\Delta x$ is fixed, then the β will vanish if grid is refined. Therefore, this method again maintain the hyperbolic system. This additional term just suppress the instabilities caused by central flux in flux function.

In the present simulations, normal shockwave is captured by using shock-capturing method with RH jump relation. The computational domain starts from $\kappa_0 x^* = -7.6$ to $\kappa_0 x^* = 29.6$ with the characteristic length $\kappa_0 = 4$, and the normal shockwave is located at $\kappa_0 x^* = 0$. Normalised values of the TKE, the principal Reynolds stresses and the turbulent dissipation rate tabulated in table 4.1 are considered at the inlet location for varying shockwave strengths.

5.2 Non-conservative errors at a shockwave

Figure (5.1) shows the amplification of the Reynolds stresses, and the turbulent dissipation rate across shock wave computed using the Eqs. (5.1) - (5.3) for varying upstream Mach number. Numerical solution obtained from the baseline model and present RSM based on shock-unsteadiness correction (SU-RSM) are compared with the DNS data. The solution obtained in the inviscid limit is also presented for comparison and referred as exact solution. The numerical solution of the baseline model, as well as the SU-RSM, show a non-physical trend in the amplification of the Reynolds stresses (see Figs. (5.1a) and (5.1b)).

In the present work, the simulation employs a shock-capturing scheme, and the mean flow variables across the shockwave are computed as part of the solution. The solution is prone to numerical error at the shockwave due to non-conservative form of the R_{11}, R_{22}, and ϵ equations given by Eqs. (5.1) - (5.3). This is due to the fact that derivatives in the source terms on the right-hand side of all the equations are multiplied by the flow variables and result in large numerical errors at shockwaves.

The amplification of the Reynolds stresses obtained from the baseline model and SU-RSM are comparable to the DNS data up to Mach number 1.5, indicating that the numerical errors are low for weak shockwaves. In the range of Mach numbers, from 1.5 to approximately 4.0, the models overpredict the jump in Reynolds stresses, due to the large amplification of turbulence attributed to the non-conservative formulation of production and rapid pressure strain terms. For the strongest shock strengths (beyond Mach 4), there is a fall in the R_{11} and R_{22} amplifications, due to the excessive prediction of the turbulent dissipation rate attributed to the same non-conservative formulation of production term in the turbulent dissipation rate equation. Thus, with increasing Mach

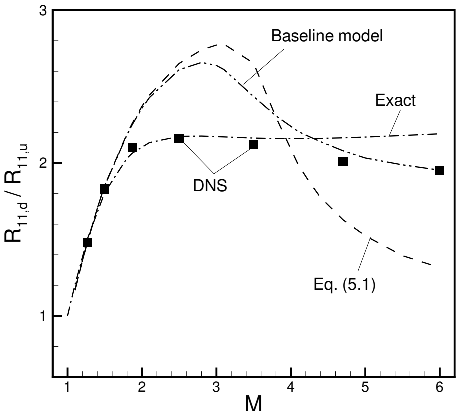

(a) R_{11} amplification

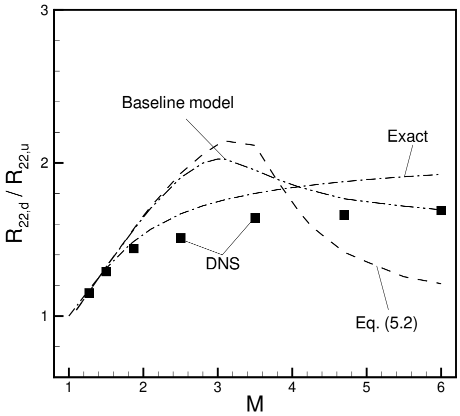

(b) R_{22} amplification

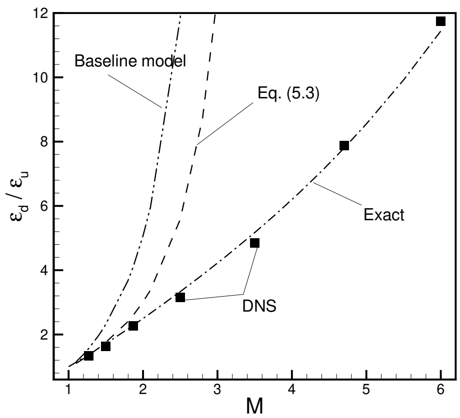

(c) ϵ amplification

Figure 5.1: The amplification in turbulent quantities across the shock obtained from the numerical simulation of the baseline model (Gerolymos *et al.* model [18]), the present modified model are compared with DNS data [9, 10] and the exact solution, for varying upstream Mach number. Solution computed on a 1000-point grid. The exact solution is obtained from closed form integration of modified transport equations.

number, the non-monotonic trend of Reynolds stresses amplifications is entirely due to the non-conservative numerical error at shockwave. The results obtained for the same model equations presented in Fig. (4.7) are obtained with hyperbolic tangent profiles prescribed for the mean flow variables across the shock. They do not have numerical errors typical of shock-capturing CFD simulations in Fig. (5.1) and isolate the physical modeling error in the models.

The post-shock dissipation rate of the baseline model and of the non-conservative form of SU-RSM increases monotonically with increasing Mach numbers. They are much higher than the DNS data and the exact solution for all but the lowest Mach numbers. Further, the amplification of Reynolds stresses decreases with increasing shock strength, which is opposite to what is observed for the turbulent dissipation rate and is physically unrealistic. This behaviour is similar to that observed in [102] and is due to the very high amplification of the turbulent dissipation rate for high Mach numbers.

The leading truncation error due to non-conservative form of production term exhibit a different behaviour at each cell. Their contribution from adjacent cells adds up and leads to the non-physical nature of the amplification of turbulent quantities. The leading error term for production due to mean compression scales as $1/\delta^2$ [102]. Here, δ is the shock thickness, and it depends on the grid cell size, such that grid refinement decreases the shock thickness.

Figure (5.2) present the numerical solutions computed using the non-conservative formulation of the SU-RSM obtained using successively refined computational grids. Three grids with 1000, 2000, and 3000 points uniformly distributed over the computational domain have grid-cell sizes of 0.037, 0.018 and 0.012, respectively. The amplification of the Reynolds stresses and the turbulent dissipation rate increases with grid refinement and does not show a converging trend (see Fig. (5.2)). This is due to the increase in the truncation error in the ϵ -equation with grid refinement since δ is proportional to the grid size. Also, for a fixed Mach number, the amplification in the turbulent dissipation rate increases with grid refinement. Similarly, owing to the large discretization error due to the non-conservative production terms in the Reynolds stress Eqs. (5.1) and (5.2), the numerical results highly over-predict the exact solution and the DNS data. For a fixed Mach number, the error in predicting the amplification of Reynolds stresses also increases on successive grid refinement. Thus, the non-conservative results (Figs. (5.2a), (5.2b), and (5.2c)) retain the non-physical trends with successive grid refinement, and the numerical error is not found to decrease even on the finest grid. The turbulent dissipation rate results, plotted on a logarithmic scale, do not show a converging trend with successive grid refinement.

The section presents the effect of different numerical schemes on the leading truncation error on the amplification of the Reynolds stresses and the turbulent dissipation rate. The inviscid fluxes are computed with a modified, low-dissipation form of the Steger-Warming flux-vector splitting (SW) method [116]. The flux vector F is evaluated at each cell face using the conserved variables vector U stored at cell centers. The Jacobian $A = \partial F/\partial U$ is diagonalized as

$$A = T^{-1}\Lambda T \tag{5.7}$$

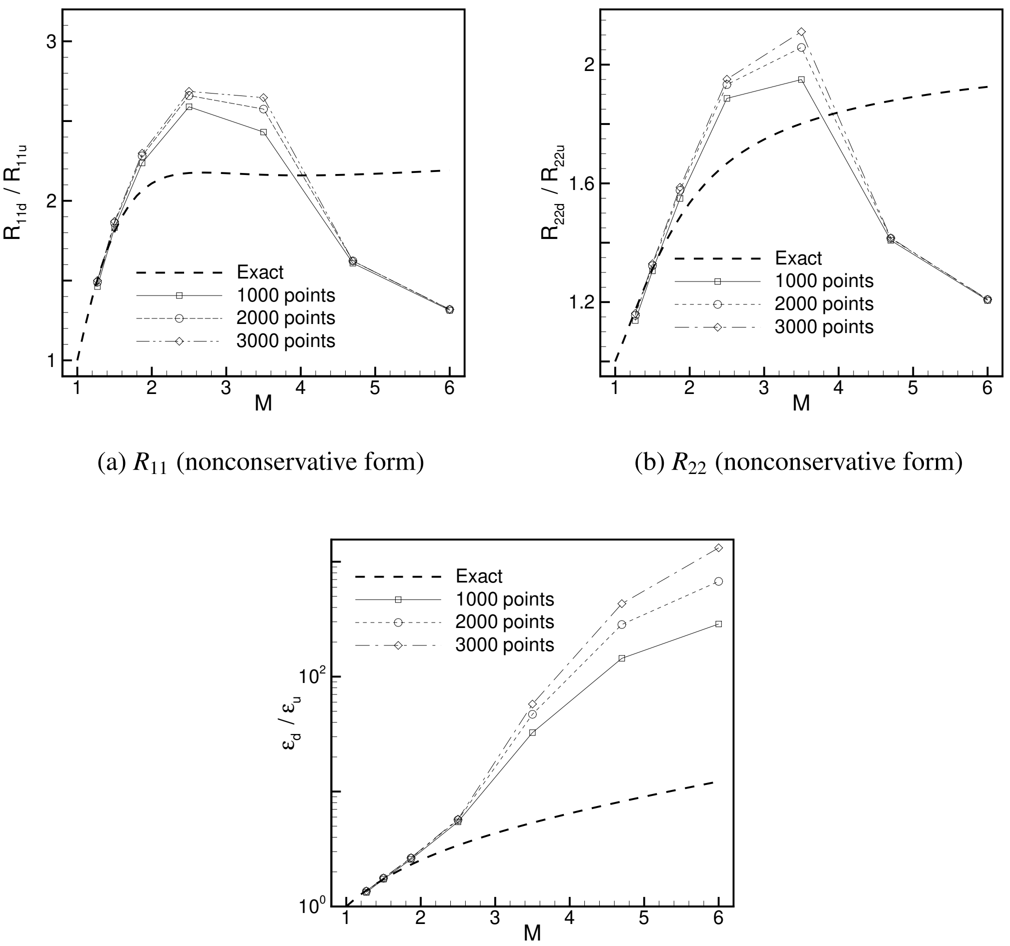

(a) R_{11} (nonconservative form)

(b) R_{22} (nonconservative form)

(c) ϵ (nonconservative form)

Figure 5.2: Effect of grid refinement on the amplification of the R_{11}, R_{22}, and ϵ with varying grid points for the new RSM compared with exact integral solution.

where Λ is a diagonal matrix consisting of the eigenvalues of the system, and T^{-1} and T are the left and right eigenvector matrices. The positive and negative eigenvalues are used to split the Jacobian matrix into A^+ and A^- . The flux vector is thus evaluated as a combination of the positive and negative flux contributions from the left and right side of a cell face $i + 1/2$ as

$$F_{i+1/2} = A^+ U_l + A^- U_r \tag{5.8}$$

For a first-order flux evaluation, $U_l = U_i$ and $U_r = U_{i+1}$. Figure (5.3) plots the amplification of Reynolds stresses obtained using two different numerical schemes on coarser meshes. The LF method results are compared with SW method. Both the methods give qualitatively similar results, where the Reynolds stresses increase with Mach number, reach a maximum and then decrease for stronger shocks. The amplification factors obtained for the SW method are higher than the corresponding LF results, and the increases further on grid-refinement.

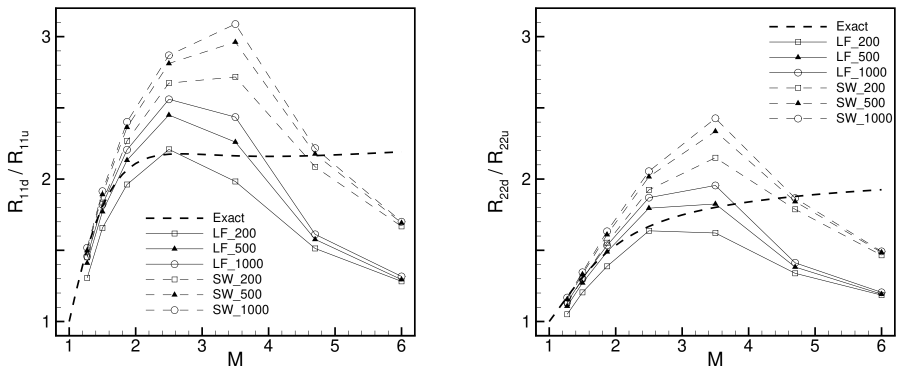

(a) R_{11} amplification (b) R_{22} amplification

Figure 5.3: Effect of numerical method on the amplification of the Reynolds stresses with grid refinement for non-conservative form of the new RSM.

5.3 Conservative formulation

Sinha and Balasridhar [102] studied the numerical issues in the STI using the shock-unsteadiness (SU) $k-\epsilon$ turbulence model equations. They showed that the convective terms in the $k-\epsilon$ equations are written in a conservative form, such that the integrated error can be written in terms of the derivatives evaluated at the cell interfaces. By taking all the cells spanning the region of shockwave together, the error contribution gets cancelled at the common interface of adjacent cells. The net error across the shockwave is thus given by the higher-order derivatives calculated outside the shockwave, where the flow solution is smooth.

To minimize the numerical truncation error at the shockwave, Sinha and Balasridhar [102] proposed an conservative form of the shock-unsteadiness $k-\epsilon$ model, obtained by transforming the turbulence variables to conserved quantities. The new equations represent identical physics as that of the original shock-unsteadiness model and are free from the numerical error due to the non-conservative source terms. The results of the conservative form of the shock-unsteadiness model, qualitatively and quantitatively match with the exact integrated solution, and also show a good match with DNS data [102].

Similar to the SU $k-\epsilon$ model equations, Eqs. (5.1) - (5.3), show non-conservative nature. Following an approach similar to that of Sinha and Balasridhar [102], the turbulent quantities such as Reynolds stresses and turbulent dissipation rate are transformed to conserved quantities. Considering the exact solution in the inviscid limit given by Eqs. (4.33), (4.34), and (4.40), the new transformed turbulent variables are framed as,

$$\begin{aligned} f_1 &= R_{11}\rho^{2(1-b_1')-4C_2/3}, \\ f_2 &= R_{22} - R_{11}\left[\frac{C_2}{3(b_1'-1)+2C_2}\right], \\ g &= \epsilon\rho^{-2C_{\epsilon 1}/3}. \end{aligned} \tag{5.9}$$

Here, the overbar on ρ is omitted to avoid potential conflict between Reynolds averaging and the sign of the exponent. Using mass conservation across the shock in the R_{11}, R_{22} and ϵ transport equations, we get the corresponding equations for f_1, f_2 and g that are devoid of non-conservative source terms, i.e., production and rapid pressure-strain. The transport equations given below, however represent identical physics as the original Eqs. (5.1) - (5.3).

$$\begin{aligned} \frac{\partial}{\partial x}(\rho\widetilde{u}f_1) &= -\left(C_1 a_{11} + \frac{2}{3}\right)\rho g \rho^{2(1-b_1')-2(C_{\epsilon 1}+2C_2)/3}, \\ \frac{\partial}{\partial x}(\rho\widetilde{u}f_2) &= -\widehat{C}_1 \rho g \rho^{2C_{\epsilon 1}/3}, \\ \frac{\partial}{\partial x}(\rho\widetilde{u}g) &= -C_{\epsilon 2}\frac{\rho g^2}{k}\rho^{2C_{\epsilon 1}/3}. \end{aligned} \tag{5.10}$$

The f_2 equation is written in compact form in terms of

$$\widehat{C}_1 = \left[((3(1-b_1') - 2C_2)(3a_{22}C_1 - 2) + 3C_1C_2a_{11} + 2C_2)/(9(1-b_1') - 6C_2)\right].$$

The model constants for the pressure-strain closure are given as $C_1 = 1$, and $C_2 = 0.55$, respectively. Here, a_{11} and a_{22} represents the anisotropy in Reynolds stresses, and b_1' is the shock-unsteadiness model coefficient. The new transformed turbulent variables f_1, f_2 and g are conserved across the shock, if we neglect the dissipation effect on the RHS of Eq. (5.10), as discussed above.

The mean flow is solved by the one-dimensional RANS equations, and the f_1, f_2 and g Eqs. (5.10) are solved for turbulence closure. All the equations are cast in non-dimensional form, where flow variables are normalized by the mean density and the mean speed of the sound, a_∞^*, taken at inlet station. The conservative form of the governing equations along with the turbulent transport equations are solved using a finite volume approach, where the conserved variables, U, inviscid fluxes, F, and source terms, S are written in vector form as,

$$\frac{\partial}{\partial t}\underbrace{\begin{bmatrix}\rho\\ \rho\widetilde{u}\\ \rho\widetilde{E}\\ \rho f_1\\ \rho f_2\\ \rho g\end{bmatrix}}_{U}+\frac{\partial}{\partial x}\underbrace{\begin{bmatrix}\rho\widetilde{u}\\ \rho\widetilde{u}^2+\overline{p}+\frac{2}{3}\rho k\\ \rho\widetilde{E}+\overline{p}\\ \rho\widetilde{u}f_1\\ \rho\widetilde{u}f_2\\ \rho\widetilde{u}g\end{bmatrix}}_{F}=\underbrace{\begin{bmatrix}0\\ 0\\ 0\\ -\left(C_1a_{11}+\frac{2}{3}\right)\rho g\rho^{2(1-b_1')-2(C_{\epsilon1}+2C_2)/3}\\ -\widehat{C}_1\rho g\rho^{\frac{2C_{\epsilon1}}{3}}\\ -C_{\epsilon2}\frac{\rho g^2}{k}\rho^{\frac{2C_{\epsilon1}}{3}}\end{bmatrix}}_{S}. \tag{5.11}$$

Here, $\widetilde{E}$ is the total mean energy and is given by $\frac{\overline{p}}{\gamma-1}+\frac{1}{2}\rho\widetilde{u}^2+\rho k$ with $\gamma=1.4$.

The LF scheme [112] is first order accurate and more dissipative than the SW scheme [116]. However, the SW results can be matched by using larger number of grid points in the LF simulations, as reported in [108, 109]. The initial conditions given in table 4.1 for the non-conservative formulation are transformed to the new variables f_1, f_2 and g as per Equation (5.9). The same inlet values are specified at the upstream boundary and RH jump relations of the mean flow quantities are used to set up the shockwave at $\kappa_0 x^* = 0$. At the exit boundary, a Neumann condition is used, i.e., the gradient of the conserved variables are maintained at zero. Explicit time integration is achieved using the forward Euler method with the given initial conditions.

Figure (5.4) shows the amplification of the Reynolds stresses, the turbulent dissipation rate and the Reynolds stress anisotropy across shockwave for varying upstream Mach number. Data for the non-conservative model are compared with conservative form of the SU-RSM and the DNS data [9, 10].

The amplification of the turbulent quantities computed using the conservative form of the SU-RSM qualitatively follows the same trend as the exact inviscid solution. The results are also comparable to those presented in Fig. (4.7). R_{11} amplification (see Fig. (5.4a)) shows a good match with DNS data except for a slight overprediction at high Mach numbers. The post-shock R_{22} of the conservative formulation also overpredicts the DNS data for Mach numbers beyond 2, but it is a significant improvement over the non-conservative results presented in Fig. (5.4b).

In Fig. (5.4c), the post-shock dissipation rates of conservative formulation show a good match, both quantitatively and qualitatively, with the DNS data and the exact solution, for all Mach numbers. The anisotropy of the Reynolds stresses generated behind the shockwave shows the same qualitative behaviour for all the numerical solutions, and it matches the non-monotonic trend in the DNS data (see figure 5.4d). The conservative results underpredict R_{11}/R_{22} for much of the Mach number range, but is comparable to the DNS data for the strongest shockwave interaction. The non-conservative form of

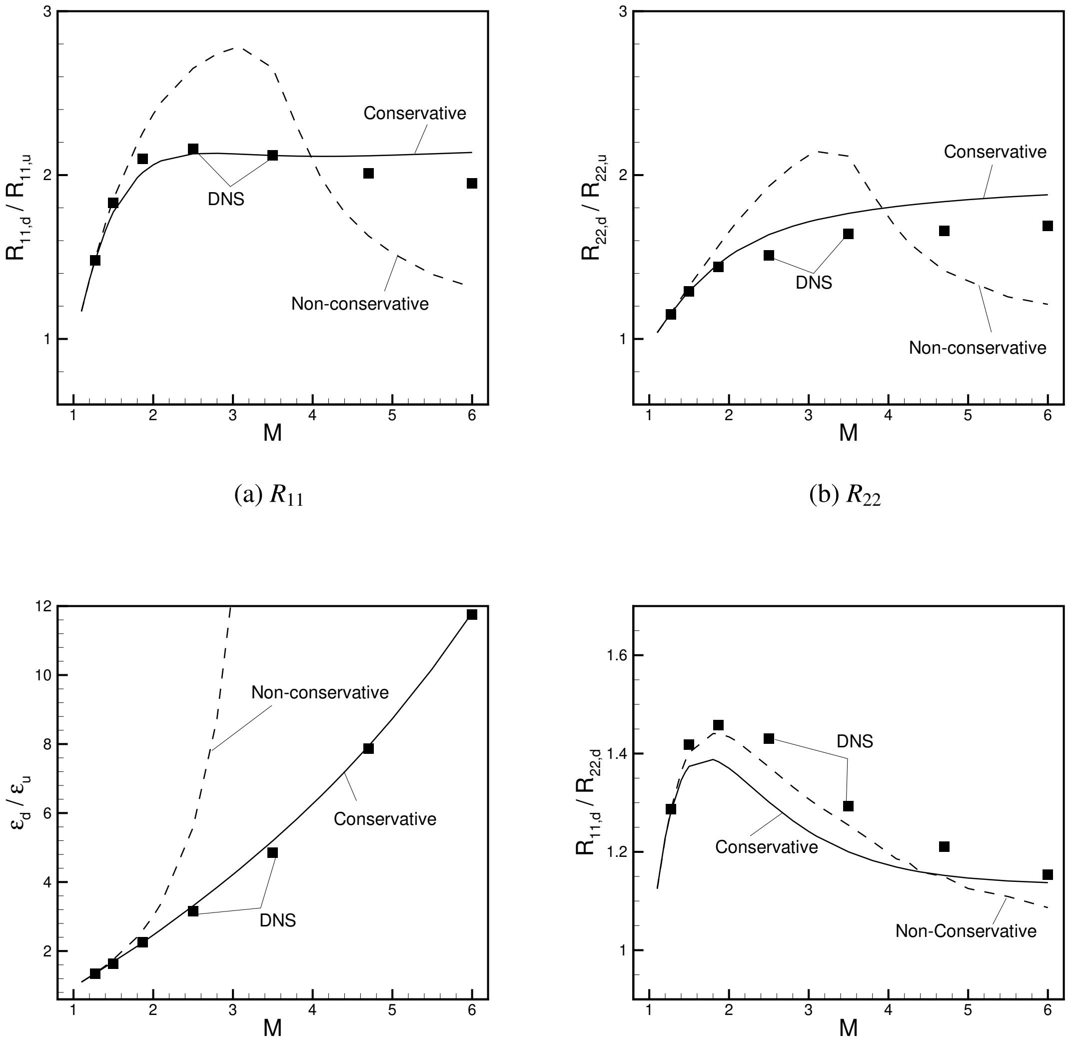

(a) R_{11}

(b) R_{22}

(c) ϵ

(d) R_{11}/R_{22}

Figure 5.4: The amplification in turbulent quantities across the shock obtained from the numerical simulation of new RSM with non-conservative and conservative form of modified transport equations are compared with DNS data [9, 10], for varying upstream Mach number. Solution computed on a 1000-point grid.

SU-RSM results appear to be closer to the DNS data, but they are more sensitive to the numerical grid (see Fig. (5.2)).

Figure (5.5) present the numerical solutions computed using the conservative formulation of the SU-RSM on successively refined computational grids. The conservative results for R_{11}, R_{22}, and ϵ approach the exact inviscid solution as the shockwave gets thinner on finer grids and the effect of turbulent dissipation decreases with shockwave thickness. Note that molecular and turbulent diffusion terms are not included in the simu-

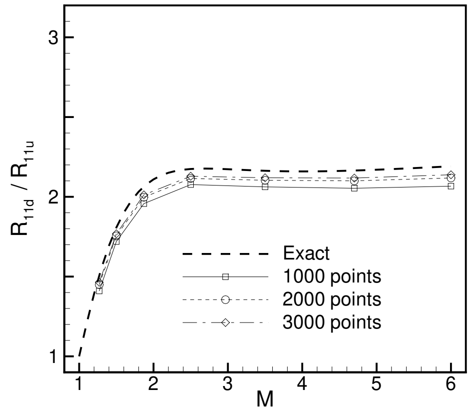

(a) R_{11} (conservative form)

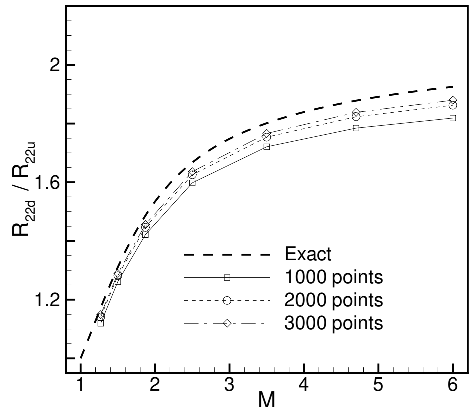

(b) R_{22} (conservative form)

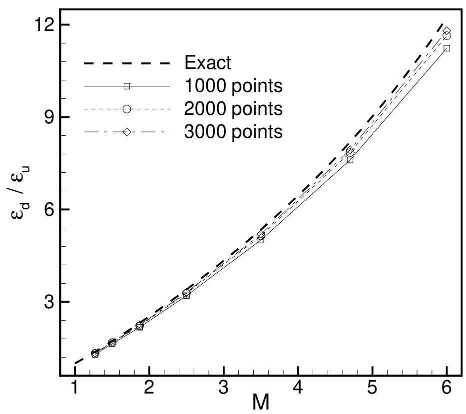

(c) ϵ (conservative form)

Figure 5.5: Effect of grid refinement on the amplification of the R_{11}, R_{22}, and ϵ with varying grid points for the conservative form of the new RSM compared with exact integral solution.

lations, because their effect is found to be small in the region of the shockwave [109]. The conservative formulation also shows a converging trend towards a grid-independent solution. Application of different numerical schemes to the conservative formulation shows very little effect.

5.4 Streamwise evolution of Reynolds stressess

Next, the streamwise evolution of turbulent quantities for the SU-RSM and the baseline model are compared with the DNS data. Both non-conservative and conservative formu-

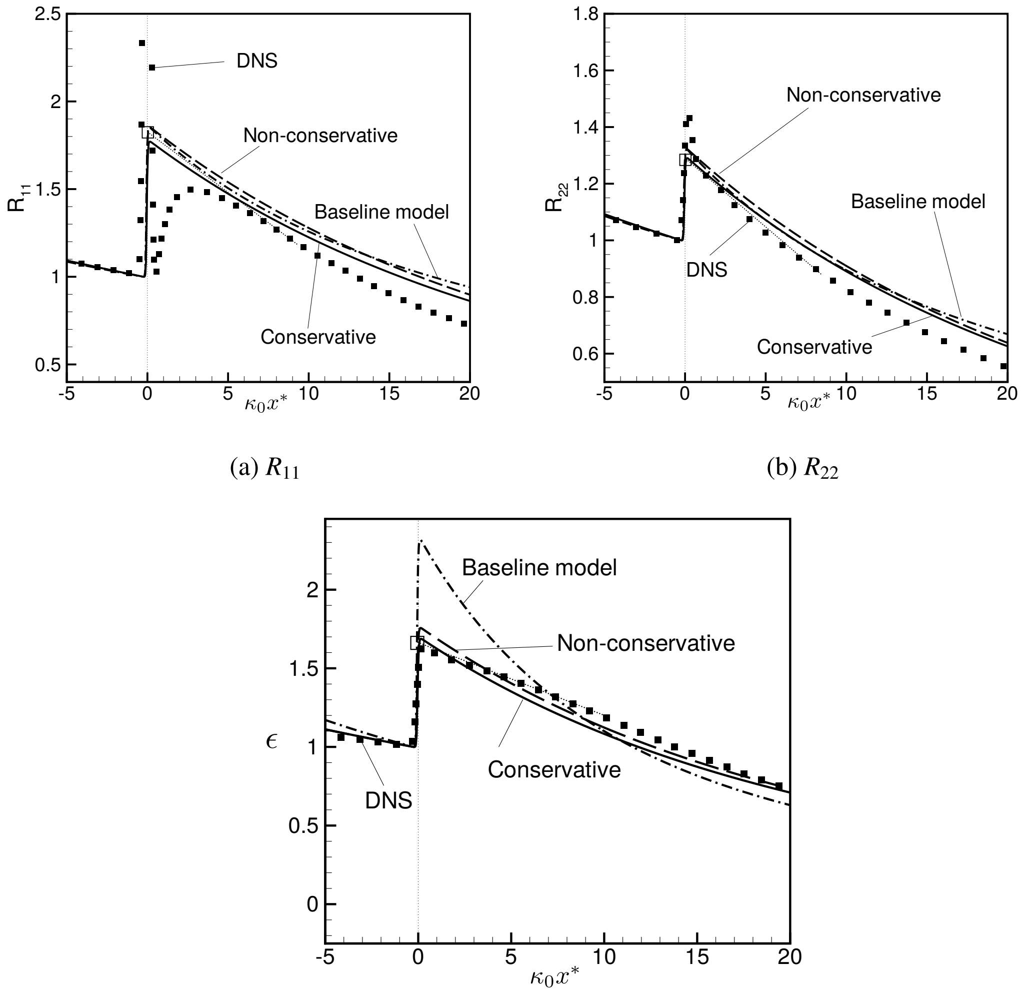

(a) R_{11}

(b) R_{22}

(c) ϵ

Figure 5.6: Streamwise evolution of the turbulence quantities in a Mach 1.5 canonical STI. Numerical solution computed using the Lax-Friedrich scheme for the baseline (dash-dot), the non-conservative form (long-dash) and the conservative form (solid-line) of the present RSM are compared with DNS data (symbol). The amplification in turbulent quantities obtained by extrapolation of the DNS data to mean shock location is shown by open square.

lations are used in the simulations and the results are presented, along with DNS data, in Figs. (5.6) - (5.8). The turbulent quantities decay on either side of the shockwave and amplify across the shockwave due to a sudden change in mean velocity. The DNS data shows very large values of R_{11} in the region of the shockwave. This does not represent actual amplification of R_{11}, and is not captured by the turbulence models. There is a non-monotonic variation in the R_{11} immediately after the shockwave. This non-monotonic

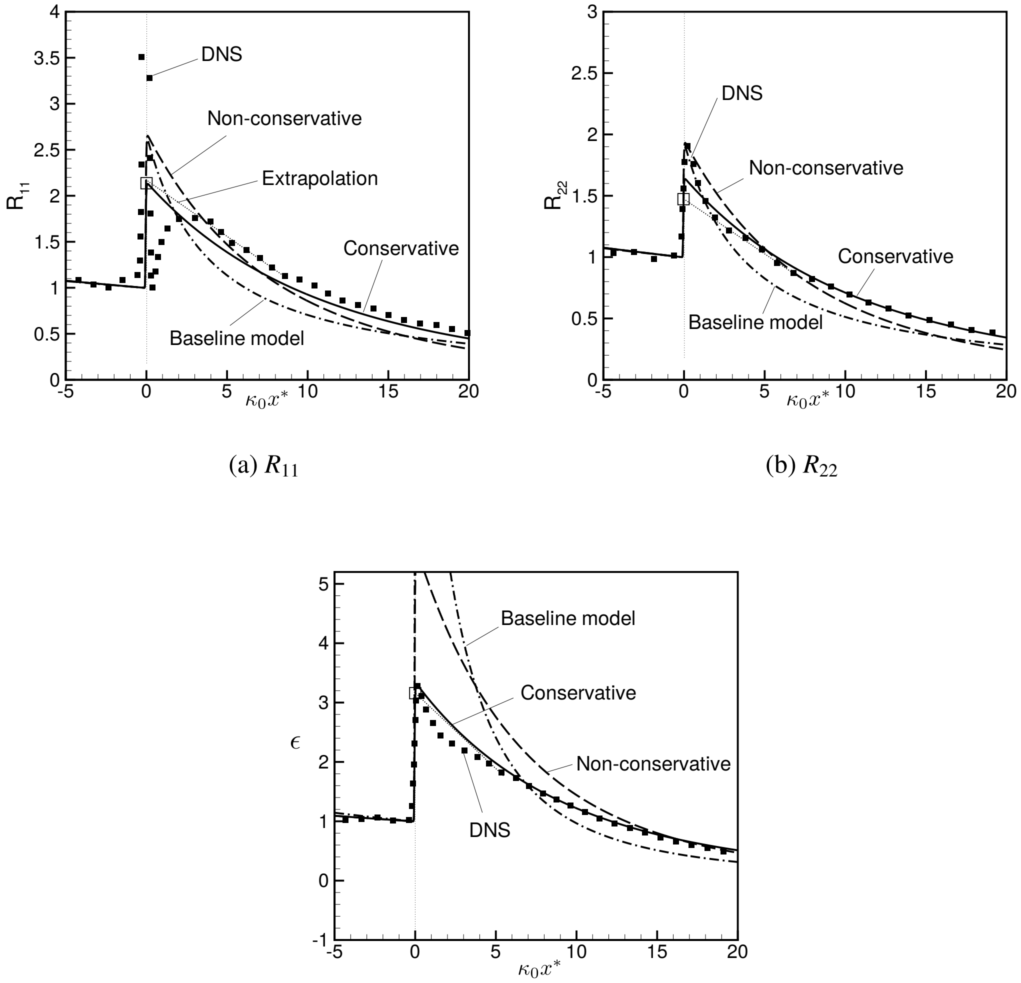

(a) R_{11}

(b) R_{22}

(c) ϵ

Figure 5.7: Streamwise evolution of the turbulence quantities in a Mach 2.5 canonical STI. Numerical solution computed using the Lax-Friedrich scheme for the baseline (dash-dot), the non-conservative form (long-dash) and the conservative form (solid-line) of the present RSM are compared with DNS data (symbol). The amplification in turbulent quantities obtained by extrapolation of the DNS data to mean shock location is shown by open square.

behaviour is due to the acoustic decay, as per by Mahesh *et al.* [75], and is not explicitly modeled in the present work. The post-shock DNS data is extrapolated back to the shock-center location ($\kappa_0 x^* = 0$) to get an estimate of the effective jump (shown by an open square) in the turbulent quantities across the shock.

Figure (5.6) shows the streamwise evolution of the Reynolds stresses and the dissipation rate for Mach 1.5 STI. The amplification in R_{11} and R_{22} in all three solutions–baseline, non-conservative and conservative, are comparable to the DNS data extrapolated to the mean shockwave location of $\kappa_0 x^* = 0$. The streamwise evolution of Reynolds stresses for non-conservative and conservative models decays monotonically and have an approximately same decay rate as that of baseline model both upstream and downstream of the shockwave. The models slightly underpredict the decay of the Reynolds stresses downstream of the shockwave in comparison with the DNS data. Here, the non-conservative and conservative RSMs show similar results indicating a small magnitude of numerical error for interaction with weak shockwaves. The turbulent dissipation rate predictions show similar trends in Fig. (5.7c), with the model results matching DNS data well. The only exception is the baseline model that gives too high an amplification in ϵ across the shockwave.

For the Mach 2.5 case shown in Fig. (5.7), the best predictions are obtained using the conservative form of the SU-RSM. The jump in R_{11} matches the extrapolated shockwave value in the DNS data. The R_{22} predictions match the DNS data over the entire domain, except for a small region immediately behind the shockwave. The turbulent dissipation rate matches the peak DNS value at the shockwave, overpredicts ϵ for $\kappa_0 x^* \leq 5$ and overlaps with DNS data further downstream. The trend is identical to that presented in Sinha [74], and this results in a slight underprediction of R_{11} in the downstream flow. The non-conservative simulation overpredicts R_{11}, R_{22}, and ϵ at the shockwave and exhibits a substantially higher post-shock decay rate than that in the DNS. The baseline model follows a similar trend, but the errors are higher than the non-conservative form of the current RSM based on the shock-unsteadiness correction.

The non-conservative errors at the shockwave are even higher in the Mach 3.5 interaction presented in Fig (5.8). In this case, the amplification of ϵ for the non-conservative and baseline models is higher than the DNS data by about an order of magnitude. It results in a rapid decay of the post-shock turbulence, which is very different from the trend observed in the DNS. The conservative model (with minimal numerical and physical modeling error), once again, is the closest to the DNS data. The shock-jumps in R_{11}, R_{22}, and ϵ are reproduced well by the SU-RSM, but the decay rate of the Reynolds stresses is overpredicted, due to the turbulent dissipation rate being higher than DNS data in the range $0 < \kappa_0 x^* < 10$.

5.5 Generalization to multi-dimensional problems

The results presented above show that a physically consistent and numerically robust Reynolds stress model is able to predict the changes across a normal shockwave. For

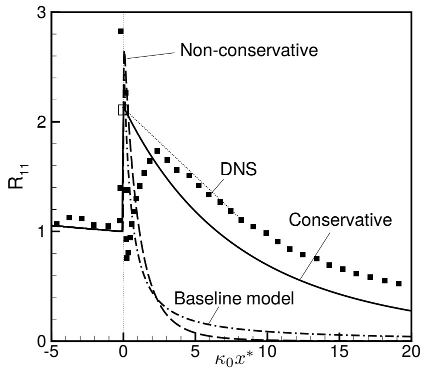

(a) R_{11}

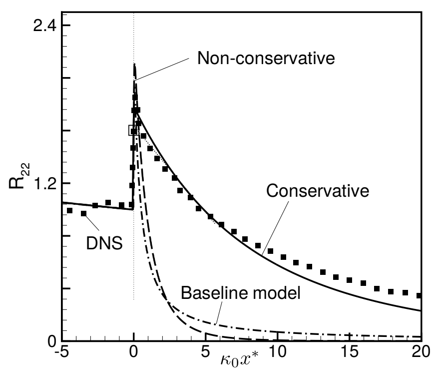

(b) R_{22}

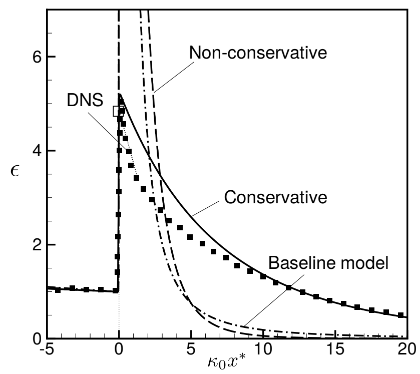

(c) ϵ

Figure 5.8: Streamwise evolution of the turbulence quantities in a Mach 3.5 canonical STI. Numerical solution computed using the Lax-Friedrich scheme for the baseline (dash-dot), the non-conservative form (long-dash) and the conservative form (solid-line) of the present RSM are compared with DNS data (symbol). The amplification in turbulent quantities obtained by extrapolation of the DNS data to mean shock location is shown by open square.

an oblique shockwave oriented at a angle θ in the $x - y$ plane (shown in Fig. (5.9)), the proposed model equations for R_{11}, R_{22} can be interpreted in terms of the shock-normal $R_{\eta\eta}$ and transverse $R_{\xi\xi}$ components. Equation (4.31) can thus be written in a general tensor form as

$$\frac{D\overline{\rho}R_{\eta\eta}}{Dt} = (2(b_1' - 1) + \frac{4}{3}C_2)\overline{\rho}R_{\eta\eta}\frac{\partial\widetilde{u}_k}{\partial x_k} - C_1\overline{\rho}\epsilon a_{\eta\eta} - \frac{2}{3}\overline{\rho}\epsilon, \tag{5.12}$$

where $a_{\eta\eta}$ is the anisotropy in the shock-normal Reynolds stress. Note that the mean derivatives in the shock-transverse directions are assumed to be small such that the shock-normal velocity gradient on the right-hand side is replaced by the mean dilatation. Simi-

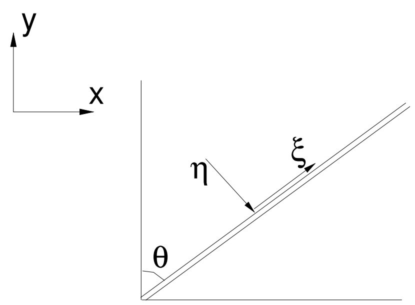

Figure 5.9: Schematic of an oblique shockwave at an angle θ to the y-coordinate in the lab frame of reference.

larly, the shock-normal convection term on the left-hand side is generalized to the material derivative.

Following identical procedure for the shock-transverse Reynolds stress $R_{\xi\xi}$, we generalize Eq. (5.12) to

$$\frac{D\overline{\rho}R_{\xi\xi}}{Dt} = -\frac{2}{3}C_2\overline{\rho}R_{\eta\eta}\frac{\partial\widetilde{u}_k}{\partial x_k} - C_1\overline{\rho}\epsilon a_{\xi\xi} - \frac{2}{3}\overline{\rho}\epsilon. \tag{5.13}$$

where $a_{\xi\xi}$ is the anisotropy in the transverse Reynolds stress. For the Reynolds stress component R_{12}, we start with Eq. (2.22) written for a shockwave normal to the x-direction,

$$\frac{\partial\overline{\rho}\widetilde{u}R_{12}}{\partial x} = (C_2 - 1)\overline{\rho}R_{12}\frac{\partial\widetilde{u}}{\partial x} - C_1\overline{\rho}\epsilon a_{12}, \tag{5.14}$$

and generalize it to an oblique shockwave to get the model transport equation for the Reynolds stress component $R_{\eta\xi}$

$$\frac{D\overline{\rho}R_{\eta\xi}}{Dt} = (C_2 - 1)\overline{\rho}R_{\eta\xi}\frac{\partial\widetilde{u}_k}{\partial x_k} - C_1\overline{\rho}\epsilon a_{\eta\xi}. \tag{5.15}$$

where $a_{\eta\xi}$ is the anisotropy in the Reynolds stress component $R_{\eta\xi}$.

The Reynolds stresses in the lab frame of reference (x, y) can be related to those in the shockwave frame by the coordinate transformation

$$\begin{aligned} R_{11} &= cos^2\theta R_{\eta\eta} + sin2\theta R_{\eta\xi} + sin^2\theta R_{\xi\xi}, \\ R_{22} &= sin^2\theta R_{\eta\eta} - sin2\theta R_{\eta\xi} + cos^2\theta R_{\xi\xi}, \\ R_{12} &= (R_{\xi\xi} - R_{\eta\eta})cos\theta sin\theta + (cos^2\theta - sin^2\theta)R_{\eta\xi}. \end{aligned} \tag{5.16}$$

The transport equations for R_{11}, R_{22} and R_{12} can now be derived in terms of the model equations for $R_{\eta\eta}$, $R_{\xi\xi}$ and $R_{\eta\xi}$ given above. On simplification, we get

$$\frac{D\overline{\rho}R_{11}}{Dt} = (A_{11}\overline{\rho}R_{11} + A_{12}\overline{\rho}R_{22} + A_{13}\overline{\rho}R_{12})\frac{\partial\widetilde{u}_k}{\partial x_k} - C_1\overline{\rho}\epsilon a_{11} - \frac{2}{3}\overline{\rho}\epsilon, \tag{5.17}$$

$$\frac{D\overline{\rho}R_{22}}{Dt} = (A_{21}\overline{\rho}R_{11} + A_{22}\overline{\rho}R_{22} + A_{23}\overline{\rho}R_{12})\frac{\partial\widetilde{u_k}}{\partial x_k} - C_1\overline{\rho}\epsilon a_{22} - \frac{2}{3}\overline{\rho}\epsilon, \tag{5.18}$$

$$\frac{D\overline{\rho}R_{12}}{Dt} = (A_{31}\overline{\rho}R_{11} + A_{32}\overline{\rho}R_{22} + A_{33}\overline{\rho}R_{12})\frac{\partial\widetilde{u_k}}{\partial x_k} - C_1\overline{\rho}\epsilon a_{12}, \tag{5.19}$$

where the reverse transformation is used to express $R_{\eta\eta}$, $R_{\xi\xi}$ and $R_{\eta\xi}$ on the right-hand side in terms of R_{11}, R_{22} and R_{12}. The model coefficients in the above equations are as follows,

$$A_{11} = (-2 + 2b_1' + \frac{4}{3}C_2)cos^4\theta - \frac{2}{6}C_2 sin^2 2\theta + \frac{(C_2-1)}{2}sin^2 2\theta,$$

$$A_{12} = (-1 + b_1' + \frac{4}{6}C_2)sin^2 2\theta - \frac{2}{3}C_2 sin^4\theta - \frac{(C_2-1)}{2}sin^2 2\theta,$$

$$A_{13} = \left((2 - 2b_1' + \frac{4}{3}C_2)cos^2\theta + \frac{2}{3}C_2 sin^2\theta\right) sin2\theta + \frac{(C_2-1)}{2}sin4\theta,$$

$$A_{21} = (-1 + b_1' + \frac{4}{6}C_2)sin^2 2\theta - \frac{2}{3}C_2 cos^4\theta - \frac{(C_2-1)}{2}sin^2 2\theta,$$

$$A_{22} = (-2 + 2b_1' + \frac{4}{3}C_2)sin^4\theta - \frac{2}{6}C_2 sin^2 2\theta + \frac{(C_2-1)}{2}sin^2 2\theta,$$

$$A_{23} = \left((2 - 2b_1' - \frac{4}{3}C_2)sin^2\theta + \frac{2}{3}C_2 cos^2\theta\right) sin2\theta - \frac{(C_2-1)}{2}sin4\theta,$$

$$A_{31} = (1 - b_1' - C_2)sin2\theta cos^2\theta + \frac{(C_2-1)}{4}sin4\theta,$$

$$A_{32} = (1 - b_1' - C_2)sin2\theta sin^2\theta + \frac{(C_2-1)}{4}sin4\theta,$$

$$A_{33} = (1 - b_1' - C_2)sin^2 2\theta + (C_2 - 1)cos^2 2\theta$$

The Reynolds stress R_{33} is transverse to the oblique shock defined in Fig. (5.9). It behaves akin to $R_{\xi\xi}$ across the shockwave and the model transport equation takes the form

$$\frac{D\overline{\rho}R_{33}}{Dt} = -\frac{2}{3}C_2\overline{\rho}R_{\eta\eta}\frac{\partial\widetilde{u_k}}{\partial x_k} - C_1\overline{\rho}\epsilon a_{33} - \frac{2}{3}\overline{\rho}\epsilon,$$

which is derived from Equation (5.13), and can be written as,

$$\frac{D\overline{\rho}R_{33}}{Dt} = -\frac{2}{3}C_2\overline{\rho}\left(cos^2\theta R_{11} - sin2\theta R_{12} + sin^2\theta R_{22}\right)\frac{\partial\widetilde{u_k}}{\partial x_k} - C_1\overline{\rho}\epsilon a_{33} - \frac{2}{3}\overline{\rho}\epsilon, \tag{5.20}$$

Finally, the dissipation rate Eq. (4.39) is cast in general tensor form as,

$$\frac{D\overline{\rho}\epsilon}{Dt} = -\frac{2}{3}C_{\epsilon 1}\overline{\rho}\epsilon\frac{\partial\widetilde{u_k}}{\partial x_k} - C_{\epsilon 2}\overline{\rho}\frac{\epsilon^2}{k}. \tag{5.21}$$

The above five Eqs. (5.17)-(5.21) represent a physically consistent Reynolds stress model for flows with shockwaves oriented at an angle θ in the $x - y$ plane. The equations can be further generalized for shockwaves with any arbitrary orientation in a three-dimensional flow.

An existing CFD code can be modified to implement these equations in regions of shock wave, identified in terms of large negative values of mean dilatation. A shock detector function can be used [42, 104] such that the modifications are restricted to high-compression regions, without altering the base model in the flow outside of shockwaves. The shock angle θ can be calculated using the local mean pressure gradient vector. The model coefficients depend on θ, which is physically consistent with the directional nature of a shock wave. A shockwave alters the normal and transverse Reynolds stresses differently and this information is retained in the new physics-based RSM. The local pressure gradient can also be used to obtain the shock-normal component of the Mach number. This has been successfully implemented in SBLI flows with a single oblique shockwave [42] and with multiple shockwaves [104]. Newer approaches which eliminate the dependence of the model coefficient b_1' on M_u are also being explored [108].

We note that the above RSM Eqs. (5.17)-(5.21) for a shockwave are in non-conservative form. They are expected to give accurate prediction for shockwave with M_u upto 1.5 (see Fig. (5.6)) and possibly as high as $M_u = 2$. The corresponding upstream flow Mach number can be much higher (up to $M_u = 5$) for weak oblique shockwaves. For stronger shockwaves, we need to employ a conservative formulation to eliminate large numerical error at the shockwave discontinuity. This is achieved by writing the conserved variables f_1, f_2 and g, in Equation (31), in terms of the shock-normal and transverse Reynolds stresses.

$$\begin{aligned}
f_1 &= R_{\eta\eta}\rho^{\alpha_1},\\
f_2 &= R_{\xi\xi} - \beta R_{\eta\eta},\\
f_3 &= R_{\eta\xi}\rho^{(1-C_2)},\\
g &= \epsilon\rho^{-2C_{\epsilon 1}/3},
\end{aligned} \tag{5.22}$$

where $\alpha_1 = 2(b_1' - 1) + 4C_2/3$ and $\beta = 2C_2/3\alpha_1$, and a new conserved variable f_3 is defined for the Reynolds stress component $R_{\eta\xi}$. Here, the overbar on ρ is temporarily omitted to avoid potential conflict between Reynolds averaging and the sign of the exponent. The model transport equations for the conserved variables, Eq. (5.10) can be generalized to

$$\frac{D(\rho f_1)}{Dt} = -(C_1 a_{\eta\eta} + \frac{2}{3})\rho g\rho^{\alpha_1+2C_{\epsilon 1}/3}, \tag{5.23}$$

$$\frac{D(\rho f_2)}{Dt} = -\widehat{C}_1\rho g\rho^{2C_{\epsilon 1}/3}, \tag{5.24}$$

$$\frac{D(\rho f_3)}{Dt} = -C_1 a_{\eta\xi}\rho g\rho^{1-C_2+2C_{\epsilon 1}/3}, \tag{5.25}$$

$$\frac{D(\rho g)}{Dt} = -C_{\epsilon 2}\frac{\rho g^2}{k}\rho^{2C_{\epsilon 1}/3}, \tag{5.26}$$

where $\widehat{C_1}$ is in terms of $a_{\eta\eta}$ and $a_{\xi\xi}$, and the diffusion terms are neglected at the shockwave.

The Reynolds stresses R_{11}, R_{22}, and R_{12} available upstream of a shockwave can be rotated to the shockwave coordinate system (shown in Fig. (5.9)).

$$
\begin{aligned}
R_{\eta\eta} &= cos^2\theta R_{11} - sin2\theta R_{12} + sin^2\theta R_{22}, \\
R_{\xi\xi} &= sin^2\theta R_{11} + sin2\theta R_{12} + cos^2\theta R_{22}, \\
R_{\eta\xi} &= (R_{11} - R_{22})cos\theta sin\theta + (cos^2\theta - sin^2\theta)R_{12},
\end{aligned}
\tag{5.27}
$$

which can then be used to arrive at the upstream values of the conserved variables, as per Eq. (5.22). The post-shock values obtained by solving Eqs. (5.23)-(5.26) across the shockwave can then be converted back to R_{11}, R_{22}, and R_{12} by invoking the reverse transformation.

The R_{33} equation not included in the above discussion can be transformed to a conservative form by following a similar approach. The resulting RSM equations can be used effectively for the entire range of Mach numbers.

5.6 Summary

The mean flow is solved by using the RANS equations with the Reynolds stress model transport equations. The amplification of the turbulent quantities show the non-physical nature with large numerical error across the shockwave due to the non-conservative form of the source terms. The numerical schemes and grid refinement applied to the present model problem show high effect on the results especially for the non-conservative form of turbulence model. We propose a novel transformation of the Reynolds stresses and the turbulent dissipation rate into new turbulence variables that are conserved across a shockwave. This minimises numerical error and gives well-behaved results, which converge to closed-form analytical solution on successive grid refinement. The new RSM equations are thus physically consistent and numerically robust for modelling high-speed turbulent flows with shockwaves. The new proposed conservative form of SU-RSM give a better match of Reynolds stresses and the turbulent dissipation with DNS data. The anisotropic nature of the turbulence is also well predicted. The new model equations for the normal Reynolds stresses, along with the transport equations for the Reynolds shear stress are generalised to a tensor form that can be applied to multi-dimensional flows with shock waves of arbitrary orientation.

Chapter 6

Explicit algebraic Reynolds stress model

Application of the generalized model of the SU-RSM to realistic flows like SBLI is very cumbersome. Therefore, in this chapter, we evaluate an ARSM in the canonical STI, as the shockwave amplifies the Reynolds stresses in the streamwise and the transverse directions differently. Next, the limitations of the existing EARSM are presented, and appropriate corrections are described. Subsequently, a new set of algebraic equations for the Reynolds stresses are derived using the LIA to capture the anisotropy across the shockwave.

ARSM belong to the class of non-linear two-equation models, where the anisotropy tensor is expressed as a non-linear relation between the Reynolds stresses, and the vorticity and strain-rate tensors. Different levels of approximation have been used to solve the algebraic expression for Reynolds stress tensor explicitly [8, 30–33]. The general form of the anisotropy tensor consists of ten independent tensorial terms with combination of the rate of strain and rotation tensors, and their invariants. The coefficients are also written in terms of the mean flow quantities.

6.1 Baseline EARSM

In the present work, we adopt Wallin and Johansson's [8] explicit algebraic Reynolds stress model (WJ-EARSM), because of its simplicity and ease of extension to compressible flows [64]. In this model, the Reynolds stress tensor ($R_{ij} = \widetilde{u_i'' u_j''}$) is written explicitly in terms of an effective turbulent viscosity μ_T and an extra anisotropy term a_{ij}^{ext}, as

$$\overline{\rho} R_{ij} = \frac{2}{3}\overline{\rho} k \delta_{ij} - 2\mu_T S_{ij}^{*} + \overline{\rho} k a_{ij}^{ext}. \tag{6.1}$$

For two-dimensional mean flows,

$$\mu_T = -\frac{1}{2}\beta_1 \overline{\rho} k \tau, \quad \text{and} \quad a_{ij}^{ext} = \beta_4 (S_{ik}\Omega_{kj} - \Omega_{ik} S_{kj}) \tag{6.2}$$

are given in terms of two non-zero coefficients β_1 and β_4. Here, S_{ij} and Ω_{ij} are the strain and vorticity tensors, normalized with the turbulent time scale $\tau = max\left(k/\epsilon, 6\sqrt{\nu/\epsilon}\right)$ with a Kolmogorov limiter. S^*_{ij} and Ω^*_{ij} are dimensional strain and vorticity tensors respectively, and are given as

$$S^*_{ij} = \frac{1}{2}\left(\frac{\partial\widetilde{u_i}}{\partial x_j} + \frac{\partial\widetilde{u_j}}{\partial x_i} - \frac{2}{3}\frac{\partial\widetilde{u_k}}{\partial x_k}\delta_{ij}\right), \tag{6.3}$$

$$\Omega^*_{ij} = \frac{1}{2}\left(\frac{\partial\widetilde{u_i}}{\partial x_j} - \frac{\partial\widetilde{u_j}}{\partial x_i}\right). \tag{6.4}$$

The model coefficients β_1 and β_4 are defined as,

$$\beta_1 = -\frac{6}{5}\frac{N}{(N^2 - 2II_\Omega)}, \text{ and } \beta_4 = -\frac{6}{5}\frac{1}{(N^2 - 2II_\Omega)}, \tag{6.5}$$

and N is obtained from the solution of a cubic polynomial equation

$$N = \begin{cases} \frac{c'_1}{3} + \left(P_1 + \sqrt{P_2}\right)^{1/3} + \text{sgn}(P_1 - \sqrt{P_2})|P_1 - \sqrt{P_2}|^{1/3}, & \text{for } P_2 \geq 0 \\ \frac{c'_1}{3} + 2(P_1^2 - P_2)^{1/6}\cos\left(\frac{1}{3}\arccos\left(\frac{P_1}{\sqrt{P_1^2 - P_2}}\right)\right), & \text{for } P_2 < 0 \end{cases} \tag{6.6}$$

with

$$P_1 = c'_1\left(\frac{c'^2_1}{27} + \frac{9}{20}II_S - \frac{2}{3}II_\Omega\right), \text{ and } P_2 = P_1^2 - \left(\frac{c'^2_1}{9} + \frac{9}{10}II_S - \frac{2}{3}II_\Omega\right)^3. \tag{6.7}$$

Here, $II_S = S_{ij}S_{ji}$ and $II_\Omega = \Omega_{ij}\Omega_{ji}$ are the tensor invariants of the strain and vorticity tensors, and $c'_1 = 1.8$.

For one-dimensional mean flow in canonical STI, where the velocity gradients are finite only in the streamwise direction, the extra anisotropy term a^{ext}_{ij} in Reynolds stress tensor becomes zero. Thus, the shock-normal and transverse Reynolds stresses simplify to

$$\overline{\rho}R_{11} = \frac{2}{3}\overline{\rho}k + \overline{\rho}k\beta_1 S_{11}, \tag{6.8}$$

$$\overline{\rho}R_{22} = \frac{2}{3}\overline{\rho}k + \overline{\rho}k\beta_1 S_{22}, \tag{6.9}$$

where $S_{11} = \frac{2}{3}\tau(\partial\widetilde{u}/\partial x)$ and $S_{22} = -(\tau/3)(\partial\widetilde{u}/\partial x)$. The effective turbulent viscosity, $\mu_T = -0.5\beta_1\overline{\rho}k\tau$ with $\beta_1 = -6/(5N)$. By considering the only II_S contribution in P_1 and P_2, the solution for N reduces to $1.8(P_1^2 - P_2)^{1/6}$. The approximate values of N and coefficient β_1 becomes 1.39 $\tau|\partial\widetilde{u}/\partial x|$ and -0.86/$(\tau|\partial\widetilde{u}/\partial x|)$, respectively (see Appendix C). Substituting the approximated value of β_1 in the Eqs. (6.8) and (6.9), we get

$$\overline{\rho}R_{11} = \frac{2}{3}\overline{\rho}k + 0.573\overline{\rho}k, \tag{6.10}$$

$$\overline{\rho}R_{22} = \frac{2}{3}\overline{\rho}k - 0.286\overline{\rho}k. \tag{6.11}$$

The above relations are used to calculate the Reynolds stresses on a two-equation $k - \epsilon$ platform; the simplified transport equation for TKE in a one-dimensional mean flow is given as,

$$\overline{\rho}\widetilde{u}\frac{\partial k}{\partial x} = -\overline{\rho}R_{11}\frac{\partial \widetilde{u}}{\partial x} - \overline{\rho}\epsilon. \tag{6.12}$$

where the diffusion terms are assumed to be small [109]. The dissipation rate term is neglected at the shock [102] to get a closed-form solution for the amplification of TKE across the shock.

$$\frac{k_d}{k_u} = \left(\frac{\widetilde{u}_u}{\widetilde{u}_d}\right)^{2/3+0.573}. \tag{6.13}$$

Similarly, the amplification in the normal Reynolds stresses is obtained as (see Appendix C for details),

$$\frac{R_{11,d}}{R_{11,u}} = 1.86\left(\frac{\widetilde{u}_u}{\widetilde{u}_d}\right)^{2/3+0.573}, \tag{6.14}$$

$$\frac{R_{22,d}}{R_{22,u}} = 0.57\left(\frac{\widetilde{u}_u}{\widetilde{u}_d}\right)^{2/3+0.573}. \tag{6.15}$$

with subscripts u and d denoting the locations upstream and downstream of the shock, respectively. Here, $\widetilde{u}_u/\widetilde{u}_d$ is a function of the shock Mach number and $R_{11,u} = R_{22,u} = (2/3)k_u$ for isotropic turbulence upstream of the shockwave.

The post-shock statistics obtained using WJ-EARSM are evaluated against the DNS data of Larsson *et al.* [9, 10] for varying shock strengths and are shown in Fig. (6.1). The DNS data are identical to those presented in chapter 4 for SU-RSM model development, and are obtained by extrapolating the downstream values to the shock location. WJ-EARSM based on the standard $k - \epsilon$ model yields large amplification of TKE, over-predicting the DNS data by a factor of 2 at Mach 1.87 and more at higher Mach number. A similar trend is seen in the amplification of Reynolds stresses. The effective turbulent viscosity takes high values at the shock wave, and it leads to a high amplification of TKE, R_{11} and R_{22}. Additionally, WJ-EARSM does not capture the anisotropy variation with Mach number and gives a constant anisotropy of 3.26, obtained from Eqs. (6.14) & (6.15) for varying shock strengths.

6.2 LIA based model improvement

We propose improvements to the WJ-EARSM baseline model using shock physics based on LIA and DNS data. We start with the linearized transport equation for the Reynolds stresses in the shock-normal and transverse directions, given by Sinha *et al.* [41]. The equations are written in the frame of reference attached to the instantaneous shock wave,

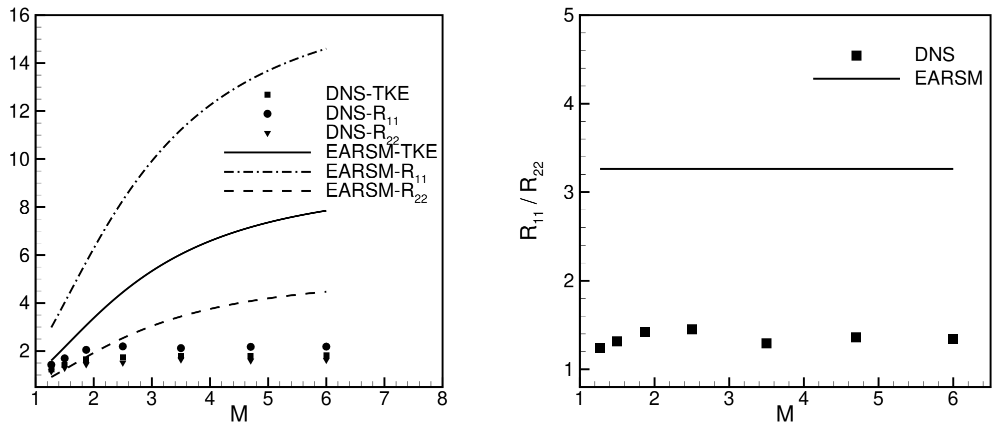

(a) (b)

Figure 6.1: Comparison of the amplification in the TKE, Reynolds stresses and their anisotropy across a normal shockwave obtained using WJ-EARSM with the DNS data [9, 10] for varying upstream Mach number.

assuming that the upstream turbulence is purely vortical in nature. Note that the Reynolds stress R_{33} follows an equation identical to R_{22}, and is not presented here.

$$\bar\rho\,\bar u\frac{\partial}{\partial x}\frac{R_{11}}{2} = -\bar\rho R_{11}\frac{\partial\bar u}{\partial x} + \bar\rho\overline{u'\xi_t}\frac{\partial\bar u}{\partial x} - \overline{u'\frac{\partial p'}{\partial x}} - \overline{u'\frac{\partial p}{\partial x}}\,, \tag{6.16}$$

$$\bar\rho\,\bar u\frac{\partial}{\partial x}\frac{R_{22}}{2} = -\bar\rho\,\bar u\overline{v'\xi_y}\frac{\partial\bar u}{\partial x}\,, \tag{6.17}$$

where ξ_t and ξ_y represent the linear shock velocity in the streamwise direction and the angular distortion of the shockwave. Note that the difference between Reynolds- and Favre-averaging is negligible in the linear framework, for example, $\bar u - \tilde u = \overline{u'\rho'}/\bar\rho$, is of higher order than the linear terms considered in LIA. The terms on the right side of Eqs. (6.16) & (6.17) are in order, production due to mean compression P_k, shock-unsteadiness term S_k^1, pressure-velocity correlation Π_k^1, production due to mean pressure gradient Π_k^3, and shock-distortion term S_k^2. The first and the third terms in Eq. (6.16) are identical to conventional turbulence models, while the other two source terms bring in the effect of unsteady shockwave oscillations.

LIA is based on linearized RH relations, which can be used to write the linearized jump conditions for the Reynolds stresses across a shockwave,

$$\frac{1}{2}\overline{\rho_u}\,\overline{u_u}(R_{11,d} - R_{11,u}) = -\overline{\rho_u}\overline{u'_u u'_m}\Delta\bar u + \overline{\rho_u}\overline{u'_m\xi_t}\Delta\bar u - \overline{u'_m(p'_d - p'_u)}, \tag{6.18}$$

$$\frac{1}{2}\overline{\rho_u}\,\overline{u_u}(R_{22,d} - R_{22,u}) = -\overline{\rho_u}\,\overline{u_u}\overline{v'_m\xi_y}\Delta\bar u, \tag{6.19}$$

where $\Delta\overline{u} = (\overline{u_d} - \overline{u_u})$, $u'_m = (u'_u + u'_d)/2$, and $v'_m = (v'_u + v'_d)/2$. Note that the above equations can be interpreted as integrated form of the transport Eqs. (6.16) & (6.17). The terms on the right-hand side of Eq. (6.18) are thus denoted by $\int P_k$, $\int S_k^1$ and $\int \Pi_k^1$, respectively, while the term in Eq. (6.19) is $\int S_k^2$. We consider purely vortical turbulence upstream of the shock, and hence $\rho'_u = p'_u = T'_u = 0$. As a result, the production due to mean pressure gradient, Π_k^3 is identically zero.

LIA provides analytical solution for the downstream disturbance field and the shock characteristics for a prescribed upstream turbulence spectrum [75]. The correlations appearing in Eqs. (6.18) & (6.19) can thus be computed using LIA. A budget of the source terms as a function of upstream Mach number is shown in Fig. (6.2) and is identical to that given in Ref. [41]. The production due to mean compression is positive for all the Mach numbers and thus amplifies R_{11}. The shock unsteadiness term, on the other hand, reduces the magnitude of shock-normal Reynolds stress. There is no production of R_{22} and R_{33} at the shockwave. Instead, the shock distortion mechanism S_k^2 is found to increase the transverse Reynolds stresses. This is opposite to the effect of the shock-unsteadiness term S_k^1, and can be interpreted as redistributing energy from the shock-normal to the transverse directions.

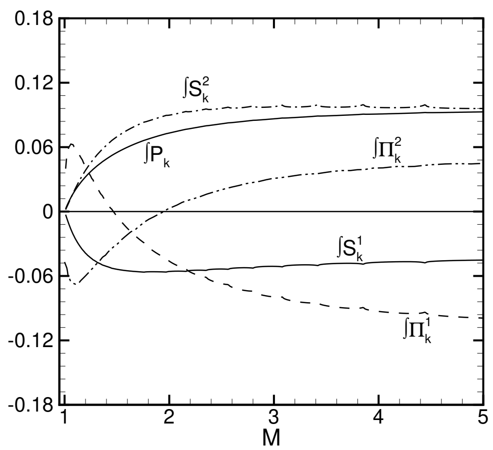

Figure 6.2: Budget of Reynolds stress Equations (6.18)-(6.19) at different Mach numbers. All terms are normalized by $\overline{\rho_u}\, \overline{u}_u^3$.

The shock-vortical turbulence interaction generates acoustic fluctuations, with finite values of $\overline{p'^2}$ and $\overline{p'u'}$ correlations immediately downstream of the shockwave. There is a rapid post-shock adjustment within one characteristic eddy size from the shockwave, where the acoustic energy decays and is transferred back to the TKE [75]. R_{11} is found to increase in the acoustic adjustment region, while R_{22} and R_{33} exhibit a rapid decrease. The overall change in TKE due to the energy transfer between vortical turbulence and acoustic energy, denoted by $\int \Pi_k^2$, is derived in appendix D and is plotted as a function of the upstream Mach number in Fig. (6.2). We note that the pressure dependent terms Π_k^1 and Π_k^2 have alternate positive and negative contribution to the Reynolds stress budget. They represent the effect of pressure fluctuations on the streamwise and transverse components. Overall, the distortion of the shock front and its unsteady movement, and the pressure dependent terms are responsible for redistribution of the TKE in the three directions.

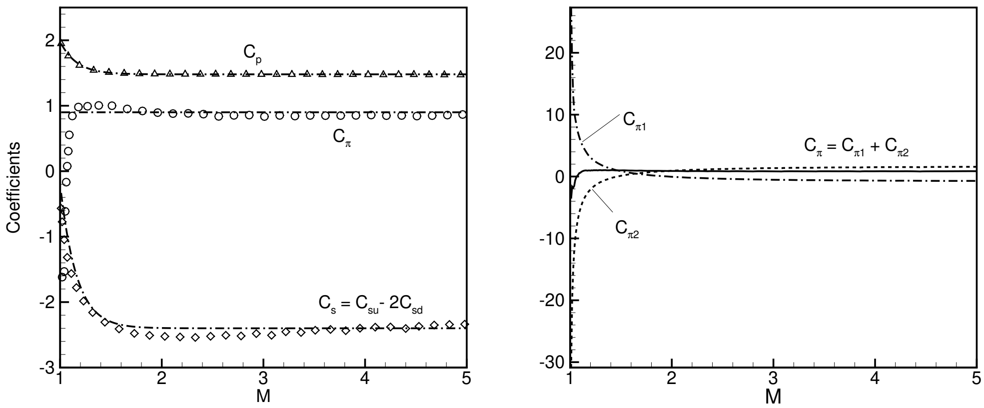

(a) (b)

Figure 6.3: Linear interaction analysis is used to obtain the model coefficients: (a) Curve-fit (lines) to the LIA data (symbols) for C_p , C_Π and C_s, (b) LIA data for C_{Π_1} , C_{Π_2} and C_Π.

Equations (6.18) & (6.19) can be recast to compute the amplification of Reynolds stresses and TKE across the shockwave.

$$\frac{R_{11,d}}{R_{11,u}} = 1 - C_p \frac{\Delta\overline{u}}{\overline{u}_u} + C_{su} \frac{\Delta\overline{u}}{\overline{u}_u} + C_{\Pi_1} \frac{\Delta\overline{u}}{\overline{u}_u}, \tag{6.20}$$

$$\frac{R_{22,d}}{R_{22,u}} = 1 - C_{sd} \frac{\Delta\overline{u}}{\overline{u}_u}, \tag{6.21}$$

$$\frac{k_d}{k_u} = 1 - \frac{C_p}{3}\frac{\Delta\overline{u}}{\overline{u}_u} + \frac{C_{su}}{3}\frac{\Delta\overline{u}}{\overline{u}_u} + \frac{C_{\Pi_1}}{3}\frac{\Delta\overline{u}}{\overline{u}_u} - \frac{2C_{sd}}{3}\frac{\Delta\overline{u}}{\overline{u}_u} + \frac{C_{\Pi_2}}{3}\frac{\Delta\overline{u}}{\overline{u}_u}, \tag{6.22}$$

where we use the fact that $k_u = \frac{3}{2}R_{11,u}$ for incoming homogeneous turbulence, and $k_d = \frac{1}{2}(R_{11,d} + 2R_{22,d})$ for the axisymmetric turbulence downstream of the shockwave. The additional effect of Π_k^2 is also included and the source terms are written in terms of the coefficients C_p, C_{su}, C_{sd}, C_{Π_1} and C_{Π_2}. The derivation is given in appendix D, and the coefficients are plotted in Fig. (6.3).

The Mach number dependence of the Reynolds stresses and the TKE amplification, as predicted by LIA Eqs. (6.20)-(6.22), is shown in Fig. (6.4). All components of the velocity fluctuation are amplified across the shockwave, and the amplifications tend to saturate beyond Mach 5. The shock-normal component is amplified more than transverse component for shockwaves with M < 2, while the opposite is seen for M > 2. In fact, the LIA prediction for R_{11} decreases with increasing Mach number beyond 2, whereas R_{22} amplification increases monotonically to reach a value of about 2.0 in the hypersonic limit. The LIA results do not match the DNS data, taken from Larsson *et al.* [9, 10], where the streamwise Reynolds stress is amplified more than the transverse velocity fluctuations for strong shockwaves (M > 2). This is similar to that reported in Fig. (5) of Larsson and Lele [9]. Reynolds stress anisotropy R_{11}/R_{22} behind the shock (Fig. (6.4d)) also shows a poor comparison between LIA and DNS. On the other hand, LIA and DNS data for TKE amplification match very well for the entire range of Mach number (Fig. (6.4c)). This could be because of the additional C_{Π_2} term included in Eq. (6.22).

We propose improvement to the LIA-based results, by noting that the streamwise Reynolds stress is under-predicted in comparison to the DNS data, while the transverse Reynolds stress is over-predicted. This is due to the effect of the shock-unsteadiness term, which reduces the streamwise Reynolds stress (see budget plot in Fig. (6.2)), and the shock-distortion term that results in a much larger amplification for the transverse Reynolds stress. The overall effect of the two terms (S_k^1 and S_k^2) seems to give the correct amplification of TKE across the shockwave. We thus propose to redistribute the shock-unsteadiness and distortion effect ($C_s = C_{su}$ - $2C_{sd}$) more equally among the different directions, so as to obtain a modified set of Reynolds stress amplification equations. A contribution of $(1/3)C_s$ is used for each component, and the R_{33} equation is not shown for brevity.

$$\frac{R_{11,d}}{R_{11,u}} = 1 - C_p\frac{\Delta\overline{u}}{\overline{u}_u} + \left[\frac{1}{3}C_s + \frac{2}{3}C_\Pi\right]\frac{\Delta\overline{u}}{\overline{u}_u}, \tag{6.23}$$

$$\frac{R_{22,d}}{R_{22,u}} = 1 + \left[\frac{1}{3}C_s + \frac{1}{6}C_\Pi\right]\frac{\Delta\overline{u}}{\overline{u}_u}, \tag{6.24}$$

$$\frac{k_d}{k_u} = 1 - \frac{C_p}{3}\frac{\Delta\overline{u}}{\overline{u}_u} + \frac{C_s}{3}\frac{\Delta\overline{u}}{\overline{u}_u} + \frac{C_\Pi}{3}\frac{\Delta\overline{u}}{\overline{u}_u}. \tag{6.25}$$

We introduce a new pressure dependent coefficient $C_\Pi = C_{\Pi_1} + C_{\Pi_2}$ to represent the combined effect of Π_k^1 and Π_k^2 and it is also redistributed among the Reynolds stresses. A higher contribution to R_{11} and a smaller fraction to R_{22} and R_{33} are found to give a reasonable match with the DNS data. Both the shock unsteadiness (C_s) and pressure dependent (C_Π) terms are redistributed in such a way that the TKE amplification remains unchanged as in Eq. (6.22). Also, the production term remains unaltered from Eq. (6.20). The model Eqs. (6.23) - (6.25) is termed as shock-unsteadiness corrected explicit algebraic Reynolds stress model (SU-EARSM).

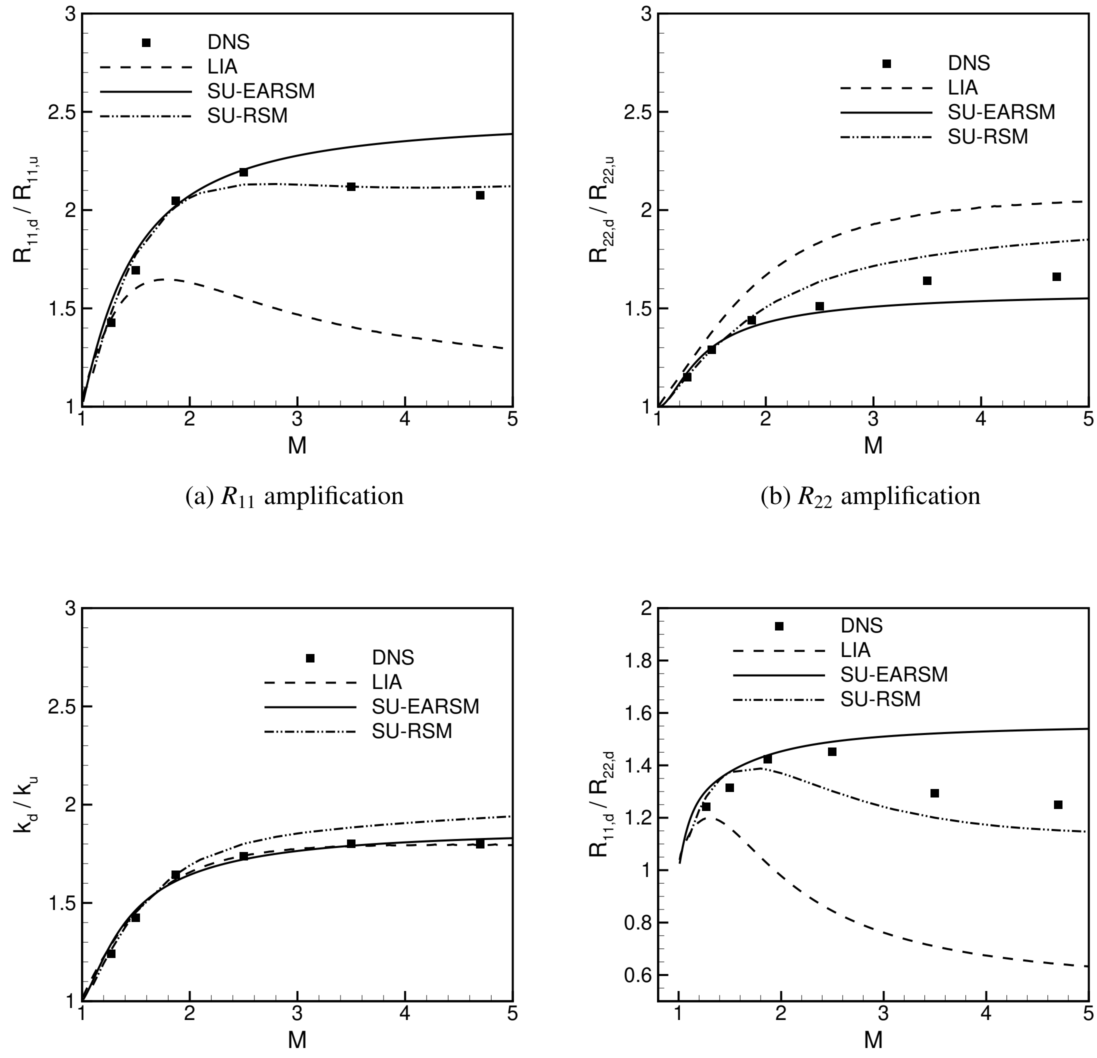

(a) R_{11} amplification

(b) R_{22} amplification

(c) TKE amplification

(d) Ratio of R_{11} and R_{22}

Figure 6.4: Comparison of the amplification of the Reynolds stresses, TKE, and their anisotropy across the normal shockwave obtained using modified algebraic equations with the DNS data [9, 10], SU-RSM and LIA for varying upstream Mach number.

The Reynolds stresses predicted by Eqs. (6.23) and (6.24) match DNS data up to a Mach number of 2.5, beyond which R_{11} is over predicted and R_{22} is under predicted. The Reynolds stress anisotropy generated by the shockwave is also predicted well for M $\leq$ 2.5, and it is a significant improvement over the baseline EARSM predictions, shown in Fig. 6.1. The amplification of TKE matches the DNS data as earlier (LIA data). We also present the results obtained using shock-unsteadiness based Reynolds stress transport model (SU-RSM). It solves partial differential equations for R_{11} and R_{22} across the shock wave, and is able to predict the redistribution of TKE in the streamwise and transverse directions for M > 2.5. The mismatch between DNS and SU-EARSM predictions could be because of the particular choice of the model fractions (1/3, 2/3 and 1/6), and could be improved by a better choice of these coefficients. The TKE amplification is very close to the DNS data, and small changes with respect to the LIA results are due to the fact that the model coefficients are approximated as curve-fits to the LIA data (see Fig. (6.3)).

$$\begin{aligned} C_p &= 1.48 + 0.5e^{(6.2(1-\mathrm{M}))}, \\ C_s &= C_{su} - 2C_{sd} = -2.5 + 2.2e^{(6.2(1-\mathrm{M}))}. \end{aligned}$$

The pressure dependent terms Π_k^1 and Π_k^2 have large variation in the transonic regime M < 1.3, and they show a change of sign beyond Mach 2 (see budget plot in Fig. (6.2)). The combined effect of the two terms is modelled as $C_\Pi = 0.9$, and it appears to be a good fit for the majority of the Mach number range shown in Fig. (6.3). However, it does not capture the negative values of C_{Π_1}, as a result of which the new model is not able to reproduce the slight decrease in R_{11} and the non-monotonic trend in Reynolds stress anisotropy beyond Mach 2.5.

We note that there are many similarities between the SU-EARSM proposed here and the SU-RSM source terms given in chapter 4. The production term in SU-RSM is equivalent to the C_p-term in Equation (22); C_p varies in the range of 1.98 to 1.48 as compared to a constant value of 2 in RSM. The model coefficient in the shock-unsteadiness term is -2b_1' for SU-RSM and it varies between 0 and -0.8 with increasing Mach number. The corresponding coefficient $(1/3)C_s$ in SU-EARSM has a similar variation, with an asymptotic value of -0.83 in the hypersonic limit. The pressure-strain correlation plays a vital role in Reynolds stress modeling. The corresponding model coefficient is $C_2 = 0.55$ for SU-RSM and $(2/3)C_\Pi = 0.6$ for SU-EARSM. There are additional dissipation and slow pressure strain terms in the RSM equation, and their effect is discussed in the next section.

6.3 Application to STI

The newly developed SU-EARSM is implemented with the shock-unsteadiness (SU) $k-\omega$ model equations given below. The SU correction [41] is based on LIA of the canonical STI and was developed previously for the $k-\epsilon$ model [74]. It is converted to the $k-\omega$ framework using the transformation $\epsilon = \beta^* \omega k$, where $\beta^* = 0.09$ and ω is the specific dissipation. See Appendix A for the derivation.

$$\bar{\rho}\widetilde{u}\frac{\partial k}{\partial x} = -\frac{2}{3}c_0\bar{\rho}k\frac{\partial \widetilde{u}}{\partial x} - \bar{\rho}\beta^*\omega k, \tag{6.26}$$

$$\bar{\rho}\widetilde{u}\frac{\partial \omega}{\partial x} = -\frac{2}{3}\gamma\bar{\rho}\omega\frac{\partial \widetilde{u}}{\partial x} - \bar{\rho}\beta\omega^2. \tag{6.27}$$

Here, we write the equations in terms of Favre averaged velocity under the linearity assumption at shockwaves, which ensures negligible difference between Favre- and Reynolds averaging. The coefficient $c_0 = 1 - b_1'$ combines the production and the shock-unsteadiness source terms, with $b_1' = 0.4\,(1 - e^{(1-\mathrm{M})})$ as the shock-unsteadiness parameter. In the ω-equation, $\gamma = C_{\epsilon_1} - c_0$ and $\beta = (C_{\epsilon_2} - 1)\beta^*$ are based on the ϵ-coefficients $C_{\epsilon_1} = 1.0 + 0.21$ M and $C_{\epsilon_2} = 1.2$ given in Ref. [74]. The shock-unsteadiness $k - \epsilon$ model has been validated against DNS data of shock-turbulence interaction for a wide range of Mach numbers [74]. The above $k - \omega$ equations are mathematically equivalent to the $k - \epsilon$ model and hence give identical results.

Equations (6.26) and (6.27) are used to compute TKE in the canonical STI, and the normal Reynolds stresses are evaluated in terms of the Reynolds stress anisotropy $\hat{a}$, obtained from Eqs. (6.23) and (6.24),

$$\hat{a} \;=\; \frac{R_{11}}{R_{22}} = \frac{\left[1 - C_p \frac{\Delta\widetilde{u}}{\widetilde{u}_u} + \left(\frac{1}{3}C_s + \frac{2}{3}C_\Pi\right)\frac{\Delta\widetilde{u}}{\widetilde{u}_u}\right]}{\left[1 + \left(\frac{1}{3}C_s + \frac{1}{6}C_\Pi\right)\frac{\Delta\widetilde{u}}{\widetilde{u}_u}\right]} \tag{6.28}$$

which gives

$$R_{11} \;=\; \frac{2k\hat{a}}{\hat{a}+2}\,, \tag{6.29}$$

$$R_{22} \;=\; \frac{2k}{\hat{a}+2}. \tag{6.30}$$

The above equations consist of dimensionless and normalized quantities where the freestream mean density and the freestream mean speed of sound are used as the characteristic variables. The characteristic length scale is taken from the peak wave number $\kappa_0 = 4$ in the incoming turbulence field.

We solve Eqs. (6.26) - (6.27) with the mean conservation equations for mass, momentum and energy using the finite-volume approach. The inviscid fluxes at the cell faces are evaluated using the Lax-Friedrich scheme and the mean flow gradients in the source terms are computed using a second-order accurate central difference scheme. A first-order forward Euler method is used to integrate the equations in time to reach steady state solution. The method is identical to that used for SU-RSM and additional details can be found in chapter 5.

We use the DNS data of Larsson *et al.* [9, 10] for evaluating the SU-EARSM proposed above. The DNS dataset covers a Mach numbers from 1.27 to 6, with turbulent Mach number M_t in the range of 0.15–0.22, and $Re_\lambda = 40$. The normalized values of the Reynolds stresses, TKE and the specific dissipation rate for the different test cases are listed in Table 4.1.

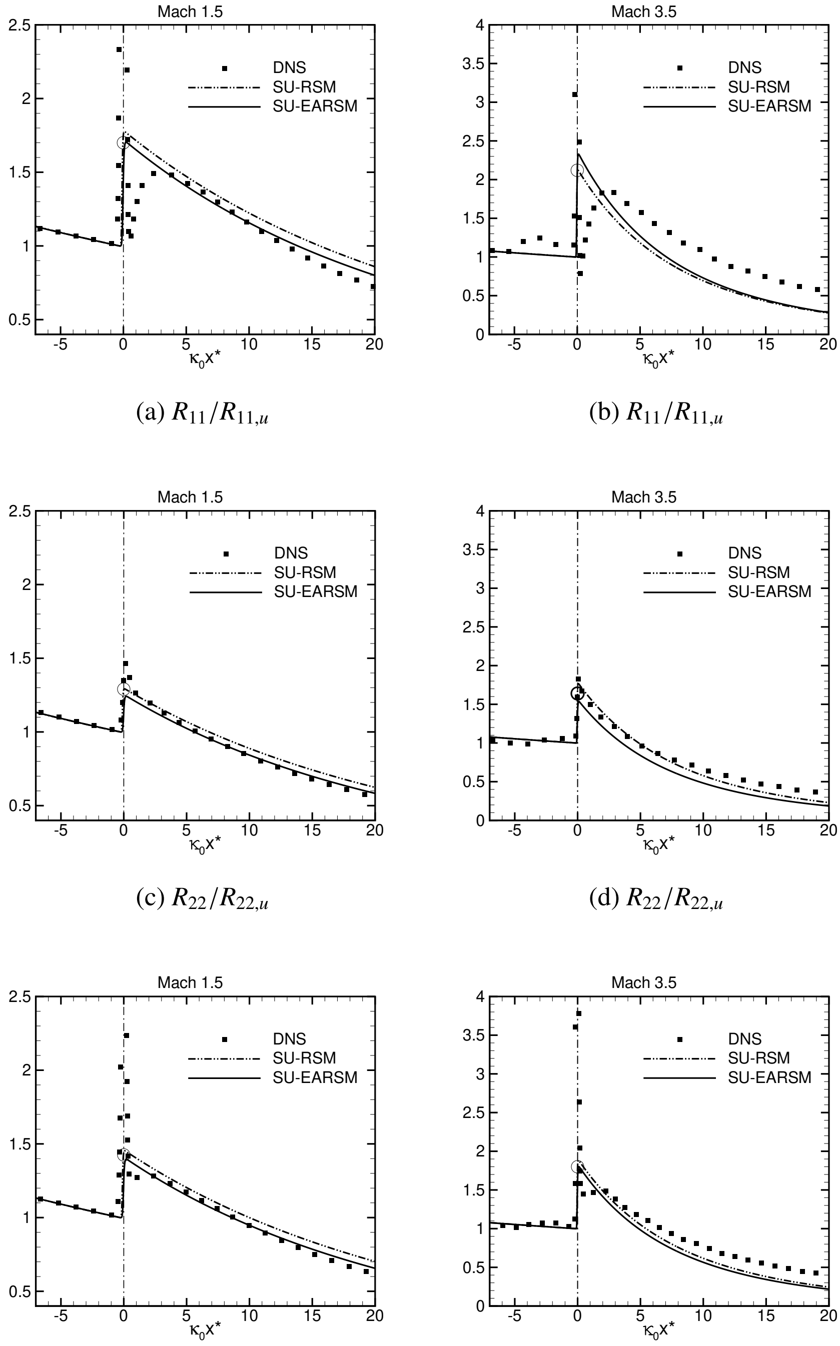

(a) $R_{11}/R_{11,u}$ (b) $R_{11}/R_{11,u}$

(c) $R_{22}/R_{22,u}$ (d) $R_{22}/R_{22,u}$

(e) k/k_u (f) k/k_u

Figure 6.5: Comparison of spatial variation of the R_{11}, R_{22}, and TKE obtained using SU-EARSM with DNS data [9, 10] and SU-RSM for M = 1.5 and 3.5 for shock/turbulence interaction. The open circle at $\kappa_0 x^* = 0$ denote the effective jump in the turbulent quantities at the shock location, shown on the vertical line.

Figure (6.5) show the streamwise variation of the the turbulent quantities obtained from DNS [9, 10], as well as those computed using the SU-EARSM described above.

Predictions of SU-RSM are also presented for comparison. The turbulence quantities are normalized by their respective values just upstream of the shockwave. Results are shown for two Mach numbers and the other cases are found to exhibit similar trend. Mach 1.5 is representative of the low supersonic range, while M = 3.5 is representative of the high supersonic cases listed in Table 4.1.

The Reynolds stresses and the TKE shows a monotonic decay before the shockwave, a jump at the shockwave ($\kappa_0 x^* = 0$), followed by a faster decay away from the shockwave. The DNS data has large values of R_{11} and TKE in the vicinity of the shockwave, which is an artifact of unsteady shock motion [9, 10]. The non-monotonic variation of R_{11} and, to a smaller extent, in TKE immediately behind the shockwave is caused by the acoustic transient, as described in Appendix D. The SU model does not reproduce the non-monotonic trend [41]. In stead, it attempts to predict the effective jump in the turbulent quantities across the shock and the acoustic transient. This is obtained from the DNS data by extrapolating the post-shock decay back to the shock-center location (shown by open circle at $\kappa_0 x^* = 0$ in Fig. (6.5)). Similar extrapolation is used, as in chapter 4.

At Mach 1.5, the model predictions for R_{11}, R_{22} and TKE match the DNS data well. There are small differences in the post-shock decay rates, and they are discussed subsequently. The jump in TKE is governed by the coefficient c_0 in Eq. (6.26), and it is distributed among the normal Reynolds stresses as per the anisotropy parameter $\hat{a}$ given in Eq. (6.28). The anisotropy parameter includes the effect of turbulence production, shock-unsteadiness and pressure-velocity correlation via the model coefficients C_p, C_s and C_Π respectively.

The SU-RSM on the other hand, solves separate transport equations for the normal Reynolds stresses. The jump in R_{11} and R_{22} are governed by the production, shock-unsteadiness and rapid pressure strain terms in the respective equations. The TKE jump is thus obtained by summing the changes in the individual Reynolds stresses. In spite of the differences in approach between SU-EARSM and SU-RSM, both models predict almost identical jump in R_{11}, R_{22} and TKE at the shockwave. This is because of the fact that both models are based on the same physical mechanisms. Using comparable coefficients, as discussed in section 6.2, the SU-EARSM is able to achieve the accuracy of the more elaborate SU-RSM at low supersonic Mach numbers.

This is not the case for stronger shockwaves. The SU-RSM is able to reproduce the jump in R_{11} at Mach 3.5; the model prediction at $\kappa_0 x^* = 0^+$ matches the DNS-extrapolated value (shown by open circle). A quantitative comparison is given in Table 6.1, which shows a -0.03% error in R_{11} for SU-RSM. By comparison, the SU-EARSM prediction exceeds the DNS data by 9.5%. The error in R_{22} amplification at the shockwave is comparable in the two models, whereas TKE jump is better matched by the current SU-EARSM.

	M = 1.5			M = 3.5		
	DNS	RSM	EARSM	DNS	RSM	EARSM
R_{11}	1.69	1.78 (4.75%)	1.79 (5.61%)	2.12	2.12 (-0.03%)	2.32 (9.50%)
R_{22}	1.29	1.29 (0.15%)	1.30 (0.88%)	1.64	1.77 (7.70%)	1.53 (-6.98%)
TKE	1.42	1.45 (1.96%)	1.46 (2.76%)	1.80	1.88 (4.66%)	1.79 (-0.51%)
R_{11}/R_{22}	1.31	1.37 (4.59%)	1.38 (4.69%)	1.29	1.20 (-7.17%)	1.52 (17.72%)

Table 6.1: Turbulence quantities from DNS are compared with the model predictions at the shockwave location ($\kappa_0 x^* = 0^+$) for Mach 1.5 and 3.5. The values extracted from Fig. (6.5) are reported along with the corresponding percentage error with respect to DNS (in bracket).

The most prominent difference between the two models is in the Reynolds stress anisotropy predicted at the Mach 3.5 shock wave. SU-RSM underpredicts the post-shock R_{11}/R_{22} by about 7%, while SU-EARSM exceeds the DNS value by more than 17%. This is representative of the limitations of the current model for Mach numbers exceeding 2.5, as shown in Fig. (6.2). It is due to the particular choice of model coefficient C_Π, as discussed in section 6.2. The Reynolds stress anisotropy predicted by the two models are almost identical for the Mach 1.5 case, and the deviation from the DNS data is less than 5%; see Table 6.1. The model predictions for the jumps in R_{11}, R_{22} and the TKE across the shock ($\kappa_0 x^* = 0^+$) are also comparable for Mach 1.5.

	M = 1.5			M = 3.5		
	DNS	RSM	EARSM	DNS	RSM	EARSM
R_{11}	1.15	1.22 (6.23%)	1.16 (0.51%)	1.07	0.69 (-35.26%)	0.73 (-31.83%)
R_{11}	0.84	0.89 (6.30%)	0.84 (0.87%)	0.67	0.58 (-13.16%)	0.48(-27.60%)
TKE	0.95	1.00 (5.67%)	0.95 (0.18%)	0.78	0.62 (-20.56%)	0.56 (-27.23%)
R_{11}/R_{22}	1.38	1.38 (-0.06%)	1.37 (-0.36%)	1.61	1.20 (-25.44%)	1.52 (-5.85%)

Table 6.2: Turbulence quantities from DNS are compared with the model predictions downstream of the shockwave (at $\kappa_0 x^* = 10$). The values extracted from Fig. (6.5) are reported along with the corresponding percentage error with respect to DNS (in bracket).

Table 6.2 lists the values of the turbulence quantities farther away from the shockwave. The model predictions are compared with the DNS data at $\kappa_0 x^* = 10$, where the results are governed mainly by the post-shock decay rate. At this location, the SU-EARSM predictions are within 1% of the DNS data for Mach 1.5, whereas SU-RSM results shows a higher deviation (up to about 6%). At the higher Mach number, the error increases up to 30-35% for both models, and it is due to a faster post-shock decay than the DNS (see Fig. (6.5 b,d,f)).

From the table 6.2, we observe a change in sign of the percentage error for the TKE with increasing the shock strength. This phenomenon can be elucidated from Fig. (6.6) to Fig. (6.7), which shows the decay rate of the TKE obtained from models (SU-RSM and SU-EARSM) in comparison with the DNS data for different Mach numbers. From the tables, (6.3) - (6.4), the SU-EARSM turbulence model overpredicts the TKE value for the weaker shock strengths and underpredicts for stronger shocks, compared to the DNS data. For the SU-EARSM turbulence model, the mean flow of Mach 2.5 acts as a limiting Mach number, where we observe the change in a sign of the percentage error in the TKE value. Both SU-RSM and SU-EARSM results shows a high deviation in percentage error as the shock strength increases.

	M = 1.87			M = 2.5		
	DNS	RSM	EARSM	DNS	RSM	EARSM
R_{11}	1.01	1.08(6.55%)	1.01(-0.56%)	1.06	0.92(-12.81%)	0.90(-14.74%)
R_{22}	0.63	0.78(24.26%)	0.70(12.11%)	0.64	0.71(10.70%)	0.61(-5.03%)
TKE	0.74	0.88(18.51%)	0.80(8.51%)	0.76	0.78(2.32%)	0.71(-7.39%)
R_{11}/R_{22}	1.62	1.39(-14.25%)	1.44(-11.30%)	1.65	1.30(-21.24%)	1.49(-10.22%)

Table 6.3: Turbulence quantities from DNS are compared with the model predictions downstream of the shockwave (at $\kappa_0 x^* = 10$).The values extracted from Fig. (6.6) are reported along with the corresponding percentage error with respect to DNS (in bracket).

	M = 4.7			M = 6.0		
	DNS	RSM	EARSM	DNS	RSM	EARSM
R_{11}	1.13	0.53(-53.15%)	0.58(-48.80%)	1.20	0.41(-56.34%)	0.45(-59.86%)
R_{22}	0.69	0.46(-33.50%)	0.38(-45.22%)	0.71	0.36(-49.82%)	0.29(-59.06%)
TKE	0.82	0.48(-41.13%)	0.45(-45.70%)	0.86	0.37(-56.34%)	0.34(-59.86%)
R_{11}/R_{22}	1.64	1.15(-29.55%)	1.53(-6.54%)	1.20	1.05(-12.99%)	1.18(-1.94%)

Table 6.4: Turbulence quantities from DNS are compared with the model predictions downstream of the shockwave (at $\kappa_0 x^* = 10$).The values extracted from Fig. (6.7) are reported along with the corresponding percentage error with respect to DNS (in bracket).

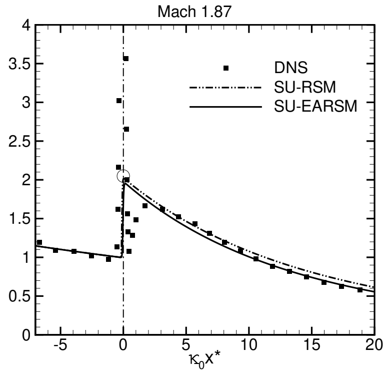

(a) $R_{11}/R_{11,u}$

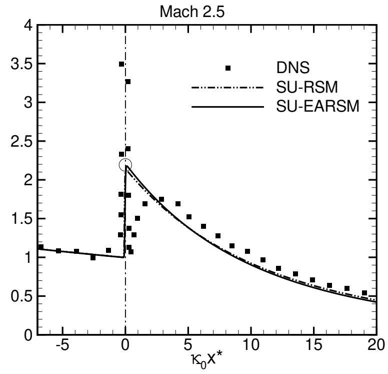

(b) $R_{11}/R_{11,u}$

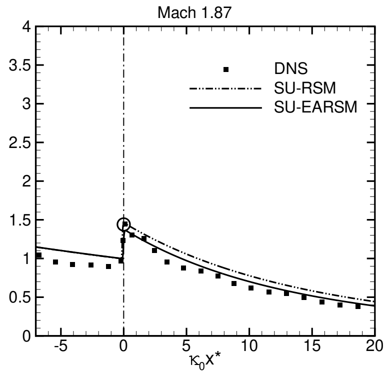

(c) $R_{22}/R_{22,u}$

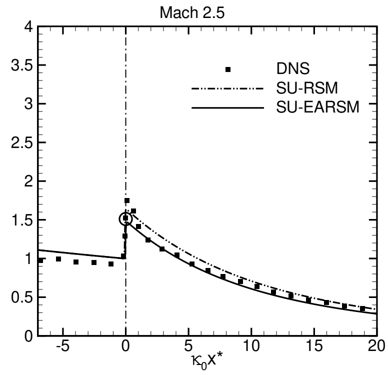

(d) $R_{22}/R_{22,u}$

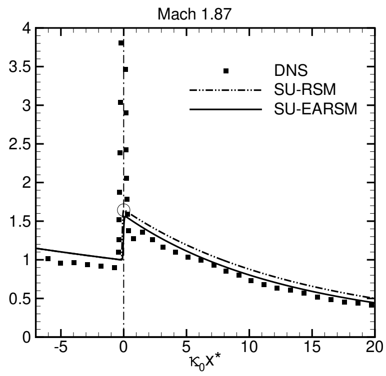

(e) k/k_u

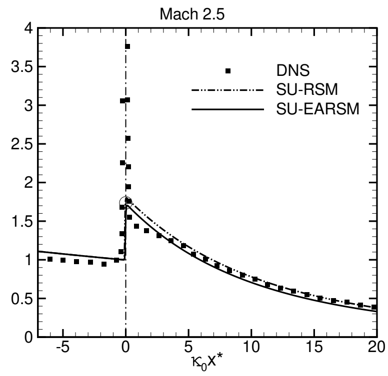

(f) k/k_u

Figure 6.6: Comparison of spatial variation of the R_{11}, R_{22}, and TKE obtained using SU-EARSM with DNS data [9, 10] and SU-RSM for M = 1.87 and 2.5 for shock/turbulence interaction. The open circle at $\kappa_0 x^* = 0$ denote the effective jump in the turbulent quantities at the shock location, shown on the vertical line.

The post-shock predictions obtained using SU-EARSM are depended on the particular choice of the model coefficients (1/3, 2/3, and 1/6), and we note that the downstream

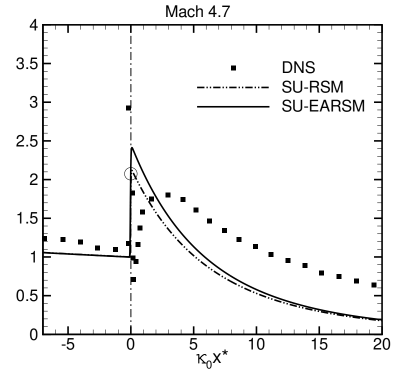

(a) $R_{11}/R_{11,u}$

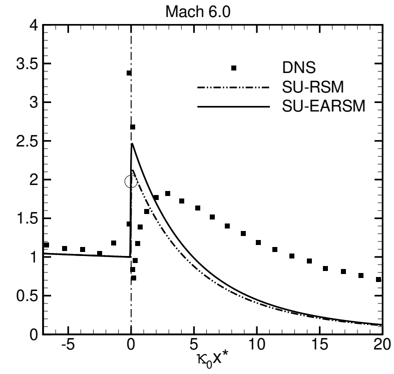

(b) $R_{11}/R_{11,u}$

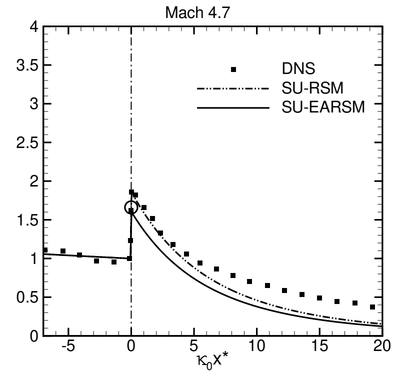

(c) $R_{22}/R_{22,u}$

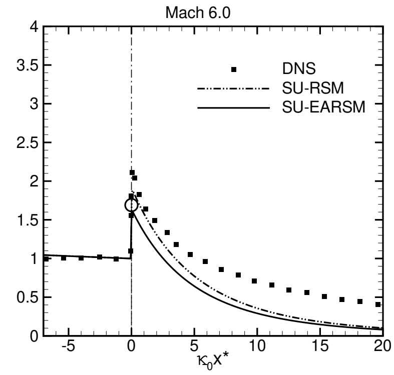

(d) $R_{22}/R_{22,u}$

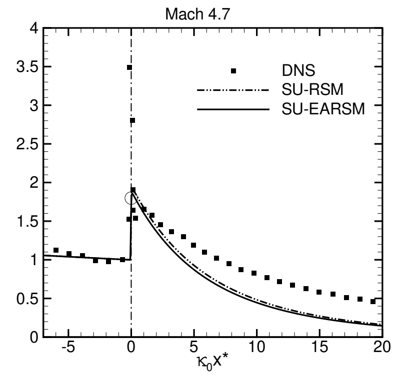

(e) k/k_u

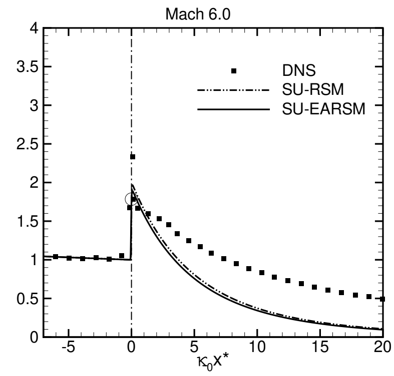

(f) k/k_u

Figure 6.7: Comparison of spatial variation of the R_{11}, R_{22}, and TKE obtained using SU-EARSM with DNS data [9, 10] and SU-RSM for M = 4.7 and 6.0 for shock/turbulence interaction. The open circle at $\kappa_0 x^* = 0$ denote the effective jump in the turbulent quantities at the shock location, shown on the vertical line.

decay rate is determined to a large extent by the model parameter C_{ϵ_1}. The sign change in the percentage error from weaker to stronger shock strength is dependent on model coefficients.

The value of C_{ϵ_1} = 1 + 0.21 M, taken from [74], is used in the current work. An alternate value of C_{ϵ_1} = 1.44 [15] gives a much better comparison with the DNS data. A representative results obtained using SU-EARSM is shown in Fig. (6.8), and it points to potential future improvement of the models.

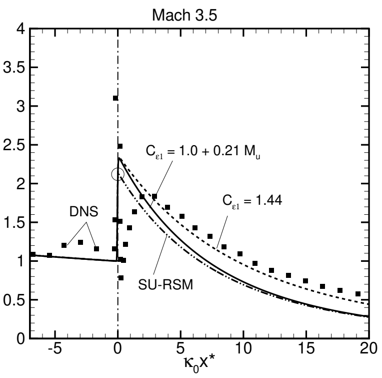

(a) $R_{11}/R_{11,u}$

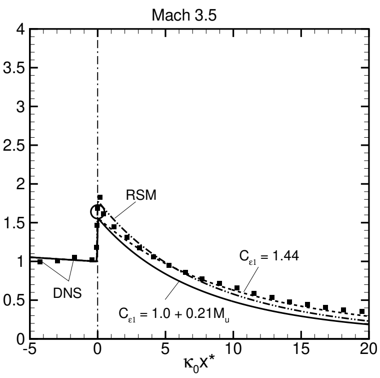

(b) $R_{22}/R_{22,u}$

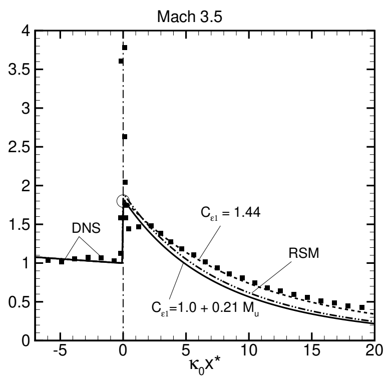

(c) k/k_u

Figure 6.8: Comparison of spatial variation of the R_{11}, R_{22}, and TKE obtained using the SU-EARSM for C_{ϵ_1} = 1.0 + 0.21 M and 1.44, with the DNS data [9, 10] and SU-RSM at M = 3.5 for shock/turbulence interaction. Normalized with the values immediately upstream of the shockwave.

6.4 Summary

The Reynolds stresses in streamwise and transverse directions are amplified differently across the shockwave. Modification, such as shock-unsteadiness correction, has significantly improved in predicting turbulent kinetic energy in two-equation $k - \epsilon$ and $k - \omega$ framework. Still, these models cannot reproduce this shock-induced anisotropy in the Reynolds stresses, as they model the total effect of the amplification in the form of the turbulent kinetic energy.

We evaluated the Wallin and Johansson EARSM model for the canonical STI. The amplification, decaying, and nature of turbulence are obtained by solving the simplified 1D mean flow equations using the Lax-Friedrich numerical method. Across the shockwave, the WJ EARSM based on the $k - \omega$ turbulence model can capture the nature of the anisotropy in Reynolds stresses, but it highly overpredicts.

We linearized the principal Reynolds stress transport equations about the uniform mean flow and investigated the significant terms responsible for the amplification post-shock principal Reynolds stresses through budget analysis. The principal Reynolds stresses are modified based on LIA to capture the anisotropy in turbulence across the shockwave. Further, we adopted a shock unsteadiness correction from Sinha *et al.* [41] to limit the production across the shockwave. The proposed model predicts the post-shock amplification, and the decay of the Reynolds stresses very well for the range of Mach numbers considered in this study.

Chapter 7

Application to shock wave boundary layer interactions

To compute a compressible turbulent flow, one needs to solve the RANS along with the turbulent transport equations. In this chapter, we numerically computed the flow of the oblique shock wave interacting with the turbulent boundary layer using four different turbulence models. The first model is the standard $k - \omega$ model, modified standard $k - \omega$ model based on shock-unsteadiness correction (SU $k - \omega$), and the other two are WJ-EARSM and SU-EARSM based on the standard $k - \omega$ turbulence model. We note that the generalization and application of the SU-RSM turbulence model to SBLI is very cumbersome, therefore we considered only four turbulence models. Computed flow properties such as surface pressure distribution and skin friction coefficient are compared with experiments. In the following sections, we present the RANS equations along with the turbulence models for the sake of completeness, and the numerical method to solve these governing equations. Subsequently, we discuss the flow topology and results generated for the flow with SBLI computed using different turbulence models.

7.1 Reynolds averaged Navier-Stokes equations

Applying the Reynolds averaged approach to the instantaneous Navier-Stokes equations, and with Favre decomposition of the flow variables except for pressure and density, we will get the compressible form of the Reynolds averaged Navier-Stokes equations as follows,

$$\frac{\partial \overline{\rho}}{\partial t} + \frac{\partial (\overline{\rho}\widetilde{u_k})}{\partial x_k} = 0, \tag{7.1}$$

$$\frac{\partial(\overline{\rho}\widetilde{u_i})}{\partial t} + \frac{\partial(\overline{\rho}\widetilde{u_i}\widetilde{u_k})}{\partial x_k} + \frac{\partial(\overline{\rho}R_{ik})}{\partial x_k} = \frac{\partial\overline{p}}{\partial x_i} + \frac{\partial\overline{\tau}_{ik}}{\partial x_k}, \tag{7.2}$$

$$\begin{aligned}\frac{\partial(\overline{\rho}E)}{\partial t} + \frac{\partial(\overline{\rho}H\widetilde{u_k})}{\partial x_k} + \frac{\partial(\overline{\rho}R_{ik}\widetilde{u_i})}{\partial x_k} &= \frac{\partial(\overline{\tau}_{ik}\widetilde{u_i})}{\partial x_k} - \frac{\partial(\overline{q}_k)}{\partial x_k} \\ &+ \frac{\partial}{\partial x_k}\left(\frac{1}{2}\overline{\rho u_i'' u_i'' u_k''} - \overline{u_i''\tau_{ik}} - \overline{\rho h'' u_k''}\right).\end{aligned} \tag{7.3}$$

The unclosed term in the Reynolds averaged governing equations are Reynolds stress tensor R_{ij}, the turbulent diffusive transport $\overline{u_i''\tau_{ik}}$ and $\frac{\overline{\rho u_i'' u_i'' u_k''}}{2}$, and the turbulent heat flux vector $\overline{\rho h'' u_k''}$. Modeling of these unclosed turbulent correlation terms are discussed in chapter 2.

7.2 Turbulence closure

Additionally, two turbulent transport equations are solved apart from conservation equations. The $k-\omega$ turbulence model of Wilcox [15] is a well known and widely tested two-equation eddy viscosity model. We refer to this model as the standard $k-\omega$ model. It demonstrates superior performance for wall-bounded and low Reynolds number flows. The model also gives good agreement with experimental results for mild adverse pressure gradient flows in the logarithmic region of the boundary layer.

7.2.1 Standard $k-\omega$ model

In the $k-\omega$ turbulence model [15], one equation describes the turbulent kinetic energy k, and another equation is for turbulence length scale in terms of ω. The standard $k-\omega$ model is approximated as follows,

$$\overline{\rho}\frac{\partial k}{\partial t} + \overline{\rho}\widetilde{u_j}\frac{\partial k}{\partial x_j} = -\overline{\rho}R_{ij}\frac{\partial\widetilde{u_i}}{\partial x_j} - \beta^*\overline{\rho}k\omega + \frac{\partial}{\partial x_j}\left[(\mu + \frac{\mu_T}{\sigma_k})\frac{\partial k}{\partial x_j}\right], \tag{7.4}$$

$$\overline{\rho}\frac{\partial\omega}{\partial t} + \overline{\rho}\widetilde{u_j}\frac{\partial\omega}{\partial x_j} = -\alpha\frac{\omega}{k}\overline{\rho}R_{ij}\frac{\partial\widetilde{u_i}}{\partial x_j} - \beta\overline{\rho}\omega^2 + \frac{\partial}{\partial x_j}\left[(\mu + \frac{\mu_T}{\sigma})\frac{\partial k}{\partial x_j}\right], \tag{7.5}$$

where α , β , and β^* are the closure coefficients: $\alpha = \frac{5}{9}, \beta = \frac{3}{40}, \beta^* = \frac{9}{100}, \sigma = 2$, and $\sigma_k = 1$ (see chapter 2 for details).

7.2.2 EARSM based on standard $k-\omega$ model

In the eddy-viscosity model, such as in the standard $k-\omega$ model [15], the Reynolds stress tensor is obtained from

$$\overline{\rho}R_{ij} = \frac{2}{3}\overline{\rho}k\delta_{ij} - 2\mu_T S^*_{ij}, \tag{7.6}$$

with

$$\mu_t = \frac{\overline{\rho}k}{\omega},\ S^*_{ij} = \frac{1}{2}\left[\frac{\partial\widetilde{u}_i}{\partial x_j} + \frac{\partial\widetilde{u}_j}{\partial x_i} - \frac{2}{3}\frac{\partial\widetilde{u}_k}{\partial x_k}\delta_{ij}\right],\ \text{and}\ \Omega^*_{ij} = \frac{1}{2}\left[\frac{\partial\widetilde{u}_i}{\partial x_j} - \frac{\partial\widetilde{u}_j}{\partial x_i}\right].$$

In EARSM, Reynolds stress tensor is expressed in terms of effective turbulent viscosity and an extra anisotropy.

$$\overline{\rho}R_{ij} = \frac{2}{3}\overline{\rho}k\delta_{ij} - 2\mu'_T S^*_{ij} + \overline{\rho}ka^{ext}_{ij} \tag{7.7}$$

where

$$\mu'_T = -\frac{1}{2}\beta_1\overline{\rho}k\tau,\ \text{and}\ a^{ext}_{ij} = \beta_4(S_{ik}\Omega_{kj} - \Omega_{ik}S_{kj}) \tag{7.8}$$

Here,

$$S_{ij} = \tau S^*_{ij},\ \Omega_{ij} = \tau\Omega^*_{ij},\ \text{and}\ \tau = max\left(\frac{1}{\beta^*\omega}, 6.0\sqrt{\frac{\mu}{\beta^*\overline{\rho}\omega k}}\right) \tag{7.9}$$

More details of the WJ-EARSM formulation are provided in the chapters 2 & 5.

7.3 Numerical method

The RANS equations govern the flow features of any turbulent fluid flow. The exact analytical solutions of these equations are difficult to obtain and become more complicated for flows such as shockwave/turbulent boundary-layer interactions. We can discretize these partial differential equations into a system of algebraic equations employing different discretization methods available like finite difference, finite element, and finite volume [112]. In this chapter, we restrict ourselves to the finite volume technique [112–114, 116]. We use RANS equations for solving the high-speed supersonic flows. The terms in these equations are viewed in three categories: the inviscid or convective terms, the viscous terms, and the source terms.

The shockwave/boundary-layer interaction flow includes high-pressure gradient regions, separation bubble, shock-waves, expansion waves, shear-layer, boundary-layer flow separation point, and reattachment point. Using appropriate CFD techniques, all these physical features in the flowfield can be captured. For shock dominated flows at a steady-state solution, both the hyperbolic and elliptic nature of the equations dominate the flowfield; the convective (hyperbolic) terms dominate in the inviscid flow region, and the diffusive (elliptic) terms dominate in the boundary layer and separated flow regions. In a separation bubble, the flowfield information passes in all the directions, and the flow possesses elliptic nature in this confined region. The central difference scheme can be used to discretize the viscous/diffusive terms.

A finite volume formulation is used to discretize the governing mean flow equations fully coupled with turbulence model equations. The inviscid fluxes are solved using a modified, low-dissipation form of the Steger-Warming flux splitting method [116]. This method reduces the numerical dissipation, which is very useful for high speed flows with strong shock waves and viscous-inviscid interactions with boundary layers. As a result, very thin and well-defined shock waves are captured over minimal grid cells. The discretization method is second-order accurate in space. The viscous fluxes and the turbulent source terms are calculated using a second-order accurate central difference method. The implicit Data-Parallel Line Relaxation (DPLR) method of Wright *et al.* [117] is used to integrate the equations in time to reach a steady-state solution.

In the following, we briefly discuss the finite volume formulation and flux-vector splitting scheme of Steger - Warming [111] and modified Steger - Warming [116] for solving RANS equations using the $k-\omega$ turbulence model for a perfect gas.

Conservation form

We used an in-house CFD code capable of parallel computing, and it has been well validated for several high-speed applications. It solves two - dimensional RANS equations along with the $k-\omega$ model to calculate the turbulent eddy viscosity. A total of six equations are solved simultaneously to obtain six conservative variables $\overline{\rho}, \overline{\rho}\widetilde{u}, \overline{\rho}\widetilde{v}, \overline{\rho}\widetilde{E}, \overline{\rho}k, \overline{\rho}\omega$. Here $\widetilde{E}$ is the total mean flow energy. From these conservative variables, the six primitive mean flow quantities are calculated as, streamwise velocity $\widetilde{u}$, wall-normal velocity $\widetilde{v}$, density $\overline{\rho}$, temperature $\widetilde{T}$, TKE k and the specific dissipation rate of turbulent kinetic energy ω. The mean pressure $\overline{p}$ is obtained from the perfect gas equation. The two-dimensional RANS system of equations can be written in conservation form as,

$$\frac{\partial U}{\partial t} + \nabla.\left(\vec{F} + \vec{G}\right) = Q, \tag{7.10}$$

where U is the set of conservative variable, $\vec{F}$ is the flux vector in the streamwise direction, $\vec{G}$ is the flux vector in flow normal direction, and Q is the source term. The total fluxes are split into the inviscid and viscous part. The subscripts I and V represent the inviscid and viscous terms.

$$\frac{\partial U}{\partial t} + \nabla.\left(F + G\right) = Q, \tag{7.11}$$

where

$$F = F_I - F_V; \qquad G = G_I - G_V; \tag{7.12}$$

and

$$U = \begin{bmatrix} \overline{\rho} & \overline{\rho}\widetilde{u} & \overline{\rho}\widetilde{v} & \overline{\rho}\widetilde{E} & \overline{\rho}k & \overline{\rho}\omega \end{bmatrix}^{\mathrm{T}}, \tag{7.13}$$

here superscript T stands for the transpose of the matrix.

$$F_I = \begin{bmatrix} \overline{\rho}\widetilde{u} \\ \overline{\rho}\widetilde{u}^2 + \overline{p} + \frac{2}{3}\overline{\rho}k \\ \overline{\rho}\widetilde{u}\widetilde{v} \\ \left(\overline{\rho}\widetilde{E} + \overline{p} + \frac{2}{3}\overline{\rho}k\right)\widetilde{u} \\ \overline{\rho}\widetilde{u}k \\ \overline{\rho}\widetilde{u}\omega \end{bmatrix}; \qquad G_I = \begin{bmatrix} \overline{\rho}\widetilde{v} \\ \overline{\rho}\widetilde{u}\widetilde{v} \\ \overline{\rho}\widetilde{v}^2 + \overline{p} + \frac{2}{3}\overline{\rho}k \\ \left(\overline{\rho}\widetilde{E} + \overline{p} + \frac{2}{3}\overline{\rho}k\right)\widetilde{v} \\ \overline{\rho}\widetilde{v}k \\ \overline{\rho}\widetilde{v}\omega \end{bmatrix} \tag{7.14}$$

$$F_V = \begin{bmatrix} 0 \\ \overline{\tau}_{xx} + \overline{\rho}R_{xx} \\ \overline{\tau}_{xy} + \overline{\rho}R_{xy} \\ (\overline{\tau}_{xx} + \overline{\rho}R_{xx})\widetilde{u} + \left(\overline{\tau}_{xy} + \overline{\rho}R_{xy}\right)\widetilde{v} + (\kappa + \kappa_T)\frac{\partial \widetilde{T}}{\partial x} + \left(\mu + \frac{\mu_T}{\sigma_k}\right)\frac{\partial k}{\partial x} \\ \left(\mu + \frac{\mu_T}{\sigma_k}\right)\frac{\partial k}{\partial x} \\ \left(\mu + \frac{\mu_T}{\sigma}\right)\frac{\partial \omega}{\partial x} \end{bmatrix} \tag{7.15}$$

$$G_V = \begin{bmatrix} 0 \\ \overline{\tau}_{xy} + \overline{\rho}R_{xy} \\ \overline{\tau}_{yy} + \overline{\rho}R_{yy} \\ \left(\overline{\tau}_{xy} + \overline{\rho}R_{xy}\right)\widetilde{u} + \left(\overline{\tau}_{yy} + \overline{\rho}R_{yy}\right)\widetilde{v} + (\kappa + \kappa_T)\frac{\partial \widetilde{T}}{\partial y} + \left(\mu + \frac{\mu_T}{\sigma_k}\right)\frac{\partial k}{\partial y} \\ \left(\mu + \frac{\mu_T}{\sigma_k}\right)\frac{\partial k}{\partial y} \\ \left(\mu + \frac{\mu_T}{\sigma}\right)\frac{\partial \omega}{\partial y} \end{bmatrix} \tag{7.16}$$

$$Q = \begin{bmatrix} 0 & 0 & 0 & 0 & (P_k - \beta^* \overline{\rho} k\omega) & \left(\alpha\frac{\omega}{k}P_k - \beta\overline{\rho}\omega^2\right) \end{bmatrix}^T \tag{7.17}$$

Here $\overline{\rho}$ is the mean density of the fluid, $\overline{\tau}_{xx}$, $\overline{\tau}_{xy}$, $\overline{\tau}_{yy}$ are the mean viscous stresses acting on fluid particles, R_{xx}, R_{xy}, R_{yy} are the Reynolds stresses, P_k represents the production term of the turbulent kinetic energy. The conservation Eq. (7.10) is integrated over the control volume (see Fig. (7.1)) to give:

$$\frac{\partial}{\partial t}\iiint_{CV} U\,dV + \iint_{CS}\left[\left(\vec{F}_I + \vec{G}_I\right) + \left(\vec{F}_V + \vec{G}_V\right)\right].(\hat{n}dS) = Q \tag{7.18}$$

$$\frac{\partial U}{\partial t} = -\frac{1}{V_{i,j}}\left[\vec{F}_{i+1/2,j}.\vec{S}_{i+1/2,j} + \vec{F}_{i-1/2,j}.\vec{S}_{i-1/2,j} + \vec{G}_{i,j+1/2}.\vec{S}_{i,j+1/2} + \vec{G}_{i,j-1/2}.\vec{S}_{i,j-1/2}\right] + Q, \tag{7.19}$$

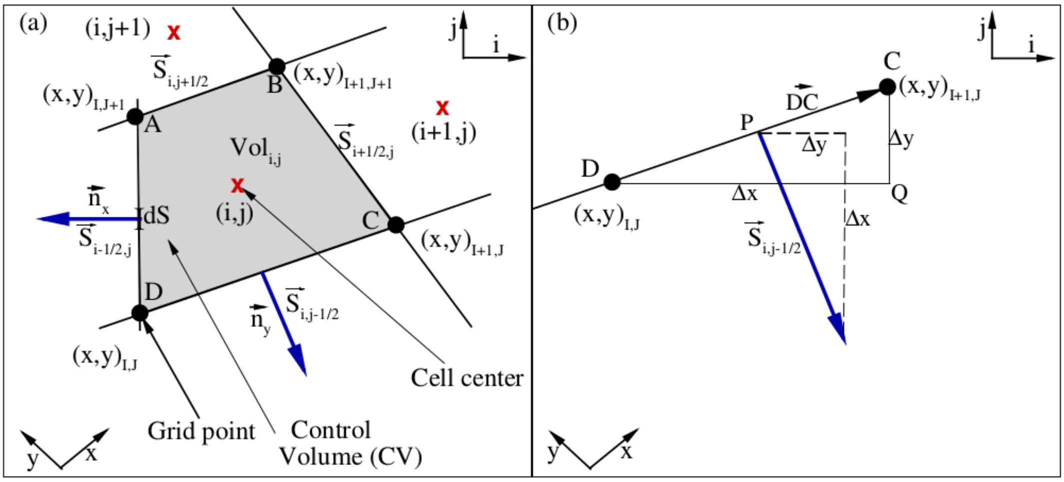

Figure 7.1: (a) Two-dimensional control volume used in finite volume formulation, where the grid points are represented by black solid circles with capital indices of I and J and cell centers are shown by crosses represented by small indices of i and j and (b) Calculation of normal surface vector $\vec{S}_{i,j-1/2}$ [115].

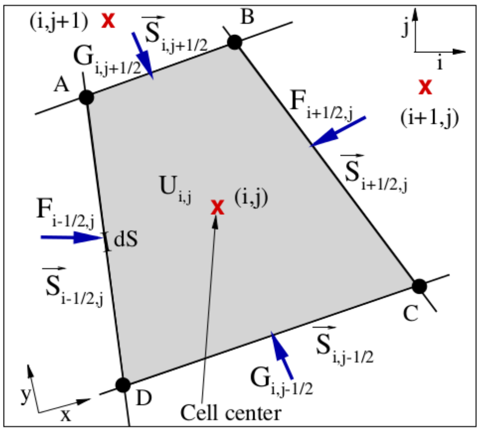

Figure 7.2: The conservative variable $U_{i,j}$ at cell center calculated from the fluxes F and G passing through the cell boundaries in the x-and y-directions [115].

where

$$\begin{aligned}\vec{S}_{i+1/2,j} &= \left(y_{i+1,j+1} - y_{i+1,j}\right)\hat{i} - \left(x_{i+1,j+1} - x_{i+1,j}\right)\hat{j}\\ \vec{S}_{i-1/2,j} &= -\left(y_{i,j+1} - y_{i,j}\right)\hat{i} + \left(x_{i,j+1} - x_{i,j}\right)\hat{j},\end{aligned} \tag{7.20}$$

and

$$\begin{aligned}V_{i,j} = [|&\left(x_{i,j} - x_{i+1,j}\right)y_{i+1,j+1} + \left(x_{i+1,j} - x_{i+1,j+1}\right)y_{i,j} + \left(x_{i+1,j} - x_{i,j}\right)y_{i+1,j}|\\ &+ |\left(x_{i,j} - x_{i+1,j+1}\right)y_{i,j+1} + \left(x_{i+1,j+1} - x_{i,j+1}\right)y_{i,j} + \left(x_{i,j+1} - x_{i,j}\right)y_{i+1,j+1}|]\end{aligned} \tag{7.21}$$

Here $\hat{n}$ is unit normal vector to surface area dS as shown in Fig. (7.1) and $\vec{S}_{i+1/2,j}$, $\vec{S}_{i-1/2,j}$ are the surface area vectors and $\hat{i}$, $\hat{j}$ are unit vectors in i and j direction respectively. x

and y are the coordinates of the grid points and $V_{i,j}$ is the control volume. The calculation of $\vec{S}_{i,j-1/2}$ is explained in Fig. (7.1b). The vector $\vec{DC} = \left(x_{i+1,j} - x_{i,j}\right)\hat{i} + \left(y_{i,j+1} - y_{i,j}\right)\hat{j}$. Hence the normal vector is evaluated as $\vec{S}_{i,j-1/2} = \left(y_{i,j+1} - y_{i,j}\right)\hat{i} - \left(x_{i+1,j} - x_{i,j}\right)\hat{j}$. The normal vector $\vec{S}_{i,j+1/2}$ is calculated in a similar way. The numerical methodology is the same approach used in Ref.[115].

7.3.1 Steger-Warming method

The Steger - Warming method [111] is used for high-speed inviscid flows to capture shock waves by taking advantage of the hyperbolic nature of the Euler equations. The essential requirement for hyperbolic flow is that the eigenvalues should be real, distinct, and positive [114]. The upwind schemes use the local wave propagation information, and the eigenvalues provide the direction of the information in the flowfield. Spatial differencing is done on the mesh points, towards the side of which the information flows. To demonstrate the Steger - Warming method [111], we take the case of one-dimensional Euler equations for simplicity. The same methodology can be extended to the two- and three-dimensional flows.

$$U = \begin{bmatrix} \overline{\rho} \\ \overline{\rho}\widetilde{u} \\ E \end{bmatrix} = \begin{bmatrix} U_1 \\ U_2 \\ U_3 \end{bmatrix}, \tag{7.22}$$

$$F_I = \begin{bmatrix} \overline{\rho}\widetilde{u} \\ \left(\overline{\rho}\widetilde{u}^2 + \overline{p}\right) \\ \left(E\widetilde{u} + \overline{p}\widetilde{u}\right) \end{bmatrix} = \begin{bmatrix} F_1 \\ F_2 \\ F_3 \end{bmatrix}, \tag{7.23}$$

where U is the conserved variables vector, $E = \overline{\rho}e + \frac{1}{2}\overline{\rho}\widetilde{u}^2$ is the total energy and $e = c_v\widetilde{T}$ is the internal energy. The flux vector is function of the conservative variable vector and is evaluated as,

$$[F] = [A]\,[U] \tag{7.24}$$

The Jacobian matrix, A is calculated by taking the partial derivative of the flux-vector with respect to the vector of conserved variables.

$$A = \begin{bmatrix} \frac{\partial F_1}{\partial U_1} & \frac{\partial F_1}{\partial U_2} & \frac{\partial F_1}{\partial U_3} \\ \frac{\partial F_2}{\partial U_1} & \frac{\partial F_2}{\partial U_2} & \frac{\partial F_2}{\partial U_3} \\ \frac{\partial F_3}{\partial U_1} & \frac{\partial F_3}{\partial U_2} & \frac{\partial F_3}{\partial U_3} \end{bmatrix} = \begin{bmatrix} 0 & 1 & 0 \\ (\gamma-3)\widetilde{u}^2/2 & (3-\gamma)\widetilde{u} & (\gamma-1) \\ (\gamma-1)\widetilde{u}^3 - \gamma e\widetilde{u}/\overline{\rho} & \gamma e/\overline{\rho} - 3(\gamma-1)\widetilde{u}^2/2 & \gamma\widetilde{u} \end{bmatrix} \tag{7.25}$$

With this Jacobian matrix we write the characteristic equation to find the eigen values as

$$det\,[A - \lambda I] = 0, \tag{7.26}$$

where I is the identity matrix. The three eigen values of the above matrix are

$$\Lambda = \begin{bmatrix} \widetilde{u} & 0 & 0 \\ 0 & \widetilde{u} + a & 0 \\ 0 & 0 & \widetilde{u} - a \end{bmatrix} \tag{7.27}$$

Here $\widetilde{u}$ is speed of the flow and a corresponds to the speed of the sound. The corresponding left eigen vector matrix and right eigen vector matrix is evaluated as T^{+} and T^{-}. For each eigen value the corresponding eigen vectors are calculated as,

$$[A]\left[r_1^1 r_1^2 r_1^3\right] = \lambda_1 \left[r_1^1 r_1^2 r_1^3\right]^{\mathrm{T}} \tag{7.28}$$

$$[A]\left[r_2^1 r_2^2 r_2^3\right] = \lambda_2 \left[r_2^1 r_2^2 r_2^3\right]^{\mathrm{T}} \tag{7.29}$$

$$[A]\left[r_3^1 r_3^2 r_3^3\right] = \lambda_3 \left[r_3^1 r_3^2 r_3^3\right]^{\mathrm{T}} \tag{7.30}$$

Each of the these single column 1×3 matrix of eigen vectors are arranged in three columns of a 3×3 square matrix to form a right eigen vector matrix T as given by Eqs. 7.31.

$$[T] = \left[|r_{\mathrm{k}}^{p}||r_{\mathrm{k}}^{p}||r_{\mathrm{k}}^{p}|\right] \tag{7.31}$$

Here r is a 1×3 single column eigen vector with $p = (1, 2, 3)$ and $\mathrm{k} = (1, 2, 3)$. $|r_{\mathrm{k}}^{p}|$ corresponds to the right eigen vector single column matrix formed by calculating the three eigen vectors in Eqs. 7.30, for corresponding eigenvalues. The left eigen vector matrix is calculated by taking the inverse matrix of the right vector matrix. Using T^{+} and T^{-}, we calculate two Jacobian matrices containing positive and negative eigenvalues, such that the diagonal matrix Λ_{+} contains only positive eigenvalues and a diagonal matrix Λ_{-} has only negative eigenvalues [115].

$$A = A_{+} + A_{-} \tag{7.32}$$

$$\lambda_k = \lambda_{k+} + \lambda_{k-} \tag{7.33}$$

$$\lambda_{k+} = \frac{\lambda_k + |\lambda_k|}{2} \tag{7.34}$$

$$\lambda_{k-} = \frac{\lambda_k - |\lambda_k|}{2} \tag{7.35}$$

$$\Lambda = \Lambda_{+} + \Lambda_{-} \tag{7.36}$$

$$\Lambda_+ = diag\left(\frac{\lambda_k + |\lambda_k|}{2}, \frac{\lambda_k + |\lambda_k|}{2}, \frac{\lambda_k + |\lambda_k|}{2}\right) \tag{7.37}$$

$$\Lambda_- = diag\left(\frac{\lambda_k - |\lambda_k|}{2}, \frac{\lambda_k - |\lambda_k|}{2}, \frac{\lambda_k - |\lambda_k|}{2}\right) \tag{7.38}$$

$$A_+ = T^+\Lambda_+T^-; \quad A_- = T^+\Lambda_-T^- \tag{7.39}$$

The information in the flowfield can come from an upstream or downstream direction. Depending on it, the discretization is done to the fluxes. In a control volume, as shown in Fig. (7.3), the fluxes are calculated at the cell faces and the values of conservative variables at the cell center. According to the Jacobians' sign as positive and negative parts, the fluxes are split into

$$F = F_+ + F_- \tag{7.40}$$

$$F_+ = F_+U \quad F_- = F_-U \tag{7.41}$$

The above fluxes are evaluated for subsonic flows. For supersonic flows, the information moves in a downstream direction, and no information influences the upstream direction flowfield. Hence for supersonic flows $F_+ = F$ and $F_- = 0$.

The first order fluxes are given as

$$F_{+_i} = A_{+i}U_i, \tag{7.42}$$

$$F_{-_{i+1}} = A_{-_{i+1}}U_{i+1}. \tag{7.43}$$

For the hyperbolic nature of the Euler equations, the eigenvalues are real and distinct. In the Steger-Warming method [111], the modification is made to the eigenvalues when they become either zero or one. This can happen when the flow becomes sonic for local Mach = 1 or stagnant for M = 0 in some regions. One of the examples in the regions at blunt-nosed of the vehicle. Therefore, the eigenvalues are corrected (λ) with a small value of a constant, $\epsilon = 0.3$.

$$\widetilde{\lambda}_\pm = \lambda_\pm \pm \sqrt{\lambda_\pm + \epsilon^2 a^2} \tag{7.44}$$

The high-quality solutions of undisturbed supersonic boundary-layers are obtained by setting $\epsilon = 0$, and the original eigenvalues are restored from this modified eigenvalue.

7.3.2 Modified Steger-Warming method

The Steger-Warming method [111], when applied to the viscous flows, results in large numerical dissipation [116] across the boundary-layer. Also, it creates a fictitious pressure gradient, which causes unrealistic convection within the layer. It has similar problems across free shear-layers. MacCormack and Candler [116] modified the Steger-Warming method [111] to reduce the excessive numerical mixing in the boundary layer and free shear-layer flows. In the Steger-Warming method [111], the evaluation of Jacobians at the cell centers results in excessive numerical dissipation in the boundary-layer. In the modified Steger-Warming method [116] the Jacobians are modified and are calculated at cell-interfaces (see Fig. (7.3)), and from these values, the first order fluxes were calculated as given by Eq. 7.45

$$\begin{aligned} F_{+_i} &= A_{+_{i+1/2}} U_i \\ F_{-i+1} &= A_{-_{i+1/2}} U_{i+1} \\ A_{\pm_{i+1/2}} &= A_{\pm}\left[\frac{1}{2}\left(U_i + U_{i+1}\right)\right] \end{aligned} \tag{7.45}$$

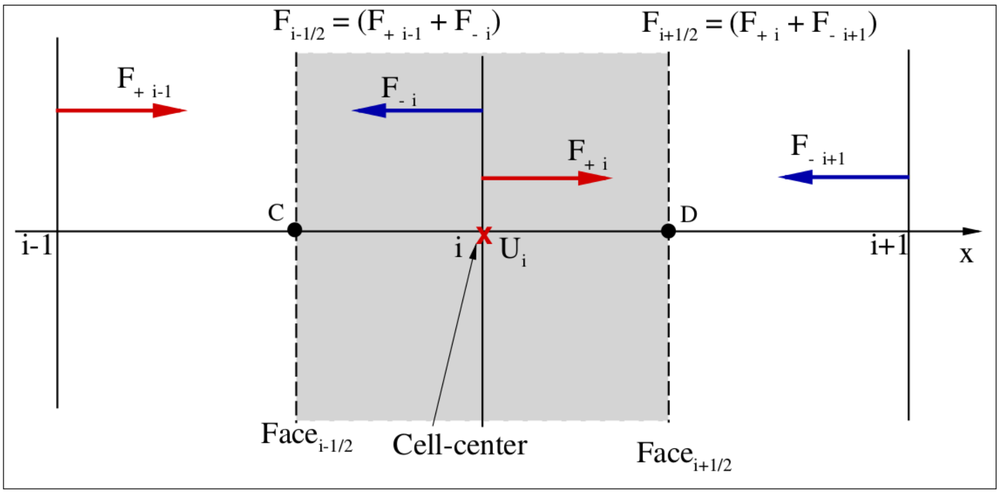

Figure 7.3: Physical interpretation for evaluation of conservative variable at cell-center, using fluxes at cell-interfaces, for the first-order method (reproduced from Hirsch [113]).

7.3.3 Time integration

The explicit time integration is carried out by

$$U_i^{n+1} = U_i^n - \frac{\Delta t}{\Delta x}\left[\left(F_{i+1/2} - F_{i-1/2}\right)\right]^n, \tag{7.46}$$

$$U_i^{n+1} = U_i^n - \frac{\Delta t}{\Delta x}\left[\left(F_{+_i} + F_{-i+1}\right) - \left(F_{+_{i-1}} + F_{-i}\right)\right]^n, \tag{7.47}$$

$$U_i^{n+1} = U_i^n - \frac{\Delta t}{\Delta x}\left[\left(F_{+_i} - F_{+i-1}\right) + \left(F_{-_{i+1}} - F_{-i}\right)\right]^n, \tag{7.48}$$

The one-dimensional Euler equation is solved using the explicit method as in Eq. 7.47, where the forward differencing is used. In this explicit formulation, the conservative variables at time step $n + 1$ are evaluated as U_i^{n+1} from the known conservative variables U_i^n and fluxes at time step n, and the solution is marched in time to obtain a steady-state solution. Here, n represents the previous time step and $n + 1$ represents the updated or new time step. The only unknown term is U_i^{n+1} and is calculated explicitly in the known terms on RHS; hence the name explicit method is coined to this approach.

Fig. (7.3) shows the physical interpretation for evaluating the fluxes with the first-order scheme of Eq. (7.48). The positive and negative fluxes in Fig. (7.3) are attached to the characteristics of positive and signs (eigenvalues). To evaluate the conservative variable at cell center the fluxes are evaluated at cell faces $i + 1/2$ and $i - 1/2$. Fig. (7.3) shows that the flux at interface $F_{i+1/2}$, at D is calculated from the positive flux vector F_{+_i} coming from left hand side and negative flux vector $F_{-_{i+1}}$ coming from right hand side of U_i. Similarly, the flux at interface $F_{i-1/2}$, at C is evaluated. Both of these fluxes, $F_{i+1/2}$ and $F_{i-1/2}$ contribute to the conservative variable U_i at cell center. Fig. (7.3) shows that for an upwind direction of positive fluxes, the backward difference method is used, and for negative fluxes of downwind direction, the forward difference method is used (see Eq. (7.48).). Hence the discretization of the fluxes is done on the side of wind flow (information).

Stability analysis had been carried by Steger and Warming method [111] for one-dimensional Euler equations using Von-Neumann stability condition [113]. In this analysis, the Jacobian matrix is frozen, and decoupling is done to system of simple advection equations. The Fourier analysis is done by assuming the solution in the form of waves and satisfying the condition of the ratio of amplification of solution error to be less than 1. It is shown that taking the only positive direction of eigenvalues in the upwind scheme resulted in instability. From stability analysis, the Courant-Friedrichs-Lewy (CFL) number is restricted to less than 1 in the explicit method, due to which only small time steps can be taken while solving the flow.

7.3.4 Second order flux evaluation

Second order Steger-Warming method [111]

The first-order upwind schemes are less accurate as they contain less number of points in a stencil. They are more dissipative and do not give any oscillations across the high gradient regions, such as shock waves. The second-order central differencing schemes are more accurate than first-order upwind schemes and are less dissipative, but they are unstable across the shock waves. The second-order upwind schemes possess less numerical dissipation than the first-order upwind schemes and are more accurate because of more points in the cell face. By increasing the number of points minute details of flow, physics can be accurately captured by the numerical method.

$$\begin{aligned} F_{+_i} &= A_{+_i} U^L_{i+1/2} \\ F_{-_{i+1}} &= A_{-_{i+1}} U^R_{i+1/2} \end{aligned} \tag{7.49}$$

$$\begin{aligned} U^L_{i+1/2} &= \frac{3}{2}U_i - \frac{1}{2}U_{i-1} \\ U^R_{i+1/2} &= \frac{3}{2}U_{i+1} - \frac{1}{2}U_{i+2} \end{aligned} \tag{7.50}$$

Second order modified Steger-Warming method [116]

$$\begin{aligned} F_{+_i} &= A_{+_{i+1/2}} U^L_{i+1/2} \\ F_{-_{i+1}} &= A_{-_{i+1/2}} U^R_{i+1/2} \end{aligned} \tag{7.51}$$

$$\begin{aligned} U^L_{i+1/2} &= \frac{3}{2}U_i - \frac{1}{2}U_{i-1} \\ U^R_{i+1/2} &= \frac{3}{2}U_{i+1} - \frac{1}{2}U_{i+2} \end{aligned} \tag{7.52}$$

Here U_L and U_R correspond to the left and right states. Fig. (7.4) gives the physical interpretation for evaluating the fluxes using a second-order scheme. The fluxes are extrapolated [113] to the interfaces defining the flux equal to the numerical scheme. Here, the flux is evaluated by summing up the first-order and second-order fluxes from the left and right states of the cell interface $i + 1/2$, as shown in Fig. (7.4). The second-order

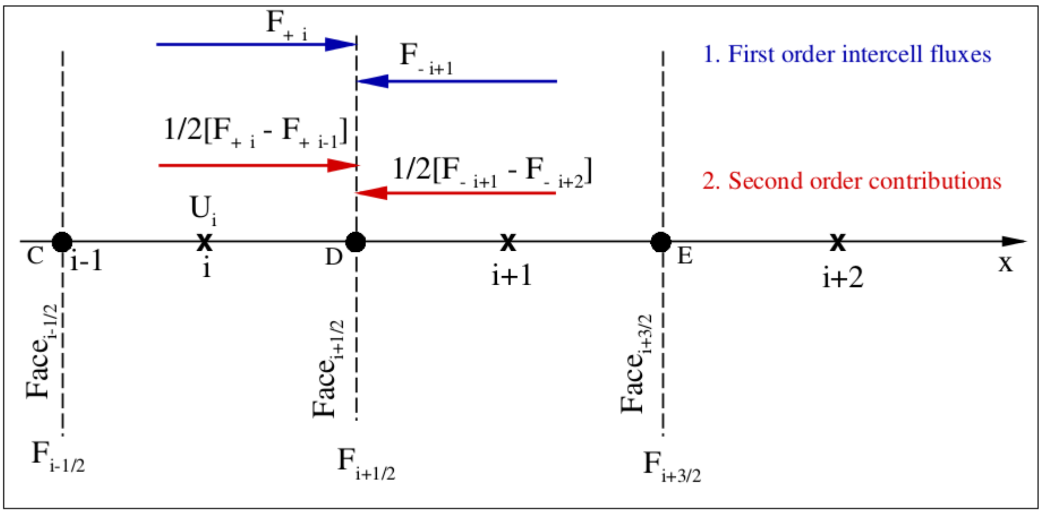

Figure 7.4: Physical interpretation for evaluation of fluxes for the second-order method (reproduced from Hirsch [113]).

schemes give spurious non-physical oscillations across high gradients regions, such as shockwaves. Flux limiters are used to avoid these spurious oscillations and to limit the spatial derivatives to physically realistic values. Moreover, the modified Steger-Warming method [116] gives less dissipation in the boundary-layers and result in oscillations in the high gradient regions such as shockwaves. In contrast, the standard Steger-Warming gives more numerical dissipation in the boundary-layers and is stable across the shockwaves. To take advantage of both the methods, a hybrid scheme is used to evaluate the fluxes, and the pressure limiter [118] is used to switch from a modified Steger-Warming scheme to the standard Steger-Warming scheme across the shockwaves. When the pressure gradient is more than 50% across the shockwaves, the scheme is reverted to the Steger-Warming method of first-order, and when the pressure gradient is less, the scheme is reverted to modified Steger-Warming method in the boundary-layer regions. The pressure jump across high gradients is detected with the use of pressure limiter [118]. For smooth gradient regions, these flux limiters are not active.

7.3.5 Boundary conditions

Computational domain with different boundary conditions for supersonic flow over flat-plate is shown in Fig. (7.5). Here, $mx \times my$ are the total number of cells, where mx and my are the number of cells in flow-parallel direction and flow-normal direction, respectively. Dashed-lines represent the dummy cells, and circles mark their cell centers. Solid-lines represent the inner cells, and cross marks their cell centers. Dummy cells serve to calculate the fluxes at the cell faces of inner cells along the boundaries, as shown in Fig. (7.5). Dummy cells are used to impose boundary conditions. Dummy cells are assigned appropriate values to obtain the required flow condition at the boundaries. We refer to the dummy cell as the 1^{st} cell and the interior cell adjacent to the boundary as 2^{nd} cell.

The viscous boundary condition (no-slip condition) is achieved by setting an opposite sign condition to the velocity value taken from the 2^{nd} cell, so the wall velocity to be zero. For isothermal boundary condition, the temperature at the 2^{nd} cell is extrapolated to the 1^{st} cell, such that the wall will have a specified and constant temperature. For the inviscid boundary condition, we calculate the wall-normal velocity component at the 2^{nd} cell and put the value at the dummy cell so that this wall-normal component becomes zero. The symmetry boundary condition is similar with an added clause that the gradients of all the variables should be zero. In Fig. (7.5), the extrapolation boundary condition at the exit plane means that the mass flux should be balanced, and the diffusion fluxes for all the variables should be zero. By which the dummy cells do not affect the interior flowfield. For the inlet boundary, the dummy cell values are always set to freestream values.

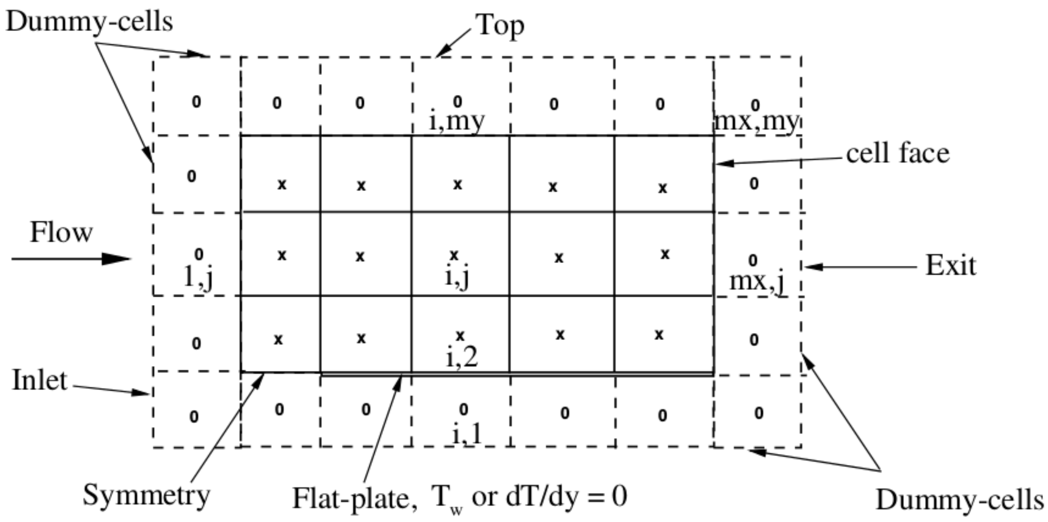

Figure 7.5: Computational domain along with boundary conditions for a flat plate configuration.

The free stream and wall boundary conditions for $k - \omega$ turbulence model are stated below with subscript ∞ and w representing the freestream and wall conditions: $\omega_\infty = (10\widetilde{u}_\infty)/L$ and $k_\infty = 0.01\nu_\infty\omega_\infty$ and $\omega \to 6\nu_w/(\beta y^2)$ as $y \to 0$; $\omega_w = 106\nu_w/(\beta_1 \Delta y_1^2)$ as $y \to 0$; for $\Delta y_1^+ < 3$ (for smooth wall), where Δy_1 is the normal distance to the next point nearest from the wall, $\beta_1 = 3/40$ and L is the length of the domain.

Inlet

The free-stream conditions are assigned at $i = 1$ with j varying from 1 to my.

$$u(1, j) = V_\infty, \quad (7.53)$$

$$\rho(1, j) = \rho_\infty, \quad (7.54)$$

$$v(1, j) = 0, \quad (7.55)$$

$$T(1, j) = T_\infty. \quad (7.56)$$

Top

The free-stream conditions are assigned at top boundary at $j = my$ with i varying from 2 to (mx-1).

Symmetry

The symmetry conditions are assigned at $j = 1$ and $i = 2$. The variables are mirrored over symmetry boundary.

$$u(2,1) = u(2,2), \tag{7.57}$$

$$v(2,1) = -v(2,2), \tag{7.58}$$

$$\rho(2,1) = \rho(2,2), \tag{7.59}$$

$$T(2,1) = T(2,2). \tag{7.60}$$

Wall

The physical boundary conditions applied at stationary flat-plate for the viscous flow are,

$$\vec{v} = 0, \quad \text{no slip condition} \tag{7.61}$$

$$\partial P/\partial n, \quad \text{constant pressure boundary layer} \tag{7.62}$$

$$T_w = constant, \quad \text{isothermal wall} \tag{7.63}$$

$$\partial T/\partial n, \quad \text{adiabatic wall} \tag{7.64}$$

Here, $\vec{v}$ is the velocity vector with components u and v and n is the normal direction to wall. The above conditions are applied numerically at $j = 1$ with i varying from 3 to mx. The density is calculated using the equation of state.

$$u(i,1) = -u(i,2), \tag{7.65}$$

$$v(i,1) = -v(i,2), \tag{7.66}$$

$$\rho(i,1) = \rho(i,2)T(i,2)/T(i,1), \tag{7.67}$$

$$T(i,1) = 2T_w - T(i,2), \tag{7.68}$$

$$T(i,1) = T(i,2) \tag{7.69}$$

Exit

At the exit, the supersonic extrapolation condition is applied where the computed flow variable values are extrapolated from inner cells with $i = mx$ and j varying from 2 to my.

$$u(mx,j) = u(mx-1,j), \tag{7.70}$$

$$v(mx,j) = v(mx-1,j), \tag{7.71}$$

$$\rho(mx,j) = \rho(mx-1,j), \tag{7.72}$$

$$T(mx,j) = T(mx-1,j) \tag{7.73}$$

7.4 Verification of implementation and validation of turbulence model

Flat Plate at Zero Pressure Gradient

This section verified and validated the WJ-EARSM turbulence model for the zero pressure gradient boundary layer on a flat plate. A real developing zero pressure gradient boundary layer is computed accurately using the WJ-EARSM model and compared with the experimental data [14] available in the literature. Schulein *et al.* [14] conducted the experiments for SBLI in the DLR Gottingen Ludwig tube wind tunnel at nominal Mach number 5.0 with a wall temperature of 300K, the static temperature of 68.3 K, and Reynolds number based on a unit length of 3.67×10^7. Here verification refers to the objective that a turbulence model, here the WJ-EARSM, is implemented correctly (i.e., according to the specified model equations, including boundary conditions). The WJ-EARSM model has been implemented into our in-house code, which solves the compressible RANS equations and the respective turbulence equations, such as k and ω.

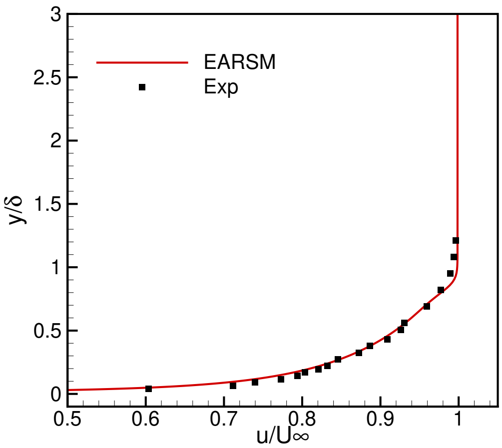

(a) δ = 3.842 mm

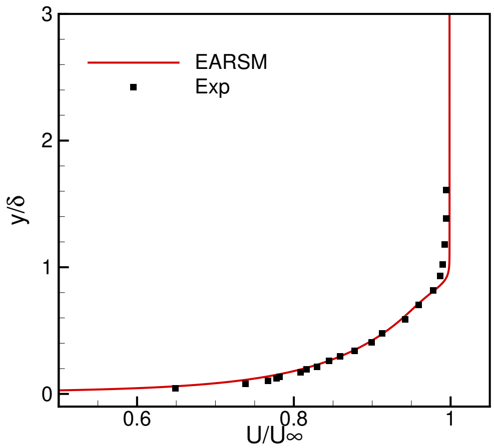

(b) δ = 4.41 mm

Figure 7.6: Comparison of velocity profile for a flat plate boundary layer computed from EARSM turbulence model with Schulein *et al.* [14] experiment data.

The computed RANS solutions are compared with the flat plate boundary layer profile obtained from experiment data at upstream of the shock boundary layer interaction [14]. The grid used for the flat plate solutions is 300 × 250, and the initial cell size of the grid is about 1E-6 m, which ensures the y+ less than 0.05. The relevant boundary layer thickness is measured and compared with the experimental data at different loca-

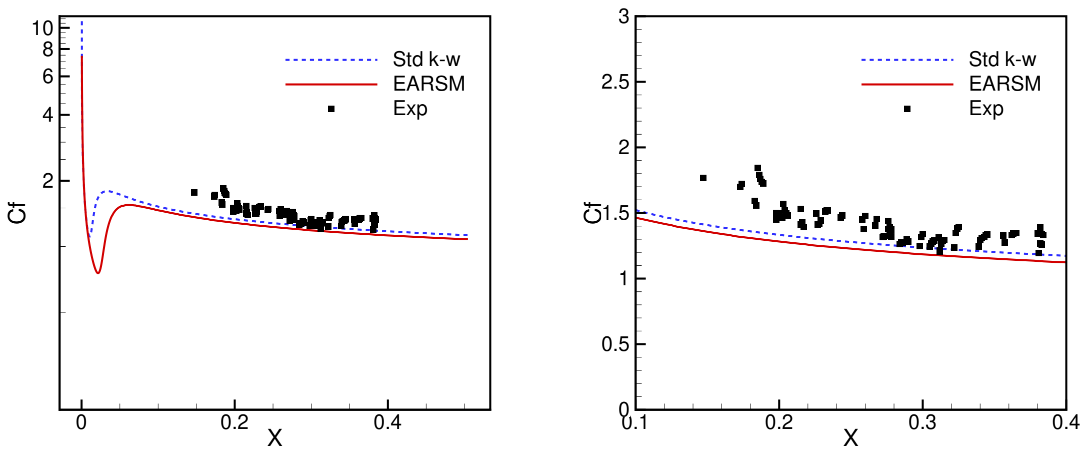

(a) (b)

Figure 7.7: Comparison of skin-friction coefficient distribution obtained from EARSM and standard $k-\omega$ turbulence models with experimental data [14].

tions along the flow direction from the computed velocity profiles. Figure (7.6) shows the comparison of the velocity in the boundary layer obtained from the WJ-EARSM turbulence model and experimental data. WJ-EARSM turbulence model solutions show a good match with the experimental data at all the locations. The skin friction coefficient plotted in Fig. (7.7) also shows a similar trend with the experimental data.

7.5 Shock unsteadiness model implementation

The accuracy of RANS with turbulence models to reliably predict the flow structure is not satisfactory in high-speed flows involving shockwave/boundary-layer interaction. Inaccuracy is due to the over-amplification of TKE across the shockwave, and the overestimation of TKE leads to a more energized turbulent boundary layer. A more energized turbulent boundary layer can sustain the adverse pressure gradient created by the shockwaves for longer, thus delaying the flow separation. These flaws in the turbulence model may be because they do not consider the unsteady nature of shockwave while interacting with the incoming upstream turbulence. Sinha *et al.* [41] modeled the unsteady effect of shockwaves by including the additional shock-physics term into the standard turbulence models. The turbulence models modified based on shock-unsteadiness correction are found to improve the flow topology significantly. This section will discuss the key features of shock-unsteadiness modification applied to WJ-EARSM based on the standard $k-\omega$ model.

We extend the SU-EARSM formulation to two-dimensional $k-\omega$ framework and apply to oblique shock impinging on turbulent boundary layer. The production term in the k-equation in the generalized tensor form is given by

$$P_k = -\overline{\rho} R_{ij} S^*_{ij} \simeq -\overline{\rho} R_{11} S^*_{11}$$

At a normal shock wave, the shock-normal gradients are dominant and P_k is expected to simplify to the form given above. For an oblique shock, the streamwise Reynolds stress R_{11} has to be replaced by the shock-normal component. The Reynolds stresses given by the new SU-EARSM Eqs. (6.29) and (6.30) can then be interpreted as for R_{nn} and R_{tt}, respectively, in the shock-normal and transverse directions. The anisotropy ratio $\hat{a}$ is computed in terms of the model coefficients C_p, C_s and C_Π, given in chapter 6, where the Mach number M is replaced by the shock-normal component of the upstream Mach number M_{1n}. The Reynolds stresses are thus function of the local shock strength, via the shock-normal Mach number M_{1n}. The orientation of the oblique shock is also to be calculated in terms of the local pressure gradient vector. The shock inclination angle is required to transform the Reynolds stresses (R_{nn}, R_{tt}) given by SU-EARSM back to the (x, y) components. The model reverts back to (R_{11}, R_{22}) components for the baseline WJ-EARSM outside of shock waves. The transition between SU-EARSM and WJ-EARSM is to be done smoothly so as to avoid any artificial discontinuity in the turbulence field. Overall, it can lead to a fairly cumbersome procedure.

We take an alternate approach. Substituting the expression for R_{ij} from Eq. (6.1) in to the general expression for TKE production, we get

$$\begin{aligned}
P_k &= R_{xx}\frac{\partial \overline{u}}{\partial x} + R_{xy}\frac{\partial \overline{u}}{\partial y} + R_{yx}\frac{\partial \overline{v}}{\partial x} + R_{yy}\frac{\partial \overline{v}}{\partial y} \\
&= \left[2\mu_T'\left(\frac{\partial \overline{u}}{\partial x} - \frac{1}{3}\left(\frac{\partial \overline{u}}{\partial x} + \frac{\partial \overline{v}}{\partial y}\right)\right) - \frac{2}{3}\overline{\rho}k - \overline{\rho}\beta_4 k a_{xx}\right]\frac{\partial \overline{u}}{\partial x} + \left[2\mu_T'\left(\frac{\partial \overline{v}}{\partial x} + \frac{\partial \overline{u}}{\partial y}\right) - \overline{\rho}\beta_4 k a_{xy}\right]\frac{\partial \overline{u}}{\partial y} \\
&+ \left[2\mu_T'\left(\frac{\partial \overline{v}}{\partial x} + \frac{\partial \overline{u}}{\partial y}\right) - \overline{\rho}\beta_4 k a_{yx}\right]\frac{\partial \overline{v}}{\partial x} + \left[2\mu_T'\left(\frac{\partial \overline{v}}{\partial y} - \frac{1}{3}\left(\frac{\partial \overline{u}}{\partial x} + \frac{\partial \overline{v}}{\partial y}\right)\right) - \frac{2}{3}\overline{\rho}k - \overline{\rho}\beta_4 k a_{yy}\right]\frac{\partial \overline{v}}{\partial y} \\
&= 2\mu_T'\left(\frac{2}{3}\left(\frac{\partial \overline{u}}{\partial x}\right)^2 - \frac{1}{3}\left(\frac{\partial \overline{u}}{\partial x}\frac{\partial \overline{v}}{\partial y}\right)\right) - \frac{2}{3}\overline{\rho}k\frac{\partial \overline{u}}{\partial x} - \overline{\rho}\beta_4 k a_{xx}\frac{\partial \overline{u}}{\partial x} \\
&+ 2\mu_T'\left(\frac{1}{2}\frac{\partial \overline{v}}{\partial x}\frac{\partial \overline{u}}{\partial y} + \frac{1}{2}\left(\frac{\partial \overline{u}}{\partial y}\right)^2\right) - \overline{\rho}\beta_4 k a_{xy}\frac{\partial \overline{u}}{\partial y} \\
&+ 2\mu_T'\left(\frac{1}{2}\frac{\partial \overline{v}}{\partial x}\frac{\partial \overline{u}}{\partial y} + \frac{1}{2}\left(\frac{\partial \overline{v}}{\partial x}\right)^2\right) - \overline{\rho}\beta_4 k a_{yx}\frac{\partial \overline{v}}{\partial x}
\end{aligned}$$

$$
\begin{aligned}
&+ \quad 2\mu_T'\left(\frac{2}{3}\left(\frac{\partial\overline{v}}{\partial y}\right)^2 - \frac{1}{3}\left(\frac{\partial\overline{u}}{\partial x}\frac{\partial\overline{v}}{\partial y}\right)\right) - \frac{2}{3}\overline{\rho}k\frac{\partial\overline{v}}{\partial y} - \overline{\rho}\beta_4 k a_{yy}\frac{\partial\overline{v}}{\partial y}
\end{aligned}
$$

$$
\begin{aligned}
&= \quad \frac{4}{3}\mu_T'\left(\frac{\partial\overline{u}}{\partial x}\right)^2 - \frac{2}{3}\mu_T'\left(\frac{\partial\overline{u}}{\partial x}\frac{\partial\overline{v}}{\partial y}\right) - \frac{2}{3}\overline{\rho}k\frac{\partial\overline{u}}{\partial x} - \overline{\rho}\beta_4 k a_{xx}\frac{\partial\overline{u}}{\partial x} + \mu_T'\frac{\partial\overline{v}}{\partial x}\frac{\partial\overline{u}}{\partial y} + \mu_T'\left(\frac{\partial\overline{u}}{\partial y}\right)^2\\
&- \quad \overline{\rho}\beta_4 k a_{xy}\frac{\partial\overline{u}}{\partial y} + \mu_T'\frac{\partial\overline{v}}{\partial x}\frac{\partial\overline{u}}{\partial y} + \mu_T'\left(\frac{\partial\overline{v}}{\partial x}\right)^2 - \overline{\rho}\beta_4 k a_{yx}\frac{\partial\overline{v}}{\partial x} + \frac{4}{3}\mu_T'\left(\frac{\partial\overline{v}}{\partial y}\right)^2\\
&- \quad \frac{2}{3}\mu_T'\left(\frac{\partial\overline{u}}{\partial x}\frac{\partial\overline{v}}{\partial y}\right) - \frac{2}{3}\overline{\rho}k\frac{\partial\overline{v}}{\partial y} - \overline{\rho}\beta_4 k a_{yy}\frac{\partial\overline{v}}{\partial y}
\end{aligned}
$$

$$
\begin{aligned}
&= \quad \frac{4}{3}\mu_T'\left(\frac{\partial\overline{u}}{\partial x}\right)^2 + \frac{4}{3}\mu_T'\left(\frac{\partial\overline{v}}{\partial y}\right)^2 - \frac{4}{3}\mu_T'\left(\frac{\partial\overline{u}}{\partial x}\frac{\partial\overline{v}}{\partial y}\right) + \mu_T'\left(\frac{\partial\overline{u}}{\partial y}\right)^2 + \mu_T'\left(\frac{\partial\overline{v}}{\partial x}\right)^2\\
&+ \quad 2\mu_T'\left(\frac{\partial\overline{u}}{\partial y}\right)\left(\frac{\partial\overline{v}}{\partial x}\right) - \frac{2}{3}\overline{\rho}k\frac{\partial\overline{u}}{\partial x} - \frac{2}{3}\overline{\rho}k\frac{\partial\overline{v}}{\partial y} - \overline{\rho}\beta_4 k a_{xx}\frac{\partial\overline{u}}{\partial x} - \overline{\rho}\beta_4 k a_{xy}\frac{\partial\overline{u}}{\partial y}\\
&- \quad \overline{\rho}\beta_4 k a_{yx}\frac{\partial\overline{v}}{\partial x} - \overline{\rho}\beta_4 k a_{yy}\frac{\partial\overline{v}}{\partial y}
\end{aligned}
$$

$$
\begin{aligned}
&= \quad \frac{4}{3}\mu_T'\left[\left(\frac{\partial\overline{u}}{\partial x}\right)^2 + \left(\frac{\partial\overline{v}}{\partial y}\right)^2 - \left(\frac{\partial\overline{u}}{\partial x}\frac{\partial\overline{v}}{\partial y}\right)\right] + \mu_T'\left[\left(\frac{\partial\overline{u}}{\partial y}\right) + \left(\frac{\partial\overline{v}}{\partial x}\right)\right]^2 - \frac{2}{3}\overline{\rho}k\left[\frac{\partial\overline{u}}{\partial x} + \frac{\partial\overline{v}}{\partial y}\right]\\
&- \quad \overline{\rho}\beta_4 k a_{xx}\frac{\partial\overline{u}}{\partial x} - \overline{\rho}\beta_4 k a_{xy}\frac{\partial\overline{u}}{\partial y} - \overline{\rho}\beta_4 k a_{yx}\frac{\partial\overline{v}}{\partial x} - \overline{\rho}\beta_4 k a_{yy}\frac{\partial\overline{v}}{\partial y}
\end{aligned}
$$

$$
= \quad 2\mu_T' S^*_{ij}S^*_{ji} - \frac{2}{3}\overline{\rho}kS^*_{ii} - \overline{\rho}\beta_4 k a_{xx}\frac{\partial\overline{u}}{\partial x} - \overline{\rho}\beta_4 k a_{xy}\frac{\partial\overline{u}}{\partial y} - \overline{\rho}\beta_4 k a_{yx}\frac{\partial\overline{v}}{\partial x} - \overline{\rho}\beta_4 k a_{yy}\frac{\partial\overline{v}}{\partial y}
$$

Therefore

$$
P_k \quad = \quad 2\mu_T' S^*_{ij}S^*_{ji} - \frac{2}{3}\overline{\rho}kS^*_{ii} - \overline{\rho}k\beta_4 a^{ext}_{ij}\frac{\partial\widetilde{u}_i}{\partial x_j}, \tag{7.74}
$$

where

$$
\begin{aligned}
2S^*_{ji}S^*_{ij} &= \frac{4}{3}\left[\left(\frac{\partial\overline{u}}{\partial x}\right)^2 + \left(\frac{\partial\overline{v}}{\partial y}\right)^2 - \left(\frac{\partial\overline{u}}{\partial x}\frac{\partial\overline{v}}{\partial y}\right)\right] + \left[\left(\frac{\partial\overline{u}}{\partial y}\right) + \left(\frac{\partial\overline{v}}{\partial x}\right)\right]^2\\
S^*_{ii} &= \left[\frac{\partial\overline{u}}{\partial x} + \frac{\partial\overline{v}}{\partial y}\right].
\end{aligned}
$$

Here μ_T is the effective eddy viscosity and a^{ext}_{ij} is the extra anisotropy tensor; see chapter 6 for details. In a shockwave, $S^*_{ij}S^*_{ji} = S^{*2}_{ii}$ is very large in magnitude. This leads to high production and excessively high values of k behind the shock. At a shockwave, the turbulence is in a highly non-equilibrium state and the eddy viscosity assumption literally breaks down. A more accurate amplification of k is obtained by setting μ'_T to zero in the production of turbulent kinetic energy [42].

In the region of shock waves, the production term is required to match the shock-unsteadiness model as,

$$P_k = -\frac{2}{3}\overline{\rho}kS^*_{ii} + \frac{2}{3}b'_1\overline{\rho}kS^*_{ii} - \overline{\rho}k\beta_4 a_{ij}\frac{\partial\overline{u}_i}{\partial x_j} \tag{7.75}$$

which is identical to the production term in Eq. (6.26) with $c_0 = 1 - b'_1$. The first part represents the effect of mean compression and the second part corresponds to the shock-unsteadiness mechanism, with coefficient $b'_1 = 0.4(1 - e^{1-\mathrm{M}_{1n}})$.

The shock-unsteadiness correction is applied in the $k-\omega$ based WJ-EARSM turbulence model by multiplying the eddy viscosity term in Eq. (7.74) by the factor,

$$c'_\mu = 1.0 - f_s\left(1.0 + \frac{2b'_1\omega}{\beta_1\sqrt{6S_{ij}S_{ji}}}\right) \tag{7.76}$$

where f_s is an empirical function that locates the region of shock wave in a given flow field. We use a form of f_s given by [104]

$$f_s = 0.5 - 0.5\tanh\left(12\frac{S^*_{ii}\delta_0}{U_\infty} + 4\right) \tag{7.77}$$

where the mean dilatation S^*_{ii} is normalized by the freestream velocity U_∞ and incoming boundary layer thickness δ_0.

Incorporating the shock-unsteadiness modification in $k-\omega$ based EARSM turbulence model, the production of turbulent kinetic energy is modified as

$$P'_k = c'_\mu\mu'_T\left[2S^*_{ji}S^*_{ji}\right] - \frac{2}{3}\rho kS^*_{ii} - \overline{\rho}k\beta_4 a_{ij}\frac{\partial\overline{u}_i}{\partial x_j}$$

The function f_s takes a value of one in shockwaves and high compression regions of the flow field, such that $c'_\mu = -2b'_1\omega/\beta_1\sqrt{6S_{ij}S_{ji}}$ and the modified production term in the baseline WJ-EARSM matches the production term in Eq. (7.75) for SU-EARSM. Otherwise, $f_s = 0$ and the baseline WJ-EARSM turbulence model, with Eq. (7.74) is recovered. The additional term containing β_4 is found to be relatively small in the region of shock waves and does not make any appreciable contribution to the production of TKE in Eq. (7.75). This is not the case downstream of the shock, where the model switches back to WJ-EARSM, that includes the β_4 term.

The physics-based shock-unsteadiness parameter b'_1 is a function of the local shock strength, given in terms of the upstream normal Mach number M_{1n}. The flow variables at points upstream of the shock wave are required to evaluate b'_1, which in turn is required to solve the TKE equation at points in the shock region. The shock-unsteadiness parameter b_1' was originally defined as a function of the upstream shock-normal Mach number M_{1n}. It has to be calculated locally at each point in the shockwave to bring in the physical effect through the shock strength. Sinha & Candler [42] and Pasha & Sinha [104] computed M_{1n} by taking a dot product of the streamwise Mach number in the incoming boundary layer with the pressure gradient vector in the shock wave as,

$$\mathrm{M}_{1n} = \frac{\widetilde{u_u} \, . \, \nabla \overline{p}}{\widetilde{a_u} |\nabla \overline{p}|} \tag{7.78}$$

where $\widetilde{a_u}$ is the mean speed of sound upstream of the shock wave, $\widetilde{u_u}$ is the upstream mean velocity and $\overline{p}$ is the mean pressure. The values of upstream Mach number at different shock locations are calculated manually by identifying an upstream location along the local streamline. This makes the model non-local, and it can be severely restrictive in parallel implementation of the code. In addition, computing M_{1n} is not trivial for flows involving multiple shock waves and their interactions, especially when the shock topology is not known a prior.

To overcome this limitation, Roy *et al.* [106] employed a different approach to obtain the shock strength, where b_1' is written in terms of density ratio across the shockwave. They propose an extra transport equation for a new variable ψ given by

$$\frac{\partial \overline{\rho} \psi}{\partial t} + \frac{\partial \overline{\rho} \widetilde{u_i} \psi}{\partial x_i} = \overline{\rho} \psi S_{ii}^* - \overline{\rho}(\psi - \psi_0) \frac{\sqrt{\widetilde{u_i} \widetilde{u_i}}}{L_\epsilon} \tag{7.79}$$

where $\sqrt{\widetilde{u_i}\widetilde{u_i}}$ is the mean velocity magnitude and $L_\epsilon = \sqrt{k/\omega}$ is the dissipation length scale and $\psi_0 = 1$ is a reference value of ψ. At shock waves, ψ takes the value $1/r$, where r is the mean density ratio across the shock. The variable ψ thus captures the local strength of the shock, and the shock unsteadiness parameter b_1' is recast in terms of $\psi = 1/r$,

$$b_1' = 0.4 \left(\frac{r-1}{5} \right)^{0.3} = 0.4 \left(\frac{1-\psi}{5\psi} \right)^{0.3} \tag{7.80}$$

In the undisturbed flow ahead of shockwaves, $\psi = \psi_0$ and it returns to its reference value after the shock wave. It is particularly useful for flows with multiple shock waves, where b_1' can be evaluated at each shock wave without computing M_{1n}.

For one-dimensional steady flow across a normal shock, the transport equation takes the form

$$\frac{\partial \overline{\rho} \widetilde{u} \psi}{\partial x} = \overline{\rho} \psi \frac{\partial \widetilde{u}}{\partial x} - \overline{\rho}(\psi - \psi_0) \frac{\widetilde{u}}{L_\epsilon} \tag{7.81}$$

where $\widetilde{u}$ is the mean velocity and $L_\epsilon = \sqrt{k/\omega}$ is the dissipation length scale. Here, subscript 0 indicates the location upstream of the shockwave, with $\psi_0 = 1$. At a shock wave,

ψ takes the value $1/r$ and thus captures the shock strength that is used to compute the local value of b_1'. Figure (7.8) shows the variation of ψ for the canonical shock-turbulence interaction at Mach 2.5. A minimum value of $\psi = 0.31$ is obtained for a density ratio of 3.33 across the Mach 2.5 shock, and it relaxes back to the reference value.

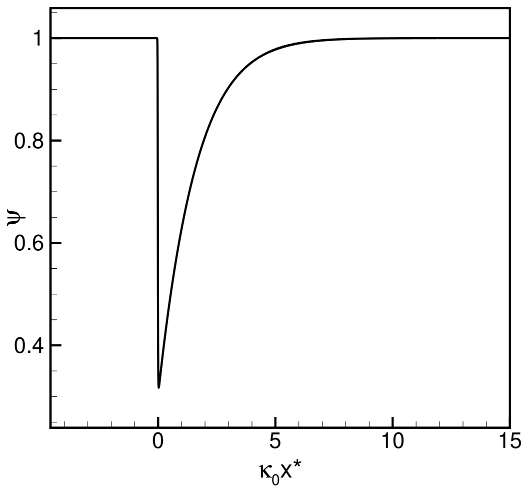

Figure 7.8: Streamwise variation of ψ for a Mach 2.5 normal shock located at $\kappa_0 x^* = 0$.

7.6 Computational domain

Schulein [14] performed the experiments for oblique shock wave/turbulent boundary layer interaction flows. The schematic of the experimental setup shown in Fig. (7.9a) consists of a 500 mm long flat plate and a shock generator with three different deflection angles of 6, 10, and 14 degrees. The inviscid shock generated by the shock generator was adjusted to impinge on the turbulent boundary layer at a fixed location of 350 mm from the tip of the flat plate. The strength of the incident shock wave increases with the deflection angle, resulting in a stronger interaction with the boundary layer. The inviscid shock from the tip of the shock generator interacts with the turbulent boundary layer developed over the flat plate.

Free stream conditions are $M_\infty = 5$, $T_\infty = 68.3$ K, $p_\infty = 4008.5$ N/m^2 and unit Reynolds number $Re_\infty = 37 \times 10^6$ m^{-1} with isothermal wall temperature condition of 300 K. Initial experiments were done for flow over a flat plate to obtain undisturbed turbulent boundary layer properties like δ, δ^*, θ and C_f at different locations. Wall data like pressure, skin friction, and heat transfer rates are obtained along with the flat plate in the interaction region.

A rectangular computational domain shown in Fig. (7.9b) is considered for the present simulations. The domain length extends 84 mm upstream and 150 mm downstream of the shock impingement point and 60 mm in the vertical direction. The incoming boundary layer thickness δ_0 of 3.5 mm and the momentum thickness of 0.1568 mm are matched with the experimental data [14] at 266 mm from the tip of the flat plate. Table 7.1 gives the freestream conditions and undisturbed incoming boundary layer details of the experiment and computation.

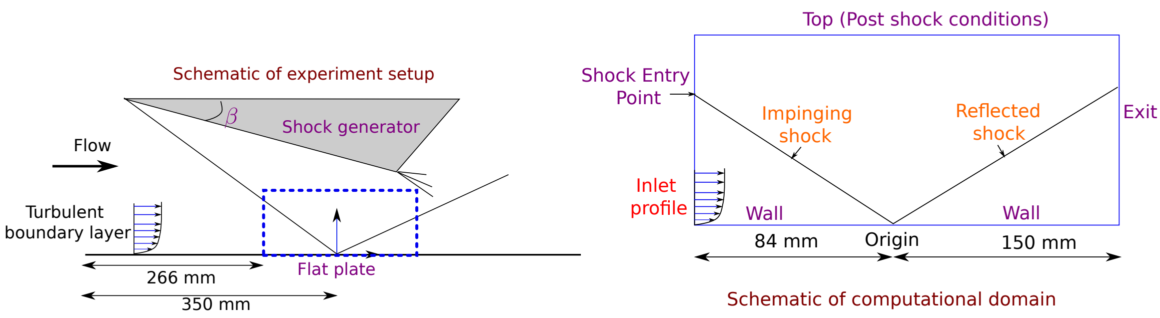

(a) Experimental configuration [14]

(b) Computational domain

Figure 7.9: Schematic of the SBLI experimental setup and the computational domain.

Parameter	experiment	computation
Freestream Mach number	5.00	5.00
Freestream temperature	68.3 K	68.3 K
Freestream density	0.203 kg/m^3	0.203 kg/m^3
Freestream velocity	828.6 m/s	828.6 m/s
Wall temperature	300 K	300 K
Reynolds number	3.67 x 10^7 /m	3.67 x 10^7 /m
Boundary layer thickness	3.814 mm	3.56 mm
Momentum thickness	0.157 mm	0.1568 mm

Table 7.1: Freestream conditions and characteristics of the incoming turbulent boundary for all the shock impingement cases.

Note that beyond Mach 2.5, the post-shock amplification obtained using the SU-EARSM reaches an asymptotic value (incrementing within 2 % up to Mach 6). Examining the available computational data for a 14-degree of Schulein *et al.* [14] SBLI experimental test case, the average values of the shock normal Mach numbers for incident, separation, reflected, and reattachment shocks are within the range of 1.25 to 2.0. Observing the advantages and limitations of the SU-EARSM for different upstream Mach numbers in the STI framework and depending upon the availability of experimental data, the Schulein SBLI test cases are well suited. Moreover, Schulein *et al.*[14] provides experimental data for skin friction coefficient, surface pressure distribution, and heat transfer data for three different shock strengths.

7.6.1 Initial/Boundary conditions

The streamwise flow axis is along the i-direction and wall-normal along j-direction. The mean flow and turbulence profiles at the inlet boundary of the computational domain are generated using a separate flat plate simulation. They are modified using inviscid shock relations to simulate the entry of the oblique shock. The domain above the shock entry point at the inlet boundary and the top boundary are maintained at post-shock conditions. The isothermal temperature of $T_w = 300$ K along with no-slip boundary conditions are specified at the wall, and extrapolation condition for the primitive variables is imposed at the exit boundary of the domain. Fig. (7.9b) shows the boundary conditions with a schematic of the SBLI.

The value of the momentum thickness reported in the experiments is matched to obtain the mean flow and turbulence profiles at the inlet boundary of the computational domain, as listed in table 7.1. The shock impingement point on the flat plate in the inviscid simulation is taken as origin of the computational domain. The shock impingement point is synchronized between the computations and experiments for comparing surface pressure and skin friction data obtained over the surface.

7.6.2 Grid convergence

A single block structured grid is generated using the code written in FORTRAN. The grid stretches exponentially in the y-direction with the first cell size of 1×10^{-6} m. In x-direction, the initial cell width of 10^{-3} m is maintained at origin and stretched exponentially in the upstream and downstream directions. The grid density is high at the shock wave impingement location. A systematic grid convergence study has been performed on the existing rectangular computational domain by varying the grid points in each direction and critical regions, such as the flow separation region. Both surface pressure and skin friction coefficient are used to identify a grid converged solution, in which the skin friction coefficient found to be the most sensitive mesh refinement. The present section explains the grid refinement study done for the flow interaction of the turbulent boundary layer with oblique shock generated by 10° ramp. First, the distance of

Grid	no. of points	Grid	no. of points
Grid 1	340×120	Grid 6	100×405
Grid 2	340×180	Grid 7	150×405
Grid 3	340×270	Grid 8	226×405
Grid 4	340×405	Grid 9	500×405
Grid 5	340×600		

Table 7.2: Grid refinement in x- and y-direction (streamwise and wall normal directions).

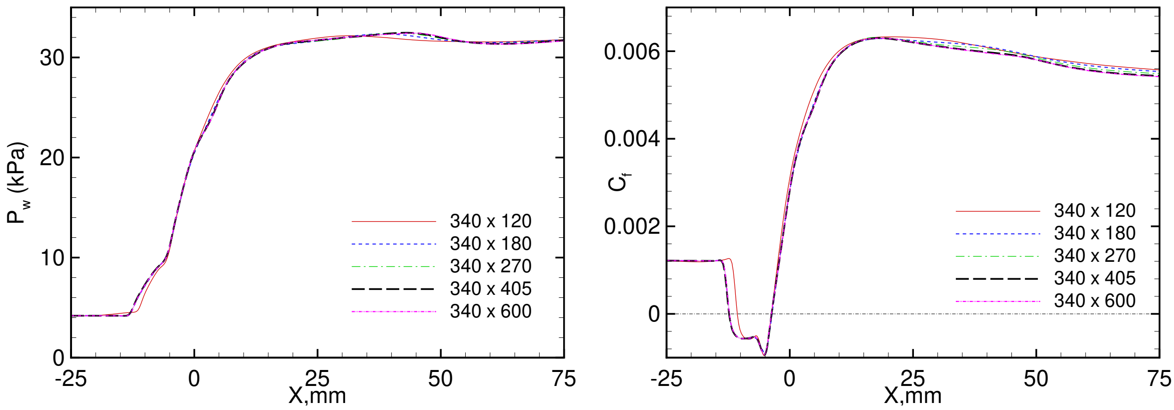

(a) Normalized pressure contour (b) Mach contour

Figure 7.10: Variation of (a) wall pressure and (b) skin friction coefficient for 10° case with changing number of wall-normal grid points.

the first cell center from the wall is maintained at 0.5×10^{-6} m and next, the number of points in the wall parallel direction is refined until the two finest grids yield overlapping results, such as the grids with 340 ×405 and 340 × 600 shown in Figs. (7.10) & (7.11). The solution obtained from the domain with 340 × 460 grid points yields less than 2% variation in wall pressure and skin friction in comparison with the solution obtained with 340 × 600 grid points. Based on the study, the solution obtained on the 340 × 405 grid is considered to be grid converged, and further simulations are carried out using 340 × 405 grid points. All the simulated cases are grid converged.

The steady converged solution is reached with optimized number of iterations by changing the Courant-Friedrichs-Lewy (CFL) number within the range of the total number of iterations. In the computations, the initial development of the flow is achieved by using a CFL of 25 for 500 iterations and is increased to 50 after the first 500 iterations. It

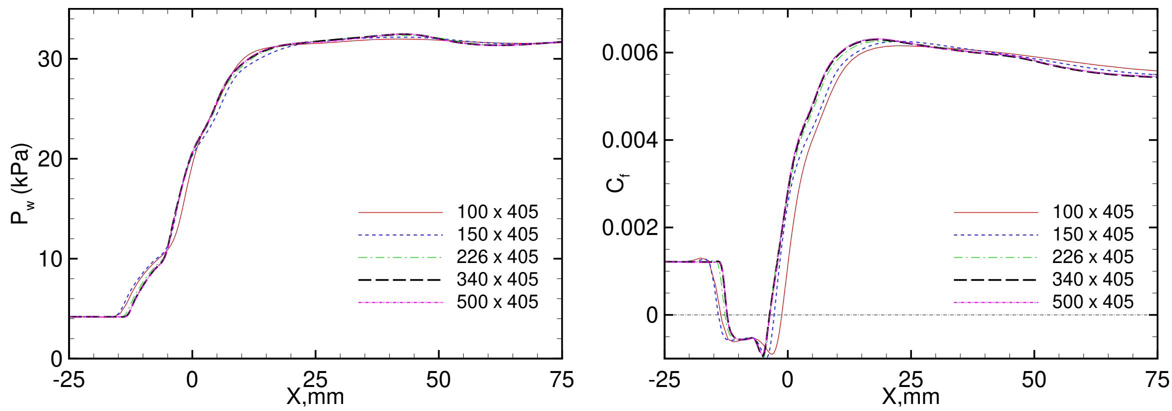

(a) Normalized pressure contour

(b) Mach contour

Figure 7.11: Variation of (a) wall pressure and (b) skin friction coefficient for 10° case with changing number of wall-parallel grid points.

is further increased to 100 at 1000 iterations, to 500 at 1500 iterations, and 1000 at 5000 iterations. The developing flow was able to handle a maximum CFL of 8000 after 10000 iterations. The computation converges in 14 CPU hrs, and it takes 15000 iterations to reach the steady-state solution. The drop of local residue is approximately from 10^3 to 10^{-5}.

7.7 Simulation results

7.7.1 14° oblique shock impingement

Figure (7.12) shows the magnified view of the interaction region of SBLI using the pressure and Mach number contours for 14° shock deflector case, computed using the EARSM turbulence model. On the flat plate surface, the adverse pressure gradient created by the incident shock wave is high enough to separate the turbulent boundary layer and form a recirculation region. Along with local flow separation and reattachment, the flow in the interaction region becomes more complicated due to the presence of multiple shock and expansion waves. S and R, respectively, identify the streamline showing the extent of separation region, and the separation and reattachment locations.

Edney type I interference has occurred when the opposite family shocks, such as separation shock and incident shocks, intersect each other. The transmitted shock and induced shock equalizes the pressures and flow directions in the downstream. The transmitted shock is short in length and terminates as the expansion waves generated by the

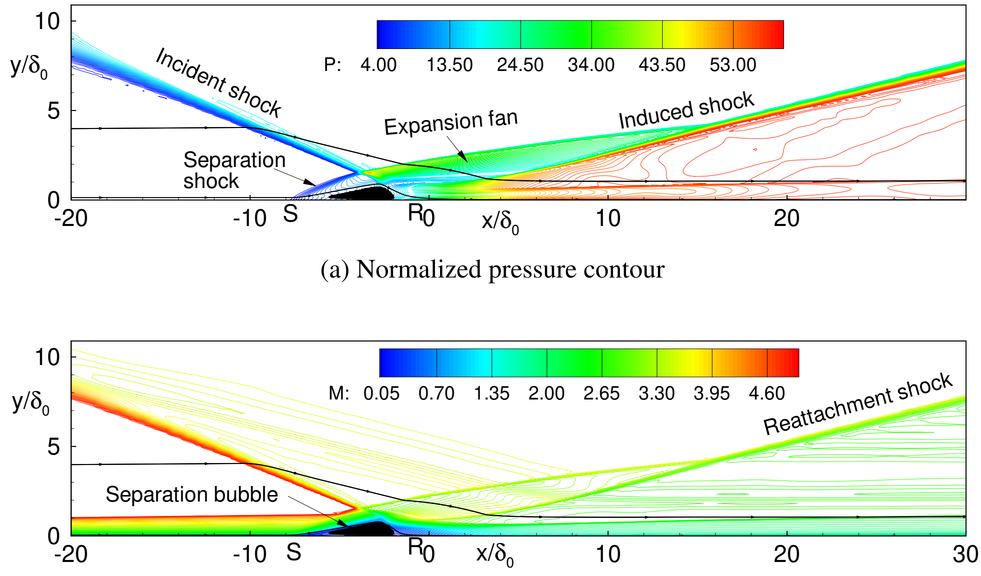

Figure 7.12: Shock structure of the oblique shockwave/boundary-layer interaction of the 14° shock deflector.

flow, turning over the separation bubble. The expansion fan is embedded between the induced and reflected shock waves. It interacts with and weakens the induced shock. It also causes the induced shock to bend and merge with the reflected shock. The compression waves generated by flow reattachment coalesce to form the reattachment shock.

Figure (7.13) shows the variation in pressure and skin friction coefficient measured along the surface of the plate. The computations using the WJ-EARSM model show a similar trend in surface pressure and skin friction coefficient variation. The significant differences compared to the experimental data are in the size of the separation bubble and the skin friction coefficient value at reattachment. Compared to experimental data, the EARSM predicted separation point is located further in the downstream. The pressure rise at the separation shock location is smaller and followed by a lower pressure gradient in the reattachment region. The computed results show some waviness in the pressure distribution downstream of reattachment. The experimental pressure data also shows a similar trend, and this may be due to the reflection of compression/expansion waves between the wall and the reflected shock. The zero-crossing of the computed C_f value determines the separation bubble size. The steep rise in skin friction at reattachment over-predicts the measurements. C_f decreases further downstream to values closer to the experimental data.

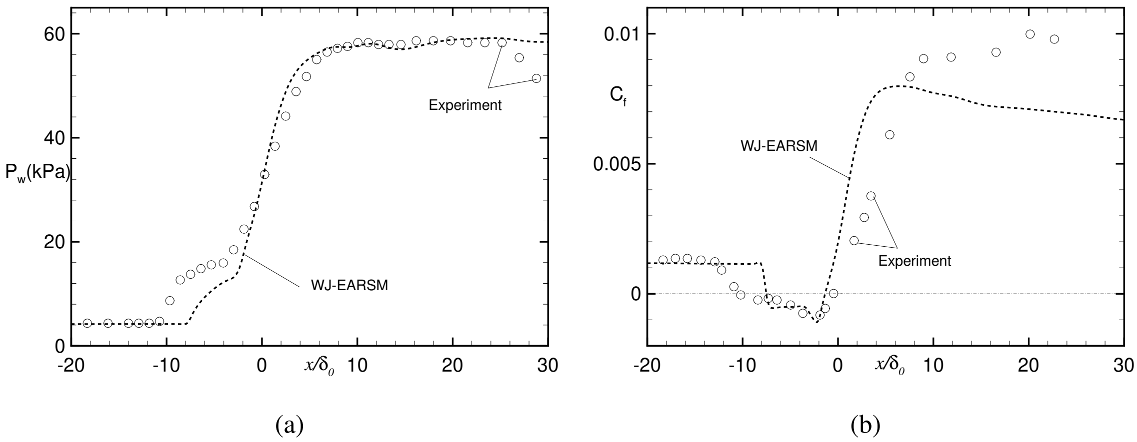

Figure 7.13: Computed (a) wall pressure and (b) skin friction with θ = 14° using EARSM with M_∞ = 5, compared with experiments.

The additional non-linear term in a Reynolds stress tensor has a very prominent role in swirl flows or curvature flowfield. Whereas, in the vicinity of the shock region, the effect is unknown. In the present section, we quantify the magnitude of β_4 and its effect in the vicinity of the shock wave region. Figure (7.14a) shows the shock structure for the 14° shock impingement case by using pressure contour. Figure (7.14b) shows the β_4 magnitude extracted for the streamline passing through the incident shock and reflected shock. The rectangular box in the figure shows the shock region and the β_4 value on the top. Across the shock, the β_4 coefficient value is very less, and its contribution or effect to the shock unsteadiness correction is negligible.

Figure (7.15a) shows the pressure contour in the interaction region of the 14° SBLI computed using the SU-EARSM turbulence model. It is qualitatively similar to the solution obtained using WJ-EARSM model shown in Fig. (7.12a).

The computed shock function f_s plotted in Fig. (7.15b) identifies the different shock waves, and the pattern matches the experimental shadowgraph in Fig. (7.15c). An expansion fan is embedded between the induced and reattachment shock waves. It interacts with and curves the shock waves, as seen in the experimental shadowgraph and schematic. The mean dilatation S_{ii} is the quantity to measure the shocks or high compression regions, and in the present computations, the function in terms of mean dilatation is used to identify the compression regions. S_{ii} becomes negative across the incident and separation shocks and attains large negative values at the intersection of these two shock waves. S_{ii} also identifies the induced and transmitted shock waves for the computed solution. It takes a positive value in the expansion fan. A region of the relatively low negative value of S_{ii} is

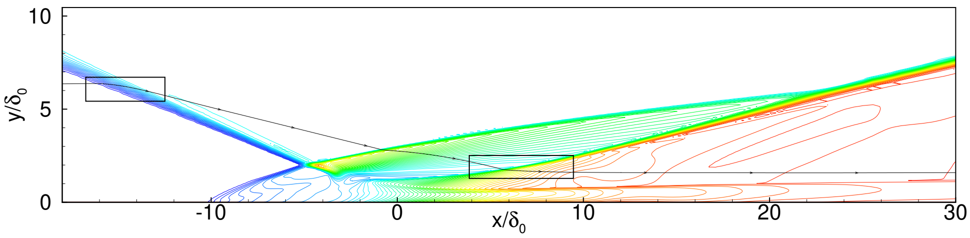

(a) Normalized pressure contour

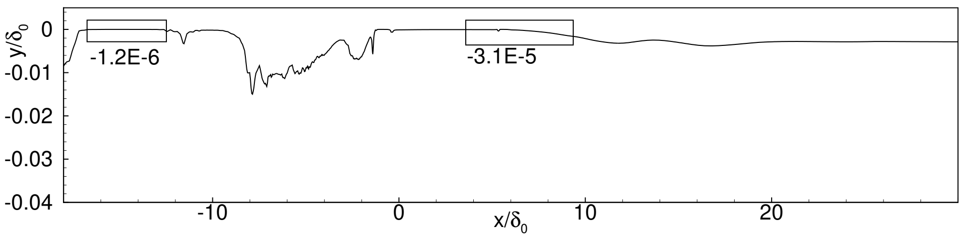

(b) β_4 coefficient variation

Figure 7.14: Computed β_4 coefficient along the streamline passing the incident and reflected shock.

observed in the reattachment region, see Fig.(7.15b). It corresponds to the compression waves generated by continuous flow turning.

In the shock function formulation, the quantity S_{ii} is normalized by the magnitude of the local velocity vector U_∞ and boundary layer thickness δ_0 calculated upstream of the interaction region. The function yields good identification of the separation shock, incident shock, induced shock, transmitted shock, and reattachment shock, see Fig. (7.15b). The characteristic length δ_0 and velocity U_∞ are specified as user input, which are priori known quantities for a given simulation.

The SU-EARSM is used in the regions where f_s is non-zero, and the base line WJ-EARSM is used elsewhere. Depending on the level of compression, it smoothly varies between 0 and 1. Care is taken to make f_s magnitude negligible in boundary layer flows where the baseline model is well-validated.

Figure (7.16) shows the variation in pressure and skin friction coefficient in the shock impingement region. The experimental pressure measurements remain at freestream value up to the separation point, and rise to about 18 kPa across the separation shock and to 58 kPa after flow reattachment. An adverse pressure gradient of the separation shock decreases the skin friction coefficient from its value measured in the undisturbed boundary layer. C_f is negative in the recirculation bubble and reaches high values downstream of the interaction region.

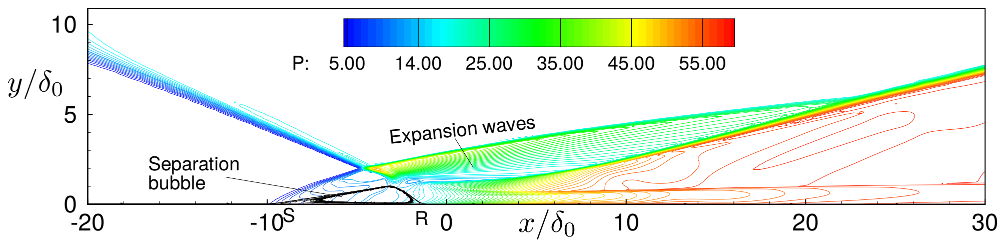

(a) Normalized pressure contour

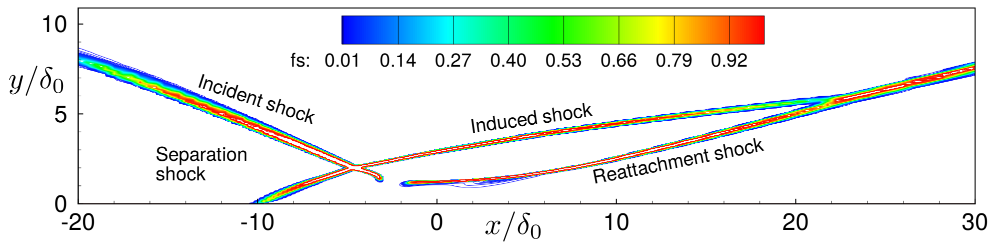

(b) shock function contour

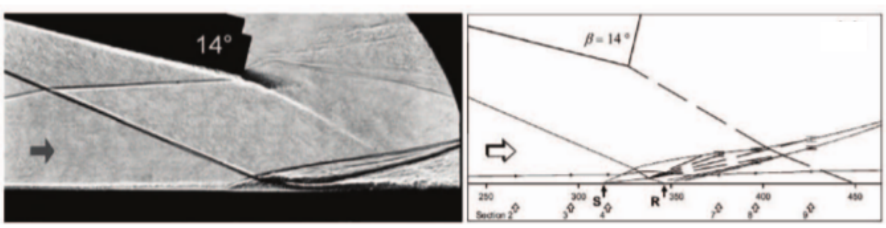

(c) Experimental shadowgraph and schematic

Figure 7.15: Comparison of the shock structure of the oblique shockwave/boundary-layer interaction obtained using SU-EARSM for $\theta = 14°$ at Mach with experimental shadowgraph and schematic [14].

The results obtained using the WJ-EARSM model follow the experimental trend in surface pressure and skin friction coefficient. The SU-EARSM model predictions show a better comparison with the measurements. In particular, the separation pressure rise is close to the location reported in the experiment. The reattachment point is almost identical to the WJ-EARSM model, and both match the skin friction data well. Post reattachment, the SU-EARSM gives a lower C_f that matches the experimental data better up to $x/\delta_0 =$ 8.

The standard $k-\omega$ model and SU $k-\omega$ model, based on Boussinesq approximation, are also shown in the figure for reference, and they grossly underpredicts the separation bubble size. Using non-linear eddy viscosity WJ-EARSM moves the separation point upstream. Further improvement is observed by using the shock-unsteadiness correction and

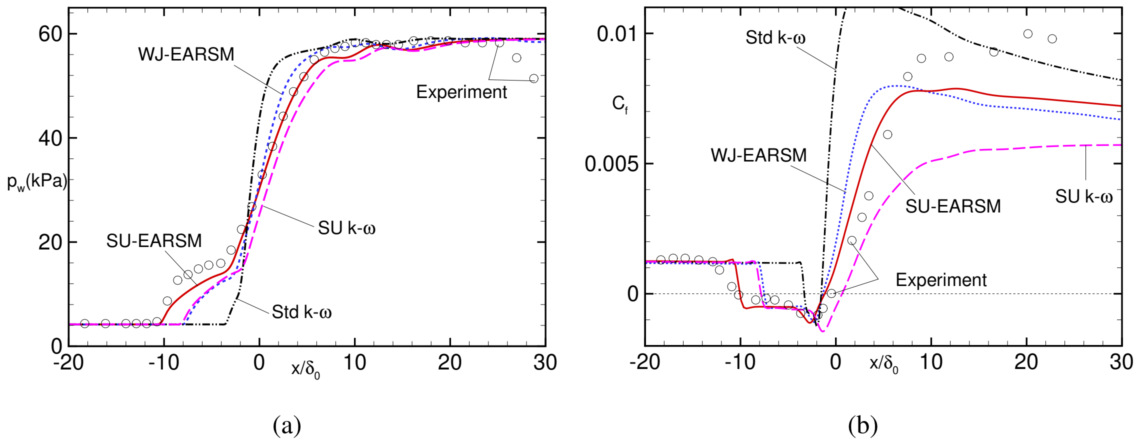

Figure 7.16: Computed (a) wall pressure and (b) skin friction for $\theta = 14°$ oblique shock impingement at $M_\infty = 5$ using WJ-EARSM, SU-EARSM, SU $k - \omega$ and standard $k - \omega$ turbulence models, compared with experimental data [14].

the separation pressure rise overlaps with the experiment. We note that the SU correction applied to the $k - \omega$ model is not able to match the separation location in this flow.

7.7.2 $\theta = 10°$ and $6°$

The results obtained for the 10° shock generator angle are presented in Fig. (7.17), and they show a trend similar to the 14° case. The strength of the interaction is weaker in this case, and it results in a smaller separation bubble than in Fig. 7.16. Once again, SU-EARSM predicts a separation location that matches the experimental pressure rise. The standard $k - \omega$ model is known to suppress separation in this flow, whereas SU $k - \omega$ and WJ-EARSM predict almost identical separation point. All the four models give overlapping reattachment pressure rise ($x/\delta_0 > 0$). There are, however, significant differences between their skin friction values downstream of the interaction region. The shock-unsteadiness correction dramatically reduces the skin friction coefficient of the standard $k - \omega$ model. It has a smaller effect in the EARSM framework, and the SU-EARSM predictions are found to match experimental measurement up to $x/\delta_0 = 4$. The skin fiction is under predicted beyond this point, and this is similar to that observed in the 14° case.

Figure (7.18) shows the pressure and skin friction values computed for the weakest interaction with a 6° shock generator. The experimental data indicate incipient separation in this case, and standard $k - \omega$ model is able to predict it. The other three models, namely SU $k - \omega$, WJ-EARSM and SU-EARSM predict a small separation bubble. The wall pressure values computed using all the models are comparable, while the post in-

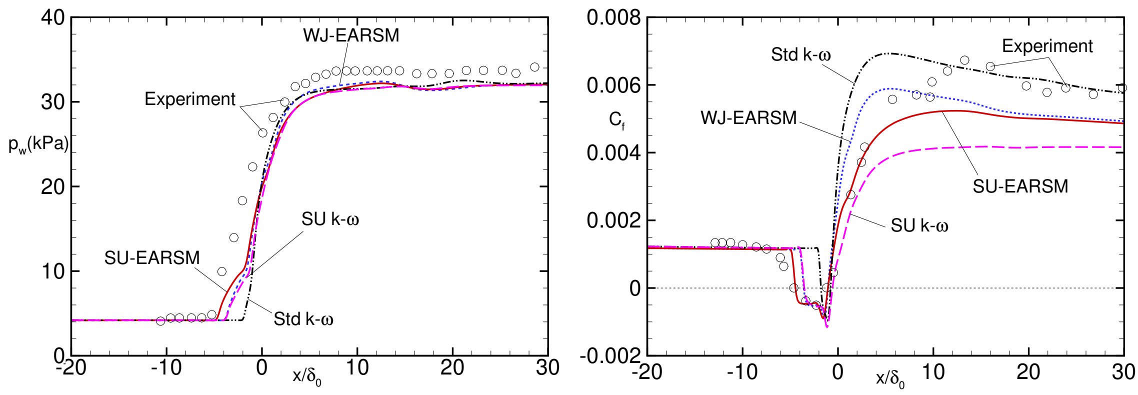

(a) (b)

Figure 7.17: Computed (a) wall pressure and (b) skin friction for $\theta = 10°$ at $M_\infty = 5$ using standard $k-\omega$, SU $k-\omega$, WJ-EARSM and SU-EARSM, compared with experimental data [14].

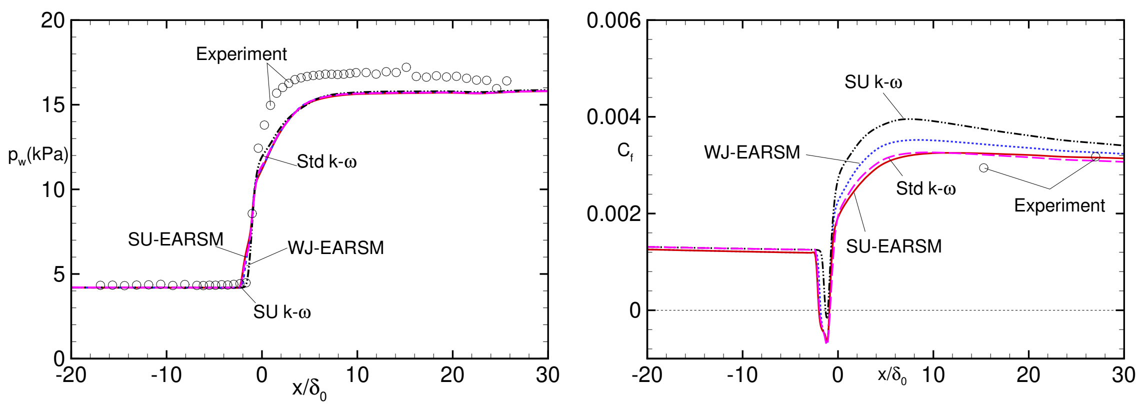

(a) (b)

Figure 7.18: Computed (a) wall pressure and (b) skin friction for $\theta = 6°$ at $M_\infty = 5$ using standard $k-\omega$, SU $k-\omega$, WJ-EARSM and SU-EARSM, compared with experimental data [14].

teraction skin friction data shows difference between the standard $k-\omega$ and the baseline WJ-EARSM results. Interestingly, both the SU models predict overlapping skin fiction coefficient in this case, and they match experimental data up to about $x/\delta_0 = 30$. The location of separation and re-attachment points computed using the standard $k-\omega$ and current shock-unsteadiness modified $k-\omega$ models is listed in Table 7.3. The corresponding points from oil flow visualization in the experiment are also tabulated. Quantitative

	Separation point			Reattachment point			Separation bubble size		
$\theta°$	14	10	6	14	10	6	14	10	6
Std. $k-\omega$	11.6	6.2	4.6	5.4	2.7	3.7	6.2	3.5	0.9
SU $k-\omega$	27.5	12.3	6.8	-2.3	2.0	2.9	29.7	10.3	3.9
WJ-EARSM	21.6	12.6	6.4	4.7	3.7	3.2	21.6	8.9	3.2
SU-EARSM	35.2	15.6	7.0	4.1	3.7	3.2	31.1	12.0	3.8
Experiment	35.7	16.2	-	1.7	4.2	-	34.0	12.1	-

Table 7.3: Comparison of computed separation point, reattachment point and separation bubble size with experiments. All distances are measured from origin in upstream direction.

comparison shows that the shock-unsteadiness correction markedly improves separation location. Coincidentally, the separation point computed by WJ-EARSM and SU $k-\omega$ turbulence models is very close, but the main difference between the two computational results is the separation bubble size (see Table 7.3). Standard $k-\omega$ model predictions are found to be grossly inaccurate for SBLI flows. SU correction improves the prediction, but the modified model cannot reproduce the shock-induced anisotropy in the Reynolds stresses. On the other hand, non-linear eddy viscosity based turbulence models, such as an EARSM, can predict the non-equilibrium effects in the SBLI flowfields. However, the model predictions still show discrepancies compared to the experiments. SU and pressure strain distribution corrections to the EARSM improve the predictions and match better with the experimental data.

Figure 7.19 show the different y/δ_0 locations used to extract the streamwise variation of pressure and Mach number obtained using different turbulence models for SBLI at $\theta = 10°$. The streamwise variation of pressure at different y/δ_0 locations are shown in Fig. 7.20 for different turbulence models. At $y/\delta_0 = 0.25$ as seen in Fig. (7.20a), it becomes clear that the standard $k-\omega$ model highly underpredicts the size of separation bubble compared to other turbulence models, which is also observed from the streamwise variation of Mach number shown in Fig. (7.21a). At $y/\delta_0 = 1.2$, the SU-EARSM shows the significant difference as the SU-EARSM predicts the height and size of the separation bubble better than the other turbulence models. At $y/\delta_0 = 3$ and 7 located far above the separation region, the SU-EARSM shows slight decrement in Mach number and increment in pressure in comparison to WJ-EARSM, this is due to reduction of the generation of turbulence obtained from using the shock unsteadiness modification. How-

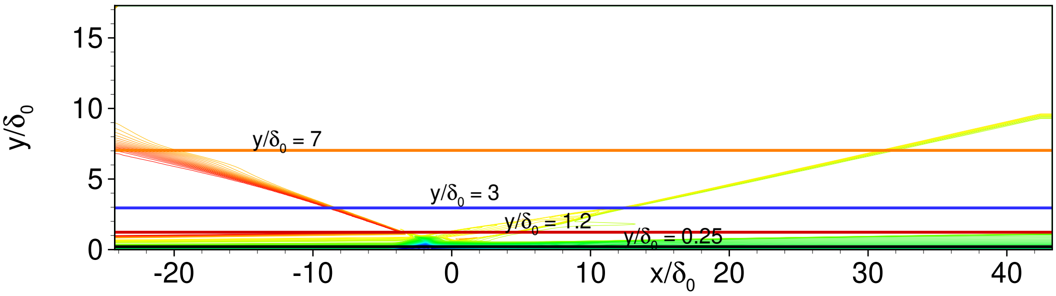

Figure 7.19: Representation of the line of extraction of pressure and Mach number for different turbulence models (y/δ_0 = 0.25, 1.2, 3, 7).

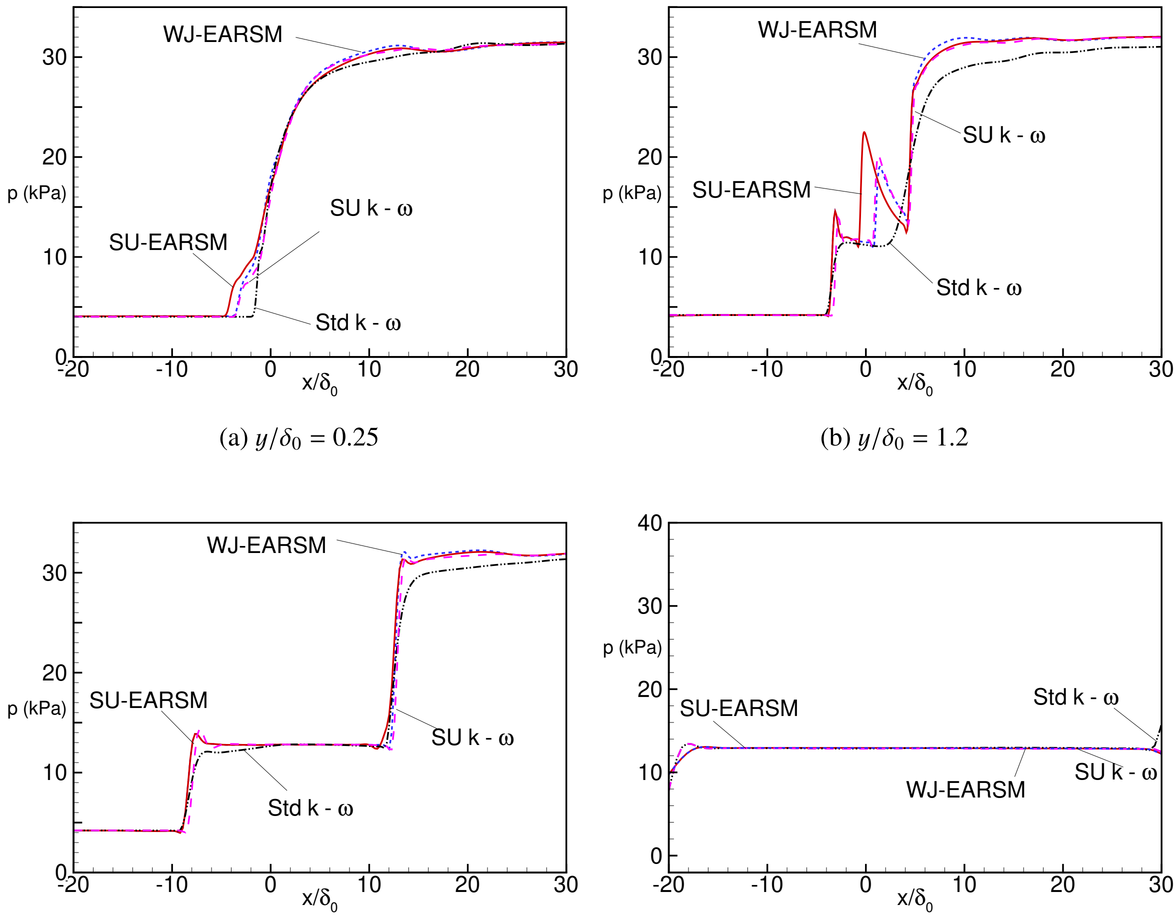

(a) $y/\delta_0 = 0.25$

(b) $y/\delta_0 = 1.2$

(c) $y/\delta_0 = 3$

(d) $y/\delta_0 = 7$

Figure 7.20: Comparison of the streamwise variation of pressure for different turbulence models at $\theta = 10°$.

ever, the shock unsteadiness modification shows significant improvement in prediction the separation point of the turbulent boundary layer.

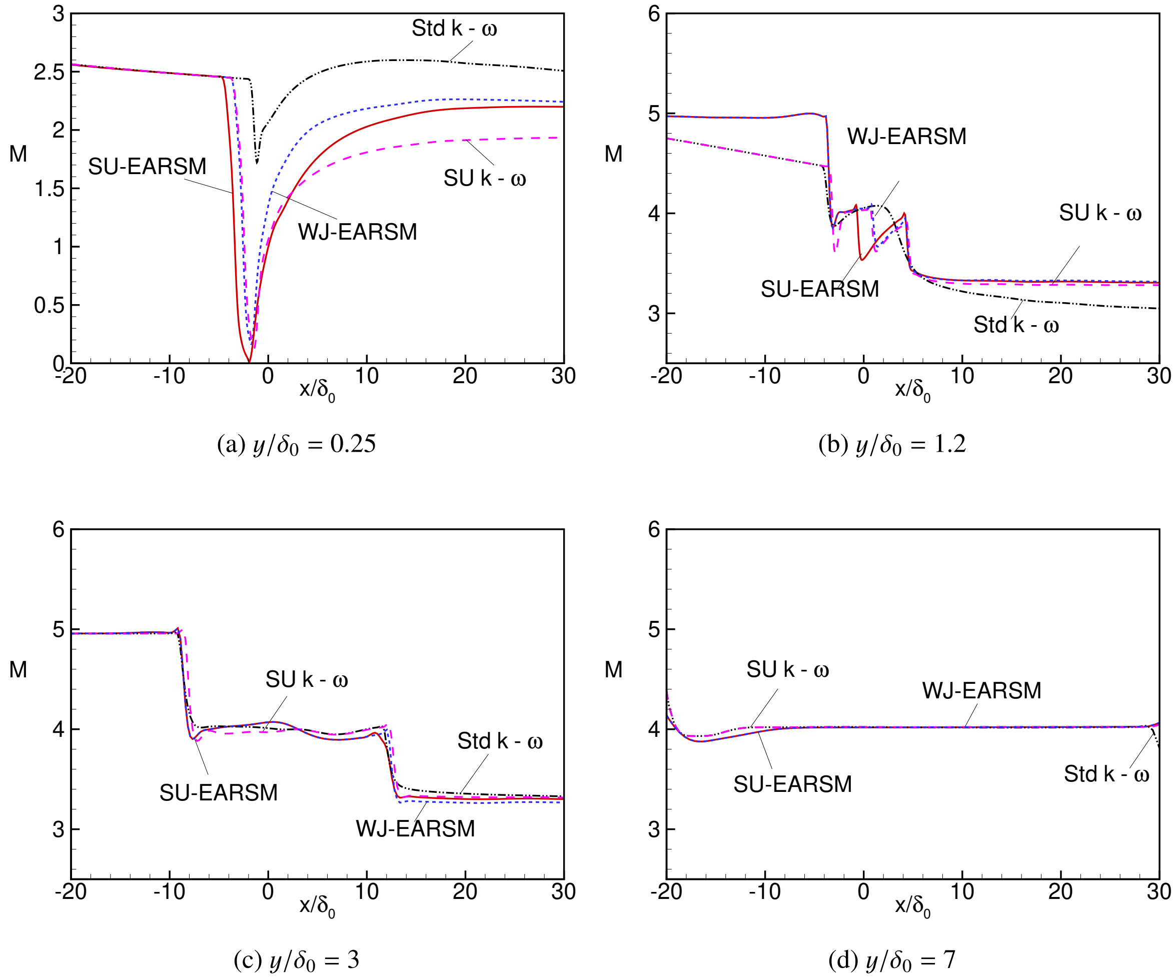

(a) $y/\delta_0 = 0.25$

(b) $y/\delta_0 = 1.2$

(c) $y/\delta_0 = 3$

(d) $y/\delta_0 = 7$

Figure 7.21: Comparison of the streamwise variation of Mach number for different turbulence models at $\theta = 10°$.

The shock strength changes the generation of the turbulence in the flowfield. The increasing shock strength generates an excessive rise in the Reynolds stress components for the case with $\theta = 14°$, as suggested by the tendency observed when comparing for different turbulence models at $\theta = 10°$. Similar for the $\theta = 6°$ case also, which are not shown. However, the variation of pressure, Mach number, and Reynolds stresses contours obtained using SU-EARSM turbulence model show better improvement than other turbulence models.

Figure (7.22) shows the comparison of contour of R_{11}, R_{22} and R_{12} for 10 deg case in vicinity of SBLI to compare the numerical results qualitatively for all analyzed turbulence models. Reynolds stresses computed using WJ-EARSM and SU-EARSM exhibit signifi-

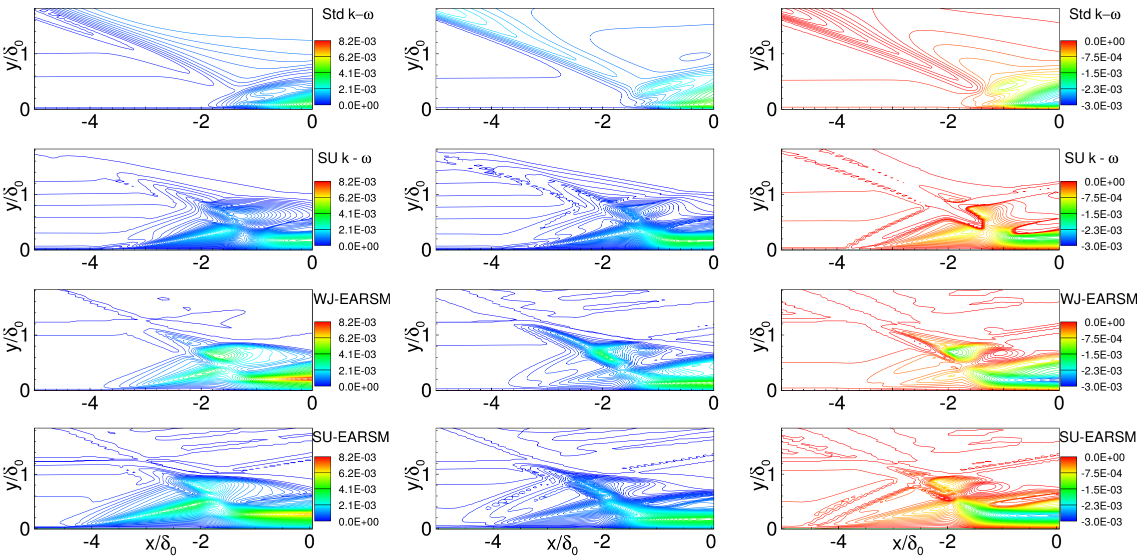

Figure 7.22: Comparison of the streamwise Reynolds stress, transverse Reynolds stress and Reynolds shear stress for different turbulence models at $\theta = 10°$.

cant growth in turbulence enhancement and its anisotropy in the adverse pressure gradient region. This is due to the nonlinear constitutive relationship between the Reynolds-stress tensor and the mean strain-rate tensor used in EARSM turbulence models. In comparison, $k - \omega$ and SU $k - \omega$ turbulence models do not show anisotropy in normal Reynolds stresses since these models use the Boussinesq hypothesis. R_{12} plays a vital role in the flow recirculation and the boundary layer separation (see Fig. (7.22c)). The effect of the shock unsteadiness modification in predicting the size of the separation bubble is noticeable. The SU-EARSM result shows a significant improvement and apparent difference from other turbulence models.

EARSM based models play a crucial role in energy redistribution from streamwise to transverse Reynolds stress components. The WJ-EARSM turbulence model predicts higher production of Reynolds stresses than SU-EARSM in the shock impinging region that crosses the shear layer above the separation bubble. In WJ-EARSM simulation results, excess production results in incorrect energy redistribution and gives by inaccurate anisotropy. SU modification to WJ-EARSM shows an improvement in capturing the Reynolds stresses and their anisotropy in post-impinging shock, separation bubble, and post-reflected shock regions.

7.8 3D simulations

Several experiments have been conducted in the past to investigate the 3D flowfield of a transverse jet interacting supersonic cross flow [119–123], and various RANS models have been assessed by many researchers using the data set from Aso *et al.* [119, 120]. The primary challenge in getting experimental data is that the supersonic flow structure is highly susceptible to minute changes in the geometry and flow conditions. Thus, care must be taken that the measuring instruments cause minimum interference with the actual flow. Aso *et al.* [119, 120] carried out experiments for two-dimensional and three-dimensional mixing flow fields in supersonic flow induced by injected secondary flows through slot perpendicularly. Schlieren visualization of the shock structure and oil flow visualization on the plate are obtained to understand the shock and flow topology. Surface pressure distribution was measured from ports located along several lines at constant span-wise distances from the injection port.

In Aso *et al.,* [119, 120] experimental cases, gaseous nitrogen jet is injected normally into the external flow of Mach 3.75 through a transverse slot nozzle mounted on a flat plate model. The freestream total pressure was 1.2 MPa, and the Reynolds number was $2{\times}10^7$. The experiments were conducted with different widths of the slot and varying total pressure ratios of the jet to the free stream. The experimental setup was similar to that of Spaid and Zukoski [121, 122]. The set of experiments was performed with and without aerodynamic fences. It was observed that the fences had a significant impact on maintaining the two-dimensionality of the flow, thus improving the data set for validation with the numerical simulations.

Standard RANS turbulence models, like $k-\epsilon$ and $k-\omega$, cannot accurately predict flows with strong shocks and their interaction with turbulence, which leads to an unsatisfactory prediction of the separation bubble size and peak heat transfer rates at reattachment. This drawback is seen in the model problem of JICF, where the standard $k-\omega$ model highly under-predicts the upstream separation length and peak pressures. We found that shock-unsteadiness correction enhances flowfield results with an interaction of the sonic jet and supersonic crossflow. However, a thorough investigation (in terms of SU-model parameter b_1^1) is needed, and evaluation of shock function f_s and upstream normal Mach number M_{un} will be essential. Further, a comparison of the surface properties, jet penetration height, and the upstream separation length between the standard $k-\omega$, EARSM, and SU model is needed to see the shock-unsteadiness modification effect.

7.9 Summary

The chapter presents RANS and turbulent transport equations along with a finite-volume based numerical method used for simulating high-speed flows. An in-house code is used for the computations presented in this chapter. It uses a modified Steger-Warming flux splitting approach for computing the inviscid fluxes and second-order central differencing for the viscous fluxes and turbulent source terms. The method and the code have been validated for a series of hypersonic flow applications.

The flowfield for an oblique shock wave impingement on a turbulent boundary layer generated with three different shock generator angles of 6°, 10°, and 14° are computed. Despite the geometric simplicity, multiple shock waves and flow expansion in the interaction region make the flow very complicated to compute numerically. Different turbulence models, such as standard $k-\omega$, SU $k-\omega$, WJ EARSM, and SU-EARSM turbulence models are applied to SBLI, and results are compared with the available experimental data. The standard $k-\omega$ model predicts delayed flow separation and yields too high skin-friction at reattachment, whereas WJ-EARSM shows better improvement than standard $k-\omega$, but still underpredicts the separation point.

The damping effect of shock-unsteadiness correction moves the separation location much closer to the experiment result. This, in turn, leads to close matching of the separation point with the experimental data. Comparing the surface measurements, the shock-unsteadiness modification yields excellent improvement over the WJ-EARSM and standard $k-\omega$ models, especially near the separation point and in the reattachment region.

Chapter 8

Summary and future work

8.1 Summary

Presence of shockwaves in high-speed turbulent flows pose significant challenge for computational fluid dynamic methods using Reynolds averaged turbulence models. Eddy viscosity based turbulence models with modification, such as shock-unsteadiness, have improved in the prediction of the turbulent quantities, surface pressure, and skin friction coefficient for the shock dominant flows in comparison with the standard turbulence models. Still, these modified models cannot reproduce the shock-induced anisotropy in the Reynolds stresses.

The primary objective of the present work is to improve the existing turbulence models to capture the shock-induced anisotropy, within moderate computational cost. To achieve the goal, we used the existing Reynolds stress-based turbulence models (RSM and EARSM) as the platform to overcome the Boussinesq approximation for calculating the Reynolds stresses.

We evaluate the three existing RSMs for the canonical shock-turbulence interaction (STI). The canonical STI is the simplest and most fundamental model problem, where isotropic homogeneous turbulence interacts with a nominally normal shock wave. The amplification, decaying, and nature of turbulence are obtained by solving the simplified equations. In comparison with the DNS data, all the RSMs show a very poor match and considered for further model improvement. We incorporated the physics-based correction to include the effect of unsteady oscillations into the existing RSM to accurately predict shock-induced anisotropy.

The model predictions show non-physical behaviour due to significant numerical error across the shockwave due to the non-conservative form of the source term. To minimize the numerical error at the shockwave, we developed new transformed conservative form of transport equations for the new RSM (SU-RSM). The SU-RSM with conservative source terms is found to match DNS data for canonical STI. The amplification of the principal Reynolds stresses and their downstream evolution are predicted well for a range of Mach numbers.

A similar approach is applied to EARSM, which are based on the $k - \omega$ transport equations. We introduce the physical concept of redistribution of the total kinetic energy between the principal Reynolds stresses via pressure-velocity and shock unsteadiness effects. Using the idea, we propose a new algebraic Reynolds stress model (SU-EARSM) using closure coefficients from linear interaction analysis of STI. In comparison with the DNS data, the new model shows a significant improvement in predicting the principal Reynolds stresses and their anisotropy. They are able to match the performance of the Reynolds stress models at a much lower computational cost.

The modified EARSM, along with the shock-unsteadiness $k-\omega$ turbulence model is applied to the oblique shock impingement on the turbulent boundary layer at Mach 5. The shock-unsteadiness correction is implemented in the EARSM framework using the shock identifying function, and model coefficients based on LIA. The model predictions match experimental data for surface pressure and skin friction coefficient, and results are better than those obtained using two-equation models based on Boussinesq approximation as well as the baseline EARSM.

8.2 List of contributions

1. Physics-based correction to existing RSM to accurately predict shock-induced anisotropy.

2. Developed a new transformed conservative form of a modified RSM to minimize the numerical error at the shockwave.

3. Proposed a new algebraic Reynolds stress model (SU-EARSM) using closure coefficients from linear interaction analysis of STI.

4. The shock-unsteadiness corrected EARSM shows significant improvement in predicting surface pressure and skin friction in SBLI flows.

8.3 Future work

Following are some of the ideas inspired by the current work that could be pursued.

- Detail study for pressure strain correlation and also other compressibility corrections like pressure dilatation, dissipation dilatation etc.

- Implementing the RSM in the in-house code and extending the modified RSM for simulating flow over a compression ramp and impinging shock on a turbulent boundary layer over a flat plate.

- SU and pressure strain distribution corrections to the EARSM improve the predictions with the given model coefficients. Further, it would be interesting to study the decay behaviour of TKE, Reynolds stresses, and their anisotropy in terms of model coefficients, which are functions of upstream Mach number..

- A thorough investigation required in terms of SU and pressure strain distribution corrections for three-dimensional flowfields.

- A similar analysis of shock function, upstream normal Mach number and transport equation for a new variable ψ will be essential for three-dimensional numerical simulations.

- Applying the modified EARSM turbulence model to realistic three-dimensional viscous flow simulations, such as scramjet intake flow, sonic jet in supersonic crossflow, single and double fin configurations.

Appendix A

Homogeneous turbulent decay relations

The shock-unsteadiness (SU) $k-\epsilon$ model have the following transport equations for TKE and the turbulent dissipation rate [41, 74].

$$
\begin{aligned}
\widetilde{\overline{\rho}u}\frac{\partial k}{\partial x} &= -\frac{2}{3}c_0\overline{\rho}k\frac{\partial \widetilde{u}}{\partial x} - \overline{\rho}\epsilon, && \text{(A.1)}\\
\widetilde{\overline{\rho}u}\frac{\partial \epsilon}{\partial x} &= -\frac{2}{3}C_{\epsilon_1}\overline{\rho}\epsilon\frac{\partial \widetilde{u}}{\partial x} - \overline{\rho}C_{\epsilon_2}\frac{\epsilon^2}{k}. && \text{(A.2)}
\end{aligned}
$$

The diffusive fluxes are not included in the equations because their contribution is expected to be small [109]. The model coefficients are given in Chapter 4 and are not repeated here. Upstream of the shockwave, there is no gradient in the mean velocity. Thus, the variation in k and ϵ for steady one-dimensional uniform mean flow are governed by the corresponding dissipation terms.

$$
\begin{aligned}
\widetilde{u}\frac{\partial k}{\partial x} &= -\epsilon, && \text{(A.3)}\\
\widetilde{u}\frac{\partial \epsilon}{\partial x} &= -C_{\epsilon 2}\frac{\epsilon^2}{k}. && \text{(A.4)}
\end{aligned}
$$

The above equations are in non-dimensional form and the respective characteristic quantities used for non-dimensionalization are mentioned in chapter 4. These equations are obtained by neglecting the production terms from TKE and dissipation rate equations, as there is no gradient in the mean velocity in this region (upstream of the shockwave). Also, the velocity is constant in this region and is equal to $\widetilde{u}$, where $\widetilde{u}$ = M because of the non-dimensionalization considered. Here, $\epsilon_s \propto \epsilon$ is taken. Eqs. (A.3) and (A.4) can be written as,

$$\frac{\partial \epsilon}{\epsilon} = C_{\epsilon 2}\frac{\partial k}{k}. \tag{A.5}$$

On integration, we get

$$\epsilon = k^{C_{\epsilon 2}}C, \tag{A.6}$$

where C is the integration constant. Substituting in Eq. (A.3) and integrating along x , we get

$$k = \left[\frac{Cx + \hat{C}}{\widetilde{u}} (C_{\epsilon 2} - 1) \right]^{-\frac{1}{C_{\epsilon 2}-1}}, \tag{A.7}$$

where $\hat{C}$ is another integration constant. Using the boundary condition $k = k_0$ and $\epsilon = \epsilon_0$ at $x = 0$, we get

$$\hat{C} = \frac{\widetilde{u} k_0^{C_{\epsilon 2}-1}}{C_{\epsilon 2} - 1}, \tag{A.8}$$

$$C = \epsilon_0 k_0^{-C_{\epsilon 2}}, \tag{A.9}$$

and thus

$$k(x) = k_0 \left[1 + \frac{\epsilon_0}{k_0} \frac{x(C_{\epsilon 2})}{\widetilde{u}_u} \right]^{-\frac{1}{C_{\epsilon 2}-1}}, \tag{A.10}$$

The expression for the turbulent dissipation rate can be obtained using Eq. (A.3) as,

$$\epsilon(x) = \epsilon_0 \left[1 + \frac{\epsilon_0}{k_0} \frac{x(C_{\epsilon 2})}{\widetilde{u}} \right]^{-\frac{C_{\epsilon 2}}{C_{\epsilon 2}-1}}. \tag{A.11}$$

The above equations give the variations in k and ϵ from the inlet station to the point just upstream of the shockwave. Now, if x_{sh} corresponds to the shockwave location, then at $x = x_{sh}$, $k = k_u$ and $\epsilon = \epsilon_u$. Hence, Eqs. (A.10) and (A.11) can be written in terms of the inlet values as,

$$k_0 = k_u \left[1 + \frac{\epsilon_0}{k_0} \frac{x_{sh}(C_{\epsilon 2} - 1)}{\widetilde{u}} \right]^{-\frac{1}{C_{\epsilon 2}-1}}, \tag{A.12}$$

$$\epsilon_0 = \epsilon_u \left[1 + \frac{\epsilon_0}{k_0} \frac{x_{sh}(C_{\epsilon 2} - 1)}{\widetilde{u}} \right]^{\frac{C_{\epsilon 2}}{C_{\epsilon 2}-1}}. \tag{A.13}$$

The same expressions hold if the shock is at $x = 0$ and x_{sh} is the distance of the shockwave from the inlet station. In the present work, $x_{sh} = 6.83$ for all the computations performed. Now, given the values of k_u and ϵ_u, the inlet values of k and ϵ can be calculated from Eqs. (A.12) and (A.13) as,

$$\epsilon_0 = \epsilon_u \left[1 + \frac{1}{\left(\frac{k_u}{\epsilon_u} - \frac{x_{sh}(C_{\epsilon 2}-1)}{\widetilde{u}} \right)} \frac{x_{sh}(C_{\epsilon 2} - 1)}{\widetilde{u}} \right]^{\frac{C_{\epsilon 2}}{C_{\epsilon 2}-1}}, \tag{A.14}$$

and

$$k_0 = \epsilon_0 \left[\frac{k_u}{\epsilon_u} - x_{sh} \frac{(C_{\epsilon 2} - 1)}{\widetilde{u}} \right]. \tag{A.15}$$

The $k-\epsilon$ model [15] is converted to the $k-\omega$ framework using the transformation

$$\epsilon = \omega\beta^* k, \tag{A.16}$$

Substituting Eq. (A.16) in Eq. (A.1), we get

$$\overline{\rho}\widetilde{u}\frac{\partial k}{\partial x} = -\frac{2}{3}c_0\overline{\rho}k\frac{\partial \widetilde{u}}{\partial x} - \overline{\rho}\beta^*\omega k, \tag{A.17}$$

and Eq. (A.2) transforms into

$$\overline{\rho}\widetilde{u}\beta^* \left[k\frac{\partial \omega}{\partial x} + \omega\frac{\partial k}{\partial x} \right] = -\frac{2}{3}\beta^* C_{\epsilon_1}\overline{\rho}\omega k\frac{\partial \widetilde{u}}{\partial x} - C_{\epsilon_2}\overline{\rho}\frac{\beta^{*2}\omega^2 k^2}{k},$$

On substituting Eq. (A.17) and simplifying, we get

$$\overline{\rho}\widetilde{u}\frac{\partial \omega}{\partial x} = -\frac{2}{3}\overline{\rho}\gamma\omega\frac{\partial \widetilde{u}}{\partial x} - \overline{\rho}\beta\omega^2. \tag{A.18}$$

where $\gamma = C_{\epsilon_1} - c_0$, and $\beta = (C_{\epsilon_2} - 1)\beta^*$. The Eqs. (A.17) and (A.18) are taken as the governing equations for the SU $k-\omega$ model for canonical STI.

Thus, the variation in k and ω for steady one-dimensional uniform mean flow are governed by the corresponding dissipation terms.

$$\widetilde{u}\frac{\partial k}{\partial x} = -\beta^*\omega k, \tag{A.19}$$

$$\widetilde{u}\frac{\partial \omega}{\partial x} = -\beta\omega^2. \tag{A.20}$$

which can be combined to get

$$\frac{\partial \omega}{\omega} = \frac{\beta}{\beta^*}\frac{\partial k}{k}. \tag{A.21}$$

On integration, we have

$$\omega = k^{\frac{\beta}{\beta^*}} C, \tag{A.22}$$

where C is a constant of integration. Substituting in Eq. (A.19) and integrating in x , we get

$$k = \left[\frac{\beta^* C x - \hat{C}}{\widetilde{u}} \left(\frac{\beta}{\beta^*} \right) \right]^{-\frac{\beta^*}{\beta}}, \tag{A.23}$$

where $\hat{C}$ is another integration constant. We evaluate C and $\hat{C}$ using the boundary condition $k = k_0$ and $\omega = \omega_0$ at $x = 0$. The final expressions for the variation of k and ω are thus obtained.

$$k(x) = k_0 \left[1 + \frac{\beta\omega_0 x}{\widetilde{u}}\right]^{-\frac{\beta^*}{\beta}}, \tag{A.24}$$

$$\omega(x) = \omega_0 \left[1 + \frac{\beta\omega_0 x}{\widetilde{u}}\right]^{-1}. \tag{A.25}$$

At the shock location x_{sh} we have $k = k_u$ and $\omega = \omega_u$, which are given by Eq. (4.8) in chapter 6. These are used to evaluate the k and ω values at the inlet location (subscript 0), by inverting the relations given above.

$$k_0 = k_u \left[1 + \frac{\beta\omega_0 x_{sh}}{\widetilde{u}}\right]^{\frac{\beta^*}{\beta}}, \tag{A.26}$$

$$\omega_0 = \omega_u \left[1 - \frac{\beta\omega_u x_{sh}}{\widetilde{u}}\right]^{-1}. \tag{A.27}$$

It is to note that, in the above expressions, all the quantities are normalized and non-dimensional, with the quantities used for normalization given in chapter 4 and 6.

Appendix B

Acoustic adjustment in RANS and DNS

Figure (B.1) shows streamwise evolution of the R_{11} and R_{22} for the DNS data, where the Reynolds stresses are scaled by the respective shock-upstream values. In the unsteady shockwave region, the DNS data for R_{11} takes very high values and outside, it rapidly increases from a low post-shock value to reach a local maximum at $\kappa_0 x^* = 4$. This corresponds to the acoustic adjustment region in LIA (see Fig. (B.1c)), where R_{11} increases due to the post-shock redistribution between the vortical and acoustic fluctuations. In the absence of viscous and non-linear effects in LIA, the Reynolds stresses reach asymptotic far-field values, whereas the DNS data shows a monotonic decay far away from the shockwave ($\kappa_0 x^* > 4$). The transverse Reynolds stress R_{22} has a peak at the shockwave, followed by a rapid decrease in the acoustic adjustment region to reach the far-field value.

The extent of the acoustic adjustment region in a STI is about one wavelength of the most-energetic upstream wave number. This is equivalent to the integral scale of turbulence upstream of the shockwave, approximately equal to one boundary layer thickness in a SBLI, this region is expected to be small and the far-field values away from the shockwave are important. We extrapolate the monotonic decay in R_{11} and R_{22} back to the shockwave center to obtain an equivalent far-field value from the DNS. This value is shown by an open square at $\kappa_0 x^* = 0$ and it serves as a benchmark for model evaluation.. The extrapolated value includes the jump in Reynolds stresses at the shock as well as the net effect of the acoustic adjustment in the region immediately following the shockwave.

For the Reynolds stress model, Equations (4.1) and (4.2) are applied to the Mach 2.5 STI and the results are shown for comparison. The model transport equations include production and rapid pressure strain terms that are active in the region of non-zero mean velocity gradient. They lead to a jump in R_{11} and R_{22} across the shockwave. The viscous dissipation results in a monotonic decay both upstream and downstream of the shockwave. On the other hand, the slow pressure strain term is responsible to make the post-shock

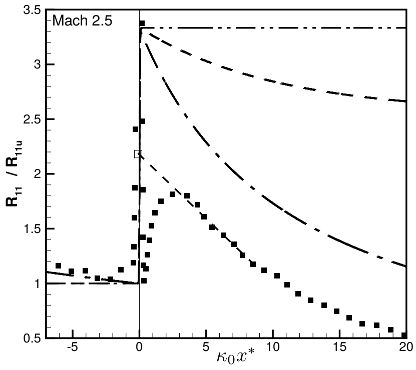

(a) R_{11} amplification

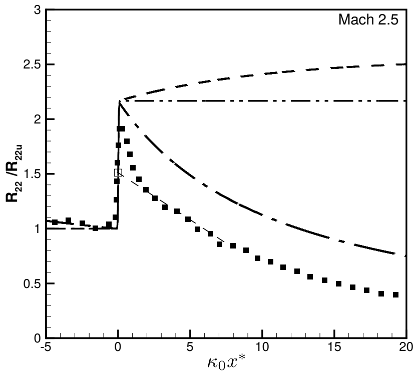

(b) R_{22} amplification

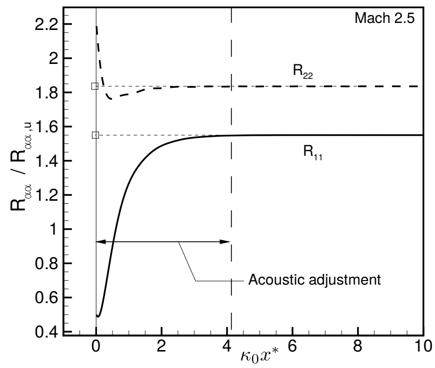

(c) R_{11} & R_{22} amplifications from LIA

Figure B.1: Streamwise evolution of the turbulence quantities in a Mach 2.5 canonical STI. Numerical solution computed for the baseline (dash-dot), baseline model without dissipation term (dashed) and baseline model without the slow pressure strain and dissipation terms (dash-dot-dot) are compared with DNS data (symbol). The post-shock Reynolds stresses predicted by the linear interaction analysis (LIA) are plotted in (c).

field isotropic. It leads to a decrease in R_{11} and an increase in R_{22} behind the shockwave (see the dashed line in Fig. B.1 (a) and (b)), and thus, its effect is qualitatively different from the acoustic adjustment of the Reynolds stresses observed in the DNS and LIA. In addition, the slow pressure strain term acts over a much larger length scale than the acoustic adjustment region in STI and can be effectively represented as a modification of the viscous decay rates of R_{11} and R_{22} in the post-shock flow. The effect of the viscous dissipation and the slow pressure strain terms is therefore neglected in evaluating the model capability in predicting the jump in R_{11} and R_{22} across the shockwave.

Appendix C

Simplification of WJ-EARSM turbulence model

In WJ-EARSM turbulence model, the solution to the cubic equation N is given by Eq. (6.6), where P_1 and P_2 are calculated as per Eqs. (6.7). For shock/turbulence interaction, the mean flow is one-dimensional. Thus, the magnitude of II_Ω becomes zero, and II_S reduces

$$II_S = S_{ij}S_{ij} = \frac{2}{3}\tau^2\left(\frac{\partial\widetilde{u}}{\partial x}\right)^2. \tag{C.1}$$

At the shock $II_s >> 1$ and

$$P_1 = c_1'\left(\frac{c_1'^2}{27} + \frac{9}{20}II_S - \frac{2}{3}II_\Omega\right) \simeq c_1'\frac{9}{20}II_s \tag{C.2}$$

$$P_2 = P_1^2 - \left(\frac{c_1'^2}{9} + \frac{9}{10}II_S - \frac{2}{3}II_\Omega\right)^3 \simeq P_1^2 - \left(\frac{9}{10}II_s\right)^3 \tag{C.3}$$

$$\tag{C.4}$$

The value of P_2 is less than zero and the solution for the term N is

$$N = \frac{c_1'}{3} + 2(P_1^2 - P_2)^{1/6}\cos\left(\frac{1}{3}\arccos\left(\frac{P_1}{\sqrt{P_1^2 - P_2}}\right)\right), \tag{C.5}$$

and it simplifies to

$$N \simeq 1.8(P_1^2 - P_2)^{1/6} \tag{C.6}$$

Here,

$$P_1^2 - P_2 \simeq \left(c_1'\frac{9}{20}II_s\right)^2 - \left(c_1'\frac{9}{20}II_s\right)^2 + \left(\frac{9}{10}II_s\right)^3 \tag{C.7}$$

$$\left(P_1^2 - P_2\right)^{1/6} \simeq \left(\frac{9}{10}II_s\right)^{3/6} = 0.77\tau|\partial\widetilde{u}/\partial x| \tag{C.8}$$

Substituting the Eq. (C.8) in Eq. (C.6) gives

$$N \approx 1.39\tau\left(\frac{\partial\widetilde{u}}{\partial x}\right). \tag{C.9}$$

Coefficient β_1 from Eq. (6.5) reduces to

$$\beta_1 = -\frac{6}{5N} \simeq -\frac{0.86}{\tau}\left|\frac{\partial\widetilde{u}}{\partial x}\right|^{-1}. \tag{C.10}$$

and

$$\mu_T = -\frac{1}{2}\beta_1\overline{\rho}k\tau \simeq 0.43\overline{\rho}k\left|\frac{\partial\widetilde{u}}{\partial x}\right|^{-1} \tag{C.11}$$

Substituting μ_T in Eq. 6.1 gives the streamwise Reynolds stress as

$$\overline{\rho}R_{11} \;=\; \frac{2}{3}\overline{\rho}k - \frac{4}{3}\mu_T\frac{\partial\widetilde{u}}{\partial x} \;=\; \frac{2}{3}\overline{\rho}k + 0.573\overline{\rho}k \tag{C.12}$$

Similarly,

$$\overline{\rho}R_{22} \;=\; \frac{2}{3}\overline{\rho}k + \frac{2}{3}\mu_T\frac{\partial\widetilde{u}}{\partial x} \;=\; \frac{2}{3}\overline{\rho}k - 0.286\overline{\rho}k. \tag{C.13}$$

where $a_{ij}^{ext} = 0$ on account of $\Omega_{ij} = 0$ for all i and j. Amplification in the streamwise Reynolds stress is obtained as,

$$\frac{R_{11,d}}{k_u} = \left(\frac{2}{3} + 0.573\right)\frac{k_d}{k_u}, \tag{C.14}$$

$$\frac{R_{11,d}}{R_{11,u}} = \frac{3}{2}\left(\frac{2}{3} + 0.573\right)\frac{k_d}{k_u}. \tag{C.15}$$

Thus, the Streamwise Reynolds stress is given as

$$\frac{R_{11,d}}{R_{11,u}} = 1.86\left(\frac{\widetilde{u}_u}{\widetilde{u}_d}\right)^{2/3+0.573}, \tag{C.16}$$

Similarly, the transverse Reynolds stress is given as

$$\frac{R_{22,d}}{R_{22,u}} = 0.57\left(\frac{\widetilde{u}_u}{\widetilde{u}_d}\right)^{2/3+0.573}. \tag{C.17}$$

Appendix D

Linear interaction analysis prediction

For a purely vortical turbulence ($p'_u = 0$) interacting with a normal shock, the change in R_{11} and R_{22} across the shock can be written using the linearized RH relations,

$$\frac{1}{2}\overline{\rho_u}\ \overline{u_u}(R_{11,d} - R_{11,u}) = \underbrace{-\overline{\rho_u}\overline{u'_u u'_m}\Delta\overline{u}}_{\int P_k} + \underbrace{\overline{\rho_u}\overline{u'_m \xi_t}\Delta\overline{u}}_{\int S_k^1} \underbrace{-\overline{u'_m p'_d}}_{\int \Pi_k^1}, \tag{D.1}$$

$$\frac{1}{2}\overline{\rho_u}\ \overline{u_u}(R_{22,d} - R_{22,u}) = \underbrace{-\overline{\rho_u}\ \overline{u_u}\overline{v'_m \xi_y}\Delta\overline{u}}_{\int S_k^2}, \tag{D.2}$$

where higher order terms are assumed to be small, See Ref. [41] for details. By substituting the definition of $u'_m = (u'_u + u'_d)/2$ and $v'_m = (v'_u + v'_d)/2$ in the Eqs. (D.1) and (D.2) and normalizing with the respective upstream Reynolds stresses, we get

$$\frac{R_{11,d}}{R_{11,u}} = 1 - \underbrace{\left(1 + \frac{\overline{u'_u u'_d}}{R_{11,u}}\right)}_{C_p}\frac{\Delta\overline{u}}{\overline{u_u}} + \underbrace{\left(\frac{\overline{u'_u \xi_t}}{R_{11,u}} + \frac{\overline{u'_d \xi_t}}{R_{11,u}}\right)}_{C_{su}}\frac{\Delta\overline{u}}{\overline{u_u}} - \underbrace{\left(\frac{\overline{u'_u p'_d} + \overline{u'_d p'_d}}{\overline{\rho_u} R_{11,u}\Delta\overline{u}}\right)}_{C_{\Pi_1}}\frac{\Delta\overline{u}}{\overline{u_u}} \tag{D.3}$$

$$\frac{R_{22,d}}{R_{22,u}} = 1 - \underbrace{\left(\frac{\overline{v'_u \xi_y}}{R_{22,u}}\overline{u_u} + \frac{\overline{v'_d \xi_y}}{R_{22,u}}\overline{u_u}\right)}_{C_{sd}}\frac{\Delta\overline{u}}{\overline{u_u}} \tag{D.4}$$

where, the model coefficients are computed using LIA and plotted in Fig. (6.3).

$$C_p = 1 + \frac{\overline{u'_u u'_d}}{R_{11,u}}; \quad C_{su} = \frac{\overline{u'_u \xi_t}}{R_{11,u}} + \frac{\overline{u'_d \xi_t}}{R_{11,u}}; \quad C_{sd} = \frac{\overline{v'_u \xi_y}}{R_{22,u}}\overline{u_u} + \frac{\overline{v'_d \xi_y}}{R_{22,u}}\overline{u_u}; \quad C_{\Pi_1} = \frac{-\overline{u'_u p'_d} - \overline{u'_d p'_d}}{\overline{\rho_u}\Delta\overline{u}R_{11,u}}.$$

The Reynolds stresses and TKE show rapid variation in the acoustic adjustment region behind the shock; see Fig. (D.1). In this region, Mahesh *et al.* [75] showed that the quantity

$$\frac{\gamma \mathrm{M}}{2}\left[\frac{2k}{\overline{a}^2} + \frac{\overline{p'^2}}{\gamma\overline{p}^2}\right] + \frac{\overline{p'u'}}{\overline{pa}} \tag{D.5}$$

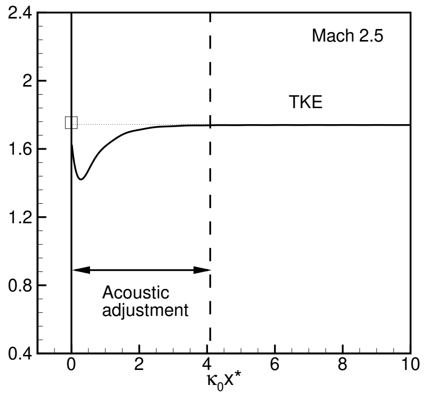

(a)

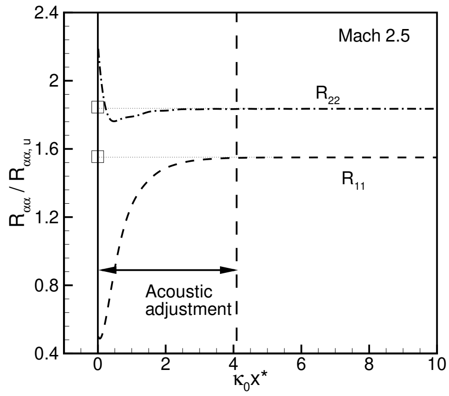

(b)

Figure D.1: LIA prediction for purely vortical isotropic turbulence interacting with a normal shock: streamwise variation of (a) turbulence kinetic energy, and (b) Reynolds stresses. The data is normalised by the respective upstream values and the wavelength corresponding to the peak upstream energy level κ_0. The shock is located at $\kappa_0 x^* = 0$, and the acoustic adjustment region is identified.

is conserved along a mean streamline behind the shockwave. The pressure fluctuations immediately behind the shock p'_d have a finite magnitude, but $p' \to 0$ beyond the acoustic adjustment region. This fact can be used to compute the net change in TKE downstream of the shock

$$\Delta k = \frac{\overline{a}_d^{\,2}}{2}\left[\frac{\overline{p'^2_d}}{\gamma \overline{p}_d^{\,2}} + \frac{2}{\gamma \mathrm{M}_d}\frac{\overline{p'_d u'_d}}{\overline{p}_d \overline{a}_d}\right]. \tag{D.6}$$

It is the integrated value of the vortical-acoustic exchange in the acoustic adjustment region described in Chapter 4 & 6 and is denoted by $\int \Pi_k^2$. An additional model coefficient C_{Π_2} is defined as

$$C_{\Pi_2} = \frac{2\bar{u} \int \Pi_k^2}{(R_{11,u}\Delta\overline{u})}$$

so that the effect of Π_k^2 can be added to the overall change in TKE in Eq. (6.22).

References

[1] H. Babinsky, J. K. Harvey, *Shock wave-boundary-layer interactions*, New York: Cambridge University Press, 2011.

[2] A. Grebert, J. Bodart, S. Jamme and L. Joly, *Simulations of shock wave/turbulent boundary layer interaction with upstream micro vortex generators*, International Journal of Heat and Fluid Flow, 72 (2018), pp. 73–85.

[3] W. Hongyu, L. Jun, J. Di, Z. Zhibo, T. Mengxiao, and W. Yun, *Manipulation of ramp-induced shock wave/boundary layer interaction using a transverse plasma jet array*, International Journal of Heat and Fluid Flow, 67 (2017), pp. 133–137.

[4] J. Boussinesq, *Theorie de l'Ecoulement Tourbillant*, Mem. Presentes par Divers Savants Acad. Sci. Inst. Fr. 23 (1877), pp. 46–50.

[5] A. N. Kolmogorov, *Equations of Turbulent Motion of an Incompressible Fluid*, Izvestia Academy of Sciences, USSR; Physics. 6 (1942), pp. 56–58.

[6] J. C. Rotta, *Statistich theorie nichthomogener turbulenz I*, Zeitschrift fur physik. 129 (1951), pp. 547–573.

[7] W. Rodi, *A new algebraic relation for calculating the Reynolds stresses*, Mechanics of Fluid. 56 (1976), T219 – T221.

[8] S. Wallin, and A. V. Johansson, *An explicit algebraic Reynolds stress model for incompressible and compressible turbulent flows*, Journal of Fluid Mechanics. 403 (2000), pp. 89–132.

[9] J. Larsson, and S. K. Lele, *Direct numerical simulation of canonical shock / turbulence interaction*, Physics of Fluids. 21 (2009), 126101.

[10] J. Larsson, I. Bermejo-Moreno, and S. K. Lele, *Reynolds- and Mach-number effects in canonical shock-turbulence interaction*, Journal of Fluid Mechanics. 717 (2013), pp. 293–321.

[11] A. A. Zheltovodov, *Some advances in research of shock wave turbulent boundary layer interactions*, AIAA Paper. 496 (2006), pp. 1–25.

[12] C. J. Roy, and F. G. Blottner, *Review and assessment of turbulence models for hypersonic flows*, Progress in Aeropsace Sciences. 42 (2006), pp. 469–530.

[13] D. Gaitonde, *Progress in shock wave/boundary layer interactions*, Prog Aerosp Sci. 72 (2015), pp. 80–99.

[14] E. Schulein, *Optical Skin Friction Measurements in Short-duration Facilities*, AIAA Journal, 44 (2006), pp. 1732–1742.

[15] D. C. Wilcox, *Turbulence Modelling for CFD*, DCW industries, Inc. (2000).

[16] S.B. Pope, *A more general effective-viscosity hypothesis*, Journal of Fluid Mech. 72 (1975), pp. 331–340.

[17] G. A. Gerolymos, and I. Vallet, *Wall-normal-free near-wall Reynolds-stress closure for 3-D compressible separated flows*, AIAA Journal. 39 (2001), pp. 1833–1842

[18] G. A. Gerolymos, E. Sauret, and I. Vallet, *Contribution to the single-point-closure Reynolds-stress modelling of inhomogeneous flow*, Theor. Comput. Fluid Dyn. 17 (2004), pp. 407–431.

[19] G. A. Gerolymos, C. Lo, I. Vallet, and B. A. Younis, *Term-by-term analysis of near-wall second moment closures*, AIAA Journal. 50 (2012), pp. 2848–2864.

[20] B. E. Launder, G. J. Reece, and W. Rodi, *Progress in the development of a Reynolds-stress turbulence closure*, Journal of Fluid Mechanics. 68 (1975), pp. 537–566.

[21] G. C. Zha, and D. Knight, *Three-Dimensional Shock / Boundary-Layer Interaction Using Reynolds Stress Equation Turbulence Model*, AIAA Journal. 34 (1996), pp. 1313–1320.

[22] J. Lee, D. B. Taulbee, and M.S. Holden, *Study of Turbulence on Supersonic Compression Surfaces Using Reynolds Stress Model*, AIAA Journal 30. (1992), pp. 1738–1746.

[23] B. E. Launder, and B. I. Sharma, *Application of the energy-dissipation model of turbulence to the calculation of flow near a spinning disc*, Letters in Heat and Mass Transfer. 1(1974), pp. 131–137.

[24] B. J. Daly, and F. H. Harlow, *Transport Equations in Turbulence*, Phys. Fluids. 13 (1970), pp. 2635–2649.

[25] B. M. Johnson, and O. Schilling, *Reynolds-averaged Navier-Stokes model predictions of linear instability.II.Shock-driven* , Journal of Turbulence. 12 (2011), pp. 1–31.

[26] J. Griffond, and S. Olivier, *Evaluation of augmented RSM for interaction of homogeneous turbulent mixture with shock and rarefraction waves*, Journal of Turbulence. 15 (2014), pp. 569–595.

[27] V. K. Veera, and K. Sinha, *Modeling the effect of upstream temperature fluctuations on shock/homogeneous turbulence interaction*, Physics of Fluids. 2 (2009), pp. 025101.

[28] C. Pantano, and S. Sarkar, *A study of compressibility effects in the high-speed turbulent shear layer using direct simulation*, Journal of Fluid Engineering. 451 (2002), pp. 329–371.

[29] W. P. Jones and B. E. Launder, *The Prediction of Laminarization with a Two-Equation Model of Turbulence*, Int. J. Heat and Mass Transfer, 15 (1972), pp. 301–314.

[30] S. S. Girimaji, *Fully Explicit and Self-Consistent Algebraic Reynolds Stress Model, Theoretical and Computational Fluid Dynamics*, 8 (1996), pp. 387-402.

[31] D. B. Taulbee, *An Improved Algebraic Reynolds Stress Model and Corresponding Nonlinear Stress Model*, Physics of Fluids A, 4 (1992), pp. 2555–2560.

[32] D. B. Taulbee, J. R. Sonnenmeier and K. M. Wall, *Stress Relation for Three-Dimensional Turbulent Flows, Physics of Fluids*, 6 (1994), pp. 1399–1401.

[33] T. B. Gatski and C. G. Speziale, *On Explicit Algebraic Stress Models for Complex Turbulent Flows*, J. of Fluid Mech., 254 (1993), pp. 59–78.

[34] W. W. Liou, G. Huang, and T.-H. Shih, *Turbulence model assessment for shock-wave/turbulent boundary layer interaction in transonic and supersonic flows*, Comput. Fluids. 29 (2000), pp. Pages 275–299.

[35] J. Forsythe, K. Hoffmann, and H.-M. Damevin, *An assessment of several turbulence models for supersonic compression ramp flow*, 29th AIAA, Fluid Dynamics Conference (1998), 98-2648.

[36] T. J. Coakley and P. G. Huang, *Turbulence modeling for high speed flows*, 30th Aerospace Sciences Meeting and Exhibit (1992). 92-0436.

[37] F. R. Menter, *Two-Equation Eddy-Viscosity Turbulence Models for Engineering Applications*, AIAA Journal. 32 (1992), pp. 1598–1605.

[38] T. J. Wray, and R. K. Agarwal, *A New Low Reynolds Number One Equation Turbulence Model Based on a k-omega Closure*, AIAA Journal. 53 (2015), pp. 2216-2227.

[39] B. Morgan, K. Duraisamy, N. Nguyen, S. Kawai, and S. K. Lele, *Flow physics and RANS modelling of oblique shock/turbulent boundary layer interaction*, Journal of Fluid Mechanics. 79 (2013), pp. 231–284.

[40] P. E. Hamlington, and W. J. A. Dahm, *Reynolds Stress Closure for Nonequilibrium Effects in Turbulent Flows*, Physics of Fluids. 20 (2008), 1151101.

[41] K. Sinha, K. Mahesh, and G. V. Candler, *Modeling shock unsteadiness in shock/turbulence interaction*, Physics of Fluids. 15 (2003), 2290.

[42] K. Sinha, K. Mahesh, and G. V. Candler, *Modeling the effect of shock unsteadiness in shock/turbulent boundary layer interactions*, AIAA Journal. 43 (2005), 586–594.

[43] C. G. Speziale, S. Sarkar, and T. B. Gatski, *Modelling the pressure-strain correlation of turbulence: an invariant dynamical systems approach* , Journal of Fluid Mechanics. 227 (1991), pp. 245–272.

[44] J. L. Lumley, *Turbulence modeling*, Advance of Applied mechanics. 18 (1978).

[45] M. M. Gibson, and B. E. Launder, *Ground effects on pressure fluctuations in the atmospheric boundary layer* , Journal of Fluid Mechanics. 86 (1978), pp. 491–511.

[46] B. E. Launder, and N. Shima, *Second-Moment Closure for the Near-Wall Sublayer : Development and Application*, AIAA Journal. 27 (1989), pp. 1319–1325.

[47] G. A. Gerolymos, E. Sauret, and I. Vallet, *Oblique-Shock-Wave/Boundary-Layer Interaction Using Near-Wall Reynolds Stress Models*, AIAA Journal. 42 (2004), pp. 1089–1100.

[48] G. A. Gerolymos, and I. Vallet, *Near-wall Reynolds stress three dimensional transonic flow computation*, AIAA Journal. 35 (1997), pp. 228–236.

[49] E. Sauret, and I. Vallet, *Near-wall turbulent pressure diffusion modelling and influence in 3-D secondary flows*, ASME J. Fluids Eng. 129 (2007), pp. 634–642.

[50] I. Vallet, *Reynolds-stress modelling of M= 2.25 shock-wave/turbulent-boundary-layer interaction*, Int J. Numer. Methods Fluids. 56 (2008), pp. 525–555.

[51] F. Ladiende, *Supersonic flux-split procedure for second moments of turbulence*, AIAA Journal. 33 (1995), pp. 1185–1195.

[52] M. Gnedin, and Doyle Knight, *A Reynolds stress equation turbulence model for compressible flows, Part-I: Flat plate boundary layers*, AIAA Journal. (1995).

[53] O. Zeman, *Dilatational dissipation: The concept and application in modeling compressible mixing layers*, Phys. Fluids A. 2(1992), pp. 178–188.

[54] R. F. Vieira, and J. L. F. Azevedo, *Turbulence Model Assessment for Simulation of Shock Wave–Boundary Layer Interaction Flows*, 31st AIAA Applied Aerodynamics Conference, 2013, 3024.

[55] J. Liu, and Z. Zhao, *Reynolds-Stress Turbulence Models for Hypersonic ShockWave/Turbulent-Boundary-Layer Interactions* , AIAA SPACE Conference and Exposition, 2014, 4413.

[56] T. Jongen, and T. B. Gatski, *General explicit algebraic stress relations and best approximation for three-dimensional flows*, International Journal of Engineering Science. 36 (1998), pp. 739–763.

[57] C. A. Gomez, and S. S. Girimaji, *Explicit algebraic Reynolds stress model (EARSM) for compressible shear flows*, Theor. Comput. Fluid Dyn. 28 (2014), pp. 171–196.

[58] T. Coratekin, J. Van Keuk and J. Ballmann, *Preliminary investigations in 2D and 3D Ramjet Inlet Design*, AIAA 99-2667.

[59] N. N. Fedorova, I. A. Fedorchenko, and E. Schulein *Experimental and numerical study of oblique shock wave/turbulent boundary layer interaction at M=5*, Comput. Fluid Dyn. J. 10 (2001), pp. 376–81.

[60] N. N. Fedorova, I. A. Fedorchenko, *Computations of interaction of an incident oblique shock wave with a turbulent boundary layer on a flat plate*, Journal of Applied Mechanics and Technical Physics. 45 (2004), pp. 358–366.

[61] R. P. Nance RP, H. A. Hassan, *Turbulence modeling of shock- dominated flows with a k2z formulation*, AIAA paper (1999), 99–0153.

[62] X. Xiao, J. R. Edwards, H. A. Hassan, R. L. Gaffney, *Role of turbulent Prandtl number on heat flux at hypersonic Mach numbers*, AIAA Paper (2005), 2005-1098.

[63] J. L. Brown, *Hypersonic shock wave impingement on turbulent boundary layers: computational analysis and uncertainty*, Journal of Spacecraft and Rockets, 50 (2013), pp. 96–123.

[64] Lindblad, I. A. A., Wallin, S., Johanson, A., Freiedrich, R., Lechner, R., Krogmann, P., Schulein, E., Courty, J., Ravachol, M., and Giordano, D., *A Prediction Method for High Speed Turbulent Separated Flows with Experimental Verification*, AIAA Paper, (1998), pp. 2547.

[65] Q. Li and G. N. Coleman, *DNS of an oblique shock wave impinging upon a turbulent boundary layer*, in Direct and Large-Eddy Simulation V, edited by R. Friedrich, B. J. Geurts, and O. Mettais Kluwer Academic, Dordrecht, 2003, pp. 387–396.

[66] S. Priebe, M. Wu, and M. P. Martín, *Direct Numerical Simulation of a Reflected-Shock- Wave/Turbulent-Boundary-Layer Interaction*, AIAA JOURNAL, 47 (2009), pp. 1173–1185.

[67] M. Wu, P. Bookey, M.P. Martin, and A.J. Smits, *Analysis of Shockwave/Turbulent Boundary Layer Interaction Using DNS and Experimental Data*, 43rd AIAA Aerospace Sciences Meeting and Exhibit, Jan 10–Jan 13, Reno, Nevada, AIAA 2005-310.

[68] S. Pirozzoli, and F. Grasso, *Direct numerical simulation of impinging shock wave/turbulent boundary layer interaction at* $M = 2.25$, Phys. Fluids, 18 (2006), pp. 065113.

[69] S. Pirozzoli, and M. Bernardini, *Direct Numerical Simulation Database for Impinging Shock Wave/Turbulent Boundary-Layer Interaction*, AIAA Journal, 49 (2011), pp. 1307–1312.

[70] J. Fang, A. A. Zheltovodov, Y. Yao, C. Moulinec, and D. R. Emerson, *On the turbulence amplification in shock-wave/turbulent boundary layer interaction*, J. Fluid Mech., 897 (2020), pp. A32-1–37.

[71] E. Garnier, P. Sagaut, and M. Deville, *Large eddy simulation of shock/boundary layer interaction*, AIAA J. 40 (2002), pp. 1935.

[72] E. Touber and N. D. Sandham, *Oblique Shock Impinging on a Turbulent Boundary Layer: Low-Frequency Mechanisms*, 38th Fluid Dynamics Conference and Exhibit, 23 - 26 June 2008, Seattle, Washington.

[73] B. Morgan, S. Kawai, and S. K. Lele, *Large-Eddy Simulation of an Oblique Shock Impinging on a Turbulent Boundary Layer*, 40th Fluid Dynamics Conference and Exhibit 28 June - 1 July 2010, Chicago, Illinois.

[74] K. Sinha, *Evolution of enstrophy in shock/homogeneous turbulence interaction*, Journal of Fluid Mechanics. 707 (2012), pp. 74–110.

[75] K. Mahesh, S. K. Lele, and P. Moin, *The influence of entropy fluctuations on the interaction of turbulence with a shock wave*, Journal of Fluid Mechanics. 334 (1997), pp. 353–379.

[76] L. S. G. Kovásznay, *Turbulence in Supersonic Flow*, J. Aeronaut. Sci. 20 (1953), pp. 657–674.

[77] H. S. Ribner, *Convection of a pattern of vorticity through a shock wave*, Tech. Rep. NACA TR 1164 (1954).

[78] H. S. Ribner, *Spectra of noise and amplified turbulence emanating from shock-turbulence interaction*, AIAA J. 25 (1987), pp. 436–442.

[79] R. Quadros, K. Sinha, and J. Larsson, *Turbulent energy flux generated by shock/homogeneous-turbulence interaction*, J. Fluid Mech. 796 (2016), pp. 113–157.

[80] Y. P. M. Sethuraman, K. Sinha, and J. Larsson, *Thermodynamic fluctuations in canonical shock–turbulence interaction: effect of shock strength*, Theor. Comput. Fluid Dyn. 32 (2018), pp. 629–654.

[81] C. Huete, E. Abdikamalov, and D. Radice, *The impact of vorticity waves on the shock dynamics in core-collapse supernovae*, Mon. Not. R. Astron. Soc. 475 (2017), pp. 3305–3323.

[82] S. Lee, S. K. Lele, and P. Moin, *Interaction of isotropic turbulence with shock waves effect of shock strength*, Journal of Fluid Mechanics. 340 (1997), pp. 225–247.

[83] K. Mahesh, S. Lee, S. K. Lele, and P. Moin, P, *The interaction of an isotropic field of acoustic waves with a shock wave*, J. Fluid Mech. 300 (1995), pp. 383–407.

[84] S. Jamme, J. B. Cazalbou, F. Torres, and P. Chassaing, *Direct numerical simulation of the interaction between a shock wave and various types of isotropic turbulence*, Flow, Turbul. Combust. 68 (2002), pp. 227–268.

[85] S. Barre, D. Alem and J. P. Bonnet, *Experimental Study of a Normal Shock / Homogeneous Turbulence Interaction*, AIAA Journal. 34 (1996), pp. 968–974.

[86] J. Ryu, and D. Livescu, *Turbulence structure behind the shock in canonical shock-vortical turbulence interaction*, Journal of Fluid Mechanics. 756 (2014), pp. 1–13.

[87] D. Livescu, and J. Ryu, *Vorticity dynamics after the shock-turbulence interaction*, Shock Waves. 26 (2016), pp. 241–251.

[88] Y. Tian, F. A. Jaberi, Z. Li, and D. Livescu, *Numerical study of variable density turbulence interaction with a normal shock wave*, J. Fluid Mech. 829 (2017), pp. 551–588.

[89] E. Garnier, N. A. Adams, P. Sagaut, *Large-eddy simulation of shock/homogeneous turbulence interaction*, ERCOFTAC Series. 7 (2009), pp. 123–134.

[90] F. Ducros, V. Ferrand, F. Nicoud, C. Weber, D. Darracq, C. Gacherieu, and T. Poinsot, *Large-Eddy Simulation of the Shock/Turbulence Interaction*, Journal of Computational Physics. 152 (1999), pp. 517–549.

[91] N. O. Braun, D. I. Pullin, and D. I. Meiron, *Large eddy simulation investigation of the canonical shock-turbulence interaction*, J. Fluid Mech. 858 (2019), pp. 500–535.

[92] N. O. Braun, D. I. Pullin, and D. I. Meiron, *Regularization method for large eddy simulations of shock-turbulence interactions*, Journal of Computational Physics. 361 (2018), pp. 231–246.

[93] I. Bermejo Moreno, J. Larsson, and S. K. Lele,*LES of canonical shock-turbulence interaction*, In Annual Research Briefs (2010), pp. 209–222.

[94] R. V. Kaenel, L. Kleiser, N. A. Adams and J. B. Vos, *Large-Eddy Simulation of Shock-Turbulence Interaction*, AIAA JOURNAL. 42(2004), pp. 2516–2528.

[95] S. Hickel, C. P. Egerer, and J. Larsson, *Subgrid-scale modeling for implicit large eddy simulation of compressible flows and shock-turbulence interaction*, Physics of Fluids. 26 (2014), pp. 106101.

[96] H. Koo, V. Raman, *Detailed numerical simulations of a supersonic inlet-isolator*, Sixth International Symposium on Turbulence and Shear Flow Phenomena, (2009).

[97] B. Morgan, K. Duraisamy, and S. K. Lele, *Large-Eddy and RANS Simulations of a Normal Shock Train in a Constant-Area Isolator*

[98] S. Mahapatra, S. Kumar, K. P. Sinhamahapatra, and S. Ghosh, *Large-eddy simulation of shock-turbulence interaction in supersonic diffuser flows*, Journal of Turbulence. 18 (2017), pp. 512–538.

[99] J. D. Schwarzkopf et al *Two-length Scale Turbulence Model for Single-phase Multi-fluid Mixing*, Flow Turbulence and Combustion. 96 (2016), pp. 1–43.

[100] J. Griffond and O. Soulard, *Evolution of axisymmetric weakly turbulent mixtures interacting with shock or rarefaction waves*, Physics of fluid, 24(2012), 115108.

[101] O. Gregoire, D. Souffland and S. Gauthier, *A second-order turbulence model for gaseous mixtures induced by Richtmyer–Meshkov instability*, J. Turbul. 6 (2005), N29.

[102] K. Sinha, and S. J. Balasridhar, *Conservative formulation of the $k - \epsilon$ turbulence model for shock-turbulence interaction*, AIAA Journal. 51 (2013), pp. 1872–1882.

[103] R. Quadros, and K. Sinha, *Modelling of turbulent energy flux in canonical shock-turbulence interaction* Int. J. Heat Fluid Flow 61 (2016), Part B, pp. 626–635.

[104] A. A. Pasha, and K. Sinha, *Shock-unsteadiness model applied to oblique shock wave/turbulent boundary layer interaction*, International Journal of Computational Fluid Dynamics. 22 (2008), pp. 569–582.

[105] A. A. Pasha, and K. Sinha, *Simulation of hypersonic shock/turbulent boundary-layer interactions using shock-unsteadiness model*, Journal of Propulsion and Power. 28 (2012), pp. 46–60.

[106] S. Roy, U. Pathak, and K. Sinha, *Variable turbulent Prandtl number model for shockwave/boundary-layer interaction*, AIAA J. 56 (2018), pp. 342–355.

[107] M. Hallback, J. Groth, and A. V. Johansson, *An algebraic model for non-isotropic turbulent dissipation rate in Reynolds stress closures*, Physics of Fluids, 1990, pp. 2276–2277.

[108] P. Raje, and K. Sinha, *A physically consistent and numerically robust $k - \epsilon$ model for computing turbulent flows with shock waves*, Computers & Fluids. 136 (2016), pp. 35–47.

[109] K. Sinha, and R. Singh, *Numerical Error in the $k - \epsilon$ Turbulence Model applied to Eddy-viscous Shock Waves*, AIAA Journal. (2016).

[110] K. Y. Chien, *Predictions of Channel and Boundary-Layer Flows with a Low-Reynolds-Number Turbulence Model*, AIAA Journal, 20 (1982), pp. 33-38.

[111] J. L. Steger, and R. F. Warming, *Flux Vector Splitting of the Inviscid Gasdynamic Equations with Application to Finite-Difference Methods*, Journal of Computational Physics, Vol. 40, No. 2, 1981, pp. 263-293.

[112] E. F. Toro, *Riemann Solvers and Numerical Methods for Fluid Dynamics: A Practical Introduction*, Cambridge University Press, 1998.

[113] C. Hirsch, *Numerical Computation of Internal and External Flows*, Vol. 1 and Vol. 2, John Wiley and Sons, 1991

[114] R. J. Leveque, *Finite Volume Methods for Hyperbolic problems*, Cambridge University Press, 2002.

[115] A. A. Pasha, 2011, *Application of shock-unsteadiness model to hypersonic shock/turbulent boundary-layer interaction*, Ph.D. thesis (IIT Bombay).

[116] R. W. MacCormack, and G. V. Candler, *The Solution of the Navier-Stokes Equations Using Gauss-Siedel Line Relaxation*, Computers and Fluids, 17 (1989), pp. 135–150.

[117] M. J. Wright, G. V. Candler, and D. Bose, *Data-Parallel Line Relaxation Method for the Navier-Stokes Equations*, AIAA Journal, 36 (1998), pp. 1603–1609.

[118] M. C. Druguet, G. V. Candler, and I. Nompelis, *Effect of Numerics on Navier-Stokes Computations of Hypersonic Double-Cone Flows*, AIAA Journal, Vol. 43, No. 3, 2005, pp. 616-623.

[119] Aso, S., Okuyama, S., Kawai, M., and Ando, Y. "Experimental study on the mixing phenomena in supersonic flows with slot injection," AIAA Paper 91-0016, 1991.

[120] Aso, S., Okuyama, S, Ando, Y., and Fujimori, T., "Two-dimensional and three-dimensional mixing flow fields in supersonic flow induced by injected secondary flows through traverse slot and circular nozzle," In 31st Aerospace Sciences Meeting, pp. 489. 1993.

[121] Spaid, F. W., and Zukoski, E., "Secondary injection of gases into a supersonic flow," AIAA journal, Vol. 2, No. 10, 1964, pp. 1689-1696.

[122] Spaid, F. W., and Zukoski, E., "A study of the interaction of gaseous jets from transverse slots with supersonic external flows," AIAA journal, Vol. 6, No. 2, 1968, pp. 205-212.

[123] Amick J. L., and Hawk, N. E., "Two-dimensional secondary jet interaction with a supersonic stream," AIAA Journal, Vol. 5, No. 4, 1967, pp. 655-660.

List of Publications

Journals:

1. **Vemula, J. B.** and Sinha, K. "Reynolds stress models applied to canonical shock-turbulence interaction", Journal of Turbulence, Vol. 18, No. 7, 2017, pp. 653–687.

2. **Vemula, J. B.** and Sinha, K. "Explicit Algebraic Reynolds stress models applied to shock wave turbulent boundary layer interaction flows", International Journal of Heat and Fluid flow, Vol. 85, 2020, 108680.

International Conferences

1. **Vemula, J. B.** and Sinha, K. "Reynolds stress models applied to canonical shock-turbulence interaction", 9^{th} International Symposium on Turbulence and Shear Flow Phenomena (TSFP-9), July, 2015, Melbourne, Australia.

2. **Vemula, J. B.** and Sinha, K. "Study of Reynolds stress anisotropy across shock turbulence interaction using EARSM", 32^{nd} International Symposium on Shock Waves (ISSW32), July, 2019, National University of Singapore, Singapore.

National Conferences

1. **Vemula, J. B.**, Pathak, U. and Sinha K. "Comparative analysis of ramp-type and Busemann intakes of air-breathing engine", National Aerospace Propulsion Conference (NAPC-2017), March 15-17, 2017, IIT Kanpur, India.

2. **Vemula, J. B.**, Raje P., Singh, R., Roy, S. and Sinha K. "Parameteric study of the performance of two-dimensional Scramjet Intake", 18th Annual AeSI CFD Symposium, August 10-11, 2016, CSIR-National Aerospace Laboratories, Bangalore, India.

The author of this dissertation wrote these papers and manuscripts in part or in full, performed the required numerical simulations, and analyzed the results of the simulations. The co-authors on these works provided feedback during these studies, assisted in editing the manuscripts, and were instrumental in determining the model problem and solution procedures.

Acknowledgements

I would like to express my deep sense of gratitude to my advisor, Prof. Krishnendu Sinha, Dept. of Aerospace Engg., Indian Institute of Technology (IIT) Bombay, Mumbai, India, for his invaluable help and guidance. I am highly indebted to him for giving his critiques on my work and for the thought provoking discussions. His guidance during the model development was immense, and is duly appreciated.

I thank the entire faculty and staff of the Dept. of Aerospace Engg., IIT Bombay (past and present) who supported me directly and indirectly during my PhD tenure. The courses of Profs. Avijit Chatterjee (*Numerical methods*), Prof. Amitabh Bhattacharya (*Turbulence*) and Krishnendu Sinha (*Computing of High Speed Flows*) were very interesting, and I was able to use some of the concepts in my research.

I thank my fellow labmates (past and present), Drs. Russell and Bijaylakshmi, Ashwin, Rachit, Yeshwanth, Naveen Rohilla, Vishnu, Pratik, Subhajit, Utkarsh, Pranav, and Yogesh for their help and support. Special thanks are due to our lab secretary, Mukesh, running errands for me during this long tenure of mine.

I thank my dear friends, Deepak, Sourab, Abhinav, Malay, Pranav Patel, and Abhimanyu for their amazing support during my Ph.D. There are many others whom I have not mentioned here, but I thank them all for their helping over the years. A huge thanks to the open-source community for obvious reasons. Financial support was provided as Ph.D. Teaching Assistantship by the Ministry of Human Resources and Development (MHRD) and additional financial support was availed from the Industrial Research & Consultancy Centre, IIT Bombay.

Last but not the least, I thank my parents and brothers for their continuous support and encouragement during my Ph.D. at IIT Bombay. Their contribution in every aspect of my education and life, cannot be overstated.

Jagadish Babu Vemula

IIT Bombay